Development of the two-dimension Digital Image Correlation method (2D-DIC) at high temperatures applicable for titanium alloys forming process

Linh Phuong Luong

Université Fédérale

Toulouse Midi-Pyrénées

THÈSE

en vue de l'obtention du

DOCTORAT DE L'UNIVERSITÉ DE TOULOUSE

délivré par

IMT – École Nationale Supérieure des Mines d'Albi-Carmaux

---

présentée et soutenue par

Linh Phuong LUONG

le 08 Mars 2021

Development of the two-dimension Digital Image Correlation method (2D-DIC) at high temperatures applicable for titanium alloys forming process

---

École doctorale et discipline ou spécialité :

MEGEP : École Doctorale Mécanique, Énergétique, Génie civil & Procédés

Spécialité : Génie Mécanique, Mécanique des Matériaux

Unité de recherche :

Institut Clément Ader, UMR CNRS 5312, IMT Mines Albi

Directeurs de thèse :

Luc PENAZZI, Maître-Assistant, HDR, IMT Mines Albi

Rébecca BONNAIRE, Maître-Assistante, IMT Mines Albi

Autres membres du jury :

Hervé LAURENT, Professeur, Université de Bretagne Sud, Lorient *(Rapporteur)*

Bertrand WATTRISSE, Professeur, Université de Montpellier, Montpellier *(Rapporteur)*

Franck TOUSSAINT, Professeur, Université de Savoie Mont Blanc, Annecy *(Président)*

Jean-Noël PERIE, Maître de conférence, HDR, Université Paul Sabatier, Toulouse *(Examinateur)*

Vincent VELAY, Maître-Assistant, IMT Mines Albi, Albi *(Invité)*

Cette thèse de doctorat a fait l'objet d'un co-financement entre la région Occitanie et l'établissement IMT Mines Albi (Programme 09A61 909 9092, Dossier : 2017 001838)

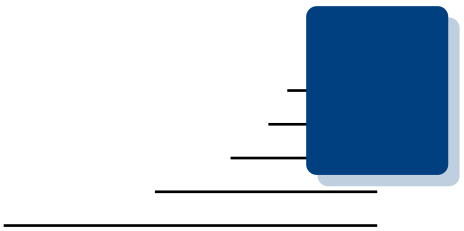

Acknowledgment

Time flies so fast. I still remembered the interview for the Ph.D thesis and now, I have finished my Ph.D thesis after three years and five months in the ICA laboratory at IMT Mines Albi.

The author would like to begin by thanking the IMT Mines Albi engineering school and the Occitanie Region for financial aid towards this PhD project ("program 09A61 909 9092, Dossier: 2017 001838").

I would like to thank Professor Thierry Cutard and Professor Thierry Sentenac and the directional board for the their warm welcoming in the ICA lab in Albi.

I would like to thank my supervisors: Dr. Luc Penazzi and Dr. Rébecca Bonnaire for all their support, investment and guidance. I thank them for their confidence in me when giving me a such challenging Ph.D thesis, a complex research theme yet motivation subject. I also thank Mr. Pierre Montmitonnet for his kindness when writing his recommendation letters to apply this Ph.D thesis.

I would like to thank Professor Frank Toussaint at the Université de Savoie Mont Blanc for giving me the honor of chairing the jury. I thank equally Professor Hervé Laurent at the Université de Bretagne-Sud and Professor Bertrand Wattrisse for agreeing to be the reviewers of this manuscript. I send my acknowledgment to Dr. Jean-Noël Périé and Dr. Vincent Velay for his participation as the member of the jury and his scientific advice during this thesis.

I thank all the researchers in ICA lab for their scientific help (Professor Orteu, Professor Le Maoult, Dr. Pottier, Dr. Berthet, Dr. Gaborit (expert in LaTeX)), the technical board of the ICA lab (Dr. Rémi, Dr. Medhi, Didier, Thomas, Fabrice, Karine, Adrien, Sabine and Jean-Michel) and of course Mr. Philippe Farenc and also the directory assistance board (Esther and Kathy). Specially thanks to my colleagues Anh Tuan, Cong Hanh, Maxime, William, Quentin, Camille, Lisa, Jennyfer, Morgane, Laurie, Florian, Stella, Abdel, Benjamin, Ji Won, Lilia, Tarek and Sabrine, we really had a good time together. Some of them became my best friends, we shared difficulties and happiness of the Ph.D lifetime. I thank them for their technical help and mental support, I can not finish my thesis without them.

Finally, I thank all the members of my family, my Mom and my brother for supporting me through all the up and down moments during more than three years. I don’t forget my best Vietnamese friends: Thu, Ha Phuong, Loan, Tien, Quynh, Son for their supports. Last but not least, I send a big hug to Maria and Anna (Maria and Anna, I wrote this thesis for you!)

A page closed and another opens, hope that I will stay curious, "opened eyes" to science as I was in my Ph.D thesis. Thank you all!

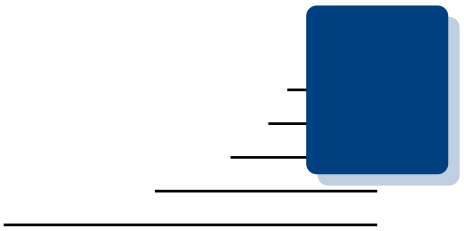

Contents

List of Figures

List of Tables

Resumé étendu de thèse en français

Introduction

Introduction aux procédés de mise en forme à chaud et à la méthode de corrélation d'images numériques (DIC)

Depuis les années 1960, l'alliage de titane est un des matériaux le plus utilisé dans plusieurs domaines industriels dont l'industrie aéronautique et spatiale grâce à ses avantages : léger, bonne résistance mécanique et thermique, bonne résistance à la corrosion et bonne compatibilité avec les matériaux composites (Vanderhasten, 2007). Parmi les alliages de titane, le Ti-6Al-4V (TA6V) représente 40% du volume total employé pour un avion depuis l'année 2000 (Inagaki *et al.*, 2014). Ce matériau est fréquemment utilisé sous formes de tôles pour fabriquer des composants de la structure du fuselage et de l'aile, de la structure et du carénage du mât réacteur, du bouclier d'entrée d'air de réacteur, par des procédés de mise en forme à chaud tel que l'emboutissage à chaud ou le formage superplastique (Figure 2).

Le procédé de formage supersplastique (SPF) consiste à chauffer la tôle de TA6V à une température de 880 °C à 920 °C puis déformer le matériau avec une faible vitesse de déformation (de $10^{-5}s^{-1}$ à $10^{-2}s^{-1}$) (Ghosh *et al.*, 1979). Cette opération est contrôlée par les cycles de pression d'un gaz neutre (type Argon) (Figure 3a) (Rollin *et al.*, 2016). A la fin de cette opération, la pièce a une épaisseur homogène et elle ne possède pas de contrainte résiduelle. Mais le refroidissement de la pièce et son extraction de l'outil (moule) peut créer des contraintes résiduelles qui induisent une distorsion géométrique de la pièce (Figure 3b).

Le procédé d'emboutissage à chaud (de 750 °C à 890 °C) (Stutz *et al.*, 2014) ou à tiède (de 400 °C à 600 °C) (Sirvin *et al.*, 2019) pourrait être une des solutions alternatives pour réduire le temps et l'énergie consommée dans le formage superplastique. Dans les conditions de l'emboutissage à tiède, l'élongation maximale du matériau est deux fois plus grande et l'effet du retour élastique (springback) est diminué d'un facteur par rapport à celui du matériau à température ambiante. Un exemple de procédé d'emboutissage à chaud proposé par Stutz et al. est présenté dans la Figure 4a (Stutz *et al.*, 2014). Tout d'abord, l'outil (matrice, serre-flan) et la tôle sont chauffés à la température de mise en forme par un four. Ensuite, le poinçon se déplace verticalement avec une vitesse constante pour déformer la tôle. A la fin de sa course, il retrouve sa position initiale. Enfin, la pièce est refroidie et extraite de la matrice.

L'effet du retour élastique pendant le refroidissement est encore une problématique dans l'emboutissage à chaud / à tiède. Une meilleure compréhension de cet effet pendant le refroidissement est nécessaire afin de réduire la distorsion de la pièce. Par exemple, la Figure 4b présente la forme d'une pièce en forme Omega (en 2D) après l'emboutisage à 400 °C et à 500 °C (Sirvin *et al.*, 2019). L'auteur a remarqué une différence entre la forme finale (en rouge et en vert) et celle de référence (en noir) à cause du retour élastique du matériau, caractérisée par deux angles α et β. Sur cette figure, il est observé que le retour élastique à 400 °C est plus important que celui à 500 °C. Le retour élastique dépend non seulement de la température mais aussi des propriétés mécaniques (le module de Young) du matériau dans les conditions d'emboutissage à chaud. Pour comprendre le retour élastique du matériau, il est nécessaire d'identifier son comportement mécanique en fonction de la température (Sirvin *et al.*, 2019 et Odenberger, 2005).

Actuellement, l'utilisation de jauges de déformation est l'une des méthodes les plus fiables pour accéder à la déformation du matériau (Sciammarella *et al.*, 2012). Cependant, cette méthode offre seulement une mesure moyennée de la déformation sur la Zone d'Intérêt (ZOI). D'autre part, la mesure par les jauges de déformations n'est pas adaptée pour suivre la mise en forme des

tôles. De plus, les jauges de déformation pourraient influencer la rigidité du matériau à hautes températures lors de la mise en place qui induirait une mesure biaisée (Sharpe, 2008).

Les méthodes sans contact telles que l'interférométrie, la méthode des grilles, etc. pourraient être des solutions alternatives (Sciammarella *et al.*, 2012). Ces méthodes permettent d'accéder à des champs de mesure de déplacement / déformation, et parfois sans limites (certaines méthodes, par exemple la méthode Corrélation d'Images Numériques (DIC) peuvent mesurer jusqu'à près de la rupture, ce qui est un énorme avantage par rapport aux jauges de déformation. La corrélation d'images numériques est actuellement la plus utilisée grâce à son implémentation simple (Sutton *et al.*, 2009). Depuis les années 1980, la méthode a été appliquée pour plusieurs types de matériaux dans le domaine de la mécanique du solide : des biomatériaux, des métaux et alliages, des polymères aux céramiques, des matériaux réfractaires. Cette méthode est réputée pour sa bonne précision et résolution spatiale. Dans les "meilleures conditions expérimentales", la résolution spatiale de cette méthode peut atteindre le sous-pixel (Sutton *et al.*, 2017). Elle peut être appliquée pour mesurer les champs cinématiques (le déplacement / la déformation surfacique) (2D-DIC ou 3D-DIC) ou dans le volume des matériaux. D'après Dong et al., depuis les années 2000, le nombre de publications liées au développement et application en méthode DIC dans la mécanique expérimentale a augmenté exponentiellement (Dong *et al.*, 2017).

Problématiques de la méthode DIC pour la mesure de champs cinématiques à hautes températures

Les développements récents de la méthode 2D-DIC et 3D-DIC visent à augmenter la résolution spatiale. De plus, les algorithmes développés sont améliorés pour adapter aux conditions défavorables des tests expérimentaux : une faible intensité de l'éclairage ou des problèmes de saturation à hautes températures (Sutton *et al.*, 2017). Le développement de la méthode DIC pour les conditions extrêmes, en particulier à hautes températures dans un espace limité est encore un challenge dans ce domaine (Chartrel, 2016).

Les conditions d'emboutissage à chaud ne sont pas favorables pour les mesures de déformation par la méthode DIC. Tout d'abord, des mesures en grandes déformations (plus de 50%) et à hautes températures (de 400 °C à 750 °C) avec des mouchetis sont requises. La méthode de création des mouchetis à partir de peintures sont celles les plus utilisées (Dong *et al.*, 2017). Cependant, la plupart des peintures peuvent résister seulement pour une déformation de 20% à 50% (Dong *et al.*, 2017). Il est donc nécessaire de développer une méthode de création des mouchetis qui permet une mesure de déformation dans la gamme de température d'emboutissage à chaud et en grandes déformations.

Deuxièmement, la mise en place d'un système DIC appliquée à l'emboutissage à chaud est difficile car la matrice, le poinçon et la tôle sont souvent chauffés dans un four fermé. De plus, pendant l'emboutissage, le matériau est déformé plastiquement et souvent associé à un déplacement et une déformation hors plan. Dans ce cas, une décorrélation aurait lieu à cause de défocalisation de l'image (Chartrel, 2016). En plus, en raison de la radiation du four à hautes températures, le rapport Signal / Bruit (S/N) est diminué quand la température augmente, la mesure serait donc moins fiable (Thai *et al.*, 2019). Certains auteurs ont même mentionné que la saturation des pixels a rendu les mesures impossibles (Valeri *et al.*, 2017, B. Pan *et al.*, 2010a). Pour ces raisons, il est important de trouver une mise en place du système DIC approprié aux conditions du procédé d'emboutissage à chaud (à hautes températures et dans un espace limité) pour minimiser les erreurs.

Enfin, l'effet mirage ou des vagues de chaleurs, causé par un gradient de température entre la caméra et l'objet est aussi un challenge dans le domaine de la DIC. L'effet mirage peut être facilement observé dans la vie quotidienne, par exemple, l'effet d'une plaque d'eau sur la route dans une journée très chaude en été, une île virtuelle observée au milieu d'un désert ou un objet vu à travers d'un flux de gaz très chaud. L'effet mirage cause une distorsion permanente de l'objet (Delmas *et al.*, 2013). Dans la méthode DIC, une mesure influencée par l'effet mirage est mal interprétée comme un déplacement ou une déformation mécanique du matériau. Ces "fausses" mesures de déformations peuvent atteindre de 0,2% à 5% (Jones *et al.*, 2018). Les mesures cinématiques par la méthode DIC sont donc moins fiables à hautes températures (moins précises et plus dispersées). Il est donc impératif de corriger les erreurs en mesure cinématique à hautes températures pour améliorer la précision de la méthode.

Objectif de la thèse

Après avoir identifié les problématiques majeures de la méthode DIC à hautes températures, l'objectif de cette thèse est d'améliorer la méthode DIC en deux dimensions (2D-DIC) pour la mesure de champs cinématiques dans les conditions d'emboutissage à chaud (400 °C-750 °C). Cette thèse est focalisée sur trois problématiques : la création des mouchetis, la perte de contraste et l'effet mirage. L'objectif de cette thèse est de :

1. proposer une méthode de création des mouchetis qui pourrait résister de hautes températures et de grandes déformations ($\geq$100 % de déformation mécanique)
2. trouver une méthode de mise en place de système 2D-DIC dans les conditions de l'emboutissage pour obtenir des images de haute qualité (meilleur contraste, sans problème de saturation)
3. suggérer une méthode de correction pour le champ de déformation "faussé" à cause de l'effet mirage

Structure de la thèse

Le manuscrit de thèse est composé de cinq chapitres :

Le chapitre 1 présente des différentes méthodes de mesures de champs cinématique appliquées dans la mécanique expérimentale. Les méthodes en contact (les jauges de déformation et le capteur de fibre optique) ainsi que les méthodes sans contact comme la photoélasticité, l'interférométrie, les méthodes non-interférométrique périodiques, les méthodes non-interférométriques aléatoires tel que la 2D-DIC avec deux approches locale et globale sont détaillés.

Du chapitre 2 au chapitre 5, chaque chapitre aborde une problématique de la méthode DIC à HT citée ci-dessus. Chaque chapitre est structuré de manière identique : l'état de l'art sur la problématique spécifique, la méthodologie, les résultats et discussions pour finir avec les conclusions et perspectives.

Le Chapitre 2 est dédié aux méthodes de création mouchetis pour des mesures à haute température et en grandes déformations. Six techniques de création des mouchetis, classifiées en deux familles : additive et soustractive sont présentées. Les mouchetis créés par ces six techniques sont comparés en termes de contraste et d'adhérence à la surface de l'éprouvette / la tôle TA6V pour trouver une méthode appropriée aux conditions de l'emboutissage à chaud.

Le Chapitre 3 aborde le problème de perte de contraste à hautes températures et la mise en place du système 2D-DIC dans un espace limité (four fermé). Le chapitre commence par une synthèse des éléments influençant le contraste de l'image. Ensuite, un plan d'expériences qui détermine l'influence de chaque facteur sur le contraste de l'image est présenté. Le chapitre se termine par une configuration du système 2D-DIC adapté aux conditions des essais expérimentaux.

Le Chapitre 4 est dédié aux caractérisations des erreurs de mesure de la méthode 2D-DIC à hautes températures. Ces erreurs dépendent probablement du flux convectif dans le four fermé. Elles sont mesurées par la technique de plan-arrière (BOS). Les caractéristiques de ces erreurs (la fréquence et l'amplitude) qui dépendent de la température sont ensuite utilisées dans le chapitre suivant.

Le Chapitre 5 suggère des méthodes de correction pour réduire l'erreur de mesure 2D-DIC à cause de l'effet mirage. En se basant sur la caractéristique spatio-temporelle de l'erreur, un post-traitement en utilisant les filtres passe-bas est utilisé. Cette méthode est ensuite appliquée pour deux types d'essais mécaniques pour montrer la faisabilité des méthodes de corrections : le premier est des essais de traction à hautes températures pour mesurer le module de Young du matériau et le second correspond à des essais de mesure du coefficient de dilatation du TA6V de 100 °C à 600 °C.

Présentation des résultats expérimentaux du manuscrit

Chapitre 2 : Méthodes de créations des mouchetis pour la méthode DIC à hautes températures

Ce chapitre est focalisé sur les techniques de création des mouchetis pour le but d'améliorer la résolution spatiale et la précision de mesure par la méthode 2D-DIC en respectant des critères "bons mouchetis" pour la méthode DIC. De plus, les mouchetis doivent résister à de hautes températures et de grandes déformations. Après une revue sur les méthodes de création des mouchetis à haute température, six techniques de réalisation des mouchetis ont étudiés. Elles sont :

- Peinture (M1)
- Anodisation directe (M2)
- Anodisation inversée (M3)
- Gravure laser (M4)
- Combinée gravure laser et anodisation (M5)
- Combinée gravure laser et peinture (M6)

Les six motifs sont similaires car ils sont bien définis à partir d'un motif numérique qui respecte des critères pour les mouchetis recommandées pour la méthode DIC (Dong *et al.*, 2017). Les six techniques sont divisées en deux groupes. Dans le premier groupe, les mouchetis sont fabriqués par une méthode "additive" (M1, M2, M3) dont les motifs sont copiés à partir des motifs d'un masque polymère et la technique de lithographie. Dans le deuxième groupe, les mouchetis sont fabriqués par une méthode "soustractive" (M4, M5, M6) à partir d'une source laser. Les six

motifs de mouchetis (M1-M6) sont ensuite comparés et évalués en termes de caractéristiques morphologiques (la densité, le rayon et la distance entre les mouchetis) ainsi que la qualité (le contraste global caractérisé par le gradient de l'intensité moyennée (MIG), le niveau de gris dynamique, l'entropie de Shannon (E) et le pourcentage de pixels saturés) et enfin l'adhérence de ces mouchetis aux éprouvettes de TA6V lors des essais mécaniques.

Dans la technique "additive", le masque avec des motifs de mouchetis, qui peut être réutilisé est d'abord produit. Pour créer ce masque, un plan d'expériences de neuf essais qui combine les trois paramètres de la source laser (vitesse (V), puissance (P) et stratégie (S) est réalisé. Les valeurs des paramètres finaux pour créer proprement ce masque sans les endommager sont : Puissance (P) = 80 W, Vitesse (V) = 80 mm s^{-1} et Stratégie mixte de hatchure (H) et de contour (C) (H + C).

Les Figures 2.9 et 2.13 présentent six motifs de mouchetis créés par les méthodes "additives" et "soutractives" à température ambiante.

Tout d'abord, il est observé que les motifs de mouchetis créés par la technique M1 et M2 sont bien répliqués à partir du celui du masque polymère. Cependant, avec la technique M3, les motifs sont moins bien définis. Les mouchetis créés par les techniques M4, M5, M6 sont similaires à ceux du mouchetis numériques.

Les mouchetis créés par les techniques M1, M2, M3 ont les rayons de 100 µm à 150 µm, les densités sont de 0,1 à 0,34 et la distance entre les mouchetis est environ 300 µm. Pour les mouchetis créés par les méthodes soustractives, une source de laser de P = 30 W, V = 80 mm s^{-1} et S = C + H ne modifie pas la microstructure du matériau TA6V et donc le comportement mécanique après la gravure laser. Ces techniques pourraient créer des mouchetis ayant le rayon de 89 µm à 114 µm et une distance entre les mouchetis de 185 µm.

Les Tableaux 2.7 et 2.8 comparent la qualité des mouchetis (le MIG, l'entropie et le % de pixels saturés) crées par six techniques à température ambiante, à 600 °C et à 700 °C. Les mouchetis présentant les grandes valeurs de MIG, d'entropie et d'un faible pourcentage de pixels saturés présentent la meilleure qualité. Les résultats montrent qu'à 600 °C, le contraste de l'image des motifs de mouchetis est diminué à cause de l'oxydation de TA6V. Le motif de mouchetis créé par la technique M4 est le plus affecté. Son MIG à 600 °C est diminué de 62% par rapport celui à 25 °C. Les autres motifs créés par les autres techniques M1, M5 et M6 ont la valeur MIG de moins de 20% à 600 °C. Parmi ces motifs de mouchetis, celui créé par la technique M5 présente la meilleurs qualité. A 700 °C, la qualité de mouchetis continue à diminuer. Parmi les motifs, ceux créés par les techniques M2 et M4 sont les plus affectés. Ils ne sont pas clairement visibles à l'oeil. Les valeurs de MIG sont respectivement diminuées de 53% et 46% pour les motifs M2 et M4. Le motif créé par la technique M5 ne présente pas le meilleur contraste à cette température car sa valeur de MIG est diminuée de 32%. Parmi les motifs, ceux crées par les techniques M1 et M6 sont encore visibles à l'oeil nu. Malgré la dimimution en valeur de MIG et de l'entropie, ils présentent le meilleur contraste à 700 °C.

L'adhérence de mouchetis sur les éprouvettes TA6V créés par les quatre techniques est présentée en Figure 2.16. Il est observé que les motifs créés par les techniques de gravure laser (M4 et M5) ont bien résisté de grandes déformations (200%) alors que ceux créés en utilisant les peintures (M1 et M6) n'ont tenu qu'à 20% de déformation.

Un guide pour le choix de technique de réalisation des mouchetis a été proposé. A température ambiante, les mouchetis créés par la technique M2 (anodisation directe) présente une meilleure qualité en termes de morphologie et de qualité d'image. A 600 °C, les mouchetis fabriqués par

la technique M5 (combinée anodisation et gravure laser) présente le meilleur contraste (MIG = 12,5 et Entropie = 6,86) et une bonne adhérence sur la surface de TA6V : déformation = 200%), malgré un faible pourcentage de pixels saturés à cause de l'oxydation. A 700 °C, les mouchetis créés par la technique M1 (peinture) et M6 (combinée gravure laser et peinture) présentent un meilleur contraste que les autres techniques. Cependant, ils ne peuvent tenir que jusqu'à une déformation de 20% en raison de problème d'écaillage de peinture en grandes déformations.

Chapitre 3 : Contraste de l'image et mise en place du système 2D-DIC adapté pour les essais mécaniques à hautes températures

Dans ce chapitre, la mise en place du système 2D-DIC adapté aux conditions de l'emboutissage à chaud a été étudiée. La difficulté de mise en place du système est que de 400 °C à 750 °C, une saturation des pixels pourrait se produire et une mise en place est réalisée dans un espace limité (four fermé). La mise en place du système 2D-DIC a été réalisée avec les matériels disponibles au laboratoire (Figure 3.7) : une caméra avec un capteur CCD, un filtre infrarouge IR, une source d'éclairage et un verre couleur pour changer la couleur de la source d'éclairage. Après avoir étudié les conditions de mesures expérimentales et caractérisé les spectres de l'éclairage, du filtre IR, du verre de couleur, l'efficacité quantique du capteur CCD, le système 2D-DIC comprenant les différents équipements est rangé dans l'ordre suivant : filtre IR-camera-verre couleur-éclairage.

Pour évaluer l'influence des paramètres (source d'éclairage, filtre IR, couleur de l'éclairage et intensité de l'éclairage) à 600 °C, un plan d'expériences de quatre facteurs et deux niveaux a été réalisé. Le résultat par analyse de variance montre que deux facteurs ont une influence majeure sur le contraste global et l'entropie de l'image. C'est pour le jeu de paramètres : filtre IR pour atténuer la radiation de l'objet et de l'environnement ainsi qu'un temps d'exposition de 120 ms, que l'image pour la mesure de champs de déformations présente le meilleur contraste (MIG = 21,45 et entropie = 6,90) (Figure 3.8).

Par ailleurs, à hautes températures (plus de 600 °C), les pixels sont saturés à cause de l'oxydation du TA6V développée à la surface du matériau. Il est probable que la réflexion qui cause la saturation des pixels est venue de la couche d'oxyde créée après la gravure laser (Figure 3.14). Dans cette étude, il n'y a pas encore de solution. Pour franchir ce problème, la taille de l'imagette (subset) doit être suffisamment large : 39 pixels x 39 pixels (équivalent à une dimension de 308 µm x 308 µm).

Chapitre 4 : Influence de l'effet mirage aux mesures mécaniques à hautes températures par la méthode 2D-DIC

Dans ce chapitre, l'erreur de mesure en déformation de la méthode 2D-DIC liée à l'effet mirage a été caractérisée par la technique du plan arrière (BOS) (Raffel, 2015). L'erreur de mesure est caractérisée à chaque température, de 400 °C à 750 °C par les essais mécaniques dans les conditions isotherme et statique dans un four à résistances électriques (Figure 4.5). La zone d'intérêt (ZOI) de l'éprouvette plane TA6V est utilisée comme le plan arrière pour la mesure d'erreur de la méthode 2D-DIC à hautes températures. La valeur d'erreur de mesure est superposée à celle de l'erreur aléatoire qui dépend du flux convectif présent dans le four.

Les Figures 4.18a et 4.18b présentent l'erreur spatiale dans les deux directions du plan de l'éprouvette (Ox et Oy) de la méthode 2D-DIC en déformation, caractérisée par la différence

entre les valeurs de déformation maximale et minimale $\Delta e = e_{max} - e_{min}$ pour la gamme de température de 25 °C à 750 °C. L'erreur spatiale à 25 °C est inférieure à $2 \cdot 10^{-4}$. De 400 °C à 750 °C, cette erreur est plus importante, plus de $2 \cdot 10^{-3}$. En particulier, à 750 °C, l'erreur spatiale est environ de $6 \cdot 10^{-3}$, ce qui est du même ordre de grandeur que la déformation élastique du matériau (Lemaitre *et al.*, 2020).

Les Figures 4.20 et 4.21 présentent respectivement l'erreur de mesure de déformation par la méthode 2D-DIC dans les directions horizontale et verticale d'un point fixe situé sur la zone utile pendant 30 secondes. Il est observé que l'erreur de mesure est probablement aléatoire en présence des valeurs très hautes (pics) et des basses (vallées) à chaque instant. Cette erreur temporelle augmente avec la température car le nombre de perturbations (pics et vallées) augmente avec la température.

L'erreur spatio-temporelle de la mesure 2D-DIC à haute température est enfin calculée par la distribution normale des erreurs mesurées à tous les points de la zone utile pendant les essais. Les valeurs moyennes varient avec la température : $-4 \cdot 10^{-5} \pm 9{,}0 \cdot 10^{-5}$ en direction horizontale et $-1{,}6 \cdot 10^{-4} \pm 5{,}4 \cdot 10^{-5}$ en direction verticale à 25 °C, $7{,}7 \cdot 10^{-5} \pm 4{,}4 \cdot 10^{-4}$ en direction horizontale et $-3{,}83 \cdot 10^{-4} \pm 1{,}2 \cdot 10^{-3}$ en direction verticale à 750 °C. Les variations sont plus grandes que les valeurs moyennes car le flux convectif est probablement turbulent et les mesures à un instant sont aléatoires.

Chapitre 5 : Méthodes de corrections minimisant les erreurs de mesures de déformations par la méthode 2D-DIC due à l'effet mirage

Ce dernier chapitre est dédié aux méthodes proposées pour corriger les erreurs de mesure de la méthode 2D-DIC et dans les cadres d'essais mécaniques à hautes températures. A partir des valeurs d'erreur spatiale et temporelle de la méthode 2D-DIC à hautes températures, des filtres numériques passe-bas sont appliqués aux mesures de déformations par la méthode 2D-DIC pour les essais mécaniques à haute températures.

Tout d'abord, un filtre temporel est appliqué pour corriger l'erreur pour les valeurs de déformation en fonction du temps lors des essais mécaniques. Il est montré que parmi les filtres temporels, le filtre fréquentiel passe-bas est plus efficace en éliminant les valeurs aléatoires (bruit) due à l'effet mirage rencontré pendant l'essai mécanique. La Figure 5.6 présente la courbe de déformation du matériau TA6V lors de l'essai de traction à 500 °C. Il est montré qu'à partir des fréquences inférieures à 0,2 Hz (fréquence de coupure du filtre numérique), le bruit (erreur temporelle) est quasiment éliminé tout en gardant les valeurs de déformation mécanique, qui sont les signaux apparaissent à basse fréquence (0 Hz).

Ensuite, l'erreur spatiale est corrigée par le filtre spatial Gaussien. Un algorithme (L'algorithme 1) est appliqué pour les champs de déformation ayant une erreur spatiale supérieure à $2{,}5 \times 10^{-4}$ pendant les essais mécaniques à hautes températures. Les mesures "totales" comprenant la déformation mécanique et l'erreur à un temps donné pendant les essais sont utilisées comme des entrées. Tout d'abord, l'initialisation est calculée à partir de l'erreur spatiale en direction longitudinale à 25 °C et utilise les paramètres de filtre Gaussien avec un rayon $r_o = 5$ et une intensité $\sigma_o = 5$ (valeurs impaires). Une boucle d'optimisation qui minimise les erreurs inférieures à celle à 25 °C par la recherche des valeurs de r_o et σ_o puis applique le filtre Gaussien sur les mesures totales et réévalue l'erreur de mesures spatiales à chaque itération.

Un exemple de champs de déformation à un instant donné (t = 200 s) pendant l'essai de traction d'une éprouvette de TA6V à 500 °C est présenté à la Figure 5.11 (Figure 5.11b : avant et Figure 5.11a : après filtrage spatial). On observe qu'après le filtrage spatial, l'erreur de mesure à hautes températures soit une valeur de 0,012 est réduite à une valeur équivalente de celle de la température ambiante.

Enfin, la méthode de correction en utilisant les filtres spatiaux et temporels précédents est appliquée aux essais mécaniques à hautes températures pour déterminer les paramètres élastiques (le module de Young et le coefficient de dilatation) du matériau TA6V à hautes températures. Deux types d'essais mécaniques sont réalisés : les essais de traction pour déterminer le module de Young et un essai de dilatation thermique sur l'éprouvette de traction pour déterminer le coefficient de dilatation thermique du matériau. Les champs de déformation sont mesurés par la méthode 2D-DIC puis corrigés par les filtres temporels et spatiaux passe-bas.

La Figure 5.18 compare une courbe de traction chargement-déchargement d'un essai mécanique de TA6V à 400 °C avant et après la correction. Il est montré qu'avant le filtrage, la courbe de traction est bruitée à cause de l'erreur spatio-temporelle en déformation à haute température. Après le filtrage, la courbe devient plus lisse que celle initiale, le champ de déformation est plus homogène, car l'éprouvette reste encore en déformation élastique.

Le Tableau 5.8 présente la valeur de module Young du matériau TA6V avant et après la correction et le coefficient de régression linéaire R^2. Après la correction, les valeurs apparentes de module du Young de TA6V à 400 °C et à 500 °C sont similaires à celles initiales. Le coefficient de régression linéaire R^2 est excellent. Les valeurs apparentes de modules de Young et le coefficient R^2 à 600 °C et 700 °C sont beaucoup améliorées.

La Figure 5.20 présente la courbe de déformation de l'éprouvette plane de TA6V (zone utile) en fonction de températures (de 120 °C à 600 °C) et les champs de déformation avant et après la correction. Le coefficient de dilatation apparent dans la direction longitudinale α_{yy} n'est pas changé après la correction : il est de $1{,}4 \times 10^{-5} \pm 5 \times 10^{-6}$ °C^{-1}. Le coefficient de régression linéaire R^2, passant de 0,984 à 0,996 après la correction montre que le résultat de déformation par la méthode 2D-DIC après la correction est plus fiable.

Conclusions et perspectives

Conclusions

Dans le contexte industriel, l'objectif global de cette thèse est de développer une méthode de mesure de champs de déformation à hautes températures pour mesurer la distorsion d'une pièce mécanique aéronautique pendant le refroidissement, après l'emboutissage à chaud (400 °C à 750 °C). Parmi les méthodes de mesures cinématiques (avec et sans contact) actuelles, la méthode de corrélation d'images numérique 2D-DIC a été choisie pour cette étude de thèse. Cependant, cette méthode de mesure à hautes températures présente trois verrous scientifiques majeurs. Le but de cette thèse est d'améliorer cet méthode en appuyant sur trois aspects :

- Trouver une méthode de création des mouchetis qui résiste à hautes températures et en grande déformation
- Améliorer le contraste de l'image à hautes températures

- Corriger l'erreur spatio-temporelle à cause de l'effet mirage pour rendre les mesures plus fiables.

Pour atteindre ces objectifs, la thèse a été déroulée en quatre parties. Tout d'abord, les méthodes de créations des mouchetis ont été étudiées. Un guide pour le choix des mouchetis répondant aux différents critères d'exigence a été proposé. Ensuite, une étude pour la mise en place du système corrélation d'images 2D-DIC adaptée aux contraintes d'espace limité et aux hautes températures pour obtenir un meilleur contraste de l'image a été réalisée. La caractérisation des erreurs spatiales et temporelles liées à l'effet mirage a été ensuite étudiée, suivie par la proposition de méthodes de correction d'erreurs en utilisant un filtre passe-bas spatial et un filtre temporel. Des résultats obtenus pour deux applications pour les essais mécaniques à hautes températures montrent que la méthode 2D-DIC après la correction présente un grand potentiel pour des mesures de déformations fiables à hautes températures.

Perspectives

Comme indiqué au Chapitre 2, il est intéressant d'optimiser les paramètres de laser pour obtenir le masque polymère avec une meilleure résolution, d'analyser la viscosité de la peinture sur le transfert de peinture sur la surface de l'éprouvette (création des motifs par les peintures), d'analyser la compostion chimique de la couche d'oxyde développée sur les motifs de mouchetis à hautes températures pour comprendre le problème de saturation des pixels.

Afin d'améliorer le contraste des images (Chapitre 3), des études étendues peuvent se focaliser sur un plan d'expériences aux plus hautes températures, par exemple à 750 °C car à cette température, le contraste de l'image peut être changé à cause de l'oxydation. A cette température, il est intéressant d'étudier l'effet de l'auto-échauffement de la caméra sur la mesure de déformation et de confirmer de l'origine du problème des pixels saturés (couche de l'oxyde de l'aluminium).

En ce qui concerne l'effet mirage (Chapitre 4), il serait intéressant de développer des méthodes optiques, par exemple l'ombroscopie pour visualiser le flux convectif présente dans le four (Delmas *et al.*, 2013). A partir de la méthode d'ombroscopie, il serait possible de confirmer l'erreur aléatoire de la mesure par la méthode DIC à hautes températures.

Enfin, les résultat obtenus avec les méthodes de correction appliquées aux essais de tractions sont très encourageant (Chapitre 5). Il serait intéressant d'appliquer la méthode de corrélation 2D-DIC dans le cas industriel, par exemple pour un cas de refroidissement d'une pièce aéronautique et puis de continuer à développer la méthode 3D-DIC pour les configurations de géométries plus complexes nécessitant des descriptions géométriques 3D.

Remerciements

L'autrice remercie la région Occitanie et l'établissement IMT Mines Albi (Programme 09A61 909 9092, Dossier : 2017 001838) pour le co-financement de cette thèse de doctorat préparée à l'Institut Clément Ader site d'Albi.

Introduction

Industrial context

Ti–6Al–4V (TA6V) alloy in aeronautic industry

Since 1960s, titanium alloys have been the materials widely used in aeronautic, space, chemical, marine, power generation, biomedical, sport, recreation and architecture (Vanderhasten, 2007). In the aeronautic industry, they are excellent candidates thanks to weight saving, high strength-to-weight ratio, heat resistance, resistance to embrittlement at low temperature, high corrosion resistance and composite compatibility (Boyer, 1996, Inagaki *et al.*, 2014). TA6V is the most commonly used titanium alloy in aerospace industry. It accounted for 45% of titanium consumption in the 2000s years thanks to its versatility: high mechanical resistance, good corrosion, fatigue resistance and a light density. The material is widely employed in fabricating airframe for example fuselage, wing, engine pylon, cockpit window frame (Inagaki *et al.*, 2014) (Figure 2).

a) b) c)

Figure 2: An example of aircraft pieces made of TA6V alloy: (a) in green: engine pylon, in red: engine air inlet, (b) heat exchanger cover in engine pylon fairing (Lauak, 2020), (c) segment of A380 engine air inlet bulkhead (Harvent, 2010)

TA6V has $\alpha + \beta$ phases at room temperature (8 % of β-phase - body centered cubic and α-phase - hexagonal compact at room temperature). Due to the main hexagonal crystal phase structure, a low elongation (10%) is observed at room temperature. However, at high temperature (880 °C -

920 °C) and low strain rate (1×10^{-5} - 1×10^{-2} s^{-1}), the material exhibits a superplastic behavior with a grain boundary sliding mechanism (Ghosh *et al.*, 1979 and T. Zhang *et al.*, 2014). This property allows to produce aeronautic parts, for instance the air inlet by the superplastic forming or the hot or warm stamping processes (Figure 2b-c).

Problematics of shape distortions of the part after forming processes
The superplastic forming conditions require high forming temperatures (880 °C - 920 °C) and low strain rates (1×10^{-5} - 1×10^{-2} s^{-1}), controlled by the pressure cycle (Rollin *et al.*, 2016). At the end of the forming operation, the piece has a homogeneous thickness and it is free of stress, but **the cooling and the extraction from the tools can lead to deformations and residual stresses, resulting in geometric distortions** (Rollin *et al.*, 2016). Figure 3 presents an example of the superplastic forming process and the shape distortion after cooling the part to room temperature.

a) b)

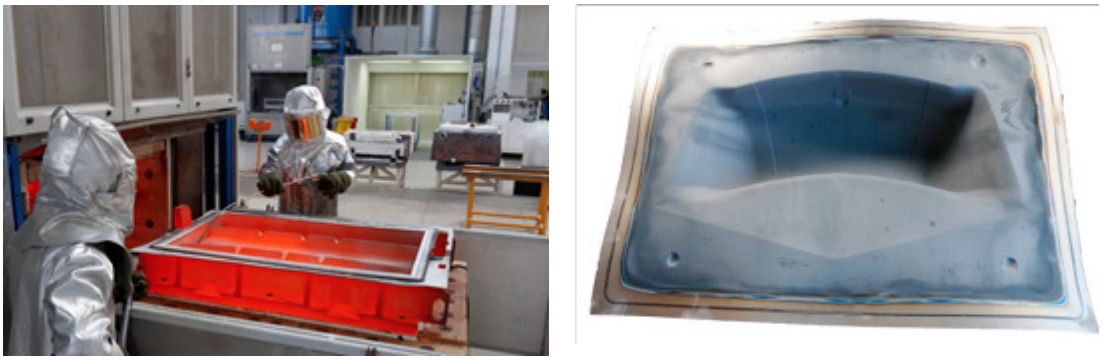

Figure 3: An example of superplastic forming process: (a) cooling part (CyrilBath, 2020), (b) shape distortion after part cooling to room temperature (Mauduit *et al.*, 2017)

The energy required for heating the sheet is proportional to the forming temperature, which is very important for the superplastic forming process. Therefore, to reduce time and energy, increase the ductility and produce parts close to the final shape with high accuracy, the setting temperature in the warm forming processes of the TA6V alloy from 400 °C to 600 °C (Sirvin *et al.*, 2019) or the hot forming process from 750 °C to 890 °C (Stutz *et al.*, 2014) can be alternative solutions. Under warm forming process conditions, TA6V sheets (temperature) present the elongation limit which is twice as high as and the elastic springback is reduced by a factor of 2 (Odenberger *et al.*, 2013). Steps in a deep drawing process are shown in Figure 4.

Nevertheless, the springback effect during the cooling phase of a piece is still a challenge of the hot/warm stamping process. The final shape of the TA6V part demands a comprehension of springback effect to avoid the shape distortion defect. For example, Figure 4b presents the final shape of the Omega part (in 2D) after a hot stamping process at 400 °C (in red) and 500 °C (in green) (Sirvin *et al.*, 2019). The authors recorded a difference of the final shape Omega and the reference one (in black), the shape of the die due to the springback effect. The difference is measured by two angles: α and β. It is shown that the springback effect is more important at 400 °C than at 500 °C. The springback effect depends on parameters, i.e., temperatures and the mechanical properties of materials in the hot stamping process. **To understand the springback effect, the material's mechanical behavior should finely be identified** (Sirvin *et al.*, 2019 and Odenberger *et al.*, 2013).

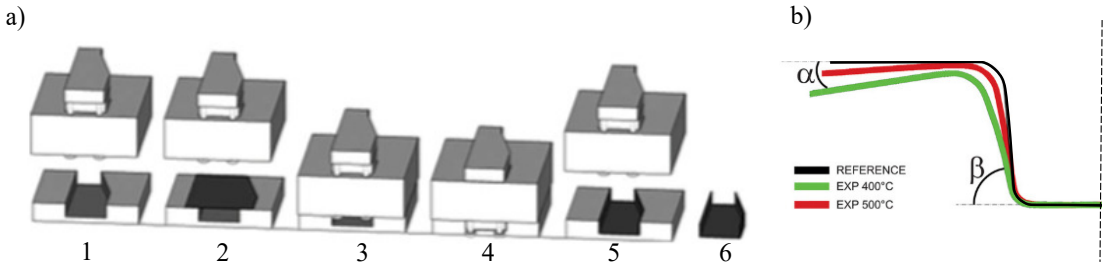

Figure 4: (a) Steps in the hot stamping process: 1-punch, blank holder and die, 2-preheated sheet, 3-closed die, 4-punch displacement, 5-punch course end, 6-open die (Stutz *et al.*, 2014), (b) Springback effect after the hot stamping process at 400 °C and 500 °C (Sirvin *et al.*, 2019)

In order to reduce the cost and to better predict the final shape of the part after the entire hot stamping process or the superplastic forming process, numerical simulations of a whole process are widely used. However, the accuracy of thermo-mechanical models requires reliable experimental data, i.e., kinematic measurements (displacement or strain) of the material at high temperatures (Odenberger *et al.*, 2013 and Sirvin *et al.*, 2019). For example, continuous strain measurements of the part during the cooling step in the hot stamping process could offer a better understanding of the origin of shape distortion defects of stamped parts (springback and/or thermal shrinkage). Therefore, to validate the numerical models, it is necessary to develop an experimental measurement method that enables reliable and accurate displacement or strain field of the part for a range of "small" strain (<0.02).

Development of contactless method for full-field kinematic measurement

Actually, the strain gage is one of the most common and reliable method to access mechanical strain of materials. However, this method offers only a global strain (or mean strain) measurement on the Zone of Interest (ZOI). Furthermore, because it is a contact method, the implementation of strain gages can influence the stiffness of the specimen that might induce bias in measurements.

Contactless methods can be alternative solutions for mechanical strain measurements, for example the Moiré interferometry method, the grid method and so on (Sciammarella *et al.*, 2012). Furthermore, optical methods offer a full-field and sometimes unlimited kinematic measurements (strains can be measured until rupture in mechanical tests), enormous advantages compared to the strain gage. Among these methods, the Digital Image Correlation method (DIC) is actually widely used in experimental mechanics because of its simplicity, flexible implementation and also sufficient accuracy. Since the year of 80s, the method is applied for many types of solid materials: from soft materials, metals and alloys, polymers, ceramic to refractory in material science and mechanical engineering. The method presents undoubtedly a good accuracy and spatial resolution. In the "best experimental conditions", the spatial resolution can reach to sub-pixel. The method can be applied for surface (2D and 3D) or volumetric displacement or strain of material. According to Dong et al., since 2000s, the number of publications related to the developments and applications of DIC in experimental tests has increased exponentially (Dong *et al.*, 2017).

Problematics of DIC applied for mechanical tests at high temperatures (HT)

The algorithms of 2D-DIC or 3D-DIC are well developed (Sutton *et al.*, 2017). At room temperature, an accuracy of 0.01 pixel in the ideal experimental condition can be achieved. Both commercial (Amaris® (GOM, Germany), Match ID® (MatchID Nv, Belgium), VIC-2D®, VIC-3D® (Correlated Solutions, USA), EikoTwim DIC® (EikoSim, France)) and open-source algorithms (µDIC, DICe, 7D, pyxel) are applied for surface full-field displacements or strains of mechanical tests and provide accurate results. The Volumic Digital Image Correlation (VDIC) algorithm is well established but only commercial software is now available (Sutton *et al.*, 2017).

Recent developments on 2D-DIC and 3D-DIC methods aim to increase the spatial resolution of measurements. Furthermore, improved-DIC algorithms and experimental set up conditions are developed to deal with "poor" mechanical test conditions, for example the low-light intensity or the pixel saturation problem at very high temperatures. The development of the DIC method in extreme conditions especially at high temperatures, and with limited space is still a challenge.

The hot stamping process has unfavorable conditions for the DIC method. First of all, the plastic deformation and high temperatures (from 400 °C to 750 °C) of the process require a speckle pattern that can resist high strains and temperatures. Paint is the most common speckle fabrication method for DIC (Dong *et al.*, 2017). Most of high-temperature paint can resist only a deformation of $\approx$ 0.2-0.5. For example, Hammer et al. noticed a disruption in correlation at the plastic deformation state at 600 °C (Hammer *et al.*, 2014). Therefore, it is necessary to develop a speckle method that enables measurements in a range of hot stamping temperature and high strain (strain is at least more than 1.0).

Secondly, in the hot stamping process, an experimental set up for DIC is difficult because the press, the die and the blank are usually heated in a closing oven. Furthermore, during the process, the material is plastically deformed and that induces the out-of-plane motion. In this case, the DIC correlation can be disrupted because of defocusing (Chartrel, 2016). Furthermore, due to high radiation intensity of the environment of the oven and the specimen's temperature, the ratio Signal-to-Noise S/N is decreased; hence, measurements can fail. Here in the Signal is the grey-level of specimen's image and the Noise is the radiation of the object and surrounding environment. Some authors mentioned that pixel saturations at high temperatures make measurements impossible (Valeri *et al.*, 2017, B. Pan *et al.*, 2010b). For these reasons, it is important to find an appropriate DIC set-up configuration adapted to high temperatures and limited space for the smallest DIC errors.

Finally, the mirage effect or heat waves due to the temperature gradient between the camera and the object is a challenging subject for the DIC method. Mirage effects are easily observed in daily life, for example a water pool on the road in very hot summer day, a virtual isle on a desert or an object being view through an exhaust gas from a jet engine. Mirage effect and heat waves cause shimmering objects or object distortions (Delmas, 2012). For DIC, they cause "false" strains or displacements that can be mis-understood as mechanical displacements or strains of materials, especially in a range of "small" strain, from 0.002 to 0.05 (Jones *et al.*, 2018). The kinematic measurements given by DIC at HT is less reliable (high dispersion and less accurate). To that end, it is imperative to correct strain or displacement errors caused by mirage effects to improve the accuracy of the DIC at high temperatures.

Objectives and scope of Ph.D. thesis

Having identified problematic issues of DIC method at HT, the objective of the Ph.D. thesis is to improve the 2D-Digital Image Correlation (2D-DIC) method for full-field kinematic measurements in hot stamping temperatures (400 °C - 750 °C). The thesis focuses on dealing with three problems: speckles at high temperatures, a loss of image contrast at high temperatures and mirage effects. Therefore, the Ph.D. thesis aims to:

- find an appropriate speckle fabrication technique that resists high temperatures (from 400 °C to 750 °C) and high strains (strain $\geq$ 1.0 (100 %))
- set-up a 2D-DIC camera system adapted to experimental conditions (HT and limited observation window) to get the best quality image (high contrast, no saturated pixels)
- suggest a methodology to correct "false" strains due to mirage effects.

This manuscript is organized as follows:

Chapter 1 introduces different kinematic measurement methods applied for mechanical tests. The chapter presents the contact methods (strain gage and optical fiber sensor) as well as non-contact methods that include the photoelasticity, interferometric methods, non-interferometric periodical-coding methods, non-interferometric random-coding method such as the 2D-DIC method with two approaches: local and global approaches.

From Chapter 2 to Chapter 5, each chapter focuses on resolving one specific problem of DIC at high temperatures mentioned above (speckle fabrication technique, experimental set-up and image contrast and mirage effects). Each chapter is written in the following order: the state-of-the-art on one specific problem of the 2D-DIC method, the methodology, the result, the discussion and the conclusion and perspectives.

Chapter 2 focuses on speckle fabrication techniques that enable strain measurements at HT and high strains. Six fabrication techniques, classified in two groups (additive and subtractive) are presented. Six speckle patterns are then compared in term of contrast and adherence to the TA6V specimens to find an appropriate speckle fabrication technique for high strain and HT.

Chapter 3 deals with the problem of image contrast at high temperatures and experiment set-up of 2D-DIC in a limited observation space (a closing furnace). The chapter gives an overview of the influence of the temperature effect: radiation on image contrast captured by 2D-DIC camera. Afterward, a design of experiment (DOE) to assess influence factors of 2D-DIC set-up parameters on image contrast is presented. The chapter concludes with a configuration of 2D-DIC system adapted to experimental conditions.

Chapter 4 refers to characterizations of strain errors at different temperatures, from 400 °C to 750 °C due to heat waves. The "false" strains, defined as 2D-DIC strain measurement errors, are supposed to be dependent on convection flows of the furnace. They are measured by the Background Oriented Schlieren (BOS) technique. The characteristic of strain errors as a function of temperatures (the order of magnitude and frequency) is then used for Chapter 5.

Chapter 5 suggests correction methods in order to reduce the uncertainty and increase the accuracy in strain measurements given by the 2D-DIC method. Based on the temporal and spatial characteristics of strain measurement errors, a post-processing using low pass filters is employed to reduce errors caused by mirage effects. The correction methods are then applied

for two types of mechanical tests: the first one is to measure the Young's modulus of TA6V titanium alloy at different temperatures and the second one is to measure the thermal expansion coefficient (TEC) of TA6V material from 100 °C to 600 °C.

Finally, the manuscript ends with a global conclusion of the whole Ph.D. thesis as well as perspectives for further studies to extend the Ph.D. subjects.

CHAPTER

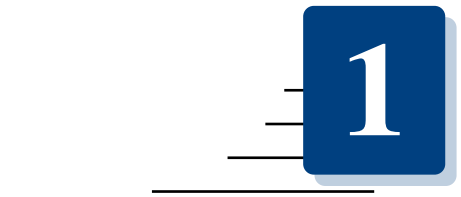

State-of-the-art on kinematic measurement methods applied in experimental mechanics

The validation of numerical simulation models in the hot stamping process requires reliable experimental data (displacement or strain on the surface of the studying specimen or piece). Such information is obtained by performing experimental mechanical tests in which the displacement or strain of the specimen is measured. This chapter presents some kinematic measurement methods applied in experimental mechanics. Measurement methods are classified into two groups: the contact methods and the non-contact (optical) methods. The contact methods include the strain gage, the extensometer and the Fiber Bragg Grating (FBG) sensor. The non-contact methods use the optical system to measure full-field displacement or strain in mechanical tests.

This chapter is composed of three main parts. In the first part, we present general definitions used in the metrology and the state-of-the-art on measurement methods. Each method is presented in the following order: the working principle, advantages and drawbacks and applications of this method in experimental mechanics. In the second part, the kinematic measurement method for mechanical tests in this Ph.D. thesis is chosen. An additional literature review focusing on sources of errors related to the local-2D-DIC method that influence "small" strain measurement and strategies for the identification of material's parameters are presented. Finally, a conclusion and perspectives of this chapter are addressed.

1.1 Metrology definitions

Before presenting different methods for displacement or strain measurements in experimental mechanics, we present some definitions that are usually used in metrology as well as in this manuscript.

In metrology, a measurement obtained by a measurement system or a measurement method may present errors. An error can be random (measurement's distribution follows the normality law) or systematic (measurement's distribution presents a bias). From a metrological point of view, two types of error are evaluated by the *uncertainty* and the *accuracy* parameters (BIPM *et al.*, 2008). The uncertainty is used to characterize the random error and the accuracy is employed to characterize the systematic error.

Uncertainty: The uncertainty is represented by the dispersion of measurements. In statistic, it is evaluated by the variance σ^2 or the standard deviation σ (STD). A measurand is certain if it has low dispersion and vice versa.

Accuracy: The accuracy is represented by the closeness of a measurement to the true quantity value. The accuracy of the measurement is evaluated by being compared with the reference value.

Spatial resolution The spatial resolution is the smallest distance between two points in space (its unity is in pixels or in m) that a system measurement can detect. In our study, the spatial resolution is the distance of two points in which the measured values are significantly different from each other. It means that the spatial resolution must be greater than the uncertainty of the system.

Figure 1.1a and Figure 1.1b present graphically the concept of the uncertainty and the accuracy of measurements. The center point (in red) represents the true quantity value of a measurand and the other points (in blue) are measured values obtained from a measurement method or system. In Figure 1.1a, measurement points are dispersed, which presents a high uncertainty. They are surrounding the true value and the distribution of these measurement points follows the normality law. Errors on measurement points are classified as the random error. On the contrary, in Figure 1.1b, measurement points are less dispersed, but they are far from the true value. They are therefore less accurate. Errors on measurements points are classified as the systematic error. In metrology, a measurement should present the smallest uncertainty and the best accuracy.

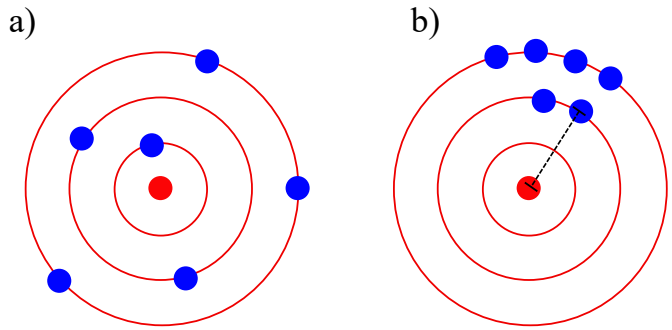

Figure 1.1: Graphical representation of: (a) the uncertainty and (b) the accuracy of measurements in metrology (BIPM *et al.*, 2008)

1.2 Contact methods for strain measurements

1.2.1 Strain gage

1.2.1.1 Working principle

Relationship between mechanical strain and electrical resistance of materials
Strain gage is firstly introduced in 1930s by E. E. Simmons and A. C. Ruge (Sciammarella *et al.*, 2012). The method is used to measure locally (one-shot) mechanical strain in solid mechanics. The working principle is based on the variation of electrical resistance of a conductor wire. The relationship of the resistance, the length and the section of a conductor's wire is presented in Equation 1.1.

$$R = \rho \frac{l}{s} \tag{1.1}$$

where:

- R [Ω] is the resistance of the conductor's wire
- ρ [Ω m] is the electrical resistivity of the conductor's wire
- l [m] is the length of the conductor's wire
- s [m^2] is the section of the conductor's wire

From the first deviation of Equation 1.1, a mechanical deformation of the wire conductor induces a variation of its resistance. It is noted that in Equation 1.2, the assumption employed is the constant resistivity of material and the elastic mechanical strain.

$$\frac{\Delta R}{R} = K \times \frac{\Delta l}{l} = K \times \varepsilon \tag{1.2}$$

where:

- K is the gage factor, K is generally = 2 for the conductor wires made of constantan or nickel-chrome alloy
- ε is the mechanical strain of the conductor wire

A strain gage contains metallic foils (several µm of thickness and variable length) an insulation support. The insulation support is usually made of polymer resin or ceramic and connectors with a reading circuit (Figure 1.2). If a strain gage is directly bonded on the specimen, the deformation of the specimen is proportional to the variation of the wire conductor resistance (Equation 1.2). The strain gage should not modify the specimen's stiffness. The electrical signal is linear to the mechanical strain.

In practice, some sources of errors can influence the electrical signal, for example the temperature effect, the transverse sensitivity, the mis-alignment of strain gage with respect to the axis of strain measurement (Sciammarella *et al.*, 2012). The temperature induces a thermal expansion of the metallic foil in the strain gage which induces an error. A correction for the temperature effect on mechanical strain to reduce this error is performed. For example, commercial strain gages are usually provided with self-compensating graphs in a form of a polynomials (Sharpe, 2008).

The transverse sensitivity (K factor) refers to a difference between the strain measurement in the primary sensing axes and the one in the perpendicular direction. The effect of transverse sensitivity on strain measurement can be corrected with a correction graph or numerical methods. The mis-alignment of strain gage refers to a difference of angles between the gage axis and the measurement axis. The small angular error induces a "small" strain measurement error. Manufacturers have studied the influence of three sources of error on output strains. They can provide correction graphs to correct the influence of these factors, for instance the correction graph of temperature versus mechanical strain measurement (Sciammarella *et al.*, 2012). Furthermore, since the metallic foil in the strain gage is thin, it can break when cyclic mechanical tests are performed. Therefore, to obtain reliable data, the strain gage for mechanical tests should be chosen by taking into account the experimental conditions, i.e., the limit of strain measurement, the type of experimental test and the testing temperature (Sharpe, 2008).

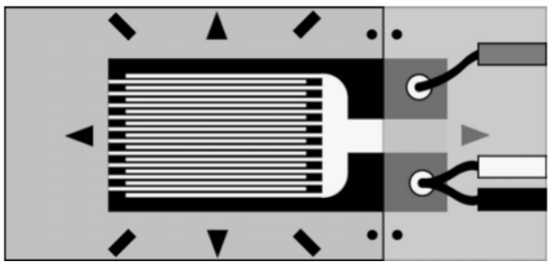

Figure 1.2: Schema of a strain gage (Sharpe, 2008)

Wheatstone bridge working principle

Since the elastic strain is generally small (less than 5%), the variation of resistance is small as well. To increase the strain gage sensitivity and to avoid parasite resistances that influence the electrical signal, the strain gage is integrated in a Wheatstone bridge circuit.

The Wheatstone bridge is an instrument used to measure the variation of output voltage. The Wheatstone bridge consists of four resistances R1, R2, R3, R4 that are arranged in Figure 1.3.

A constant input voltage E is applied between point A and C of the circuit, and the voltage of point B and D is to measure. If the ratio of two resistances R2/R1 is equal to the ratio of R3/R4 (the equilibrium state that corresponds to a free load configuration), then there is no current on the whole circuit: $I = I1 - I2 + I3 - I4 = 0$. Therefore, the measuring tension V_{BD} is null.

In case of having a mechanical strain on the resistance R1, it is changed to $R1 + \Delta R$. The bridge becomes unbalanced, there is a tension between point B and D: V_{BD} is not equal to 0. The variation of measuring voltage in the Wheatstone bridge is linear to mechanical strain:

$$V_{BD} = E \times \frac{\Delta R_1}{4R} \tag{1.3}$$

where:

- R = R1 = R2 [Ω] are electrical resistances
- ΔR [Ω] is the variation of resistance R1 in case of mechanical load
- E [V] is the input voltage applied to the Wheatstone bridge

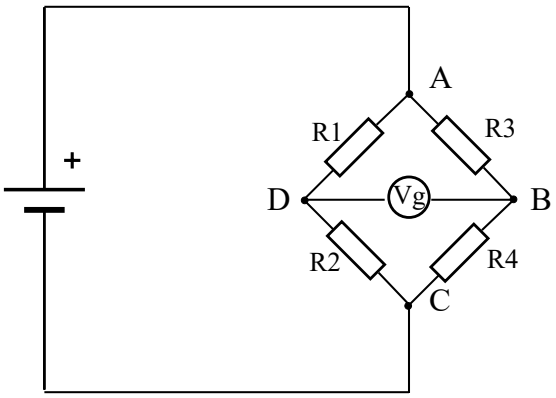

Figure 1.3: Schema of Wheatstone bridge circuit (Sciammarella *et al.*, 2012)

To measure mechanical strain in one direction, the strain gage is replaced or connected with one of four resistors (R1, R2, R3, R4). The remained resistors do not undergo mechanical load. For instance, in case of uniaxial tensile or compression tests, only one strain gage is active. Figure 1.4 presents a strain gage sticked on the ZOI of the specimen in a tensile test (Motra *et al.*, 2014). The strain gage is then connected with the Wheatstone bridge to measure the longitudinal strain of the specimen.

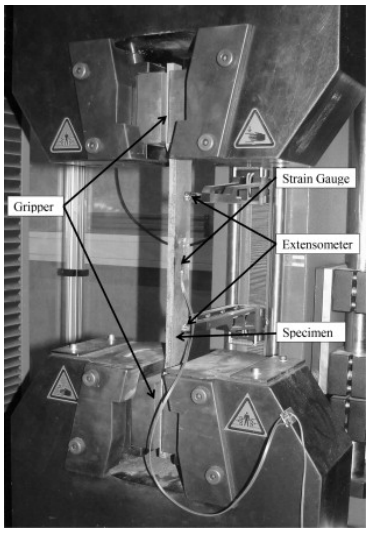

Figure 1.4: An experiment set-up of a tensile test with a strain gage sticked on the ZOI of the specimen (Motra *et al.*, 2014)

In case of measuring two or three principal strain directions, strain gage rosettes are employed. A strain gage rosette includes a number of strain gages arranged in a form of Tee, rectangle, or delta, etc...The principal mechanical strains are calculated from each strain gage in the rosette by changing the local coordinate system in the global coordinate system (Sharpe, 2008).

1.2.1.2 Advantages, limitations and application of strain gage

The advantage of the strain gage is that the method is easy and simple to implement on specimens or structures. Strain measurements are directly measured from the Wheatstone bridge tension, giving rapid results.

The main limitation of the method is that the measurement is local (one-shot measurement). A strain gage can only measure a strain in one direction. Furthermore, the strain gage performance is limited by the fatigue, elongation ability of the material strain foil in strain gages (Sharpe, 2008). In general, the "standard" strain gage can allow elastic strain, which is less than 1% of mechanical deformation. Specific materials in strain gages can allow high-performance strain measurements. For example, the strain gage using high fiber resin material can measure a maximum strain of 1-2%. The strain gage using Ni-Fe alloy can measure strain in fatigue tests with N<10×10^7 cycles (Sharpe, 2008). Nevertheless, theses strain gages are costly.

According to Le Goër et al., strain gages can be classified into three categories: i) standard usage, ii) improved accuracy and ii) high accuracy (Le Goër *et al.*, 1992). For standard usage, the accuracy of the measurement is under 2%. This type of strain gage is easy to set-up. For improved and high accuracy strain gages, they should be employed with lots of attention to get the best accuracy.

The principal applications of strain gages are quasi-statical, dynamic or fatigue tests for a temperature range of [-50 - 250 °C]. The limit of strain measurement is $\pm$ 2300 $\mu\varepsilon$ (equivalent to an deformation of 0.023) with polymer support. The accuracy of this method is generally about 1% (Sharpe, 2008). The strain gage used for high temperature measurements has limitation of about $\pm$ 5000 $\mu\varepsilon$. Some high elongation strain gages have performance up to $\pm$ 200 000 $\mu\varepsilon$ but their accuracy are moderate, from 2% to 5% (Sharpe, 2008).

Strain gages used for high temperatures is directly cemented or cured into ceramic resin for insulation. The mechanical strain is transmitted through the cement to the strain gage. The accuracy of strain measurement is about 1% to 2% because at high temperatures, the electrical connection must be protected. Furthermore, at high temperatures, the thermal effect to strain gage becomes significant. This is why few applications using strain gages at very high temperature, i.e., hot stamping temperatures, are found in mechanical tests.

1.2.2 Extensometer

1.2.2.1 Working principle

Extensometers are the most convenient and most widely used instrument for mechanical strain measurements at room temperature as well as thermo-mechanical tests at high temperatures. Extensometers are usually employed for strain measurements in tensile, compression, fatigue or creep tests (Sharpe, 2008). The extensometer includes a transducer part and an electronic part. The transducer part converts mechanical deflection into electrical signals. The electronic part performs signal processing (conditioning, sampling and filtering) and reports final readout data (mechanical strain).

At room temperature, a clip-on extensometer is commonly used to measure strains of specimens. The mechanical strain is calculated from the reference strain gage, which usually covers the ZOI of specimens and the extension length of the ZOI, measured by the transducer (Sharpe, 2008). The strain measured by an extensometer is the averaged strain over the ZOI of the specimen. In practice, the extensometer is designed to clip directly on the specimen with a pair of knife edges located on the ZOI of specimen (Figure 1.5). These knife edges are quite sharp. They are in form of clipped or spring to avoid the slip of knife edges on the surfaces of specimens.

1.2.2.2 Advantages, limitations and applications

The clip-on extensometer uses usually the strain gaged-flexure as the transducer the because it is compact and it has light weight. Its accuracy is sufficient to meet the standards ASTM E83 or ISO 9513 (the accuracy is at least 0.5%) (Sharpe, 2008). It is considered as one of the most accurate kinematic measurement methods to the measure the stiffness of materials. Nevertheless, the clip-on extensometer has limitation in the range of strain measurements. It must be removed from the specimen before ruptures because the high reaction force of rupture moment from the specimen can strongly influence the reliability of the extensometer. It is usually removed after the yield strength of the material in tensile tests.

The accuracy of strain measurements given by an extensometer depends on the set-up of this extensometer on a specimen. For example, since the knife edges of the extensometer are quite sharp, additional stress may be applied on the specimen during the implementation of the extensometer. For soft materials, for example, polymer or rubber, this additional stress can induce strain measurement errors. Sliding contact between the specimen and the knife edge can occur during the mechanical test that biases measurements. Therefore, clip-on extensometers should be carefully set-up to obtain reliable strain data.

The clip-on extensometers are not only widely used for mechanical tests at room temperature but also for thermo mechanical tests at high temperatures. The clip-on extensometers used for high-temperature are slightly different from the room-temperature ones. The transducer must be outside the heated zone (which is usually outside the heating chamber). In addition, the high-temperature clip-on extensometer uses refractory rods, made of ceramic or quartz and having long arms to protect the transducer and electronic devices. Figure 1.5b presents the side-entry high-temperature extensometer with rods which are perpendicular to the specimen surface.

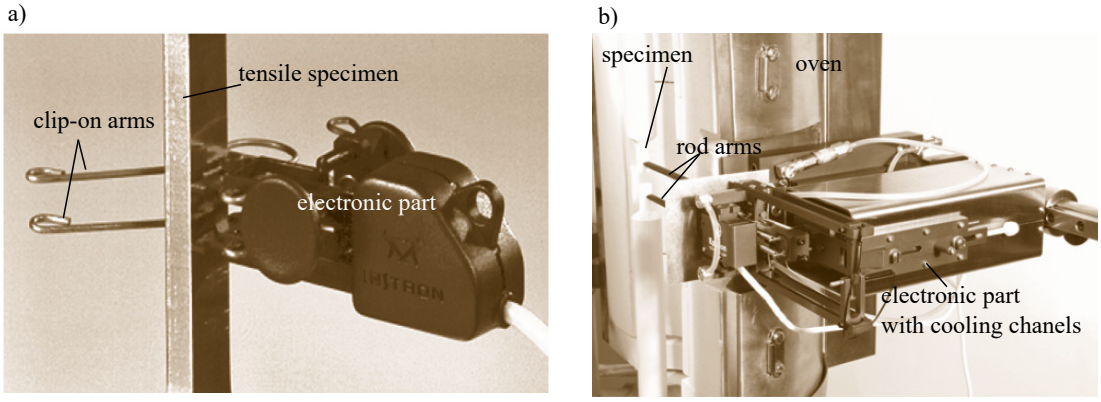

Figure 1.5: (a) A clip-on extensometer used for tensile tests at room temperature; (b) A side-entry high-temperature extensometer used for tensile tests at HT (Sharpe, 2008)

High-temperature clip-on extensometers should be implemented on the specimen with attention because slip in contact between the knife edges and the specimen may happen. Furthermore, the arms should be sufficiently constrained but not over-constrained to avoid additional stress applied on the specimen. For flat specimens, high-temperature clip-on extensometer with conical point contacts are required. Furthermore, the extensometer should be re-calibrated after a long-term testing, for example creep or fatigue tests. According to Sharpe, ideal materials for high-temperature extensometer should have high stiffness, low density and low conductivity to

avoid strain errors from the extensometer operations (Sharpe, 2008). The authors highlight that the reliability of strain data depends on not only the accuracy of the instrument but strongly on the user's operation. Therefore, the high-temperature clip-on extensometer should be implemented by a competent professional.

1.2.2.3 Optical extensometer

To avoid contact problem of clip-on extensometers, the optical extensometer is employed. Its working principle is measuring the deflection of a laser beam during the mechanical tests. The laser beam is calibrated in advance before testing. The deflection of the laser beam is proportional to the mechanical strain of the specimen (Sharpe, 2008). The optical extensometer is useful for thermo-mechanical tests at high temperatures, because the method is free from spurious hysteresis of the transducer part of a clip-on extensometer. Nevertheless, this method also has limitations. Since tensile or compression tests at high temperatures are usually performed in a heating chamber, the quality (the non-homogeneous of refractive index) of the window of the heating chamber can influence strain measurements. Tensile tests above 1000 °C require a powerful light source to avoid the loss of contrast. The optical extensometer allows only global strain measurements. The method is less attractive than full-field optical methods, which are detailed in Section 1.3 in this chapter.

1.2.3 Fiber Bragg Grating (FBG) sensor

1.2.3.1 Working principle

The Fiber Bragg Grating sensor is a contact optical method used in experimental mechanics. It means that the fiber sensor is sticked on the specimen's surface or merged in the material's volume to measure mechanical strains of materials or structures. The working principle of this method is based on the change in the optical phase of the Bragg wavelength. The Bragg grating is the periodically permanent change of the refractive index in an optical fiber. It is created by illuminating an interference pattern of UV light onto the core of the photo-sensible optical fiber (Robert, 2013). The photo-sensible optical fiber is created by exposing the fiber under UV light with periodical grating pitch. Various techniques can create the photo-sensible optical fiber, for example, the phase mask fabrication or the Lloyd mirror techniques (Sharpe, 2008). The relationship of the Bragg wavelength λ_B, the grating pitch Λ and the average refractive index of the optical fiber is presented in Equation 1.4 (Robert, 2013).

$$\lambda_B = 2n_{eff}\Lambda \tag{1.4}$$

where:

- $n_{eff} = 1.46$ is the effective refractive index (in average value)
- λ_B is the Bragg wavelength
- Λ (about 0.5 µm) is the grating pitch

The Bragg wavelength λ_B is the characteristic of the Bragg grating. Its wavelength depends on the strain and temperature of the optical fiber.

The variation of the Bragg wavelength $\Delta\lambda_B$ and fiber's temperature is given by Equation 1.5 (Robert, 2013):

$$\frac{\Delta\lambda_B}{\lambda_B} = (\alpha_f + \zeta_f)\Delta T \tag{1.5}$$

where:

- α_f [K^{-1}] is the thermal expansion of optical fiber, for optical fiber made of Silica material, $\alpha_f = 0.55 \times 10^{-6}$ K^{-1}
- ζ_f [K^{-1}] is the thermal expansion of thermo-optical doping material, for SMF-28™ material, $\zeta_f = 7.3 \times 10^{-6}$ K^{-1}

The fiber's elongation $\varepsilon_1 = \frac{\Delta L}{L}$ induces a wavelength variation compared with initial Bragg wavelength. The assumption is that strains of two other directions ε_r and ε_θ of the fiber are isotropic. If the optical fiber as well as the specimen is deformed, in case of an uniaxial tensile test and the isotropic material ($\varepsilon_1 > 0, \varepsilon_2 = \varepsilon_3 = -\nu\varepsilon_1$), the Bragg wavelength shifting $\Delta\lambda_B$ is proportional to mechanical strain (Equation 1.6) (Robert, 2013)

$$\frac{\Delta\lambda_B}{\lambda_B} = \left[1 - \frac{n_{eff}^2}{2}(-\nu p_{11} + (1-\nu)p_{12})\right] \approx 0.78 \times 10^{-6}\varepsilon_1 \tag{1.6}$$

where: p_{11} et p_{12} are Pockels coefficients: $p_{11} \approx 0.113$ and $p_{12} \approx 0.252$.

If the fiber is embedded inside the specimen, it is possible to measure mechanical strains and temperature at the same time. For example, Demirel used the "decouple" approach to separate the temperature signal and the strain of the composite resin (Demirel, 2009). The author also suggested a transfer matrix that could measure strain or temperature gradients inside the material.

1.2.3.2 Advantages, drawbacks and applications of the FBG sensor

The advantage of the FBG sensor compared with electrical-based strain sensors is that it is not influenced by variations of resistance or capacitance of the electrical sensors. The optical fiber is not affected by noise source such as the electromagnetic interference. The accuracy of FBG sensor is from 10 $\mu\varepsilon$ to 100 $\mu\varepsilon$ (Ferdinand, 1999) while it is less accurate for temperature measurement (about 20 °C) (Robert, 2013). The FBG sensor is usually embedded inside the structure to measure and to monitor its strain and temperature.

Nevertheless, the drawback of the FBG sensor is the presence of thermal gradient or strain gradient. Indeed, in the presence of strain gradient, the optical fiber becomes birefringent. The Bragg spectrum presents more than one peak; thereby, it is difficult for analysis. In case of thermo-mechanical, separation of mechanical strain and thermal strain is a challenging topic (Robert, 2013). Finally, the optical fiber is fragile and the cost for fabrication is still high.

Application of the FBG sensor is in aerospace, civil structure, composite manufacturing process for the inspection purpose but not for the identification of elastic parameters of materials. The FBG sensor is applied to monitor and to evaluate the state of materials or structures. In composite manufacturing, the sensor is embedded in polymer resin to measure the temperature and strain during the curing state (Demirel, 2009). The sensor is also embedded in building and infrastructure, oil and gas, wind power for structural health monitoring (Ferdinand, 1999).

There are only few applications of the FBG sensor in extreme conditions. This is because the germanium silicate can not resist temperatures above 600 °C (Ferdinand, 1999). N-doped technology permits the optical fiber to resist high temperatures. Recently, Zhan et al. developed a novel fiber Bragg grating in which the sensor head is comprised between one FBG and two rods (Zhan *et al.*, 2008). The new sensor which is made with two rods can measure a temperature range from 0 °C to 800 °C. High temperature FBG sensor is still a challenging subject that requires a lot of developments. Despite advantages of the FBG sensor, it might not be an appropriate method for mechanical tests in our study due to the high temperature of hot stamping process.

1.2.4 Summary on contact methods

In this section, we present the strain gage, the extensometer and the FBG sensor, the most-used contact methods for kinematic measurements in experimental mechanics.

The working principle of strain gages and extensometers is based on the relationship between the material electrical resistivity and mechanical strains. The limitations of strain measurement are variable, from 0.2 for standard extensometers to 2.0 for elastomeric extensometers (Sharpe, 2008). They provide generally a "good" accuracy in strain measurements (up to 1% for extensometers). Extensometers or strain gage instruments might be a great instrument for "small" strain measurement with respect of objectives in our study. However, this instrument is not appropriate in a closing temperature furnace in the testing configuration. In addition, additional stress on specimen during the extensometer implementation can induce errors.

The FBG sensor 's working principle is based on the variation of the Bragg wavelength created inside the optical fiber. The variation of the Bragg wavelength is proportional to the mechanical strain and temperature of the fiber, which is supposed to be similar to those of the specimen. Although advantages of this method, the FBG is rarely used to measure mechanical strain of specimens in the hot stamping temperatures. Therefore, this method is not compatible with mechanical tests in our study.

1.3 Non-contact methods

Non-contact methods consist of capturing a sequence of images on the ZOI of the specimen during mechanical or thermal load then deduce full-field kinematic measurements (displacement or strain). The huge advantage of non-contact methods is that they provide full-field displacement or strain maps without adding additional stress on specimens. Thanks to the development in computer technology (fast computation and calculation) and computer vision, these methods are widely used in experimental mechanics, in parallel with contact methods. The most popularly used non-contact methods can be classified into three groups: i) interferometric methods including the holography and the Moiré interferometry, ii) non-interferometric periodical coding methods including the fringe projection and the grid method, iii) non-interferometric random coding methods that include the laser speckle method and the DIC method. The photoelasticity is also a method used in experimental mechanics. It is noted that the previous list of full-field kinematic measurement methods is not exhaustive. In this section, we present only the basis of the method, advantages, drawbacks and applications of each method. In particular, some applications for in-plane (two dimensions) measurements at high temperatures are also cited.

1.3.1 Photoelasticity

Working principle

The history of photoelasticity starts in 1816 when Brewster discovered the birefringent phenomenon on transparent materials. The method was then rapidly developed in 1950s to become a robust stress analysis technique (Sharpe, 2008). The method is applied for transparent material or material with birefringent coating. The working principal of the method is based on the variation of the optical index of a transparent material (Brémand *et al.*, 2011). Without mechanical load, the optical index of the transparent materials, i.e., the crystal is isotropic (n_o). Under mechanical load, an elastic deformation in atomic scale occurs (Mueller, 1938). Consequently, the optical index becomes anisotropic due to the birefringent phenomenon. It has two refractive indexes: n_1 (ordinary refractive index, named "o") and n_2 (extra-ordinary refractive index, named "e"), which correspond to two perpendicular directions of light (Brémand *et al.*, 2011). The variation of two refractive index is proportional to a difference of two normal stresses σ_1 and σ_2 of specimen (Equation 1.7) (Rastogi, 2003).

$$n_2 - n_1 = C(\sigma_2 - \sigma_1) \tag{1.7}$$

where: C [Bw] is the material's photoelasticity constant. Its unit is expressed in Bw (1 Bw = 1×10^{-12} m^2 N^{-1}).

It is noted that the ratio $(n_2 - n_1)/n_1$ observed on the photoelastic material is about 1×10^{-3}.

Advantages, drawbacks and applications

The photoelasticity method is employed for stress analysis on material under mechanical load. By using a system of analyzers, it is possible to obtain a stress field on specimen by analyzing fringes contours obtained from a polariscope (Brémand *et al.*, 2011 and Patterson, 2002).

To apply the photoelasticity for stress analysis, the material must be transparent. That is why, in case of a non-transparent specimen, the specimen needs to be coated with a thin transparent film that enables the stress analysis by photoelasticity method. Nevertheless, the transparent film can not resist temperatures above 200 °C (Brémand *et al.*, 2011). Furthermore, a residual stress can appear due to a difference of stiffness of the polymer film and the material. Residual stress can induce a mistaken result (Sciammarella *et al.*, 2012). Due to the fact that the material must be birefringent or it must be coated by a birefringent material, the method is not appropriate to mechanical tensile test of metallic material in a temperature range of 400 °C and 750 °C.

1.3.2 Interferometric methods

Interferometric methods are based on the analysis of line patterns (fringes) that are created by the interference between two coherent beams, i.e., laser beams. This interference creates periodical black and white lines (fringes). Interference fringes are can be created by many techniques, for example the Michelon interferometer technique or Fabry–Pérot interferometer (Brémand *et al.*, 2011). In the following section, we present two interferometric methods: holographic interferometry and Moiré interferometry.

1.3.2.1 Holographic interferometry

Holography

Holography was first developed in 1950s by Denis Gabor (Sciammarella *et al.*, 2012). The method allow reconstructing a virtual object in three dimensions thanks to a *hologram* and a

laser beam. The reconstruction of an object requires two steps: 1) recording a hologram, 2) reconstruction of the original object (see Figure 1.6 for explanation).

1. Recording a hologram. A hologram contains dark and bright pattern lines. They are results from an interference between two laser beams: the first one is the "reference" beam and the second one is the "object" beam. Indeed, when an object (point P in Figure 1.6) is illuminated by a light source, i.e., a laser beam, each point on a surface object can reflect light and scatters it (the object beam) in Figure 1.6. The scattered light rays interferes with the "reference" beam to create interferometric pattern (interference fringes) that contains a periodical dark and bright lines. This interferometric pattern is recored on a photosensible polymeric film to form a *hologram*. The interference fringes frequency f depends on the angle α between two beams and the wavelength of the laser source (Sharpe, 2008).

2. Reconstruction: the original object in three dimension can be reconstructed from the hologram and the reference beam (Figure 1.6). The reconstruction is made by the transmission and the first-order diffraction of light in fringe patterns, results in a "virtual" image of the original object (point P2 in Figure 1.6).

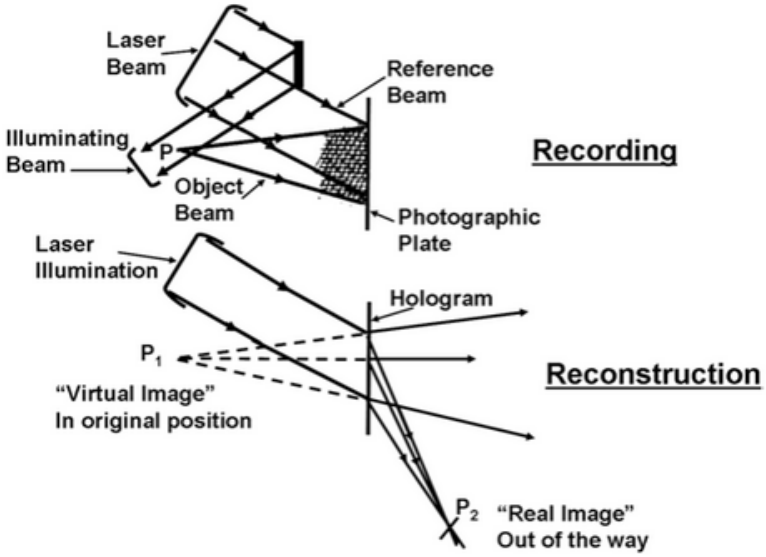

Figure 1.6: Procedure for image reconstruction of the holographic interferometry (Sciammarella *et al.*, 2012)

Holographic Interferometry

The technique of hologram interferometry is used to calculate the displacement field of the specimen. The idea is to superpose the holograms of object from "initial" state and "deformed" state. If there is a small displacement or mechanical strain, interference fringes related to the displacement is changed, for example phase shifting occurs. By superposing two interference fringes: the first one is related to initial shape, the second one is related to deformed shape of object, holographic interference fringes are obtained. From these fringes, the displacement or strain of object can be retrieved. The phase shifting $\Delta\varphi = \varphi_2 - \varphi_1$ from the holographic

interference fringes is proportional to the displacement of object by Equation 1.8 (Sharpe, 2008).

$$\Delta\varphi = \frac{2\pi.D.S}{\lambda} \tag{1.8}$$

where:

- λ [µm] is the wavelength of the laser beam
- S is the sensibility factor. The factor is linked with the hologram interferometry system
- D is the displacement of a point on the surface of the object.

Advantage, drawbacks and applications
The hologram interferometry enables not only a global visualization of displacement or strain field on the specimen but also accurate measurements. According to Smigielski, the method is considered as one of the most accurate full-field measurement method (Smigielski, 2001). The spatial resolution can reach several micrometer.

The limitation of the method is that it requires a sophisticated set-up system (laser beams with mirror system). The accuracy of the method depends on the accuracy of the holographic system (the sensibility factor in Equation 1.8).

The method is adapted for micros-scale measurements and large-scale measurement. Its application are variable: detecting defects appeared on parts, measuring strain field near crack tips, determining the vibration mode on cars and so on (Smigielski, 2001). Furthermore, because of its high accuracy, the method is usually applied for thermo-mechanical strain measurement in micro-electromechanical industry (Sharpe, 2008).

Although the method is widely used for full-field kinematic measurements with high accuracy, the system setup is quite sophisticated and it may not appropriate to the limited space configuration of the hot stamping process.

1.3.2.2 Moiré interferometry

Efficiency of the Moiré interference is demonstrated by Weissman in 1980s (Sharpe, 2008). The interference fringes are created by two mutually collimated beams having incident angle α to the normal of the specimen. To measure mechanical strain or displacements, the specimen surface is coated with a regular grid for example 1200 lines/mm $\times$ 1200 lines/mm by a specimen grating process. The regular grid on the specimen diffracts with the incident beam to create Moiré interference. The frequency of the Moiré fringes is calculated by Equation 1.9 (Sharpe, 2008).

$$f = \frac{2}{\lambda} sin(\alpha) \tag{1.9}$$

where:

- α is the incident angle of laser beam to the normal of the specimen
- λ is the wavelength of the laser beam

The deformation of specimen makes Moiré pattern change. The displacements U and V in Ox and Oy direction are respectively proportional to the number of Moire fringes which is from 0 to $N_x - 1$ in Ox and from 0 to $N_y - 1$ in Oy direction (Equation 1.10) (Rastogi, 2003).

$$\begin{aligned} N_x &= fU \\ N_y &= fV \end{aligned} \tag{1.10}$$

The strain is calculated from the fringe order N_x and N_y by Equation 1.11. They are proportional to the frequency f .

$$\begin{aligned} \varepsilon_{xx} &= \frac{\partial U}{\partial x} \approx \frac{1}{f}\frac{\Delta N_x}{\Delta x} \\ \varepsilon_{yy} &= \frac{\partial V}{\partial y} \approx \frac{1}{f}\frac{\Delta N_y}{\Delta y} \end{aligned} \tag{1.11}$$

Moiré interferometry is known as one of the referent methods for small displacement and strain field measurements in experimental mechanics (Brémand *et al.*, 2011). The method offers a high sensitivity for in-plane displacements, typically 0.471 µm per fringe order (Sharpe, 2008). Nevertheless, the method is employed for small sample, at micro-scale.

Principal applications of this methods are in the microelectronic industry, such as measuring thermo-mechanical strain or displacement of the MEMS device. With considerations to the specimen's dimension, the method might not be compatible with the aim of our study: measuring mechanical kinematic of stamped parts, from several centimeters to several meters.

1.3.2.3 Summary on the interferometric methods

Interferometric methods use the interference phenomenon of coherent light, i.e., laser beams to create periodical dark and bright lines (interference fringes). Through the analysis of the phase shifting made from the initial state and the deformed stage of the specimen, the full-field kinematic field of the specimen is retrieved. Interferometric methods are compatible with small mechanical displacement and strain (Brémand *et al.*, 2011). They offer accurate and high resolution (Sharpe, 2008). They are considered as one of the "referent" methods for kinematic measurement in experimental mechanics. Nevertheless, the methods are applied for small specimens, in micrometric scale. Therefore, they might not be appropriate to our experimental test configuration (millimeter scale, limited space).

1.3.3 Non-interference periodical coding methods

Non-interferometric periodical coding methods refer to full-field kinematic measurement methods that use the periodical patterns. However, periodical patterns are not created from an interferometric phenomenon. Compared to interferometric methods, the experimental set-up requires fewer devices. In this section, we present two widely used methods for experimental tests in millimeter scale: the fringe projection and the grid method.

1.3.3.1 Fringe projection

Working principle

Fringe projection is usually employed to measure 3D shape of the object. The method consists of projecting a fringe pattern on a planar surface (reference image) then on the study object (object image) with a projector. By subtracting fringe patterns projected on the initial and deformed

images, an image with different grey-levels is made. The grey-level is linked with out-of-plane displacement of the object. Figure 1.7 presents the 3D shape measurement of a statue from the fringe projection method. The fringe pattern (dark and white lines) is projected on the object (statue). The image of the object is captured by a camera. The intensity (grey-level) on the image I is resulted from the reflection light coming from the fringe pattern of the projector (αI^p), from the bubble light β_2 and the reflection light from the bubble on the statue $\alpha\beta_1$.

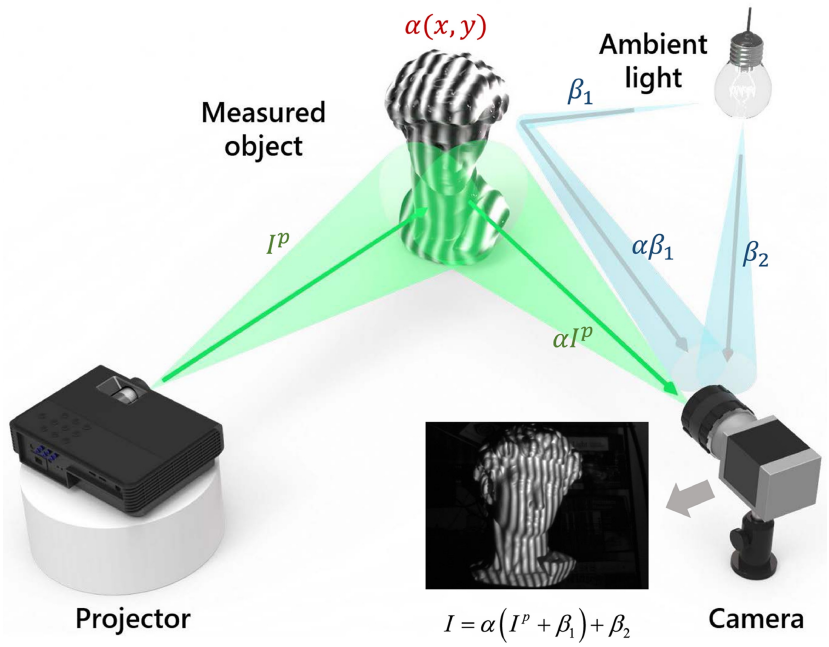

Figure 1.7: Fringe projection working principle: the fringe pattern (dark and white lines) is projected on the object (statue) (Zuo *et al.*, 2018)

From a mathematical viewpoint, a fringe pattern is described by a periodical function, for example a sinusoidal signal. The intensity of a point P with coordinate P(x,y), captured by a CCD camera on the reference image and on the object can be written respectively by Equation 1.12 and Equation 1.13 (Bonnaire, 2015):

$$I_{ref}(x,y) = a(x,y) + b(x,y)\cos\left[\phi_{ref}(x,y)\right] \tag{1.12}$$

$$I_{obj}(x,y) = a(x,y) + b(x,y)\cos\left[\phi_{obj}(x,y)\right] \tag{1.13}$$

where:

- a(x,y) is the mean intensity of the image
- b(x,y) is the amplitude of the signal (fringe pattern)
- ϕ_{ref}, ϕ_{obj} are the phase modulation of fringe pattern of the reference image and the object image

The difference of the phase shift between the reference image and the object is proportional to the height h(x,y) of the object (Equation 1.14) (Bonnaire, 2015):

$$h(x,y) = \gamma(\phi_{ref} - \phi_{obj}) \tag{1.14}$$

where: γ is a constant which depends on the configuration set-up. The system should be calibrated before experiment.

To calculate the height of the object, the phase shifting $\phi_{obj}(x,y)$ is evaluated by fringe analysis methods, for instance the Characteristic Polynomial or the Windowed Fourier Transform (Rastogi, 2003). The Characteristic Polynomial method consists of capturing the same image of object by varying the initial phase of fringe pattern an angle α of $\frac{2\pi}{N}$ where N is an integer number. The $\phi_{obj}(x,y)$ is calculated by Equation 1.15 (Bonnaire, 2015).

$$\phi_{object}(x,y) = arctan\frac{\sum_{p=0}^{N-1} I_i \sin(p\alpha)}{\sum_{p=0}^{N-1} I_i \cos(p\alpha)} \tag{1.15}$$

where: I_i is the intensity of the image i
For example, the $\phi_{object}(x,y)$ can be calculated from 4 images of the object with the same state and a phase variation of $\pi/2$ on the fringe pattern by Equation 1.16 and 1.17 (Bonnaire, 2015).

$$I_i = a(x,y) + b(x,y)\cos\left[\phi_{obj}(x,y) + \frac{i\pi}{2}\right] \tag{1.16}$$

Where: i = 0, 1, 2, 3 correspond to the 4 images

$$\phi_{obj} = arctan\left[\frac{I_4(x,y) - I_2(x,y)}{I_1(x,y) - I_3(x,y)}\right] \tag{1.17}$$

To quantify the object's height, the phase needs to be unwrapped in the continuous phase shifting by phase stepping techniques (Rastogi, 2003).

From the working principle of the fringe projection method, it is noted that the method enables only 3D shape reconstruction or quantifies the height of object. The method needs to be coupled with other methods, i.e., the DIC method to enable full-field kinematic measurements.

Advantages, drawbacks and applications

Advantages The fringe projection is widely used for measuring 3D-shape of an object from small scale (several millimeters) to large scale (several meters) (Brémand *et al.*, 2011). The method requires a simple implementation, in general a fringe projector and a CCD camera while being sufficiently accurate for quantitative measurements. The spatial resolution and the accuracy of the method depends on phase shifting evaluation methods and the experimental set-up configuration. The spatial resolution to 5/100 mm for an object of 1 m^2 (Brémand *et al.*, 2011) can be achieved. The method is widely used for the 3D shape reconstruction with complex geometry, for example objects presenting many curvatures like tissue or in biomechanics (Bonnaire, 2015).

Drawbacks The spatial and the accuracy of the method depends on the phase extraction and configuration set-up. Sciammarella et al. mentioned that the phase error is caused by several parameters such as: intensity noise, lens defocusing, phase shifting error, motion-induced error and saturation or shadow regions and illumination fluctuation (Sciammarella *et al.*, 2012). For

example, the saturation can occur while the fringe patterns are projected on a high reflectivity surface. The saturation causes non sinusoidal signals on fringe patterns, thereby causes phase reconstruction errors (Zuo *et al.*, 2018). Phase evaluation can be influenced by the miscalibration, the local variation of intensity on images and vibration. In order to avoid systematic errors caused by these problems, specific algorithms are developed. For example, Surrel developed a self-calibrating algorithm that is insensitive to the sample vibration (Surrel, 1996). Pavageau et al. developed a new algorithm that does not require calibration step for large surface profiling by the fringe projection (Pavageau *et al.*, 2004). Furthermore, the method is limited at 3D-shape reconstruction. That is why, recently the method is coupled with the DIC method to retrieve 3D kinematic measurements.

Applications of the fringe projection method The fringe projection method is useful for retrieving 3D shape with curvatures or to measure the out-of-plane displacement at room temperature. For example, Genovese et al. used the fringe projection for the out-of-plane and in-plane displacement measurements for hyperplastic materials (Genovese *et al.*, 2006). In their study, the 3D shape of materials before and after being deformed is superposed. By this way, 3D displacement field is estimated. Wang et al. used the projection fringe to validate the filling stage of the resin infusion process (P. Wang *et al.*, 2010).

The method can be combined with 2D-DIC method for in-plane kinematic measurements. In this coupling method, the fringes projection provides the 3D-shape. A couple of points (point cloud) with precise coordinates are generated. The 2D-DIC method, having the same coordinates tracks the displacements of these points. The coupling method was used by Bonnaire to measure the strain of lumbar belts (Bonnaire, 2015). Nguyen et al. and Felipe-Sesé et al. used the same method: combining the fringe projection and the 2D-DIC for 3D shape and deformation measurements (Nguyen *et al.*, 2012 and Felipe-Sesé *et al.*, 2014). The last authors compared this method with the 3D-DIC method and showed that the relative difference was only 4% for X-displacement and 6.5% for Y-displacement. The fringe projection combined with the 2D-DIC method is frequently employed in biomechanics applications.

The fringe projection method was also employed for kinematic measurement at high temperatures. Southon et al. used the fringe projection method as a quick tool to detect out-of-plane defects on samples during the laser sintering of polymer at <175 °C (Southon *et al.*, 2018). In the hot forming temperature range, Beermann et al. designed two cameras with different lenses and a projector for 3D-shape reconstruction of the hot piece (Beermann *et al.*, 2018). The method showed a great potential as a quick instrument for a 3D-visualization of an object. Nevertheless, the method is less reliable because of a saturation from object radiation and potential calibration errors.

1.3.3.2 Grid method

The grid method uses a grid pattern (vertical lines and horizontal lines) that is adhered on the surface of the specimen to measure in-plane mechanical displacements or strains (Figure 1.8). The displacement and strain are deduced from two images: the first one is the reference image (no load is applied on object) and the second one is taken when the object is deformed. The grid method was first developed in 1960s (Grédiac *et al.*, 2016). At that time, the coordinate of the points (intersection between horizontal lines and vertical lines) of deformed grid was calculated manually. The grid method with automatic displacement or strain calculations is developed in 1990s. The method has achieved a lot of progress. According to Grédiac et al., it is a suitable method for in-plane small displacement or strain (Grédiac *et al.*, 2016). The method can overcome the inaccurate small strain, which is still a challenge of 2D-DIC method.

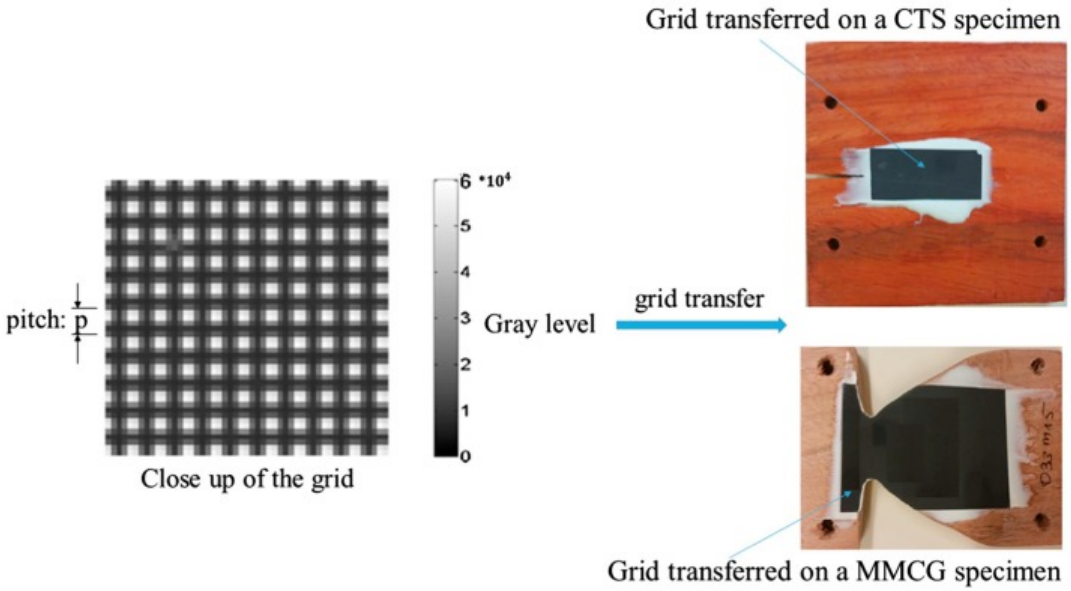

Figure 1.8: A grid pattern that is transfered on a wood specimen for mechanical test (Odounga *et al.*, 2018)

Working principle

The complete theory of the grid method is presented by Grédiac et al. (Grédiac *et al.*, 2016). Since a grid pattern contains periodical lines, the intensity (grey-level) of a point on the grid pattern, captured on a CCD sensor can be written by Equation 1.18 (Grédiac *et al.*, 2016).

$$s(x,y) = \frac{A}{2}\left(2+\gamma.frng(2\pi fx+\phi_x^1(x,y))+\gamma.frng(2\pi fy+\phi_y^1(x,y))\right) \tag{1.18}$$

where:

- A: is the mean intensity of the image
- γ is the contrast of the pattern lines, from 0 to 1
- frng is a real 2π-periodical function with an amplitude equal to 1 and the mean value equal to 0
- f is the frequency of the grid pattern f = 1/p , p [mm] is the pitch size
- $\phi_x(x,y)$, $\phi_y(x,y)$ are phase modulations, defined as modulo of 2π along the Ox and Oy axes

We denote that s_1 and s_2 are respectively the pixel intensity having a coordinate (x,y) before and after deformation. ϕ_x^1, ϕ_y^1, ϕ_x^2, ϕ_y^2 are phase modulations before and after deformation in the Ox and Oy direction. If there is no change of illumination of the specimen, after a displacement u(x), the initial pixel intensity s_1 becomes s_2 (Grédiac *et al.*, 2016).

$$s_2(x+u(x)) = s_1(x) \tag{1.19}$$

The displacement is proportional to phase modulation $\Delta\phi(x)$ (in Ox direction) (Grédiac *et al.*, 2016)

$$\Delta\phi(x) = -2\pi f u(x) \tag{1.20}$$

In practice, u(x) is unknown. It can be estimated by the iterative approach: $u^{n+1} = f(u^n)$ by Equation 1.21 (Grédiac *et al.*, 2016).

$$u(x)^{n+1} = -\frac{p}{2\pi}(\phi^2(x+u^n(x)) - \phi^1(x)) \tag{1.21}$$

The strain $\varepsilon_{ij},\ i,j = x,y$ component, for "small" strain (less than 0.05) is calculated from the derivation of displacement (Equation 1.22) (Lemaitre *et al.*, 2020).

$$\varepsilon_{ij} = \frac{1}{2}\left(\frac{\partial u_i}{\partial j} + \frac{\partial u_j}{\partial i}\right) \quad i,j = x,y \tag{1.22}$$

With assumption that:

$$\frac{\partial \Delta\phi_i}{\partial j} = \Delta\frac{\partial \phi_i}{\partial j} \quad i,j = x,y \tag{1.23}$$

The Equation 1.22 becomes Equation 1.24 (Grédiac *et al.*, 2016).

$$\varepsilon_{ij} = -\frac{p}{4\pi}\left(\Delta\frac{\partial \phi_i}{\partial j} + \Delta\frac{\partial \phi_j}{\partial i}\right), \quad i,j = x,y \tag{1.24}$$

The mechanical strain fields are calculated from the phase modulation. The phase modulation in Equation 1.24 can be evaluated by either the Fourier Transform (FT) or the Window Fourier Transform (WFT) algorithms (Grédiac *et al.*, 2016).

Practical procedure for kinematic measurements by the grid method
In practice, strain and displacement fields using the grid method are measured by following these steps below.

- Step 1: **Making a grid pattern on the specimen**. There are many methods to make grid pattern, from the atomic scale or micro scale (for microscopic experiments) to macro scale (for mechanical tensile tests) (Grédiac *et al.*, 2016). The common technique for making a grid is using paint spray and stencil for mechanical tests. Defects on the grid can appear on the specimen, such as lack of ink on a grid pattern. Defects can induce initial phase modulation, so they influence the results of kinematic measurements. The pitch size, which is defined as the distance between grid lines, is from 0.8 mm to 2 mm (Grédiac *et al.*, 2016). Figure 1.8 presents a procedure of making a grid on a wooden specimen (Odounga *et al.*, 2018). The grid pattern with a pitch size of 0.2 mm is printed on a polymeric film. The grid pattern is then transferred on the specimen by sticking the polymeric film, polymerization and peeling-off step.
- Step 2: **Capturing images during mechanical tests**. Images are then transformed in the frequency domain to determine the phase change during the test. This is called the wrapping step.
- Step 3: **Unwrapping phase**. The phase modulation is calculated by the phase evaluation algorithm, for example the WFT algorithm. The phase modulation is then unwrapped to ensure the continuous phase difference (that could be more than $-\pi$ to π in the wrapping step (step 2)). The displacement and strain field are calculated from the continuous phase difference.

Advantages, drawbacks and applications

Advantages The grid method is known as a technique suitable for "small" kinematic measurements in two dimensions (Grédiac *et al.*, 2016). The spatial resolution of the grid method can be from 1/20 to 1/100 of the pitch size p (Bonnaire, 2015). The method is used to detect the local strain heterogeneities from the local heterogeneous microstructure of the material, for example the local plastic deformation of an aluminium multicrystal (Badulescu *et al.*, 2011) or in monocrystal (Delpueyo *et al.*, 2012). For instance, Saletti et al. compared the strain measured using the 2D-DIC and the grid methods for ultra-rapid tensile tests (Saletti *et al.*, 2016). The authors showed that the strain uncertainty given by the grid method is better than that given by the 2D-DIC for small strain. Thanks to the high accuracy in small displacement or strain measurements, the method is used to identify linear elastic properties of materials at room temperature, for example tensile tests, shear tests and three point deflection tests (Grédiac *et al.*, 2016).

Drawbacks To achieve the smallest strain or displacement uncertainty and good spatial resolution, the grid pattern should be prepared with the fewest defects. This is because fluctuations on the grid pitch may lead to phase fluctuation, leading to a "false" strain. In practice, it is quite difficult and expensive to prepare an ideal grid pattern. For the micro-scale tests, perfect grids can be prepared by the Focused Ion Beam technique (FIB) which is quite time consuming and costly. For the macro-scale tests, like tensile tests, grid patterns are made by stencil but sometimes present some defects. For example, local lack of ink may cause "blobs" in the phase evaluation, which results in discontinuity in strain fields (Grédiac *et al.*, 2016). Badulescu et al. showed that it is possible to deal with "false" strain due to grid defects by low-pass filtering method (Badulescu *et al.*, 2009). The second drawback of the grid method is the appearance of parasite fringe in a strain map because of the aliasing problem. To eliminate parasite fringes, images can be filtered by low-pass filter to "keep" only the "main" fringes (Grédiac *et al.*, 2016). Finally, the grid patterns should be calibrated with the respect of camera sensor size such that the size (in pixel) of vertical or horizontal line of the grid is an odd integer number. Finally, the grid method is limited at in-plane kinematic measurements for applications of solid mechanics.

Applications Thanks to a good resolution (low uncertainty, low dispersed strain points for the same image), the grid method is appropriate for small in-plane strain measurements. The method can be coupled with identification strategy, for example the Virtual Field method (VFM) to determine the elastic properties of materials at room temperature. For example, Xavier et al. and Avril et al. used the method to determine the longitudinal, transversal and shear stiffnesses of different materials (wood or metal) (Xavier *et al.*, 2007, Xavier *et al.*, 2009 and Avril *et al.*, 2008). Pannier et al. employed the grid method for elasto-plastic behavior of materials (Pannier *et al.*, 2006).

The grid method was also employed for strain or displacement measurements at high temperatures. For example, Chiappini et al. used the grid method and the inverse Finite Element Method to identify the elasto-plastic behavior and limit of formability of aluminum alloy at 300 °C (Chiappini *et al.*, 2017). Martin et al. used the micro-grid method to detect plastic strain between grain boundary by full-field strain measurements on duplex stainless microstructure material at 950 °C (Martin *et al.*, 2013). Results obtained presented a great potential of using the grid method for the investigation of multiphase microstructure deformation or strains at high temperatures.

1.3.3.3 Synthesis on the non-interferometric periodical-coding methods

The non-interferometric periodical-coding methods use periodical patterns (by fringe projection or a grid) to measure full-field kinematic measurements. In addition to the fact the these methods are more flexible than interferometric methods, they are quite simple for experimental set-up. For fringe projection, the technique needs a fringe projector and a CDD camera. The fringe projection, however, needs to be coupled with a full-filed measurement method. The grid method requires a well-prepared grid pattern and a CCD camera. The grid method can offer accurate measurements for "small" deformation. It is compatible with in-plane full field kinematic measurements for macro-scale experimental tests in solid mechanics.

1.3.4 Non-interferometric random-coding methods

The non-interference random coding methods use random patterns to measure the displacement or strain field of a specimen. Compared with periodical coding methods, random coding methods are more flexible, and the pattern preparation is quite simple. Two common methods used in experimental mechanics are the laser speckle method and the DIC method.

1.3.4.1 Laser speckle method

Working principle

Laser speckle pattern Laser speckle pattern is made from an interference phenomenon between a coherent light (a laser beam) and the scattered light from a rough surface of a specimen (Sharpe, 2008). When a laser beam (the incident light) goes to a rough surface that has a surface roughness Rz greater than the laser wavelength λ, it is scattered. The scattered light has a different phase relative to the phase of the incident light. These wavelets interfere each other and generate a granular spatial speckle pattern, called the laser speckle pattern. The speckle pattern has some characteristics: the speckle intensity obeys the normal law distribution, and the speckle pattern has a "good" contrast (Sharpe, 2008). In addition, the speckle size can be adjusted by the aperture of the camera system. Its size can be down to hundred microns, therefore the spatial resolution of kinematic measurements (Song *et al.*, 2020) is increased.

Kinematic measurements The laser speckle method uses the cross-correlation algorithm to calculate the displacement field. The cross-correlation algorithm tracks a movement of sub-images that include speckles. The cross-correlation function is performed in the Fourier frequency to reduce the calculation time. The position of the sub-image at time t is determined if the cross-correlation is maximum (Equation 1.25) (Sharpe, 2008).

$$CC = FT\{A(i,j)\} * FT\{A'(i+d_x, j+d_y)\} \tag{1.25}$$

where:

- CC is the cross-correlation value
- $A(i,j) = \sum_{i=0}^{N-1} \sum_{j=0}^{M-1} A(i,j)$ is the pixel intensity of a sub-image before deformation
- $A' = \sum_{i=0}^{N-1} \sum_{j=0}^{M-1} A'(i+d_x, j+d_y)$ is the pixel intensity of a sub-image after deformation

The displacement field is deduced from the positions of sub-images A and A'.

Advantages, drawbacks and applications

Advantages The biggest advantage of the laser speckle method is that it requires a simple experiment set-up (a laser beam and a camera) and it enables the production of a small speckle pattern size. Therefore, the spatial resolution for displacement field is improved. In addition, the speckle size can be adjusted. The contrast of the laser speckle pattern is better than the one made by paint technique used for the DIC method (Song *et al.*, 2020). Furthermore, the laser speckle pattern is less influenced by the temperature, for example, the oxidation problem. The laser speckle pattern is employed in mechanical tests at high temperatures (Zheng *et al.*, 2020).

Drawbacks The limitations of this method is that the speckle pattern must be made on rough surfaces. The roughness of the specimen should be greater than the laser beam wavelength to create the laser speckle pattern. Moreover, the laser speckle size and quality of the laser speckle pattern depends on a number of factors such as: the roughness of the specimen, the camera aperture, the material properties of the specimen on which the laser speckle pattern is made and temperature (radiation effect). For example, Song et al. observed that the Mean Intensity Gradient (MIG), a criterion used to assess speckle quality (B. Pan *et al.*, 2010a) decreased when the specimen roughness increases (Song *et al.*, 2020). At high temperatures, due to specimen's radiation, the laser speckle pattern presents a portion of saturated pixels, which could bias the cross-correlation process (Song *et al.*, 2020). Furthermore, the laser speckle pattern, like speckle painting and other techniques is also influenced by the temperature, for example, the oxidation problem because surface of the material changes during the oxidation. Finally, the image is divided into sub-images, thereby reducing the spatial resolution. On the cross-correlation algorithm, the maximal of cross-correlation (peak) can appear twice because of the similarity of speckle motifs. The second-peak of correlation can influence the accuracy of the method.

Applications The laser speckle method is widely employed in experimental mechanics not only at room temperature but also at high temperatures. Zheng et al. used the laser speckle method to measure the plastic strain of the aluminum sheet having a thickness of 0.5 mm at 400 °C (Zheng *et al.*, 2020). This study showed a good agreement between strains measured by the laser speckles and the speckles made by the spraying technique. The laser speckles can resist a Eulerian-Almasi strain measurement of 0.6. Anwander et al. used the laser speckles, radiation filter and the cross-correlation algorithm for strain measurements at 1200 °C in order to determine the Young's modulus and the TEC of nickel-alloy material (Anwander *et al.*, 2000). The laser speckle size is about 60 µm, therefore the spatial resolution was excellent: 20 microstrains. Song et al. used the speckle laser method and the Improved Random Sample Consensus algorithm for full-filed strain measurements of tensile tests of C/C composite at 2000 °C (Song *et al.*, 2018). The strain curve obtained from this method is basically consistent with results measured by contact extensometer. Nevertheless, the correction algorithm is based on successive pairs of images (incremental correlation algorithm) which can cause systematic errors due to the change of surface roughness during tensile test. Furthermore, after weighing up the advantages, against the drawbacks of this method, we found that the laser speckle method will not be used in the mechanical tests in our study due to material and device constrain in our laboratory.

1.3.4.2 2D-Digital Image Corrrelation method (2D-DIC)

The 2D-Digital Image Correlation method (2D-DIC) is first developed in 1980s (Sutton *et al.*, 2009). Since their early development, the method has much progress. It becomes one of the most

popular optical non-contact method in experimental mechanics. In this following paragraph, we present the working principle, advantages and limitations of the method.

Working principle
In this section, 2D-DIC's working principle is presented in the following order: the pinhole model, the speckle pattern, the image matching algorithm, the subset-interpolation and the strain computation. This order is equivalent to the procedure that needs to perform for measuring full-field kinematic measurements. The pinhole model explains how an image is built. The speckle pattern displays an example of a speckle pattern used for the 2D-DIC method. The image matching algorithms include two approaches: the local and the global approach. The interpolation function describes computation of sub-pixel displacement. Finally the strain computation explains how the strain field is calculated from a displacement field.

Pinhole model
The pinhole model is used to describe how an 3D object in the real life is recorded as an image (2D) by a camera (Sutton *et al.*, 2009). The basic idea of the pinhole model is that each point on a surface of the real object with coordinate $M" = \{x" \; y" \; z"\}^T$ is projected on a plane (CCD sensor of a camera). Herein, the two coordinate systems of the object and the camera are perfectly parallel. The point M" has a coordinate $M = \{x \; y\}^T$ on an image. The relationship of the coordinate of point M" (in Cartesian system) and the coordinate of point M (in camera system), the intrinsic parameter of camera, that is the focal length and the distance object-camera, is written in Equation 1.26 (Sutton *et al.*, 2009).

$$M" = \begin{Bmatrix} x" \\ y" \\ z" \end{Bmatrix} = \begin{bmatrix} -f/z & 0 & 0 \\ 0 & -f/z & 0 \\ 0 & 0 & -f \end{bmatrix} \begin{Bmatrix} x \\ y \\ 1 \end{Bmatrix} \tag{1.26}$$

where:

- f [mm] is the focal length of the optical lens
- z [mm] is the distance of the camera and the object

From the pinhole model, it is noticed that each point on the surface has accurate coordinate on the image captured by a camera. Nevertheless, since the optical system is not always perfect, geometric aberrations (lens distortion at corners) can induce distortions in image. This image distortion can influence kinematic measurements. To reduce image distortion problem, the distortion models and calibration can be used (B. Pan *et al.*, 2013). Furthermore, if two coordinate systems of the object and the camera are not perfectly parallel, that is usually the case in real life, a rotation matrix must be added in Equation 1.26.

Speckle pattern
In 2D-DIC method, the displacement field is calculated from two images: the "reference" image at time t_0 and the "deformed" image at time t_1. In general, the "reference" image is free of load. It is captured at the beginning of a mechanical test. The "deformed" images are captured when the specimen is submitted to mechanical load. A correlation algorithm is used to track the displacement of points on the surface of the specimen. In practice, the tracking is performed thanks to speckles that are created on the surface of the specimen. Speckles are created randomly by many techniques, for example the black and white paint (Figure 1.9). To increase the accuracy and the spatial resolution of measurements using the 2D-DIC method, speckles should respect some criteria in term of size, distance and density. The speckle pattern criteria will be discussed in detail in Chapter 2.

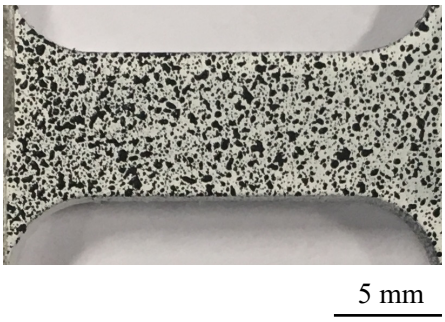

Figure 1.9: An example of a speckle pattern made by black and white paint by spraying

Image matching algorithms

The tracking is performed by image matching process that consists of minimizing the grey-level of pixels on regions of two consecutive images (Sutton *et al.*, 2009). The image matching algorithm can be classified into two approaches: the local (or subset-based) approach and the global approach. In local approach, the correlation is performed on subset windows while the global approach, the correlation is performed on "mesh" elements with defined shape function.

Local Digital Image Correlation In local-2D-DIC, matching algorithm is performed on subset-window. The subset window is the sub-domain on the image that should contain at least 3 speckles to reduce the systematic error due to aliasing (Reu, 2014). The subset size is an odd integer number because the displacement is calculated at the center of the subset window Ω (Figure 1.10).

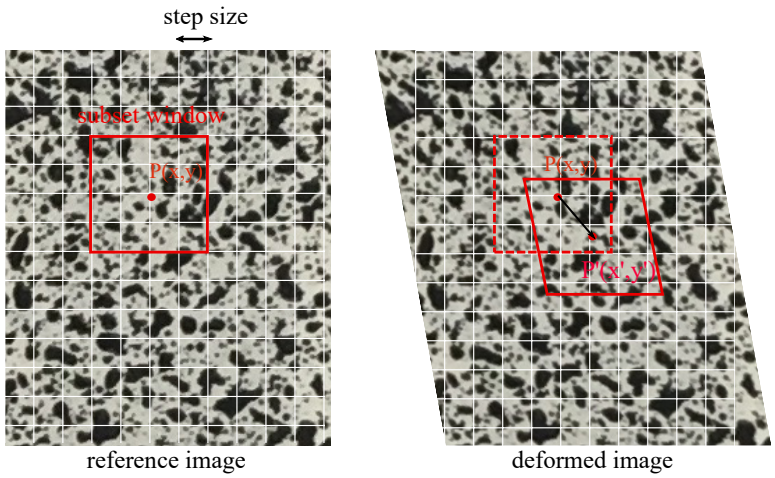

Figure 1.10: Concept of the local-DIC approach. Matching is performed on subset window (red square) (Sutton *et al.*, 2009)

The image matching is based on optimized correlation functions that aims to minimize the difference between the grey-level of subset windows of the "reference" image (at time t_0) and the one of "deformed" image (at time t_1). The matching process uses iterative optimization scheme, i.e., the Gauss-Newton iterative scheme in which the *subset-shape function* parameters are introduced and updated (Sutton *et al.*, 2009).

We suppose that $G(x+u(x,y),y+v(x,y))$ and $F(x,y)$ are respectively the pixel's grey-level on a subset window of the "reference" and "deformed" image. The correlation aims to minimize

the difference between the grey-level intensities of this subset before and after deformation, that is defined as the residual least square χ^2 (Equation 1.27) over the subset domain Ω (Sutton *et al.*, 2009).

$$\chi^2 = \int\int_{\Omega} (G-F)^2 \tag{1.27}$$

In practice, displacement u(x,y) are unknown. Therefore, the grey-level G at time t is firstly "guessed" (initialization step) as function of subset shape functions $\zeta(x,p)$ and $\zeta(y,p)$, where:

p = $p(p_0, p_1, p_2, p_3, p_4, p_5)$. p is the parameter vector of the subset shape function, $p_0, ...p_4$ are constants and unknown. The characteristic of $\zeta(y,p)$ is similar to the $\zeta(x,p)$.

Equation 1.27 becomes Equation 1.28 in which χ^2 needs to be minimized (Sutton *et al.*, 2009).

$$\chi^2 = \int\int_{\Omega} (G(\zeta(x,p), \zeta(y,p)) - F(x,y))^2 \tag{1.28}$$

The $\zeta(x,p)$ (for one dimension 1D) which integrates parameters in which p_0, p_1 are subset displacement, $p_1, ...p_5$ are subset deformation. Vector p is written in Equation 1.29 (Sutton *et al.*, 2009).

$$\zeta(x,p) = x + u + \frac{\partial u}{\partial x}\Delta x = x + \begin{bmatrix} p_0 \\ p_1 \end{bmatrix} + \begin{bmatrix} p_2 & p_3 \\ p_4 & p_5 \end{bmatrix} \Delta x \tag{1.29}$$

The subset shape function integrates the rigid body motion (second term in Equation 1.29) and deformation (third term in Equation 1.29). Equation 1.27 (minimization) is resolved by iterative approach, for example the Newton-Rapson iterative optimization scheme in which the increment Δp is solved by Equation 1.30 in a matrix form (Sutton *et al.*, 2009).

$$\Delta p = H^{-1} q \tag{1.30}$$

where:

- H is the Hessian matrix that calculates the sum of grey-level derivatives in the subset window between two images
- q is the vector of that calculates the derivative of grey-level and the change of mean intensity between two subsets.

The parameter vector p is converged after several iterations. The matching error is expressed in pixels, in general the matching is considered acceptable if the matching error is about 0.01 pixel.

In the reality, image contrast can be changed from one image to others during a mechanical test. To take into account the variation of image intensity, many optimization criteria can be employed. For example, the χ^2 criterion (SSD) in Equation 1.28 can be replaced by the normalized cross correlation criterion (NCC), the zero-mean sum of square difference (ZSSD) that takes account the offset lighting or the zero-normalized sum of squared difference criterion (ZNSSD) that takes account the offset and scale lighting (Sutton *et al.*, 2009).

Global Digital Image Correlation In the global-DIC, the Finite Element method with shape functions at nodes is integrated in the algorithm (Bathe, 2006). It means that in the first time, the specimen's geometry is meshed in priori. Speckle motifs are in "mesh" elements. The mesh elements is conceptually equivalent to the subset window. Compared with the local-DIC approach where each subset window is tracked consecutively via step size parameter (Figure 1.10), in the global approach, tracking is performed simultaneously (Figure 1.11) (Wittevrongel

et al., 2015). The global approach, like local approach, is also based on the principle of optical flow in which the image lighting is not changed from the "reference" image (f) to the "deformed" image (g) after undergoing a displacement u(x). To simplify, we present the formulation of global-DIC in one dimension 1D. The principle of optical flow is mathematically described by Equation 1.31 (Besnard *et al.*, 2006).

$$g(x) = f(x+u(x)) \tag{1.31}$$

where: f(x) and g(x) is respectively the grey-level intensity of a pixel having at coordinate x (in 1D) on "reference" image and the "deformed" image. From the first order of the Taylor's development, Equation 1.31 (Besnard *et al.*, 2006) becomes:

$$g(x) = f(x+u(x)) = f(x)+u(x).\nabla f(x) \tag{1.32}$$

where: $\nabla f(x)$ is the nabla operator with respect of the pixel's grey-level after and before deformation.

The correlation aims to minimize the difference of grey-level of pixels over a study domain Ω (Equation 1.33) (Besnard *et al.*, 2006).

$$\eta^2 = \int\int_{\Omega} [u(x).\nabla f(x) + f(x) - g(x)]^2 dx \tag{1.33}$$

The double integer represents the integration over the domain (two dimensions).

The displacement field u(x) is decomposed by a set of finite element shape function ψ (Besnard *et al.*, 2006).

$$u(x) = \sum_{n=1}^{n_e} \sum_{\alpha} u^e_{\alpha n} \psi_n(x) e_\alpha \tag{1.34}$$

where:

- α is the space dimension $\alpha = 1,2$ for 2D dimensions
- e_α is the element vector
- $\psi_n(x)$ is the finite element shape function in the elementary coordinate system
- $u^e_{\alpha n}$ is the nodal displacement in an element

By replacement the u(x) given in Equation 1.34 in Equation 1.33, the minimization of the difference of pixel's intensity leads to solve a linear system written in Equation 1.35 (Besnard *et al.*, 2006).

$$[M]\{u\} = \{b\} \tag{1.35}$$

where:

- $[M]$ is the "stiffness" matrix.
- $\{u^i\}$ is the displacement vector
- $\{b^i\}$ is the "force" vector

The $[M]$ "stiffness" matrix is calculated by Equation 1.36 (Besnard *et al.*, 2006).

$$[M]_{\alpha n \beta m} = \int \int_{\Omega} \left[\psi_n(x) \psi_m(x) \partial_\alpha f(x) \partial_\beta f(x) \right] dx \tag{1.36}$$

where:

$\partial f = \nabla f . e_\alpha$ is the directional derivative operator; m and n is the number of nodes in two directions Ox and Oy, α, β is space dimensions.

The $\{b^i\}$ vector is calculated by Equation 1.37 (Besnard *et al.*, 2006).

$$\{b_{\alpha n}\} = \int \int_{\Omega} [g(x) - f(x)] \, \psi_n(x) \partial_\alpha f(x) dx \tag{1.37}$$

In the global DIC, the Q4-DIC and Q8-DIC algorithm are most used (B. Wang *et al.*, 2016). Figure 1.11 presents the concept of the global-DIC approach with 2D-rectangular elements constituted by 4 nodes (Q4-DIC).

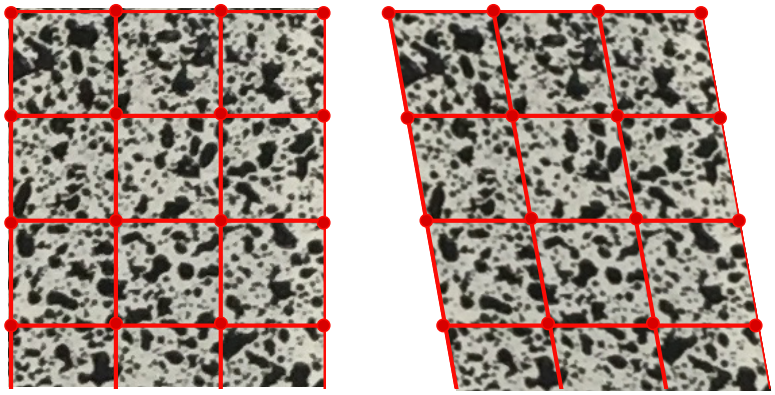

Figure 1.11: Concept of the global-DIC approach. Matching is performed on meshed element (red squares)

In case of Q4-DIC, the shape function of 4 nodes in the Cartesian coordinate are respectively: $n_1 = (1-x)(1-y)$, $n_2 = (1-x)y$, $n_3 = x(1-y)$, $n_4 = xy$. The u(x) in Equation 1.34 is rewritten in Equation 1.38 (Besnard *et al.*, 2006).

$$u(x) = \sum_{n=1}^{n_e=4} \sum_{\alpha}^{2} u^e_{\alpha n} N_n(x) e_\alpha \tag{1.38}$$

The "stiffness" matrix in Equation 1.36 is rewritten in Equation 1.39 (Besnard *et al.*, 2006).

$$[M]_{\alpha n \beta m} = \int \int_{\Omega} \left[N_n(x) N_m(x) \partial_\alpha f(x) \partial_\beta f(x) \right] dx \tag{1.39}$$

where:

α and β are space dimensions, N_n and N_m are shape functions in two dimensions, m = n = 2 nodes for each direction in a meshed element.

The "force" vector in Equation 1.37 becomes Equation 1.40 (Besnard *et al.*, 2006).

$$\{b_{\alpha n}\} = \int\int_{\Omega} [g(x) - f(x)] N_n(x) \partial_\alpha f(x) dx \tag{1.40}$$

With the same analogy with the finite element method, the "stiffness" matrix of the global-DIC approach is symmetric and parse for the linear behavior of materials. Therefore, the displacement vector in a direction can be calculated by solving linear system $[M]\{u\} = \{b\}$. It is noted that the displacement is calculated on pixels, which are integer numbers.

Subpixel interpolation function

In local and global-2D-DIC in the previous section, the matching pattern is calculated on pixels (integer number). In order to calculate the sub-pixel displacement (a displacement less than a pixel), the sub-pixel interpolation function is employed to deduce the sub-pixel intensity. By this method, a pixel is "divided" into smaller sub-pixels. The common interpolation function used in the DIC method is the linear, cubic (Chu *et al.*, 1985) for one dimension, bilinear, B-cubic, quintic spline, B-spline functions (Schreier *et al.*, 2000, Sutton *et al.*, 2009) for two dimensions for local-2D-DIC. The same interpolation functions used for local-2D-DIC can be also used for the global-DIC approach. In addition, Besnard et al. used the Fourier decomposition method as a novel sub-pixel interpolation (Besnard *et al.*, 2006). The advantage of Fourier decomposition interpolation is reducing the computation time, because the interpolation is performed in the frequency domain. Nevertheless, the Fourier decomposition presents oscillations at the edges of the ZOI (edges defects) that requires techniques to remove edges defects, for example, the padding technique (Besnard *et al.*, 2006).

Strain calculations

In solid mechanics, mechanical strain is calculated from displacement field measurements by Equation 1.41 (Lemaitre *et al.*, 2020). Calculated strain is the Green-Lagrange strain in the Cartesian coordinate system.

$$\varepsilon_{ij} = \frac{1}{2}\left(\frac{\partial u_i}{\partial j} + \frac{\partial u_j}{\partial i} + \sum_{i,j=1}^{2} \frac{\partial u_i}{\partial i}\frac{\partial u_j}{\partial j}\right) \quad i,j = x,y \tag{1.41}$$

In case of "small" mechanical strain (for example $\varepsilon = 0.02 - 0.05$), the later term in Equation 1.41 can be neglected. The mechanical strain undergoing a "small" deformation is calculated by Equation 1.42 (Lemaitre *et al.*, 2020).

$$\varepsilon_{ij} = \frac{1}{2}\left(\frac{\partial u_i}{\partial j} + \frac{\partial u_j}{\partial i}\right) \quad i,j = x,y \tag{1.42}$$

Strain field obtained from the derivative of displacement (Equation 1.42) is quite noisy because of noise in the displacement field. Therefore, strain field can be smoothed using filters. In this method, the strain value measured at a point P(x,y) is averaged by a number of neighboring points. The size of the filter is equivalent to the number of neighboring points (Reu, 2015d).

Advantages and limitation of the 2D-DIC

The advantage of the 2D-DIC method is flexible, requires simple implementation and it does not need expensive device (except the telecentric lens). The method provides also good accuracy and uncertainty. The spatial resolution can be up to 0.01 sub-pixel (Sutton *et al.*, 2009). The method is widely employed for full-filed kinematic measurement in experimental mechanics. Over 40 years, the number of publications using the 2D-DIC for displacement or strain field increased exponentially (Dong *et al.*, 2017).

Nevertheless, the method presents a number of parameters that can directly influence the reliability of kinematic measurements. The source of errors are multiple. Some sources of error are difficult to control, like lighting, sample rotation. Sources of errors related to the experimental condition as well as the 2D-DIC algorithm will be explained in section 1.5.1. In most of experimental test, the uncertainty of the method is higher than 2×10^{-3} (Pottier, 2011). Grédiac et al. showed that the limitation of this method is the "small" strain measurement (Grédiac *et al.*, 2016). Furthermore, according to Sutton et al., the DIC method lacks of standardization in metrological measurements or assessment of measurement results (Sutton *et al.*, 2017).

1.4 Choice of the full-field measurement method for measuring strain in mechanical tests

We have presented in previous sections different measurement methods that are used in experimental mechanics. Each method has advantages and also drawbacks. For example, the holography, Moiré inteferrometry is considered as "referent" methods for "small" strain measurements. Nevertheless, these methods require accurate and complex experiment set-up. The fringe projection method is easy to set-up but cannot measure the mechanical strain. The grid method is a good option for measuring in-plane and "small" mechanical strain but it requires a well prepared grid for the best accuracy. The implementation of 2D-DIC system is simple and flexible.

After considering the advantages and limitation of each method, two options are possible: the grid method or the 2D-DIC method for "small" thermo-mechanical strain at high temperatures. Finally, based on the expertise and the available devices in our laboratory, we decided to employ the local-2D-DIC method to measure thermo-mechanical strains during this Ph.D. thesis.

1.5 Focus on the local-2D-DIC method for "small" strain measurements

1.5.1 Source of errors related to local-2D-DIC method

The 2D-DIC method is well-known as a flexible method for full-field kinematic measurements. Nevertheless, the accuracy and uncertainty of displacement or strain fields depends strongly on experimental conditions as well as the 2D-DIC parameters in its algorithm. Therefore, it is worthy to identify and evaluate the influence of parameters of the 2D-DIC method. The source of error is classified into two groups: experimental conditions, which usually induce random and/or bias errors and the 2D-DIC algorithm, which causes usually bias errors.

1.5.1.1 Source of errors related to experimental conditions

Table 1.1 lists the non-exhaustive sources of 2D-DIC errors related to experimental conditions. For each source, the type of error, the estimation of error values and methods to minimize each influence factors found in literature are detailed.

Main factors influencing kinematic measurements are noise, the lighting condition, rotation of sample, the out-of-plane displacement and speckle patterns. These factors can cause random (type A) or systematic error (type B). For example, the systematic error due to lens distortion

can be corrected by a correction model and grid calibration (Sutton *et al.*, 2009, B. Pan *et al.*, 2013).

It is highlighted that the out-of-plane displacement, the in-plane rotation and the rigid body motion are among the most influence factor and the less correctable factor (Haddadi *et al.*, 2008). The systematic errors due to these factors become significant in case of small strain measurements. They should be evaluated before each mechanical test. For example, Hoult et al. demonstrated a small out-of-plane movement of specimen causes an significant error (mean values of the vertical error and the horizontal error are respectively 8.0 $\mu\varepsilon$ and -6.8 $\mu\varepsilon$) that may not adequate for strain less than 100 $\mu\varepsilon$ (Hoult *et al.*, 2013). This kind of errors should be corrected for Poisson's ratio measurement by the 2D-DIC method. Sutton et al. suggested a linear regression model in which the in-plane strain error is proportional to the out-of plane motion and the distance camera-object (Sutton *et al.*, 2008). The out-of-plane displacement problem is reduced by the use of a telecentric camera, by setting far from the object or applying the linear correction model.

The second factor, rotation of sample is usually caused by the mis-alignment of camera and sample. The in-plane displacement error is less than 0.5 pixels (Reu, 2016). In-plane displacement is usually from the rigid body motion of specimen relative to grips at the beginning of experimental tests (mis-alignment).

Speckle patterns should respect speckle criteria to reduce both random and systematic errors (Reu, 2015a, Reu, 2015b). Several experimental conditions are hardly controlled, depending on the real condition during mechanical tests for example lighting, heat disturbance, noise floor, sample rotation. In this case, a preliminary evaluation of uncertainty on displacement or/and strain is recommended before tests. Reu recommended that the DIC uncertainty should always compared with the measured signal by the ratio signal-to-noise (Reu, 2016). The author highlighted that the most challenging situation is this ratio is low. In case of the noise has the same order of value compared with the measured signal, the measurement has a high uncertainty (Reu, 2016).

Table 1.1: Sources (non-exhaustive) of 2D-DIC error related to experimental conditions

Factors	Type	Observation	Correction	Reference
Lens distortion	B	Depends on lens manufacturer	Use a correction model or a grid calibration	Sutton *et al.*, 2009
Out-of-plane displacement	B	Proportional to the distance camera -object	Use the telecentric camera	Hoult *et al.*, 2013
Camera motion	B	Due to vibration and/or camera heating, strain error is up to 2.5×10^{-3}	Use floating optical table	Reu, 2016
Sample rotation	B	Strain uncertainty is from 4×10^{-4} to 1.5×10^{-3}	Errors is acceptable if the rotation angle is less 10°	Haddadi *et al.*, 2008
Rigid body motion	B	Order of strain uncertainty: 4×10^{-4} to 1.7×10^{-3}	Subtract the displacement from the rigid body motion	Haddadi *et al.*, 2008
Lighting	A, B	Low light causes correlation disruption	Image should have highest dynamic range	
Noise floor	A	The standard deviation of displacement is less than 0.01 pixels	An evaluation of noise floor is assessed before tests with static images	Jones *et al.*, 2018
Heat disturbance	A,B	Heat disturbance from light, from convection flow (thermo-mechanical tests), the standard deviation of kinematic field is various	Influence of heat haze is evaluated before performing tests in static conditions	Jones *et al.*, 2018, Delmas, 2012
Speckle size	B	Too small speckles cause aliasing problem	Speckle size should be more than 3 pixels	Reu, 2015c
Speckle contrast	A, B	Low contrast cause the noisy kinematic fields	Image should have highest dynamic range	Reu, 2015a

A: random error; B: bias error

1.5.1.2 Source of errors related to the local-2D-DIC approach

Beside the experimental conditions, the choice of parameters in DIC algorithm influences the uncertainty and the accuracy of kinematic measurements given by the DIC method. The sources of errors are subset-shape function, subset-size, the sub-pixel interpolation function and strain computation.

Table 1.2 presents the source of errors related to the parameters of local-2D-DIC algorithm, the methods to minimize the source of errors and references. For instance, in local-2D-DIC, the choice of correlation coefficient has influence on the accuracy of measurements. Tong evaluated the choice of different correlation coefficient on the uncertainty of strain maps (Tong, 2005). In their studies, different simulated images that correspond to unfavorable experiment condition (a decrease of lighting or the contrast) are employed to evaluate the choice of correlation coefficient on strain results. The authors showed that the ZNSSD criterion presents the best robustness and the most reliable results. Reu and Lecompte et al. recommended a larger subset size in local

DIC and larger speckle patterns for a better accuracy and a lower uncertainty of measurement (Reu, 2014 and Lecompte *et al.*, 2006).

Concerning the interpolation function, Bornert et al. showed that a higher subset interpolation function presents less systematic error for a "large" displacement (Bornert *et al.*, 2009). Furthermore, sub-pixel interpolation scheme causes also systematic error due to undermatching pattern. The accuracy of sub-pixels displacement or strain depends on the choice of sub-pixel interpolation function. In general, the accuracy of measurement at subpixel is less than 0.02 pixel (Schreier *et al.*, 2000). Bicubic interpolation function is highly recommended for sub-pixel measurements.

Regarding strain computation, Sutton et al. demonstrated that the strain errors are due to displacement errors, which come from the sub-pixel interpolation (Sutton *et al.*, 2009). Furthermore, strain field, obtained from derivatives of displacement error can be noisy if the image presents a lot of noise (from lighting condition or speckle pattern). In this case, a low-pass filter can reduce noise. A large filter size can reduce the uncertainty of strain but decrease the accuracy. Therefore, the use of filter size should be used with compromise of the strain accuracy and strain resolution.

Table 1.2: Sources of error related to the local-2D-DIC algorithm

Source	Types of error	Recommendation, observation	Reference
Correlation coefficient	B	The ZNSSD coefficient presents the best robustness and reliable results	Tong, 2005
Subset size (local 2D-DIC)	A, B	Large subset size reduced measurement uncertainty and increase the accuracy of measurement	Lecompte *et al.*, 2006
Subset-shape function (local 2D-DIC)	B	Higher order of subset shape function reduced systematic error	Bornert *et al.*, 2009
Sub-pixel interpolation	B	Accuracy of sub-pixel < 0.006 pixel, B-spline interpolation function	Schreier *et al.*, 2000
Strain computation	A, B	Low-pass filter size reduced strain uncertainty	Reu, 2015d

A: random error; B: bias error

1.5.2 Strategies for identification of the material parameters using full-field measurements

With the great progress of numerical methods in recent years, in solid mechanics, numerical simulation using the finite element method is usually used to predict final shape of piece and to reduce cost and time of piece fabrication. To validate the numerical model or identify the material parameters, the full-field measurements (displacement and strain) are usually employed.

In principle, the material parameters can be identified by minimizing the difference between the full-filed measurements obtained from the 2D-DIC method and those obtained from the model with "guess" material parameters (Avril *et al.*, 2008). Nevertheless, for complex shape or experimental test or heterogeneous material, i.e., composite, many material parameters need to

be identified simultaneously. Therefore, some algorithms for identification of material properties are developed. They are the Finite Element Method Updated (FEMU), the Virtual Field Method (VFM), the Equilibrium Gap method (EGM) and so on (Avril *et al.*, 2008). With the limit of our knowledge, we only present the basis concept of the first two algorithms: FEMU, VFM and some studies using these methods to identify material parameters. The aim of presenting different strategies for identification of the material is for perspectives of this Ph.D thesis, we would use one of this strategy method to identify the material properties at high temperatures.

1.5.2.1 Update Finite Element Method (FEMU)

Background

The method consists of coupling a Finite Element model and a kinematic field measured using the DIC method in order to identify constitutive parameters of the material. Constitutive parameters are calculated by minimizing the difference of known values, i.e., displacement measured using the DIC method, prescribed force and those "predicted" from the numerical model obtained from "guess" constitutive parameters. This difference is called the residual value. The constitutive parameters of material is optimized after several iterations using the Gauss-Newton or Levenberg-Marquardt optimization scheme (Avril *et al.*, 2008). For each iteration, the predicted values, i.e., displacement and the residual values are updated. If the residual is less than a threshold value (for example 1×10^{-3}), then the solution is converged. The constitutive parameters of materials are the values from the last iteration. In FEMU method, the residual value can be evaluated by the force balance method (FEMU-F) or the displacement method (FEMU-U) (Avril *et al.*, 2008) or mixed of force balance and displacement (FEMU-U-F) (Pottier, 2011).

Applications

The FEMU is one of the most common method for the identification of material's properties. The method allows to identify a number of constitutive parameters of material for complex geometrical tests. By coupling with the full-field displacement measured using the DIC method, the method offers a complete set of material parameters.

The applications of this method are various. For example, Lecompte et al. and He et al. used the local-2D-DIC and the FEMU method to identify the orthotopic elastic parameters of composite materials (Lecompte *et al.*, 2007 and He *et al.*, 2016). The material parameters obtained are very well in agreement with the values obtained by traditional uniaxial tensile tests (Lecompte *et al.*, 2007). Furthermore, the method converges rapidly giving a full data of elastic parameters of composite material. Leclerc et al. and Passieux et al. coupled the global-DIC and the FEMU to identify in-plane elastic parameters of the composite material (Leclerc *et al.*, 2009 and Passieux *et al.*, 2015). In their method, the spatial resolution is improved thanks to the use of fine mesh from the finite element. Molimard et al. employed the Moiré interferometry and the FEMU method for the identification of four orthotopic plate stiffness of composite material (Molimard *et al.*, 2005). The Moiré interferometry is advantageous for "small" mechanical strain (strain less than 2×10^{-3}). In their study, the identification strategy is improved Leverberg-Marquardt algorithm. The Young's modulus given from the FEMU method has only 4% of difference compared with reference method.

1.5.2.2 Virtual Field Method (VFM)

Background

The method is based on the principle of virtual work, that is based on the system equilibrium. It means that if the body force is negligible, the internal force obtained must be equal to external work applied on this system (Equation 1.43) (Pottier, 2011).

$$\int_V \sigma_{ij} e^*_{ij} dV = \int_S T_i u^*_i dS \tag{1.43}$$

where:

- σ_{ij} is the stress tensor
- T_i is the external force applied on the system V
- e^*_{ij} and u^*_i are respectively the virtual strain tensor and the virtual displacement

The method was developed by Grédiac et al. in 2000s (Grédiac *et al.*, 2016). The VFM method is performed by several steps. First, the virtual displacement field is carefully chosen. The virtual strain in Equation 1.43 is expressed by a material parameter tensor and the given full-filed strain (measured by optical methods). It is noted also that at this state, the strain tensor ε_{ij} should be expressed analytically from the in-plane strain component over external surface of solid, for example the plane stress, plane strain or bending a thin plate (Avril *et al.*, 2008). Once the virtual field is chosen, Equation 1.43 can be written as M equations corresponding to M unknown material parameters (Pottier, 2011). The M material parameters are solution of these M equations.

Applications

The advantage of the VFM is the method offers a rapid solution (material parameter) if the problem is linear because few iterations are necessary (Pottier, 2011). The method provides the elastic parameters of complex shape and heterogeneous materials. An application of using the VFM for cantilever beam specimen to identify the Young's modulus of material is presented in the reference of Sutton et al. (Sutton *et al.*, 2009). A number of studies that used this method to identify the elastic properties of composite materials. For example, Grédiac et al. coupled the grid method and the VFM to identify the directional Young's modulus of complex shape (hoop-wound glass-epoxy specimen) of composite material (Grediac *et al.*, 2006). Recently, Kim et al. employed local-2D-DIC and the VFM to obtain four anisotropic elastic Young's modulus of a fiber reinforced composites sheet (Kim *et al.*, 2020). The elastic constants determined from the VFM presents only -5.94 and 0.71% of difference compared with those determined by classical tensile tests. Their study showed that the VFM with an optimized tensile test can be used as an alternative solution to replace multiple standard tensile test to access elastic constants of composite material. Furthermore, the VFM is also applied to identify the elasto-plastic behavior of material. Valerie et al. used the local-DIC and the VFM method to identify the plastic behaviour of stainless steel at high temperature (Valeri *et al.*, 2017). Bai et al. coupled the local DIC and the VFM method for identifying elastic-plastic constitutive parameters of aluminum alloy laser welding considering kinematic hardening (Bai *et al.*, 2018). Results from this identification method were then employed to assess the influence of heat generated from the weld joint on material properties. Results show that the Young's modulus of the material in the heat-affected zone is decreased, which is in good agreement with the hardness measurements on the welded zone.

1.6 Conclusion and perspectives

In this chapter, different methods for kinematic measurements: contact methods and non-contacts methods are presented. The contact methods include the strain gage, the strain extensometer and the Bragg Fiber Grating sensor. The non-contact methods include three main categories: interferometric methods, non-interferometric periodical coding methods and non-interferometric random coding methods. Each method is presented in the order: working principle, advantages, drawbacks and applications of the method in experimental mechanics. The method presented is also assessed regarding the mechanical configuration and temperature in our study.

After presenting kinematic measurement methods, the 2D-DIC method with local approach is chosen for mechanical tests of our study. The method is assessed as a flexible method and sufficient accurate for "small" mechanical strain measurements in the "optimized" condition. The 2D-DIC method seems to be appropriate to mechanical configuration of our study (strain field will be measured at high temperatures and in limited space). After choosing measurement method, an additional state-of-the-art on sources of errors that can influence the accuracy of "small" displacement or strain measurements using the local-2D-DIC is presented. Finally, strategies for the identification of material properties is addressed. For the perspective, the local-2D-DIC method will be used to measure full-field strain of specimen in mechanical tests of our study.

CHAPTER

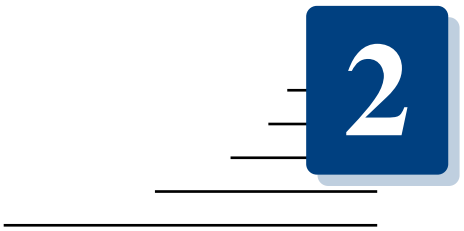

Speckle fabrication methods for DIC at high temperatures

In the first chapter, after reviewing different methods used for kinematic measurements (displacement and strain), we decide to use the local-2D-DIC method to measure strains for mechanical tests at HT during the Ph.D. thesis. In DIC method, the speckle pattern is crucial because it determines the spatial resolution and the measurement error. This chapter refers to speckle techniques developed for high temperature tensile tests. First, the problematic of high-temperature speckles and the objective of the study are presented. Next, the methodology Section 2.2, followed by the result on speckle quality created by six different techniques, Section 2.3, is presented. In the "Discussion", Section 2.4, a guideline for making a speckle pattern suitable to high-temperature mechanical tests is suggested. Finally, the chapter is ended with a conclusion and perspectives.

This chapter is based on the article published in "Luong, P., Bonnaire, R., Périé, J.-N., Sirvin, Q., Penazzi, L. Speckle pattern creation method for two-dimensional digital image correlation strain measurements applied to mechanical tensile tests up to 700 °C. Strain, 2021, 57(5), e12388. https://doi.org/10.1111/str.12388"

2.1 State-of-the-art

2.1.1 Problematic of speckles at high temperatures

In DIC, the speckle is one of the most important parameters. A “good” speckle enhances the spatial resolution and reduces measurement errors. Studies of Reu on speckles show that a "good" speckle pattern should satisfy criteria such as the speckle radius (r) (Reu, 2015c), speckle distance (d) (Reu, 2014), speckle density (ρ) (Reu, 2015b) and high contrast (Reu, 2015a).

There are many methods to prepare speckle patterns. The simplest technique is using paint, in which paint droplets are sprayed on the surface of material and become speckle dots (the speckle pattern). The painting is the most popularly used technique for speckle fabrication at ambient temperature. However, some paint is not compatible at high temperatures because it is evaporated, leading to a loss of image contrast or it flakes-off under mechanical strain. Figure 2.1 displays three images of speckle patterns made by painting technique: the first one shows the speckle pattern prepared at room temperature while the second one is the same speckles at 600 °C. The speckle pattern is no longer visible because of paint evaporation. The third image illustrates speckles that are flaked-off under thermo-mechanical strain. Therefore, the problematic of the speckle pattern at HT is that it must resist high temperatures, present a good contrast and ensure a good adherence on specimens during mechanical tests.

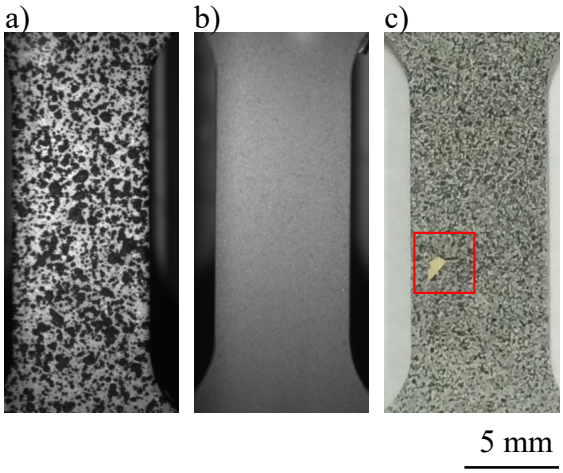

Figure 2.1: Problem of speckle at high temperature: a) a speckle pattern made by painting technique at room temperature, b) image with speckles made by painting has lost its contrast at 600 °C because speckles are evaporated, c) speckles flake-off under thermo-mechanical strain at 600 °C

2.1.2 Speckle fabrication methods at high temperatures

Searching for a speckle pattern that resists high temperature and high strain is still challenging. Table 2.1 presents a number of studies that have been developed for creating speckles on metallic materials at high temperatures. The studies are sorted by different techniques to produce speckles and the year of publications for each technique. First, Turner et al., Lyons et al., Pan et al., Hammer et al., Chartrel and Demazel et al. used high-temperature paint to create speckles, the most common speckle preparation technique (Turner *et al.*, 1990, Lyons *et al.*, 1996, B. Pan *et al.*, 2010b, Hammer *et al.*, 2014, Chartrel, 2016 and Demazel *et al.*, 2018). Speckles made

by airbrush or spraying technique, have various sizes, from 10 µm to 1 mm, with an image resolution of 20-50 µm/pixel (Dong *et al.*, 2017). The speckle radius made by these painting techniques (airbrush or spraying) depends on users and tools (nozzle tips and pressure). Speckles are not controlled and not repeatable. Furthermore, these speckles leave off from surfaces of specimens when they are subjected to a high strain (Hammer *et al.*, 2014), so disrupting the correlation process.

To overcome the speckle spallation problem, Vautrot et al. and Sirvin et al. developed the electrochemical marking on metallic samples allowing high-strain measurements (Vautrot *et al.*, 2014 and Sirvin *et al.*, 2019). The pattern is permanent speckle dots made from a thin oxide layer that has a different color compared with metallic surfaces. The technique can withstand high plastic strains (until necking state of the material), suggesting a new perspective. However, the speckle radius is large: more than 500 µm , which is equivalent to 20 pixels. Therefore, the spatial resolution is low.

The third technique is the laser engraving. Hu et al. used a laser beam to create speckle patterns on metallic surfaces (Hu *et al.*, 2018). The smallest radius is roughly 5 µm which is better for the spatial resolution. Nevertheless, the possible modifications in the microstructure and/or mechanical behavior of materials were not investigated.

Zheng et al. used a laser speckle, made by projecting a laser source on a rough surface of materials to measure the plastic strain of thin aluminum sheets (0.5 mm of thickness) at 400 °C (Zheng *et al.*, 2020). This study showed a good agreement between strains measured by the laser speckle and the spraying technique. The speckle laser can be used for strain measurement of 60%. Nevertheless, the laser speckle can be created only on a rough surface. It is difficult and less accurate to use this technique for high strains because under the mechanical load, the surface of specimen changes, so a change of light intensity that can induce bias measurements.

From speckle methods presented in Table 2.1, it is noticed that speckle fabrication techniques used in previous studies presents limitations. In painting technique, the speckle pattern is easily made but the speckle size depends on user experience, which influences spatial resolution. Speckles made by paint have the spallation problem during tensile tests under high strain rate or high strain. Speckles made by chemical marking technique can withstand high strains but the speckle dots are big, which reduce the spatial resolution. The laser speckle technique requires a rough surface samples and measurement are less reliable if light intensity changes.

Table 2.1: Summary of speckle preparation techniques used for mechanical tests in the range of hot stamping temperatures (from 400 °C to 750 °C)

Year	T°C	Speckle method	Speckle radius	Observation	References
1990	600	Manifold paint	0.2 - 2 mm	Maximum strain at 0.2	Turner *et al.*, 1990
1996	650	Boron Nitride and Alumina ceramic	100 µm	Speckles delamination of	Lyons *et al.*, 1996
2010	600	Commercial black HT paint	Unknown	Small strain measurement	B. Pan *et al.*, 2010b
2014	800	Rust®Oleum paint	Unknown	Speckles spallation	Hammer *et al.*, 2014
2016	650 - 730	Black and white paint	Unknown	Speckle degradation because of friction with tools	Chartrel, 2016
2018	600 - 10S00	High-temperature paint	Unknown	Speckles degradation	Demazel *et al.*, 2018
2014	400 - 500	Anodization	0.5 -1 mm	Speckles withstand plastic strain	Vautrot *et al.*, 2014
2018	400 - 750	Anodization	1 mm	Speckles withstand plastic strain	Sirvin *et al.*, 2019
2017	600-1000	Laser engraving	5 µm	Speckles resist HT	Hu *et al.*, 2018
2020	400	Laser projection	Unknown	Speckles resist a strain of 60%	Zheng *et al.*, 2020

2.1.3 Objectives

With the aim of increasing the resolution and the accuracy of displacement/strain, the study developed controllable and repeatable speckles that respect the criteria of a “good” speckle and resist high strains and high temperatures.

The structure of this chapter is developed as follows: First, in Section 2.2: Methodology, the speckle generator, the mask fabrication, speckle fabrication techniques and criteria for evaluating the speckle quality are detailed. Next, in Section 2.3: Results, the possibility of making six types of speckles, followed by the assessment of speckle quality at three temperatures (25 °C, 600 °C and 700 °C) is presented. From these previous results, speckles giving the best contrast are chosen for their adherence by tensile tests at high temperatures. In Section 2.4: Discussion, an appropriate speckle technique that balances “good” speckle criteria and adherence is suggested as a guideline to choose the best speckles for mechanical tests at high temperatures. Finally, in Section 2.5: Conclusion and perspectives, a summary of main results of the chapter and future work is presented.

2.2 Methodology

2.2.1 Materials

The current study involves creating speckles on (Ti-6Al-4V) TA6V alloy samples. The microstructure of this alloy at room temperature is presented in Appendix A.1: It is an equiaxed-dual phase microstructure. Smaller and brighter grains are the β-phase which is rich in the Vanadium element while bigger and darker grains belong to the α-phase (Sirvin *et al.*, 2019). From 400 °C to 700 °C, no phase transformation occurs on TA6V. The Young's modulus of TA6V at room temperature is 110 $\pm$ 20 GPa (Vanderhasten, 2007).

It is noticed that TA6V alloy is easily oxidized. The colour of TA6V oxide layer changes in the function of its thickness, due to the interference between the oxide layer and light wavelengths (Diamanti *et al.*, 2008). This characteristic is profitable to create a speckle pattern by an anodization process.

2.2.2 Creation of numerical speckles

A numerical speckle image (binary image) was developed to make a repeatable speckle. The process of creating a numerical pattern is inspired by the work of Orteu et al. (Orteu *et al.*, 2006). To obtain the best strain resolution in DIC, the speckle pattern should respect some criteria, i.e., the size and the distance between two speckle dots. Therefore, the speckle pattern is designed as circular dots whose radius is 7 pixels (equivalent to 105 µm), distance is 2 pixels (30 µm) and density is 0.4. The speckles were generated using Matlab®, (MathWorks®, Inc., Massachusetts, USA). The algorithm for creating numerical speckles is described as follow.

1. Initiation: A matrix with size of m $\times$ n (pixels $\times$ pixels), speckle radius (**r**), speckle distance (**d**), speckle density (ρ) were defined. The area of one speckle dot (A) was calculated by the equation:
$$A = \pi.r^2 \tag{2.1}$$
and assigned with the grey-level = 1.

2. Make a loop: A random lattice point $n_k(x_i, y_j)$, where i = 1 : n and j = 1 : m, was generated on the matrix (Figure 2.2a). The first speckle dot with area A was created by setting the grey-level equal to 1 (Figure 2.2b). The next dots were created if they are far enough from others, at least 2 pixels (Figure 2.2c). This process was stopped when speckle density (ratio of 1-grey level pixels to total pixels in the matrix) was around 0.4 (40% of coverage).

The speckle generation procedure is presented in Figure 2.2.

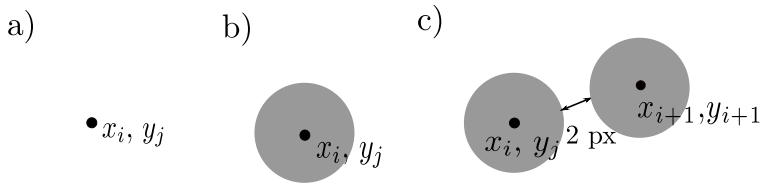

Figure 2.2: Steps to generate controllable numerical speckles: a) A randomly lattice point n_k with coordinate $n_k(x_i, y_j)$ is generated, b) The spot is created by assigning the grey-level = 1 with the area of the pattern, c) The second spot is created by respecting the distance of 2 pixels with the first one

Figure 2.3 presents the numerical speckle with respect to speckle criteria: speckle radius: 7 pixels (105 µm), speckle distance: ≈ 2 pixels (30 µm) and speckle density ≈ 0.4.

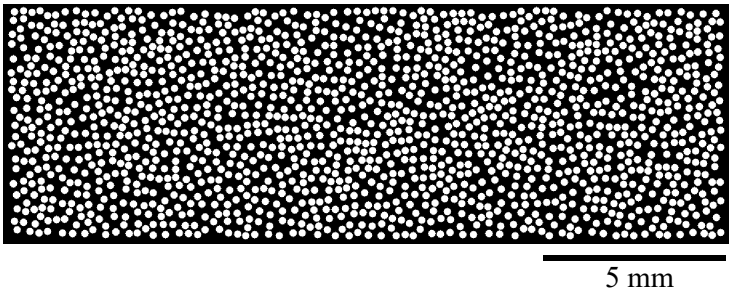

Figure 2.3: Numerical speckle pattern with respect to speckle criteria: speckle radius R_c = 7 pixels (105 µm), speckle distance d ≈ 2 pixels (30 µm) and speckle density $\rho \approx 0.4$

2.2.3 Speckle preparation methods

From the numerical speckle, six techniques were used to create speckles on TA6V samples. Six types of speckle pattern made by six techniques are classified into two groups (Dong *et al.*, 2017). The first group is the "additive" techniques (the matter is added on specimens) using a polymer mask while the second one is the "subtractive" techniques (the matter is removed) using a laser source. The techniques were:

1. "Additive" techniques
    - Painting (M1)
    - Direct anodization (M2)
    - Inverse anodization (M3)
2. "Subtractive" techniques
    - Laser engraving (M4)
    - Combining laser engraving and anodization (M5)
    - Combining laser engraving and painting (M6)

The first three techniques of speckles techniques (M1, M2, M3) require creating a polymer mask, which permits to replicate the numerical speckles. The pattern (holes) on the polymer mask, which should have a similar size to the numerical one, was drilled on a polymer thin film by a laser machine. Once the mask was made, the polymer mask was used to create speckles by matter transfer technique used in the study of Mazzoleni et al. (Mazzoleni *et al.*, 2015). For the last three techniques (M4, M5, M6), speckles were directly engraved on TA6V samples by using a laser source.

2.2.3.1 Fabrication of a reusable polymer mask

The polymer thin film was a vinyl (Vinyl Adhesive Cameo ®, Silhouette, USA) whose thickness is 0.2 mm and its melting point is between 100 °C and 200 °C. This polymer is in the form of an adhesive paper sheet that can stick on TA6V samples. The pattern was created by the laser source (a IPG Photonics fibre whose beam radius is from 70 µm to 100 µm) from the SLM125HL machine (SLM® solution, Lübeck, Germany) (Figure A.2). Variable parameters of the machine are: the power (P), the scanning speed (V) and the laser trajectory strategy (S). The power can be adjusted from 10 W to 20 W, the scanning speed is from 10 mm s^{-1} to 200 mm s^{-1}. There are three possibilities in scanning strategy: i) hatching (H), ii) contouring (C), iii) mix of hatching and contouring (H+C) (Figure A.3).

The laser system has a wide range of values for each parameter (power, scanning speed, laser strategy) which is designed principally to fabricate metallic specimens by the Selective Laser Melting method. Since the polymer mask has a low melting temperature, an investigation on laser parameters was performed to adapt to this unconventional material. Figure 2.4 presents a hold with a radius of 206 µm, equivalent to a speckle dot made on the adhesive paper sheet Vinyl Adhesive Cameo®. The laser power used was 20 W and the scanning parameter was 55 mm/s. The numerical design radius of speckle dots was 105 µm. It is noticed that although the laser power used to make speckle dots on the adhesive paper was relatively low, the polymer was melted because of high energy of the laser source. A difference of at least 100 µm between the numerical speckle radius (105 µm) and the physical one after laser (206 µm) was observed.

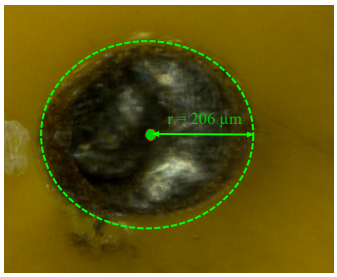

Figure 2.4: A hole, equivalent to a speckle dot made on the adhesive paper sheet Vinyl Adhesive Cameo (polymer mask) by the laser source of the SLM 125HL machine. The radius of the hold was 206 µm, larger than 100 µm compared with the numerical speckle dot (105 µm)

Results of this preliminary experiment tests showed that holes on polymer were created only if a speckle density of 0.2 and a speckle distance of about 320 µm were respected. It means that speckle densities obtained by the three techniques M1, M2 and M3 would be lower than the numerical one. To approach a set of laser parameters (P, V, S) allowing the pattern creation on the polymer, nine runs of experiments in which different values of three laser parameters (P, V, S) were combined. Theses nine experiments were set by following the orthogonal Taguchi design of experiments (DOE) (Goupy *et al.*, 2006). The response of the design of experiments was the hole's radius r [µm] on the polymer, measured by image processing using Matlab® software. Each experiment was repeated three times for the repeatability. Table 2.2 presents laser parameters in the (DOE).

Table 2.2: Nine runs of experiments in the orthogonal Taguchi design of experiment (DOE) with 3 levels-3 factors

N. exp	Factors (Level)			Factors (values)		
	P [W]	V [mm/s]	S	P [W]	V [mm/s]	S
1	-1	-1	-1	10	10	C
2	0	0	-1	55	80	C
3	+1	1	-1	110	150	C
4	0	-1	0	55	10	C+H
5	+1	0	0	100	80	C+H
6	-1	+1	0	10	150	C+H
7	+1	-1	+1	100	10	H
8	-1	0	+1	10	80	H
9	0	+1	+1	55	160	H

The influence of laser factors (P, V, S) on the hole's radius was determined by an analysis of variance (Anova, Matlab®) on the hole's radius obtained from the DOE. The variance with corresponding level i (i = -1, 0 and +1) of a factor is defined by Equation 2.2

$$\sigma_i^2 = \sum_{j=1}^{3} (s_i - \bar{s})^2 \tag{2.2}$$

where:

- s_i is the result of experiment corresponding to level i in the DOE
- $\bar{s}$ is the mean value of results on experiments corresponding to level i in the DOE

The influence of each factor, for example, factor A in the DOE matrix is evaluated on the variance of each factor (in percentage), calculated by Equations 2.3. The contribution on the variance of each factor is calculated in Equation 2.4. The effect of each laser parameter can be presented graphically by the Pareto diagram.

$$\sigma_A^2 = N \times \sum_{i=-1}^{1} (\sigma_i^2) \tag{2.3}$$

$$\%var(A) = \frac{\sigma_A^2}{\sigma_{total}^2} \tag{2.4}$$

where:

- N is the total number of experiment in the DOE
- σ_{total}^2 is the total variance of three factors in the DOE

2.2.3.2 Speckle preparation for "additive" techniques: the painting (M1), the direct anodization (M2) and the inverse anodization (M3) techniques

Polymer masks were used to create speckles by three techniques: painting M1, direct anodization M2 and inverse anodization M3. Speckles were created on TA6V rectangular samples (dimensions = 20 mm $\times$ 8 mm, equivalent to the Zone of Interest (ZOI) of TA6V specimens used for tensile tests). The technical process of making speckle is inspired by the classical lithography technique (Mazzoleni *et al.*, 2015, Z. Chen *et al.*, 2015).

For the technique M1, the high-temperature white paint Vitcas® (Vitcas Ltd, Bristol, GB) and the high-temperature black paint Rust-Oleum® (Rust-Oleum, USA) were employed. The white paint is made of silicone resin, it was used for the background while the black paint is made of n-cyclo-alkane. It was used for creating speckle dots. The technique M3 used an acrylic varnish (Jelt®, RS component, Beauvais, France), made of less than 10% of naphtha heavy petrol to create speckle dots. In the anodization process, a sulphuric acid solution of 1 g/l was prepared as the electrolyte. The voltage was generated by a tension generator.

The procedure for speckle fabrication by M1, M2 and M3 techniques is described as follows:

- Painting technique M1: Firstly, the TA6V sample was covered by the white paint to create a white background. Then the polymer mask was stuck directly on the sample. The black paint was applied on the sample surface using an airbrush (Aztek airbrush model 7778, pressure is 3 bar, nozzle tip is 0.3 mm) to create black dots through holes on the polymer mask. Finally, the mask was removed carefully.

- Direct anodization technique M2: Firstly, the polymer mask was stuck directly on the TA6V rectangle to protect regions covered by the polymer mask. Next, the metallic sample was connected to the positive electrode to process an electrochemical anodization under a tension of 30 V in 30 s. The local oxidation on polymer holes created black dots therefore, a black-on-white speckle pattern was produced by the anodization process. Finally, the polymer mask was removed.

- Inverse anodization technique M3: Firstly, the polymer mask was stuck directly on the surface sample. Then the sample was covered by Jelt® varnish using the airbrush to protect regions covered by the varnish from anodization. The polymer mask was then removed. Next, the sample was soared in the electrolyte bath for the anodization (tension: 20 V, time: 30 s) to create a white-on-black speckle pattern. Finally, the Jelt® layer was removed by the acetone solvent.

Figure 2.9 presents respectively the speckle patterns made by three techniques M1, M2, M3.

2.2.3.3 Speckle preparation for "subtractive" techniques: laser engraving (M4), combining anodization and laser (M5) and combining painting and laser (M6) techniques

Three types of speckles M4, M5 and M6 were created directly on TA6V samples surfaces (20 mm $\times$ 8 mm) by the SLM machine. Laser parameters chosen in our experiment were fixed at power P = 20 W, scanning speed V = 150 mm s^{-1} and strategy S: Hatching + Contouring H+C. These laser parameters correspond to a low energy of the laser source but sufficient to create speckle dots on the surface of TA6V specimen without modifying its bulk microstructure.

In technique M4, the speckle pattern was created by the laser engraving process. The numerical speckle pattern in the form of an image was converted in the CAD file (*stl* file) then read directly by the Magis® software (SLM® solution, Lübeck, Germany). Furthermore, to improve the image contrast and to avoid specular reflection from the smooth surface, in technique M5, prior to laser engraving, TA6V surface was covered by an oxide layer. The oxide layer's color was mat turquoise that does not reflect light, and it is made by using anodization process (tension V = 45 V, time = 30 s). In technique M6, before laser engraving, the metallic surface was covered by a white paint layer to protect the specimen from metal oxidations at HT. Images of three speckles patterns are presented in Figure 2.13.

Two experiments were performed to ensure that the laser engraving did not deteriorate the microstructure and the mechanical properties of TA6V samples. The first experiment is to characterize the microtructure of the TA6V material after laser engraving. To this end, the surface of a TA6V sample with speckles made by M5 technique was observed by an optical microscope (Leica GmbH, Germany) and by Scanning Electronic Microscopy (SEM) (FEI™, Oregon, USA). Afterward, the cross-section view through a M5 speckle dot on a TA6V specimen was observed by SEM, mode Back-Scattered Electron (BSE). The second experiment is to assess the mechanical behavior of the TA6V material before and after laser. To that end, the force-displacement curves and the stiffnesses of two TA6V tensile tests at room temperature: with and without laser-engraving speckles were compared.

2.2.4 Speckle evaluation at different temperatures

2.2.4.1 Evaluation of speckle quality at high temperatures

The speckle quality at HT was evaluated at two representative temperatures for hot stamping process: ii) 600 °C and iii) 700 °C. It was also compared with the speckle quality at 25 °C.

Speckle images were captured by the 2D-DIC camera system (f = 300 mm macro-lens (Sigma, Kanagawa, Japan), CCD sensor (2452 pixels × 2052 pixels) (Pike 505F/B, Allied Vision Technologies, Germany), Vic-Snap® (Correlated Solutions, USA)) with parameter set-up presented in Table 2.3. The magnification was 13.9 µm/pixels. Images captured were used to calculate different speckle parameters.

The speckle quality was evaluated by comparing the speckle parameters on six speckle patterns. Speckle parameters can be classified in two categories:

- the morphology that includes the speckle radius (r), speckle density (ρ), speckle distance (d)
- the image quality that includes: i) Mean Intensity Gradient (MIG), calculated by Equation 2.5 (B. Pan *et al.*, 2010a), ii) the Shanon Entropy (Dong *et al.*, 2017), calculated by Equation 2.6, and iii) the percentage of saturated pixels.

The speckle morphology parameters (r, ρ, d) were calculated automatically by an image processing procedure through a Matlab® script (Figure 2.5).

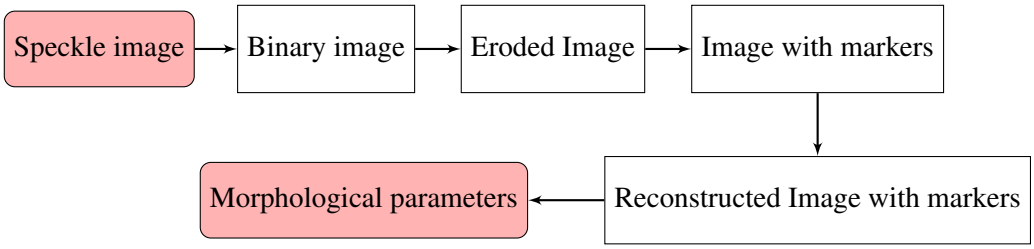

Figure 2.5: Schematic of the an image processing procedure to calculate speckle morphology (radius, distance, density)

The speckle density was the ratio between the total area of speckles dots and the total area of the ZOI. Regarding the image quality, the MIG represents local contrast of image (Equation 2.5) while the Shannon entropy (E) represents the dynamic range of grey-level of an image, calculated by Equation 2.6.

$$MIG = \frac{\sum_{i=1}^{m}\sum_{j=1}^{n}\sqrt{(f_x(x_i,y_j)^2 + f_y(x_i,y_j)^2)}}{m \times n} \tag{2.5}$$

Where $f_x(x_i,y_j), f_y(x_i,y_j)$ are gradients of grey-level of pixel (x_i,y_j) in the x and y direction; m $\times$ n is the ZOI area (pixels $\times$ n pixels)

$$E = \sum_{i=0}^{255} p_i \log_2 p_i \tag{2.6}$$

Where p_i is the count number of pixel having grey-level i on the ZOI.

The percentage of saturated pixels was defined as the ratio between the number of pixels having the grey-level of 255 and the total pixels on the ZOI.

The relative reduction of MIG and Entropy values at 600 °C and 700 °C compared with the ones at 25 °C were calculated to evaluate the influence of temperature on the speckle quality.

2.2.4.2 Evaluation of speckle adherence at high temperatures

After evaluating the speckle quality made by different techniques, four speckles M1, M4, M5 and M6 presenting the best contrast and respecting speckle morphology, were chosen for the assessment of the speckle adherence. The speckle adherence was evaluated by uniaxial tensile tests at 600 °C. The experiment set-up is shown in Figure 2.6.

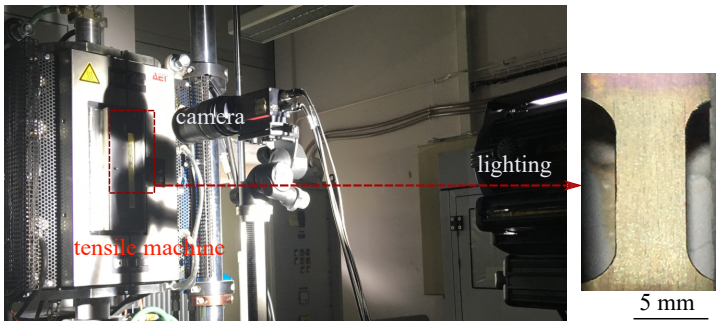

Figure 2.6: On left-hand side: Overview of tensile tests with the 2D-DIC system for the assessment of speckle adherence at 600 °C, On right-hand side: Image of a TA6V sample speckled by M5 technique (combining anodization and laser engraving) observed through the glass window

In this experiment, planar TA6V samples with dimensions 125 mm by 25 mm by 1.6 mm were chosen for uniaxial tensile tests. The geometry of the TA6V specimen was presented in Appendix A.3. The samples were heated to 600 °C by a tensile testing furnace (AET Technologies, France) with a heating rate of 10 °C min^{-1}. During the test, a difference of 2 °C, measured by three thermocouples (type K, accuracy 1 °C) was observed along the ZOI of specimens. The testing machine used is an MTS 125 model (MTS®, Minneapolis, USA) with load capacity of 50 kN. The strain rate of tensile tests was set at 0.001 s^{-1} by TestStar® software controller.

Speckle images were captured by the same camera system used for the evaluation of speckle quality at different temperatures. The acquisition frequency was 5 Hz. The exposure time was set up so that the dynamic range of grey levels was optimized varying from 4 ms to 16 ms. The true strain of the specimen was then calculated by VIC-2D® software (version 6, Correlated Solution®, USA). The limit of adherence of speckles on thes surface sample was determined as the maximum longitudinal strain measured before the correlation disruption. Table 2.3 presents the 2D-DIC parameters for setting-up and parameters used to measure strain during tensile tests.

Table 2.3: 2D-DIC parameters for strain measurements in tensile tests at 600 °C

Device		Characteristics
Distance camera-object [m]		1.2
Field -of-view [mm × mm]		40 × 28.3
Magnification [µm/pixels]		13.9
Lighting		Diffusion and white light
Exposure time [ms]		4 ms - 16 ms
Acquisition frequency (Hz)		5
VIC-2D®parameters	Subset [pixels × pixels]	57 × 57
	Step size [pixel]	19
	Correlation coefficient	ZNSSD
	Strain Window [points]	15

2.3 Results

2.3.1 Possibility of creating speckles by six different techniques

2.3.1.1 Polymer mask fabrication

The polymer mask fabrication aims to integrate numerical speckle characteristics (size, density and distance) into physical speckle patterns. However, preliminary results on the possibility of creating holes on the polymer paper show that the density of speckle on polymer had to be reduced to 0.2 and the speckle distance were more than 320 µm because of laser's energy and the lower melting temperature of the poly-vinyl polymer.

The analysis of variance shows that three factors, laser power, laser scanning speed and laser scanning strategy, have influence on the hole radius of polymer's mask. On the Pareto diagram (Figure 2.7), the scanning speed has the most significant effect (60%), followed by the laser trajectory (strategy) while the laser power has the least influence on hole's variation.

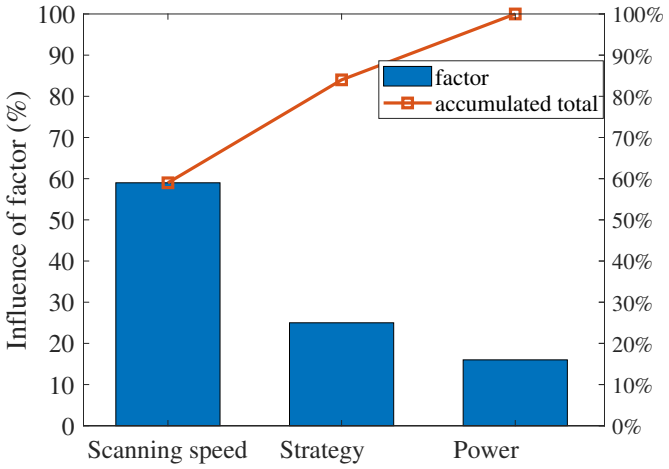

Figure 2.7: Pareto diagram on the influence of laser parameters on the hole's radius of the polymer mask

Table 2.4 presents the hole's radii (in average) obtained from the nine experiments with different laser parameters. Only two experiments allow creating holes on the polymer successfully. By considering the difference between the hole's density, radii and the numerical pattern, it is likely the set of laser parameters: P = 100 W, V = 80 mm s^{-1} and S: Mix of Contouring and Hatching (H+C) would be the best to create the polymer mask. Hole's radius obtained from the laser parameters is around 70 µm, which is the closest to the numerical size and the most favorable to paint transfer. Others experiments with laser parameters in the plan of experiment do not allow creating holes that satisfy requirements. Indeed, in experiment N°1 and N°8, any holes are created because of low laser power (P = 10 W). In experiment N° 2-4, N° 7, holes are made but the polymer is locally damaged (near the hole borders). In experiment N° 9, holes size is around 28 µm which is much smaller than the target one (105 µm).

Table 2.4: Results on hole's radius of the polymer mask from the 3 level-3 factor DOE

N. exp	Factors			Radius	Creating	Observation
	P [W]	V [mm/s]	S	µm	mask ?	
1	10	10	C	0	No	Holes were not created
2	55	80	C	187	No	Polymer was locally burned
3	110	150	C	174	No	Polymer was locally burned
4	55	10	C+H	195	No	Polymer was locally burned
5	100	80	C+H	70	Yes	Holes were made
6	10	150	C+H	0	No	Holes were not created
7	100	10	H	146	No	Holes were burned locally
8	10	80	H	0	No	Holes were not created
9	55	160	H	28	Yes	Holes were too small

With results obtained from the plan of experiment (Table 2.4), the set of laser parameter: P = 100 W, V = 80 mm s^{-1} and S: H+C is used for creating a polymer mask.

Nevertheless, even with a laser condition: P = 55 W, V = 80 mm s^{-1}, S: H+C, the polymer mask presents many local damages, so the polymer mask can not be reusable. Local damages would be from a high energy density of laser depositing on a thin polymer (Figure 2.8a). The origin of local damages on the polymer film is beyond of the scope of our study. Nevertheless, based on results given from the analysis of variance (Figure 2.7), to create the polymer mask, we decided to lower the laser power. The final laser set-up parameter: Laser power: P = 30 W, scanning speed: V = 80 mm s^{-1}, Scanning strategy: H+C are allow to create reusable polymer masks for speckle fabrication. The polymer mask characterized by the pattern radius of 150 µm, distance of 320 µm and density of 0.2 is presented in Figure 2.8b.

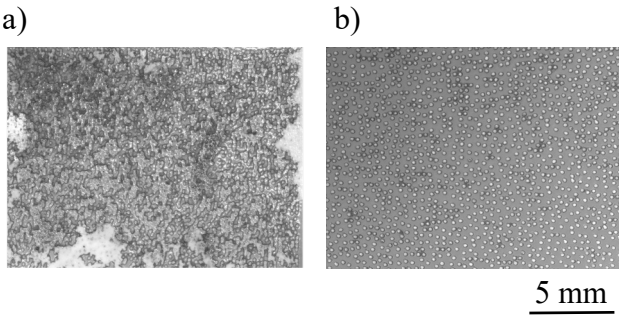

Figure 2.8: a) Polymer mask obtained with laser parameters: P = 55 W, V = 80 mm s^{-1}. The polymer is locally burnt because of too high energy of the laser source. b) Polymer mask obtained with laser parameters: P = 30 W, V = 80 mm s^{-1}. Holes are properly created on the polymer

2.3.1.2 Speckles prepared by “additive” methods: M1, M2 and M3 techniques by using a reusable polymer mask

Figure 2.9 present three types of speckle patterns produced using "addition" techniques. Table 2.5 compares the radius (r), the distance (d) (in averaged values and its standard deviation (STD)) and the density ρ of the pattern on the polymer mask and speckles produced using techniques M1, M2 and M3.

First, it is shown that speckle patterns made by M1 and M2 techniques most closely replicate the polymer mask pattern. On the other hand, with technique M3, only a few speckle dots are copied onto the TA6V sample. The speckle radius (r), speckle density (ρ) and distance (d) between dots made by the three techniques are slightly different. For the first two techniques, speckle radii are similar: r (M1) = 151 $\pm$ 230 µm and r (M2) = 152 $\pm$ 237 µm and larger than the target one (R_c = 105 µm) while speckle dots made by M3 technique is 101 $\pm$ 114 µm (r (M3) = 101 $\pm$ 114 µm). Speckle densities produced using techniques M1 and M2 are slightly lower than the target density ($\rho = 0.24$ and $\rho = 0.34$) whilst the density is only $\rho = 0.1$ for speckles made using M3 technique. The low speckle density made by M3 technique is likely due to high viscosity of Jelt® varnish that renders matter transfer difficult.

The speckle distance produced using three techniques: M1, M2 and M3 are much further than the numerical one: d (M1) = 308 $\pm$ 89 µm, d (M2) = 294 $\pm$ 81 µm, d (M3) = 296 $\pm$ 89 µm whereas numerically produced speckle is d = 30 µm. The great distance between speckle dots is explained by the polymer mask pattern distance; the distance between two holes (d (mask) = 320 µm). After comparing morphological results on speckles made using the three techniques with numerically-produced speckles, the speckles made by M2 technique are the most similar to the numerical ones.

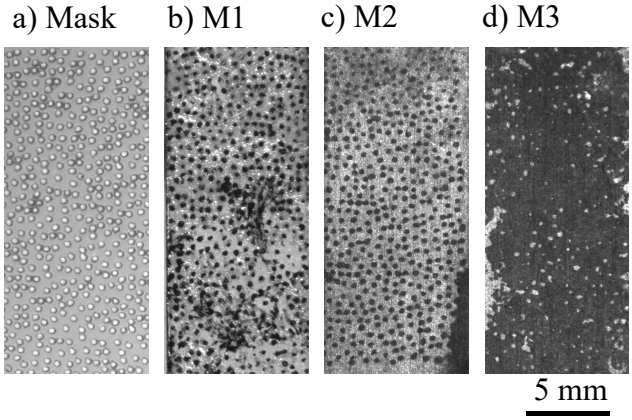

Figure 2.9: a) Speckle patterns created on the polymer mask used for the "additive" speckle techniques. From b) to d) speckle images made by: b) M1 (painting), c) M2 (direct anodization), d) M3 (inverse anodization) at room temperature

Besides the morphological parameters, TA6V surfaces were examined after speckle preparation. It was observed that the "additive" techniques using the matter transfer process presented a problem with respect to the tape holding down the polymer mask. Indeed, with technique M1, the TA6V sample presented stains from the adhesive layer of the polymer mask. With techniques M2 and M3, the borders of the TA6V samples were not covered by speckle dots because the

polymer mask was not sufficiently taped on the sample at the edges. The acid solution was able to penetrate under these edges and from these borders and oxidized the area.

Table 2.5: Speckle radii, speckle distances and speckle densities of six different techniques (M1-M6) compared with the numerical speckle and the pattern of the polymer mask

Speckle characteristics	Radius	Distance	Density
Unit	r [µm]	d [µm]	ρ
Numerical speckle	105	40	0.4
Polymer mask	150 ± 85	230	0.2
M1: painting	151 ± 230	308 ± 89	0.24
M2: direct anodization	152 ± 237	294 ± 81	0.34
M3: inverse anodization	101 ± 114	296 ± 89	0.22
M4: laser engraving	114 ± 200	185 ± 70	0.22
M5: combining anodization and laser	139 ± 50	185 ± 70	0.39
M6: combining painting and laser	89 ± 115	185 ± 70	0.29

In summary, the speckle patterns made by techniques M1 and M2 replicate the pattern of the polymer mask. The density of these speckles is lower than the numerical version because the speckle distance is much larger due to the limitations imposed by the polymer mask. Speckles made by technique M3 have the smallest speckle radius and lowest density compared to M1 and M2 techniques and far from the density of the numerical speckle pattern.

2.3.1.3 Speckle prepared by “subtractive” methods: M4, M5 and M6 techniques

In "subtractive" methods using a laser source, in order to evaluate the interaction between the laser and the material surface, the TA6V surface topography and microstructure were first characterized. The mechanical behavior of the TA6V specimen after laser engraving was evaluated as well.

Observations using optical microscopy (Figure 2.10a) and the SEM (Figure 2.10b) on a speckle dot after laser engraving show that the speckle dots have crater-like shapes. Some micro-cracks (in the red arrow in Figure 2.10c) are also observed on the speckle dots due to rapid cooling during the SLM process.

The microstructures on the cross-section of the TA6V specimen before (Figure 2.11a) and after (Figure 2.11b) are compared. SEM observations of the cross-section of a speckled region show that each speckle dot is a molten pool created by laser-metal interaction. The molten pools was around 20 µm deep. Due to the rapid cooling of the SLM process, the microstructure on speckled region changes in initial (Figure 2.11a), equiaxial state to needle-like grains (Figure 2.11c).

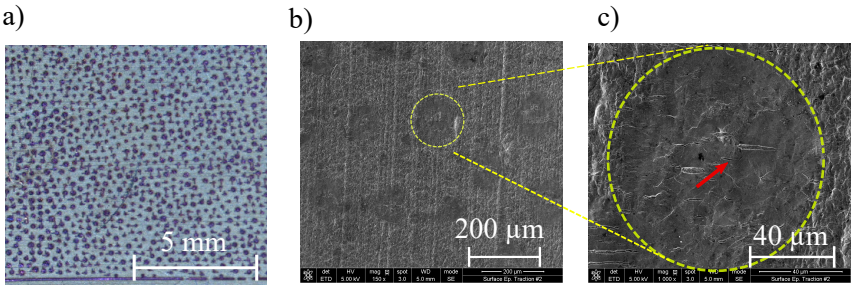

Figure 2.10: Surface observation of the TA6V sample with speckle prepared by M5 technique (combining anodization and laser engraving). a) observed by the optical microscopy; b) observed by SEM microscope; c) observed on a speckle dot (in red circle): its shape is crater-like with micro-cracks (in red arrow)

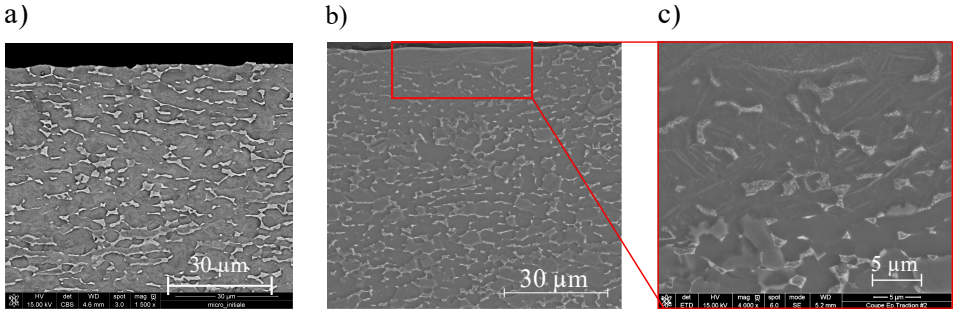

Figure 2.11: Microstructure of TA6V sample from the cross-section view a) Initial state with equiaxial grains, b) On a speckled region after the laser engraving technique M5. c) microstructure observed on a speckled dot (in yellow)

Furthermore, the mechanical behavior of the TA6V material after laser treatment is verified by comparing the force–displacement curves of two tensile tests: before and after laser engraving (Figure 2.12). These two curves are similar: the elastic stiffness measured at room temperature are respectively 12.1 kN mm^{-1} and 12.2 kN mm^{-1} (Figure 2.12). With a relative difference of 1%, it is clear that the laser source did not influence the mechanical behavior of the TA6V material.

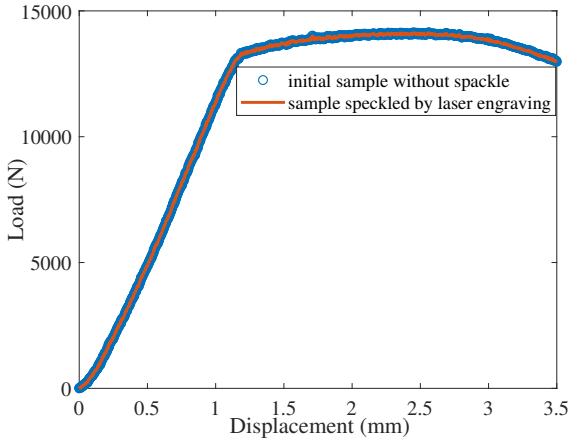

Figure 2.12: Mechanical tests of two TA6V samples: without speckle (in blue) and sample speckled by laser engraving (M4) (in orange) at room temperature

Following the characterization of TA6V specimens with speckles made by a laser source, Figure 2.13 displays speckles made by the three techniques M4, M5 and M6 respectively. Their morphological results are presented in Table 2.5.

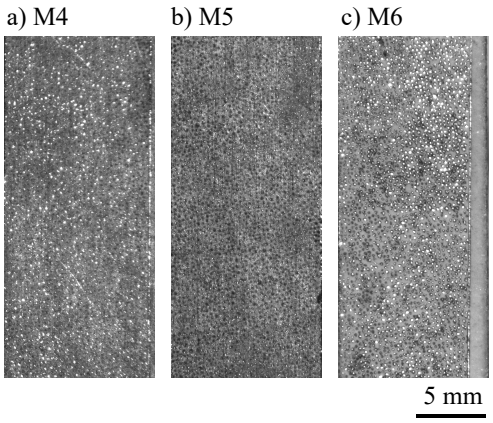

Figure 2.13: Speckle images made by "subtractive" techniques: M4, M5, M6 at 25 °C

Speckle created using the laser source (M4, M5 and M6) are closer to the target numerical speckle radius than those made using M1, M2 and M3: they are 114 $\pm$ 200 µm, 139 $\pm$ 50 µm, and 89 $\pm$ 115 µm, respectively. Speckle distances obtained from these three techniques are similar: 185 $\pm$ 70 µm but higher than the numerical equivalent (30 µm, equivalent to 2 pixels). The speckle densities from techniques M4, M5 and M6 techniques are 0.22, 0.39 and 0.29, respectively, lower than the numerical speckle density of 0.4.

Speckles created by the laser source (M4, M5 and M6) are relatively similar to the target numerical speckle (except the speckle distance). Moreover, although TA6V surface are slightly changed by the interaction laser-matter, the mechanical behavior TA6V material after using the laser engraving with parameters of: P = 20 W, V = 150 mm s^{-1} remains unchanged.

2.3.2 Speckle image quality at different temperatures

The speckle image quality was evaluated on the basis of three criteria: MIG, the Shannon entropy E and the percentage of saturated pixels. The quality of six speckle patterns was compared at different temperatures: room temperature (25 °C), 600 °C and 700 °C.

2.3.2.1 Image quality at room temperature

Images of speckles made using the "additive" methods and the "subtractive" methods at room temperature are presented in Figure 2.9b-d and Figure 2.13, respectively. Speckles made using the "subtractive" methods present specular reflection, inducing saturated pixels on images. Saturated pixels were located on or near speckle dots. Their saturation areas were from 2 pixels to 7 pixels. The glare was quantified by the percentage of saturated pixels (Table 2.6). Speckles made using techniques M1, M2, M3 and M5 have less than 1% of saturated pixels while speckles made using M4 and M6 have 2% and 4% of saturated pixels respectively. This glare is probably from light reflecting off laser-produced speckle dots. The glare could lead to disturbances when correlating. Among the six techniques, speckles made using M2 and M5 presented the highest MIG values. Speckles made using M1 and M2 have the highest entropy values (7.4). Speckles made using M5 have a slightly lower entropy value (6.9). Considering all image quality parameters, speckles made using technique M5 (combined laser engraving and anodization) and M2 (inverse anodization) present the best quality at room temperature: high MIG and entropy values and a low percentage of saturated pixels.

Table 2.6: Comparison of MIG, entropy (E) and the percentage of saturate pixel of five different speckles (M1 - M6) at 25 °C

Parameters		MIG	Entropy (E)	% Saturate pixel
Technique	M1	9.8	7.4	1.0
	M2	15.8	7.4	0.8
	M3	7.7	6.7	0.15
	M4	13.8	6.9	1.83
	M5	15.9	6.9	0.4
	M6	14.3	6.8	4

2.3.2.2 Image quality at 600 °C

Figure 2.14 shows five speckles at 600 °C (the speckle image made by M3 technique were not performed at this temperature). With the same exposure time as that used at room temperature, speckles are less visible.

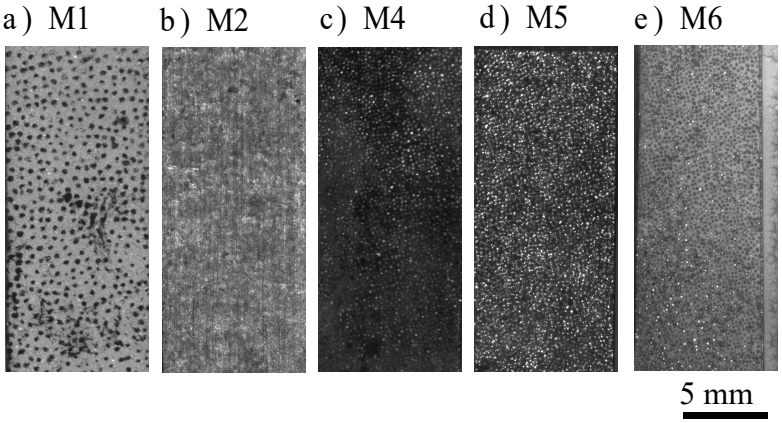

Figure 2.14: Speckle images at 600 °C: a) M1 (paint), b) M2 (direct anodization), c) M4 (laser engraving), d) M5 (combining anodization and laser engraving), e) M6 (combining painting and laser engraving). Speckle made by M3 (inverse anodization) technique was not acquired. Images of speckle made by M4 is hardly visible because of oxidation

Table 2.7 compares the image contrast, characterized by MIG and entropy of speckles at 25 °C and 600 °C. It is shown that image contrast at 600 °C is lower, which is probably due to TA6V surface oxidation. For example, saturated pixels observed on the M4 and M6 samples disappear while the saturation of pixels increases by 1% for the M5 sample. This is due to the fact that the thickness of the oxidation layer in each specimen is different. It should be reminded that when using technique M5, the TA6V surface is pre-oxidized to reduce the problem of glare. Speckles made using M4 are the most affected by oxidation: its MIG value is 62% lower than at room temperature. Furthermore, due to oxidation, the speckle patterns made using M2 cannot easily be analyzed. Its MIG value is 24% lower than at room temperature. The MIG values of speckles made using the other methods (M1, M5 and M6) were 21 - 22% lower. The same tendency is observed in the relative decreases in entropy values. Among the five methods, the speckle pattern made using M5 presents the best contrast (highest values of MIG and entropy and the least reduction in MIG and Entropy). This technique produces the best speckle quality at 600 °C.

Table 2.7: Comparison of MIG, entropy (E) and the percentage of saturate pixel of five different speckles (M1, M2, M4-M6) at i) 25 °C, ii) 600 °C

Parameters		MIG		Relative reduction of MIG %	Entropy (E)		Relative reduction of E (%)	% saturate pixel	
Temperature [°C]		25	600		25	600		25	600
Technique	M1	9.8	7.6	24	7.4	6.7	10	1.0	0
	M2	15.8	12.0	24	7.4	6.6	11	0.8	0.1
	M4	13.8	5.2	62	6.9	6.6	4	1.83	0.04
	M5	15.9	12.4	22	6.9	6.7	2	0.4	1
	M6	14.3	11.3	21	6.8	6.6	3	4	0

2.3.2.3 Image quality at 700 °C

At 700 °C, speckles made using techniques M2, M3, M4 and M5 (Figure 2.15) are barely visible to naked eyes, which may cause correlation disruptions.

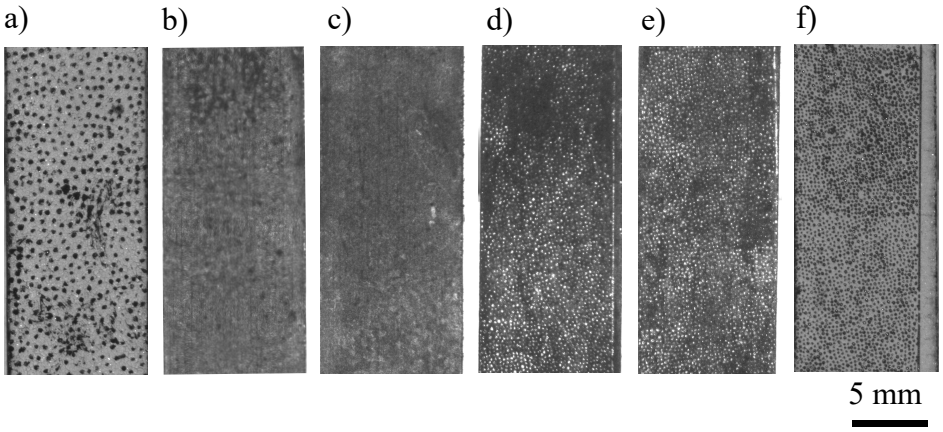

Figure 2.15: Speckle images at 700 °C made of six different techniques: a) M1 (painting), b) M2 (direct anodization, c) M3 (invers anodization), d) M4 (laser engraving), e) M5 (combining anodization and laser engraving), d) M6 (combining paint and laser)

The results on Table 2.8 show their MIG and entropy values continue to decrease. Among the six sets of speckles, those made using M2 and M4 techniques are the most influenced by oxidation. The MIG values are decreased by 53% with M2 and by 46% in M4 sample. The MIG value of speckles made by M5 method decreased by 32%. The entropy of speckles produced by M1 and M2 was significantly reduced. Nevertheless, speckles made using techniques M1 and M6 are still visible and present the best contrast (highest entropy values). The MIG values decrease by 22% and 32%, respectively. This can be explained by the white paint covering the TA6V samples. The paint protected the TA6V surface from oxidation.

Table 2.8: Comparison of MIG, entropy and the percentage of saturate pixel of six different speckles (M1-M6) at i) 25 °C, ii) 700 °C

Parameters		MIG		Relative reduction of MIG %	Entropy (E)		Relative reduction of E (%)	% saturate pixel	
Temperature [°C]		25	700		25	700		25	700
Technique	M1	9.8	7.6	24	7.4	6.7	10	1.0	0
	M2	15.8	7.4	53	7.4	6.1	18	0.8	0.1
	M3	7.7	5.9	23	6.1	5.9	3	0.2	0
	M4	13.8	8.7	46	6.7	6.4	4	1.8	0
	M5	15.9	10.7	32	6.9	6.5	6	0.4	0.1
	M6	14.3	9.7	32	6.8	6.6	3	4	0

2.3.3 Adherence of speckles at HT

The speckles made using techniques M1, M4, M5 and M6, presenting the best image quality at 600 °C and 700 °C, were chosen to evaluate the adherence of speckles to the TA6V material. Figure 2.16 presents the strain fields from TA6V tensile tests at 600 °C on samples speckled using the four techniques listed above. The areas where first spallation occurred are indicated by red rectangles on the longitudinal strain fields in Figure 2.16. The maximum longitudinal strain value measured on TA6V samples with speckles made by techniques M1 and M6 is about 0.2 on the Zone of Interest of the TA6V sample. Meanwhile, the maximum longitudinal strain measured with speckles made by techniques M4 and M5 is 2.0.

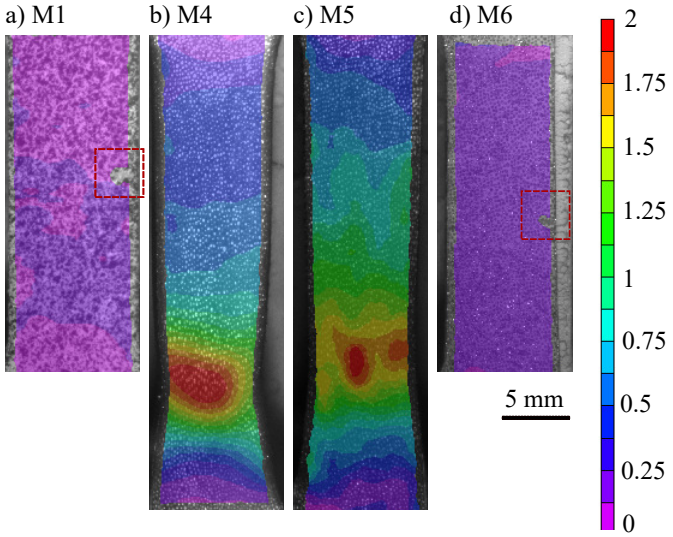

Figure 2.16: Longitudinal strain maps of TA6V tensile tests with speckles patterns made by different techniques at 600 °C: a) M1, b) M4, c) M5, d) M6. Red rectangles indicates first speckle delamination

2.4 Discussions

2.4.1 Possibility of making repeatable speckles

Previous authors have documented the importance of speckles in improving spatial resolution and reducing DIC errors (Reu, 2014, Reu, 2015a - Reu, 2015c, Dong *et al.*, 2017). They recommend that characteristics of speckle morphology such as the speckle size, speckle distance and density should be respected. However, in practice such requirements are quite difficult to achieve because, in most current preparation techniques, for example speckles made by the spraying technique, the speckle morphology is neither controlled nor repeatable. In our study, we suggest novel techniques that produce controllable speckles meeting speckle criteria in order to increase the resolution of strain measurements. The speckle pattern is first made from the numerical model then they are produced by using six different techniques. They are classified into two groups. The "additive" techniques use a polymer mask and a lithography technique (M1, M2 and M3) while the "subtractive" techniques use a laser source (M4, M5 and M6) to engrave metallic specimens.

Patterns on the reusable mask by a laser source
In the first group, making the reusable polymer mask is critical. It is shown in section 2.2.3.1 that nine experiments to find a set of laser parameters for the mask were insufficient. The vinyl polymer chosen for the mask is an unconventional material to the laser source in SLM machine. The analysis of variance on the factors influencing hole's radius on the polymer mask showed that three parameters - laser power, laser scanning speed and laser scanning strategy - and their interactions influence hole size, and thus speckle radius produced using three techniques M1, M2 and M3. These results are indeed consistent with studies on the interaction between lasers and matter, which is well known in the SLM process (Yan *et al.*, 2018). The energy emitted by a laser is proportional to its power and inverse of the laser scanning speed. The results of above experiment finally enabled us to successfully produce the polymer mask. Polymer masks produced using laser parameter P = 30 W, V = 80 mm s^{-1} do not present local damages on the polymer, so they are sufficiently resistant to operation steps in the lithography technique. To our knowledge, this is the first publication in speckle techniques involving a polymer mask with a hole size of less than 1 mm. However, the hole radius of polymer mask, density and distance differ from those on the numerical equivalent. It is necessary to maintain a minimum distance of at least 320 µm between holes when producing a polymer mask; the spatial resolution of kinematic fields measured by DIC is thereby reduced. The spatial resolution of DIC could be improved by performing additional experiments in order to determine optimized laser parameters.

Speckle sizes made by M1, M2 and M3 techniques
Three speckles patterns, M1, M2 and M3 were created with the polymer mask. Consequently, these speckles have larger distances between dots and lower densities than the numerical one. Globally, the polymer mask does create speckles on TA6V sample surfaces using techniques M1 and M2, except some marks left on TA6V samples because of adhesive problem of the polymer mask. Their speckle radii are slightly better than speckles made by air spraying techniques (Dong *et al.*, 2017). Moreover, speckle sizes are controllable. The contribution in this study is demonstrate the possibility of creating repeatable speckles on the basis of lithography techniques and of achieving a better resolution. The numerical method of producing repeatable speckles has been studied by Mazzoleni et al. and Chen et al. as well (Mazzoleni *et al.*, 2015 and Z. Chen *et al.*, 2015). The authors used laser printing and toner transfer process to create speckles with variable diameters: from 0.2 mm to 1.2 mm. Interestingly, their studies show a difference between a numerical speckle and a real one, which is in line with our results. Small speckles are difficult to prepare due to the process of toner transfer.

Nevertheless, our results relating to speckle quality when using three techniques show some limitations. For instance, speckle made by technique M3 have a low speckle density which reduces spatial resolution. This could be explained by a higher viscosity of Jelt® varnish. Jelt® varnish is made of kerosene disulphide from processed oil. Its viscosity is quite high so it can stop the spread of vanish into holes. Improving the speckles-production techniques used in our study would require further investigations into i) controlling the of Jelt® varnish droplet size; ii) reducing varnish's viscosity.

Speckle sizes made by M4, M5, M6 techniques
The last three types of speckle (M4, M5, M6) were made by using a laser source. These speckles are more precise (speckle dots are smaller), closer to numerical one thanks to the advantage of the laser system. Compared with the other three techniques, speckles made by laser engraving techniques require fewer steps, so they are less costly and time-consuming. Many studies use these techniques because of their high precision and rapidity. For example, Hu et al. used the

laser engraving technique to produce the smallest speckle size of 5 µm to increase the DIC spatial resolution (Hu *et al.*, 2018). In our study, speckle radii are from 89 µm to 114 µm. Although laser engraving is not a new technique for creating speckles, our study contributes to confirming the integrity of the material's microstructure and mechanical behavior after the laser engraving process. These material characterization steps should be verified systematically after the laser process. Surface observations made after laser engraving techniques suggest a possible reason for the glare problem that occurs occasionally on metal materials. Moreover, our study suggests that combinations of techniques, for example, laser engraving and anodization, create speckles with better contrast than those involving a single technique.

2.4.2 A guideline for choosing speckle fabrication techniques for DIC at HT

Chosen criteria for the evaluation of speckle quality
Previous studies show that speckle quality is assessed by many parameters. These parameters can be grouped in two classes: a) morphological quality that include speckle radius, distance (speckle spacing) and density, b) image quality that include the MIG value and the dynamic range of grey-levels represented by the entropy value and the percentage of saturated pixels.

Morphological quality is usually used to assess the DIC spatial resolution and the random and/or systematic errors. Several studies have demonstrated the relationship between the speckle size and the subset size used in the local DIC. For example, the study of Lecompte et al. investigated the influence of speckle radii, speckle densities and subset sizes on the accuracy of displacement field obtained by 2D-DIC (Lecompte *et al.*, 2006). Results showed that a speckle density from 0.4 to 0.7, a speckle radius of 5 pixels and a subset of 15 pixels give the most accurate 2D-DIC strain. Furthermore, Crammond et al. explained that global parameters such as Shanon entropy are insufficient to assess speckle quality (Crammond *et al.*, 2013). The authors highlight the fact that morphological quality, including the speckle density and speckle size, should be considered as additional parameters in evaluating 2D-DIC precision. Moreover, the numerical modeling study of Bornert et al. on the effect of speckle size on displacement errors in the ultimate error regime (when 2D-DIC error is no longer dependent on subset shape function) also demonstrated that for a given subset size, a lower speckle radius could decrease displacement error thanks to more information being contained in a subset (Bornert *et al.*, 2009). Finally, studies of Reu suggested using speckle distance as an additional morphological parameter in the analysis of speckle quality (Reu, 2014). The author recommends a speckle distance of 2 pixels to avoid the problem of aliasing and also published guidelines for a "good" speckles.

As a complement to morphological parameters, speckle quality is assessed by two criteria: MIG and entropy. Dong et al. considered MIG as a "global" parameter, characterizing the global contrast of images (Dong *et al.*, 2017 and B. Pan *et al.*, 2010b). However, the MIG criterion does not consider the influence of local fluctuation and image noise. An image with a lot of noise or subject to aliasing can have a high MIG, but does not show good contrast. The second image quality parameter entropy represents the breadth of grey scale dynamic range. A high-contrast image should have a wide dynamic range and thus a high entropy value. However, the entropy does not characterize the local features of speckles.

To summarize, a "good" speckle should satisfy following conditions: a speckle radius between 3 and 5 pixels, speckle density between 0.4 and 0.5, speckle distance of at least 2 pixels, the highest MIG and entropy values and the least saturated pixels as much as possible. The limitation of recent research on speckles is that each criterion, with its advantage and its drawback, cannot

permit a general method that combining all speckle criteria. In this study, speckle quality is assessed more objectively and globally by considering many aspects of speckle. With given criteria for a "good" speckle, speckle qualities made of six techniques are compared to find the appropriate speckle at different temperature.

Speckle quality made by six techniques at different temperatures

At room temperature, densities of speckles produced using polymer mask technique: M1, M2 are slightly lower than those produced by the laser engraving ones: M4, M5 and M6. Speckle distances made by M1, M2 and M3 are also greater than M4, M5 and M6 techniques. In term of speckle quality, the speckle made by M2 (direct anodization) technique and M5 (combined anodization and laser engraving) produce the best qualities. The speckle morphology is close to recommended levels and the highest contrast values are achieved. Their MIG and entropy values are of the same order of magnitudes as speckles made by classical painting techniques (Dong *et al.*, 2017). The technique combining anodization and laser engraving M5 suggests a novel technique allowing a high speckle quality.

Nevertheless, at room temperature, a high level of specular light is observed on speckle made using techniques M4 and M6 due to the crater-like shape of the speckle dots. The glare can cause a serious decorrelation in DIC. Some studies suggest solutions to deal with issue. For example, LePage et al. suggested using a cross-polarization method to attenuate the glare (LePage *et al.*, 2016). Results from their study show that setting cross polarization on the camera and using LED lighting reduced the 2D-DIC displacement error by 52%. However, in this study, the experimental set up required two LEDs at different angles. This condition could not be satisfied in our tensile tests since the size of the observation window was only 15 mm wide $\times$ 150 mm high. Poncelet et al. also demonstrated that DIC error was produced near the saturation zone because of light reflection (Poncelet *et al.*, 2015). They suggest the Multiple Illumination DIC algorithm in order to correct the glare problem. In this algorithm, the missing information in the saturated region is compensated by other images from an additional illumination source and weighting functions. However, this method uses multiple lights which might be not appropriate to our experimental set up. That is why in this study a large subset window of 57 pixels $\times$ 57 pixels was chosen to deal with the glare problem. Since the saturated pixel region was from 5 pixels - 7 pixels, the large subset could cover saturated region, thus avoiding the problem of decorrelation in local DIC. As a result, the spatial resolution of kinematic fields is reduced. Further studies for reducing glare should be conducted in order to improve the spatial resolution and reduce 2D-DIC errors.

At 600 °C, the speckle quality is reduced. It is supposed that it is due to the titanium oxidation. Consequently, the MIG value of M3 speckles was significantly reduced, by 62%. For the other laser engraving techniques, the reduction exceeded more than 20%. The MIG and entropy values are lower than results obtained in many previous studies on speckles made using painting technique at high temperatures. On the basis of the various criteria (speckle morphology, quality), the speckle made using technique M5 presents the best quality. Furthermore, these speckles show excellent adherence. The speckles resist a strain of 2.0 (the necking statement). The experimenter should use this technique for TA6V tensile tests in a temperature range of 20 °C to 600 °C to access further information about the material behavior by measuring strain fields.

At 700 °C, the speckle quality decreases considerably, probably from the acceleration of TA6V sample oxidation. The influence of oxidation on contrast of images is particularly noteworthy on samples without paintings, from M2 to M5 speckles that could induce 2D-DIC errors or even decorrelation problem. At 700 °C, only the speckle patterns made by painting techniques, M1

and M6 are visible and present the best contrast. The experimenter should choose between these two techniques to create speckles on their sample. However, speckles flake off at a strain of 0.2. Painting techniques can resist high temperature and provide a stable, high contrast images quality but cannot stand for high level of mechanical strain.

A guideline for choosing an appropriate speckle pattern at HT
Throughout this study, it is remarked that no speckle preparation techniques can provide the recommended speckle morphology, high contrast and resistance to high temperature and high strain (up to a strain of 2.0) at the same time. Mechanical experimenters should use a speckle technique that compromises between the requirement of the spatial resolution, image contrast and maximum strain values. Our study is providing a guideline for choosing appropriate speckling production technique depending on experimental temperature and strain limit measurements. However, this study does have some limitation that should be addressed. For example, only three criteria: MIG, entropy and the percentage of saturated pixels are used to assess the speckle quality. It would be evaluated more objectively using a global model that includes every speckle characteristic. Furthermore, the hypothesis that oxidation reduces image quality on all speckle patterns requires confirmation. Further investigation is required into how the thickness of the oxide layer affects the image contrast. According to Kumar et al., it is possible to predict the thickness of oxide layers created on TA6V (Kumar *et al.*, 2010). Image contrast can be indirectly inferred from oxide layer thickness. This kind of correlation model could help an experimenter to estimate speckle quality as a function of temperature and time.

2.5 Conclusion and perspectives

The chapter focuses on speckle fabrication techniques with the aim to find a speckle pattern that respects "good" speckle criteria to increase the spatial resolution and the accuracy of kinematic measurements. Furthermore, the speckles needs to resists high temperatures (less than 750 °C) and high level of mechanical strain (strain is at least 1.0 (100%)). After the state-of-the-art on speckle patterns at high temperatures, six speckle patterns are made using different techniques. Six different speckles are repeatable because they are produced from a computer-generated speckle pattern that meets guidelines for a "good" speckle pattern for DIC. The six techniques can be classified into two groups. In the first group, speckles are made using "additive" techniques (M1, M2, M3) in which speckle dots are replicated from the pattern of a reusable polymer mask and the lithography technique. In the second group, speckles are made using "subtractive" techniques by a laser source (M4, M5, M6). Six speckle patterns (M1-M6) are then compared and evaluated in term of morphology (speckle density, speckle radius and speckle distance) and quality (the global contrast characterized by MIG, the dynamic range of grey-levels characterized by the Shannon entropy and the percentage of saturated pixels) and their adherence to TA6V samples under mechanical strain.

In the "additive" techniques, a reusable polymer mask by a laser source (SLM, SLM® solution, Lübeck, Germany) is first created. To create the polymer mask, a DOE of nine experiments, combining three laser parameters (P, V and S) at various levels was performed. The final set of parameters which allows creating the polymer mask properly without local damages and sufficiently hard for lithopgraphical operation) is: the laser power of P = 30 W, V = 80 mm s^{-1} and S = H+C. The speckles produced from M1, M2 and M3 techniques have a speckle radius from 101 µm to 150 µm, speckle density from 0.1 to 0.34 and speckle distance of about 300 µm. In the "subtractive" techniques, speckle patterns are made by using a laser source with parameters: P = 20 W and V = 80 mm s^{-1} do not modify the mechanical behavior of TA6V

material and its microstructure after the laser engraving. The subtractive methods can create speckle patterns having radii from 89 µm to 114 µm, speckle densities from 0.22 to 0.39 and a speckle distance of 185 µm.

At room temperature, speckles made by M2 (direct anodization) and M5 (combining anodization and laser) techniques present the "best" quality in term of morphology and image quality criteria. At 600 °C, the speckles made by technique M5 give the best contrast (MIG: 12.35, Entropy: 6.86 and good adherence on TA6V surface: the longitudinal strain measured is 2.0) although saturated pixels appeared on TAV6 surface due to surface oxidations. At 700 °C, speckles made using technique M1 (painting) and M6 (combining laser engraving and painting) present a higher contrast than the other techniques but provide a longitudinal strain measurement of only 0.2 because of speckle spallation in the region of plastic strain.

Perspectives for further studies of speckle fabrication techniques at high temperatures are:

1. to improve the design of experiments to optimize laser parameters for a better polymer mask,
2. to analyze the droplet size of paint to facilitate the pain transfer,
3. to analyze the chemical component of the oxidation layer appeared on the speckles made by laser techniques on the TA6V specimen at high temperature
4. to develop other speckle methods that meet "good" speckle criteria and good adherence, for instance, the golden coating method coupled with laser engraving.

CHAPTER

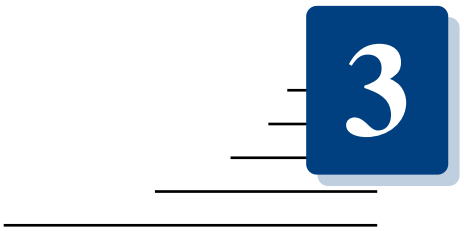

Image contrast and 2D-DIC system set-up at high temperatures

Although the 2D-DIC system is flexible to set up at room temperature, it is more difficult at high temperatures because the contrast of images is influenced by high-temperature effect, i.e., the radiation of hot object. Therefore, this chapter focuses on implementing the 2D-DIC system for to tensile tests which are performed in a closing furnace at high temperatures in our laboratory.

The chapter starts with an introduction of an image acquisition process, the state-of-the-art on main factors that influence the image contrast (quality) at high temperatures and solutions for improvements. The methodology section presents available material and devices used in the 2D-DIC system, followed by a Design of Experiment (DOE) on four factors that influence image contrast at 600 °C. The temperature of 600 °C is chosen as a representative temperature of hot forming temperatures in our study. The results and the discussion sections discuss on image contrast obtained from the 2D-DIC system at high temperatures and main influence factors. Finally, main conclusions and perspectives for further studies will be addressed.

3.1 State-of-the-art

3.1.1 Introduction to the numerical image acquisition process

3.1.1.1 Image acquisition system

A numerical image can be defined as a two-dimensional function f(x,y) which relates to the color intensity of a point having the coordinate pair (x,y) (Dey, 2018). Each coordinate pair (x,y) represents the coordinate of a picture element (pixel). The color intensity is converted in a grey-level range from 0 to $2^n - 1$, where n is the number of digital encoded. For example, if n = 2, the image is binary. Image intensity is encoded in two values: 0 or 1. If n = 8 or n = 12, the image is monochrome. Image intensity is encoded in 2^n values.

An image can be stored in a single channel. In this case, an image is considered as a matrix. With recent progress of the image processing technology, an image can be stored in three channels (color image). The color image contains three monochrome image stored in Red, Green and Blue channels. The color image contains three matrices. Figure 3.1 presents three cases of an image: a) a binary image, b) monochrome image encoded in 8 bits (256 grey levels), c) color image with three channels (Red, Green, Blue) in which each channel contains a monochrome image encoded in 8 bits.

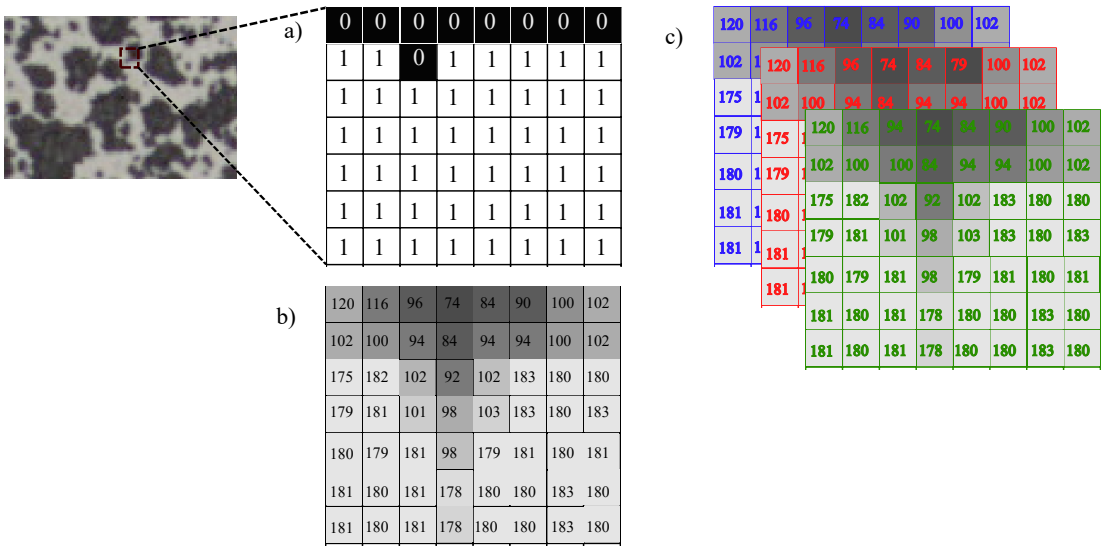

Figure 3.1: Introduction to numerical images: an image is seen as multi-dimensional array or matrices (Dey, 2018) a) a binary image; b) a monochrome image; c) a color image

.

A numerical image is obtained from a digital image acquisition process described in Figure 3.2. First, light rays reflected from the object pass through an optical system (filters and lens) and they are then captured in photodiodes of a sensor. Photons captured are converted in an electrical current then digitalized in numerical values by the analogy-digital conversion device. Each photo diode represents one pixel element. The grey-level of pixel is proportional to the amount of light captured by the photodiodes. Finally, images, which are two-dimensional arrays of pixels are stored in memory in the numerical format.

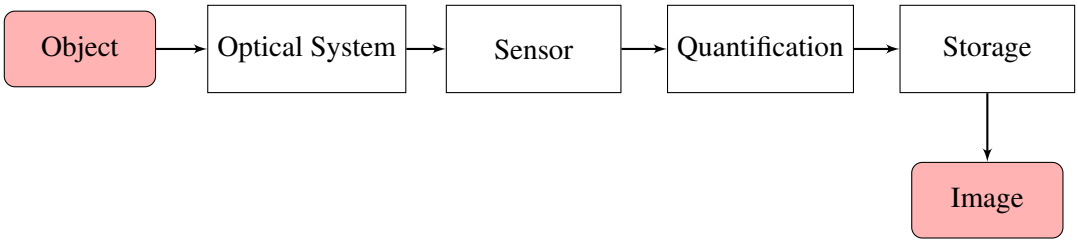

Figure 3.2: Schematic of an image acquisition chain

As can be seen in the flow chart of image acquisition chain, the quality of image depends on the image acquisition devices and process that are: the optical system, sensor, quantification and storage processes. Besides, the image quality is influenced by the photographic conditions (external condition), notably the lighting, environment temperature, floor noise.

3.1.1.2 Influence of the image acquisition system on the image contrast

Optical system

An optical system contains usually a camera (lens and shutter) and may be accessories (filters: polarizer or filters). Light rays from a point on the object go through the shutter of the camera then they are converged on a camera sensor. The imperfection of optical lens, for instance low-cost lens or zoom lens, may cause image distortions at corners, induce systematic errors on kinematic measurements (Rastogi, 2003). For example, Pan et al. demonstrated that lens distortions induced bias strain gradient in case of rigid body motion (B. Pan *et al.*, 2013). Lava et al., by experiment and simulated uniaxial tensile tests, showed that the in case of a small strain measurement, lens distortions caused an average systematic error of 200 $\mu\varepsilon$ (Lava *et al.*, 2013). To correct, a calibration before tensile test is necessary. In case that the calibration can not be performed, a high order numerical correction model of image distortion can reduce this source error (Yoneyama *et al.*, 2006). The correction model is easy to implement. It does not require a calibration step and could be applied for low-cost or zoom lens.

Polarizers and filters

Polarizers or filters are usually used in photography to manage the unnecessary reflection light. Polarizer or filter can suppress the glare therefore, they increase the image contrast. Polarizers and filters are usually used in biomedical imaging, for example the surface texture of human skin (Anderson, 1991). In mechanical tests, LePage et al. used the cross-polarization light to suppress reflected lights from specimen for higher spatial resolution (LePage *et al.*, 2016). Denis et al. used a UV-DIC system couple with a polarizer to avoid the pixel saturation problem from light reflection on specimen (Denis *et al.*, 2019).

Sensors

Sensors of a visible camera are made of photodiodes that receive light from the object then convert light to analog voltage signal. Two types of sensor are actually used for visible cameras: the Charge Coupled Device (CCD) sensors and the Complementary Metal-Oxide-Semiconductor (CMOS sensors). Technologies for CCD sensors and CMOS sensors are different. In CCD sensors, during the exposure time, all the electrons released by the coming light are accumulated at the semi-conductor oxide interface then they are transferred to an amplifier and an output reader via an interline register. In CMOS sensor technology, each pixel includes an active pixel area, a sampling capacitor and an active amplifier. Therefore, electrical signals are transferred to output readers in parallel rather than the sequential method used in CCD sensors.

With recent progress of sensor technology, both CMOS and CCD sensors have low noise that can be neglected (Bigas *et al.*, 2006). In DIC method, two types of sensor are employed. For example, Sirvin et al. and Thai et al. used the CCD sensor (Sirvin *et al.*, 2019 and Thai *et al.*, 2019) while Pan et al. and Hammer et al. utilized CMOS sensor for image acquisition process (B. Pan *et al.*, 2010b and Hammer *et al.*, 2014).

It is noted the sensor influences the image quality by dark noise (electronic noise throughout the sensibility of pixels or the amplification, read-out process) that is characterized by the standard deviation of grey-level of images (Grediac *et al.*, 2014). According to Grédiac et al., sensor noise is not constant (heteroscedastic), and it depends on temperature and the acquisition time (Grediac *et al.*, 2014). Indeed, Ma et al. demonstrated that the self-heating due to long-time working of camera (electronic circuit) or the environment temperature induced image distortions (S. Ma *et al.*, 2019). In their studies, a systematic strain error rate of 5-8 $\mu\varepsilon.C^{-1}$ for an increase of 0.2 °C min^{-1} was recorded. The authors noticed that after 1-2 hours, the systematic errors remained constant since the temperature of the sensor was stable.

3.1.2 Influence of the 2D-DIC set-up conditions on image contrast

While the factors of the image acquisition system are well identified, parameters in experimental conditions are difficult to master. Image contrast is modified when one parameter is changed. The parameters of experimental conditions are usually the lighting, the exposure time and the aperture of camera and also the environment temperature.

3.1.2.1 Lighting

Lighting plays a vital role to the image quality. According to Reu, good lighting enhances the contrast of image and vice versa. Bad lighting can cause disruptions in correlation process (Reu, 2013). The light source should be diffused. For instance, stereo rigs or light fiber are usually employed. The zone of interest is homogeneously illuminated (least of lighting variation). Lighting should not cause reflections on cameras because this can induce pixel saturations. In practice, LED illumination is preferred to white light because a light source (lamp) having a high power (for a better illumination) can be a thermal source that causes heat waves (Jones *et al.*, 2018) and white noise.

Lighting is generally set up to get the best dynamic range of grey-level, homogeneous illumination on specimen, having the least saturated pixels and the best contrast on the ZOI. However, in experimental conditions, it is difficult to satisfy these requirements. To tackle this problem, developments of optical systems are usually proposed. For example, the use cross-polarization light or polarizers to suppress the reflected light from the specimen for higher spatial resolution was developed by LePage et al. (LePage *et al.*, 2016). Pen et al. and Simončič et al. improved 2D-DIC algorithm to deal with the problem of lighting variations on the ZOI of specimens during experimental tests (Peng *et al.*, 2012 and Simončič *et al.*, 2017). Poncelet et al. used the Multiple Illumination DIC algorithm in order to correct the glare problem because of light reflection on spherical objects (Poncelet *et al.*, 2015).

3.1.2.2 Exposure time and camera aperture

In photography, exposure times and camera aperture are proportional to the amount of light to sensor. To capture a "good" image quality, the aperture, the exposure time, the lighting conditions should set-up in a harmonized manner to get the best image quality. The image

quality is usually pre-assessed by the dynamic range of grey-level. In addition, the ZOI should be in the depth-of-field that is decided by the aperture of camera. As far as we know, no model that links the lighting, the exposure time, the aperture, the filter and the quality of image is suggested. The exposure time, the aperture of camera or lighting are adjusted depending on real-time experimental set-up conditions and user's experience. It is also noted that long exposure time allows more light to sensor but risks of smear images in case of high motion (dynamic tests). For example, Hao et al. proposed a correlation model between the exposure time and the Micro Vehicle motion. The authors recommend that a span of exposure time should be respected in order to get high-quality image (Hao *et al.*, 2002).

3.1.2.3 Image noise

In experimental conditions, noise can come from the room light, sun light or air disturbances of environment (Jones *et al.*, 2018 and Reu, 2016).

Image noise is characterized by the global variance of grey-level of images (Equation 3.1).

$$\sigma^{global} = \sqrt{\frac{1}{N} \times \sum_{i=1}^{N} \sigma_{image}^{2}(x_i, y_j)} \tag{3.1}$$

where:

- σ is the grey-level variation of the pixel having a coordinate (x_i, y_j)
- N is the number of images

Reu discussed that noise due to experimental conditions is the white noise that causes random error in kinematic measurements given by DIC (Reu, 2016). The order of magnitude of displacement uncertainty caused by image noise is about 0.01 pixel, but that depends on experimental conditions. The author suggests that prior to experimental tests, the kinematic measurements uncertainty (strain or displacement uncertainty) that links to resolution of measurements should be characterized by performing the auto-correlation method. Bornert et al. mentioned that the displacement error, characterized by the standard deviation (σ_u) is proportional to the standard deviation of noise σ_n and inversely proportional to the subset size d and the mean of the square of the grey-level gradient $\overline{\nabla I^2}$ (Equation 3.2) (Bornert *et al.*, 2018).

$$\sigma_u \propto \frac{\sigma_n}{d \times \overline{\nabla I^2}} \tag{3.2}$$

In practice, white noise is inevitable but it can be reduced by avoiding source of errors, i.e., performing the mechanical tests in a turn-off light room (Denis *et al.*, 2019) or avoiding the heat source or sun light (Reu, 2016).

3.1.2.4 Speckle pattern

Speckles is one of the most important parameters in the DIC method. A "good" speckle pattern ensures a correlation process therefore improves the accuracy of kinematic measurements and vice-versa. Speckle used for the DIC method should respect criteria for size, density or distance. All details about speckles for kinematic measurement using the DIC method at HT are mentioned in Chapter 2 (Section 2.1).

3.1.2.5 Effects of temperature on image contrast

Besides the set-up conditions that are mentioned previously, at high temperatures, the quality of image is additionally influenced by heat. The temperature effects could be from the radiation of the object and the surrounding environment resulting in image noise, saturations of pixels or blur images. The later one is not the subject of the study in this chapter, readers are invited to Chapter 4 for this subject. This section focuses on state-of-the-art on influences of radiation on kinematic measurements obtained and solutions found in literature.

The relationship of the radiation intensity of a blackbody and its temperature (T > 0 K) is written by the Plank's law (Incropera *et al.*, 2007). It is proportional to the absolute temperature **T** [K] and wavelengths λ [m] (Equation 3.3).

$$I(\lambda, T) = \frac{2hc_o^2}{\lambda^5[exp(hc_o/\lambda kT) - 1]} \tag{3.3}$$

where:

- $h = 6.626 \times 10^{-34}$ [J] is the Plank's constant
- $k = 1.381 \times 10^{-23}$ [J K^{-1}] is the Boltzmann constant
- $c_o = 2.998 \times 10^8$[m s^{-1}] is the light speed in vacuum
- T [K] is the blackbody 's temperature
- λ [m] is the wavelength

The wavelength λ at which the radiation intensity of the blackbody having temperature T is maximal is calculated by the Wein's displacement law (Equation 3.4):

$$\lambda_{max} = \frac{C}{T} \tag{3.4}$$

where: $C = 2998$ [µm K] is the radiation constant.

By integrating the radiation on all wavelengths, the total emissive power **E** [W m^{-2}] of an object is calculated by the Stefan-Boltzmann law (Equation 3.5).

$$E = \varepsilon\sigma_B(T^4 - T_\infty^4) \tag{3.5}$$

- ε is the total emissivity of the object. In case of the blackbody, $\varepsilon = 1$
- $\sigma_B = 5.670 \times 10^{-8}$ [Wm^{-2}K^{-4}] is the Stefan-Boltzmann constant
- T [K] is the object's temperature
- T_∞ [K] is the ambient temperature;

Equations 3.4 and 3.5 give interesting information:

- By comparing the white light spectrum ($\lambda = [450\ \text{nm} - 700\ \text{nm}]$) and the maximum radiation intensity of the blackbody, it is noted that from 1000 K (700 °C) and above, the initial portion of emission spectrum of the black body is within the visible wavelengths. It means that, from a practical viewpoint, a visible camera or human eye starts "seeing" the color temperature of the object. For example, a metallic specimen, considered as a opaque object having the global emissivity = 1 become "red" from 750 °C.

- The radiation of the hot object increases with its temperature. Therefore, sensors will receive more radiation light, which can be considered as undesirable signals for the DIC method.

The radiation light from a hot object influence the contrast of images. Most of studies notice that the contrast of image is reduced from 600 °C, even pixel saturations can be observed (Vautrot *et al.*, 2014). For the DIC method, a low contrast image can induce significant systematic errors in kinematic measurements. Pixel saturations can disrupt the correlation, reduces the spatial resolution or the accuracy of kinematic measurements (displacement and/or strain). For example, Vautrot et al. and Grant et al. observed a pixel saturation problem because of the radiation on steel specimens at 720 °C and 800 °C (Vautrot *et al.*, 2014 and Grant *et al.*, 2009). Pan et al., Dong et al., Valeri et al., Wang et al. and Leplay et al. remarked a degradation of image contrast at high temperatures from 600 °C to 900 °C on surfaces with speckles made by paint (B. Pan *et al.*, 2010b, Dong *et al.*, 2019, Valeri *et al.*, 2017, S. Wang *et al.*, 2015 and Leplay *et al.*, 2012). The radiation of the specimen is more significant at higher temperature that leads to a total pixel saturation (Thai *et al.*, 2019 and Le *et al.*, 2017).

Facing the radiation problem, most studies used IR filters as the first solution to suppress the pixel saturations. The IR filter showed efficiency by filtering infrared wavelengths emitted by the hot sample. In case of extreme temperatures (more than 1000 °C), Thai et al. adjusted the exposure time and used a IR band-pass filter to tackle the saturated pixels (Thai *et al.*, 2019). The authors suggested an exposure time span to help an experimenter to quickly evaluate the image contrast at high temperatures. Furthermore, at very high temperatures, the use of blue light and the UV-light illumination presented more advantages than the white light because it gives a better ratio Signal/Noise. In this context, the Signal is the light reflection on the object from a light source, appearing at shorter light wavelength (UV-light) and the Noise is the radiation from a hot object which appeared at a longer wavelength (IR). Indeed, Berke et al. compared speckle images at high temperatures captured under three lighting conditions: white light, blue light and the UV light (Berke *et al.*, 2014). The image after filtered by an IR filter showed that from 600 °C and above, the blue light and the UV light can attenuate the pixel saturation due to a hot specimen. Tang et al. employed a CCD color camera to separate the radiation lights and reflected light from the object for a synchronous temperature and strain measurements (Tang *et al.*, 2019).

The second solution is using improved DIC algorithm. For example, Su et al. proposed the grey-level average method to attenuate saturated pixels due to radiation (Su *et al.*, 2015). The method increased the quality of correlation calculation (the ZNCC coefficient was decreased). The method works well from the temperature of more than 700 °C when the radiation becomes significant. Wang et al. used the thermal radiation correction model based on a method separating the radiation and the reflection parts to deal with the pixel saturation (S. Wang *et al.*, 2015 and W. Wang *et al.*, 2017). The efficiency of this method is demonstrated by providing a smoother displacement field compared with the initial one with many singularities.

3.1.3 Objective

Although many studies in the literature confirm the radiation effect and its consequence on the quality of image (pixel saturation) then suggests solutions, the influence of radiation from 400 °C to 700 °C is little mentioned. In this temperature range, the object has not yet become "red" to human eyes because the radiation intensity is low. Therefore, the necessity of IR filter and color light in experiment set-up is questioned. Furthermore, the set-up of DIC system depends on experimental conditions, for example available device, and space. This forces us to find a DIC set-up configuration which is compatible with our experimental tests and gives as good image quality as possible.

The aim of this study is to evaluate the effect of radiation on the image contrast at high temperatures, from 400 °C to 700 °C. Afterward, the set-up of the 2D-DIC system which is adapted to the tensile tests in our laboratory is suggested in order to reduce the radiation's effect and give the "best" image contrast.

3.2 Methodology

The current study involves evaluating the influence of the radiation of object at hot object (TA6V testing specimen) on the contrast of image. Solutions to improve the contrast of image at HT by using different device of the 2D-DIC is then suggested. To this end, the effect of different factors of the 2D-DIC system, such as IR filters, exposure time is studied by a design of experiments (DOE).

In this section, we present first the material and devices and the implementation of DIC system. Next, a four-factor-two-level DOE to study the effect of radiation on image contrast is performed. An observation of the image contrast versus time in order to understand the origin of contrast diminution at HT is presented.

3.2.1 Materials and devices

3.2.1.1 Materials

In this study, TA6V planar specimen was used to evaluate the contrast of image at HT. The geometry of the specimen is presented in Appendix A.3. The ZOI for strain measurements was 15 ± 0.3 mm $\times$ 8 ± 0.3 mm. Speckles were created on the ZOI of the specimen by the combining anodization and laser engraving (M5) technique.

3.2.1.2 Mechanical testing system

Experiments in the DOE were performed in a servo-hydraulic testing machine (MTS125, MTS®, Minneapolis, USA) and a closing furnace (AET, AET® technologies, France). The experiments were performed in the limited space, where further mechanical tests will be performed in next Chapter 4 and Chapter 5. The testing machine was used to hold the TA6V specimen and the closing furnace was employed to heat-up the specimen to target temperatures (about 1 hour and 30 min).

The closing furnace was equipped with a glass window (150 mm in height and 15 mm in width) for image capturing and observation. During the image capturing, the specimen was held by the grips of the MTS125 testing machine. The applied load on specimen was 100 N for the alignment of window of furnace-camera-specimen. The load was maintained constant during experiment tests by a TestStar controller.

3.2.1.3 2D-DIC system set-up

The 2D-DIC system used for the evaluation of image contrast at HT contains several devices that are listed below. The system used:

- a camera with a 2452-pixel by 2052-pixel CCD sensor (Pike 505F/B, Allied Vision Technologies, Germany) and a macron lens (focal length from 80 mm to 300 mm) (Sigma, Kanagawa, Japan) f/3.5-6.3
- a light source (white light) from 300 W (minimum power) to 575 W (maximum power), diffusion angle from 5° to 40° (Dedolight, Dedo Weigert Film GmbH, Germany). The spectrum of the light source (lamp) is characterized by the FT-IR spectrometer (Vertex 70v, Bruker, USA)
- an IR filter having a cut-off wavelength at 650 nm (KG 5 heat absorbing glass, Edmund Optics ®, USA). The spectrum of this filter is presented in Appendix B.1
- three color glasses (Red, Green, Blue) that filter some specific wavelength. The spectral transmission of the glass is characterized by the FT-IR spectrometer (Vertex 70v, Bruker, USA).

The 2D-DIC system was set-up in front of a testing machine. Images were captured by the Vic-Snap® software (Correlated Solutions®, USA). The camera's aperture was f/8 for a 5 mm depth-of field and 28 mm field-of-view. The image quality (contrast) was evaluated by two parameters: The MIG, the Shanon entropy (Readers are invited to chapter 2 for the MIG and the Shanon entropy definition and their formula). Besides, the percentage of saturated pixels is calculated for each image.

3.2.2 Implementation of the 2D-DIC system for evaluating the contrast of image

The challenge of DIC set-up is to illuminate then capture the ZOI of TA6V specimen in a closing furnace throughout a very narrow observation window. To this end, the camera, filters and light source would be set up along the optical axis. However, due to the high power that could increase the uncertainty of strain measurements, the light source was set behind the camera. To avoid the camera's shadow on the specimen, the high source was set along the optical axis but made an angle of 60° with the camera's axis. Furthermore, to reduce the heat haze from the light source and to create the light color for image contrast improvement, the glass was positioned in front of the light source. In summary, the filter, camera, color glass and light source were set in an order presented in Figure 3.3.

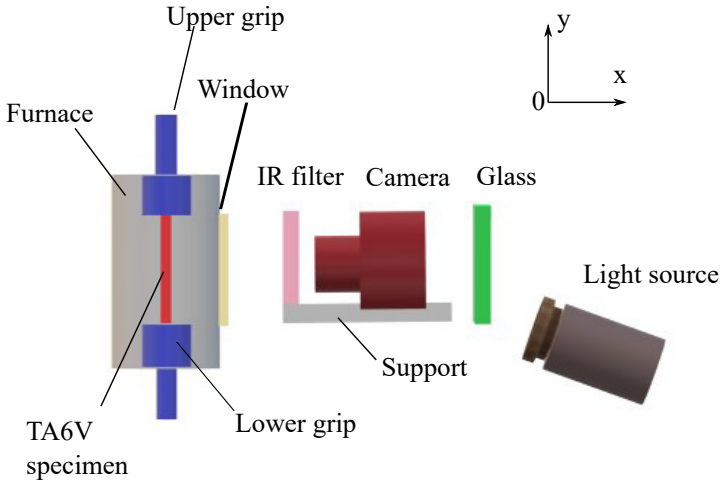

Figure 3.3: 2D-DIC system (view in Oxy plane) used for the evaluation of influence factors on the contrast of image at HT

3.2.3 Design of experience on factors influencing the image contrast at HT

As mentioned in the section 3.1.3, "Aim of study on temperature effects on image contrast", the use of filter and color light for 2D-DIC set up for temperatures from 400 °C to 700 °C is questioned. Therefore, a four-factor-two-level DOE was used to evaluate the effect of each parameter on the quality of image at 600 °C. The temperature of 600 °C was chosen as a representative temperature in the range of hot stamping temperature for TA6V alloy. Main factors that influence the image contrast at HT were: the exposure time, the use of IR filter, the lighting intensity and the use of color light (by using the color glass). It is noted that with some limitations in experiment set-up, other influence factors, i.e., the self-heating of camera, the quality of glass window on image were not studied. The error of kinematic measurements due to these factors were assumed to be neglected.

Details on 16 runs of experiments in the DOE are presented in Table 3.1 (Goupy *et al.*, 2006). Two factors: the color of light and the use of filters have discontinuous values corresponding to two levels in the DOE: Yes (level +1) or No (level -1). Two other factors: the exposure time and light intensity are continuous. The light intensity (J) for the illumination of specimen was calculated from the light power (P) and the projection angle (α) (Equation 3.6).

$$J \propto \frac{P}{sin(\alpha)} \tag{3.6}$$

The minimum light intensity (level -1) corresponded to the lowest power (300 W) and highest angle projection 40°.The maximum light intensity (level +1) corresponded to the highest power (575 W) and lowest angle projection 5°. For the exposure time, it was adjusted such that the lowest level (level -1) corresponded to images which were barely visible. The dynamic range of grey-level of these images presented peaks of 22-25 grey-level (Figure 3.4).

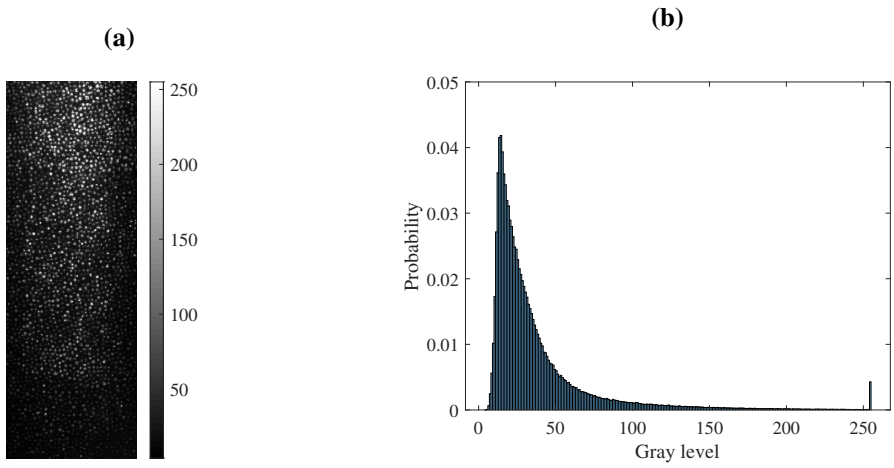

Figure 3.4: (a) Images corresponded to the shortest exposure time, (b) Dynamic range of grey-levels of images corresponded to the shortest exposure time

The longest exposure time corresponded to images that were well visible and did not present pixels saturation. The dynamic range of grey-level presented peaks of 100 grey-level (Figure 3.5).

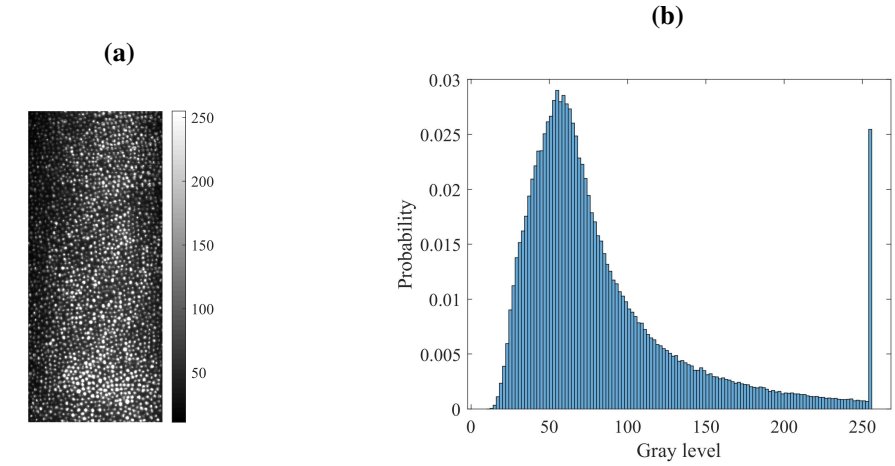

Figure 3.5: (a) Images corresponded to the shortest exposure time, (b) Dynamic range of grey-levels of images corresponded to the longest exposure time

Table 3.1 presents 16 runs of experiments of the DOE to evaluate the influence of parameters in the the 2D-DIC system on the image contrast at 600 °C. Each run corresponded to conditions defined in a four-factor-two-level of the DOE. The values in parentheses corresponded to levels (-1) and level (+1) of the DOE. In the filter, intensity and color light factors, two levels-1 and +1 corresponded to two discontinuous values "Yes"-use of the device and "No"-no use of the device. In the exposure time factor, the values of exposure time were variable and adapted to two levels -1 and +1 of the image contrast (Figure 3.4 and Figure 3.5, respectively)

Table 3.1: 16 runs of experiments in the DOE for the assessment of parameters in the 2D-DIC system on the image contrast at 600 °C

N° exp.	Filter	Intensity	Color light (Green)	Exposure time (ms)
1	No (-1)	Min (-1)	No (-1)	2 (-1)
2	No (-1)	Min (-1)	No (-1)	26 (+1)
3	No (-1)	Min (-1)	Yes (+1)	13.5 (-1)
4	No (-1)	Min (-1)	Yes (+1)	229.5 (+1)
5	No (-1)	Max (+1)	No (-1)	0.19 (-1)
6	No (-1)	Max (+1)	No (-1)	3.2 (+1)
7	No (-1)	Max (+1)	Yes (+1)	2.4 (-1)
8	No (-1)	Max (+1)	Yes (+1)	32.5 (+1)
9	Yes (+1)	Min (-1)	No (-1)	9.5 (-1)
10	Yes (+1)	Min (-1)	No (-1)	25 (+1)
11	Yes (+1)	Min (-1)	Yes (+1)	19 (-1)
12	Yes (+1)	Min (-1)	Yes (+1)	129 (+1)
13	Yes (+1)	Max (+1)	No (-1)	7.5 (-1)
14	Yes (+1)	Max (+1)	No (-1)	17.5 (+1)
15	Yes (+1)	Max (+1)	Yes (+1)	32.5 (-1)
16	Yes (+1)	Max (+1)	Yes (+1)	119.5 (+1)

The image captured from each run in the DOE were evaluated by the MIG and the Shannon entropy criteria. These two criteria are usually used to quickly assess the image contrast. The effect of each parameter in the DOE was analyzed by an analysis of the variance: Anova (Matlab, Matwork ®, USA).

3.2.4 Evolution of image contrast versus time at 600 °C

The high temperature could induce the physique and chemical modifications of surface, i.e., the oxidation. With the aim to understand the origin of pixel's saturation at 600 °C that were observed in our experiment, the evolution of TA6V surface speckled with the M5 method was followed for every minute. The surface of specimen after three hours of heating at 600 °C was then analyzed by an optical microscope (Leica GmbH, Germany) then by SEM and EDX for micro analysis (FEI™, Oregon, USA).

3.3 Results

3.3.1 Implementation of the 2D-DIC system

The objective of the current study is to implement the 2D-DIC camera system in front of the tensile machine for the best contrast of images. It is reminded that the observation window was narrow (10 mm × 150 mm) because the specimen was heated by a closing furnace. Therefore, devices in the 2D-DIC camera system should be arranged in a "delicate" manner.

3.3.1.1 Spectrum of filters used for the 2D-DIC system

In our laboratory, it is possible to change the color of the light source by using one of three color glasses: red glass, green glass and blue glass. The color light was used in previous studies to increase the image contrast at high temperatures (B. Pan *et al.*, 2010b, Berke *et al.*, 2014). To choose an appropriate color light for illuminating the TA6V specimens, the quantum efficiency of CCD sensor, the transmission spectrum of three glasses were compared.

Figure 3.6a presents the normalized intensity spectrum of the white light while Figure 3.6b displays the transmission of three color glasses (in Red, Green and Blue colors) and the quantum efficiency of CCD visible camera (Pike 505F/B) sensor versus wavelengths. It is shown that the white light had the maximum intensity from 400 nm to 700 nm which correspond to a maximum quantum efficiency of the CCD camera sensor. The transmission spectra of three glasses show that they have different absorption wavelengths. Among three glasses, the green one has the transmission wavelength closer to the quantum efficiency of the CCD sensor compared with two other glasses. The light photon captured by the sensor, which is proportional to the product: glass transmission $\times$ CCD quantum efficiency ($T(\lambda) \times \eta$) is higher when using a green glass. Therefore, the green glass is set-up in front of the light source for the study of factors that influence the image contrast at high temperatures (the DOE study).

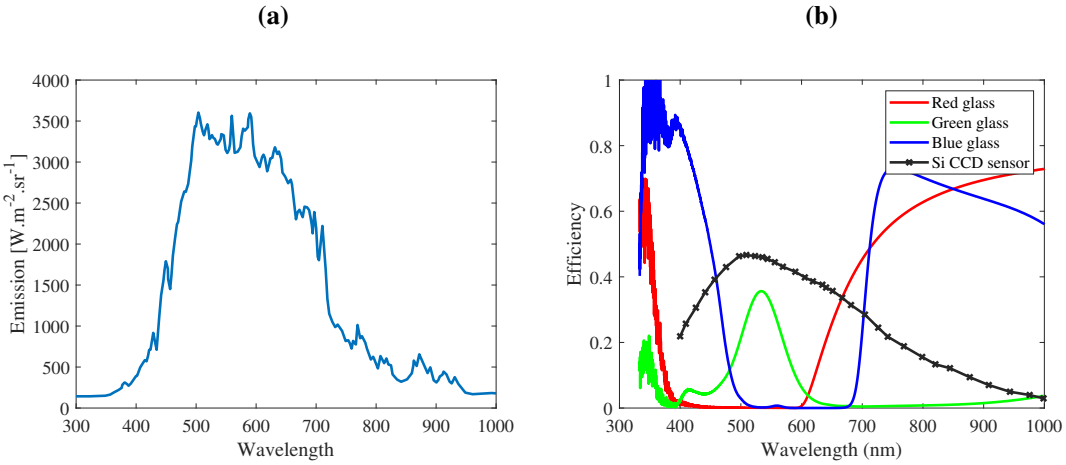

Figure 3.6: (a) White light emission [W m^{-2} sr^{-1}] in function of wavelength [nm]; (b) Transmission of three color glasses (Red, Green, Blue) and the quantum efficiency of Si CCD camera sensor

3.3.1.2 2D-DIC system set-up

After choosing the color light, the 2D-DIC camera is then implemented in front of the testing machine. Because the observation window is narrow, only 2D-DIC camera which is paralleled to the specimen that allows capturing image. Camera devices are therefore set on the optical axis and followed the order: IR filter-camera-green glass-light source from the nearest to the furthest of specimen. The focal length is set at f = 262 mm and the working distance of camera-specimen is 1.0 m to avoid the radiation from the furnace. The field-of-view and the depth-of-field are respectively 28 mm and 5 mm. The magnification was 14 µm/pixel. The IR filter is set in front of the camera. The light source and the glass window are set 30 cm far from the camera. The light source (lamp) is 36 cm lower than the height of the camera providing the projection angle

of 62° to avoid the shadow of the camera on the TA6V specimen. Figure 3.7 presents final configuration for 2D-DIC system (In this figure, the green glass for green light set in front of the light source is not presented).

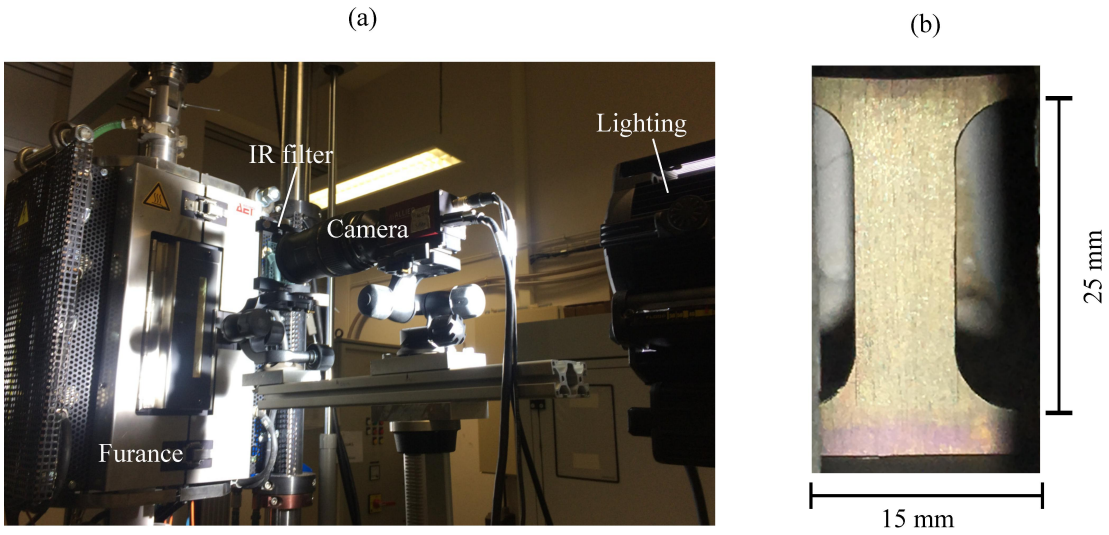

Figure 3.7: a) Overview for the 2D-DIC system for capturing images, b) ZOI of the TA6V specimen observed though the glass window of the closing furnace. The green glass is missing in this figure

To obtain a "good" image, the exposure time is adjusted from 4 ms to 230 ms. For this range of exposure time, blur images caused by a long exposure time are not observed, the correlation is ensured.

Figure 3.8a presents an image captured from the DIC system. Its histogram of grey-level is displayed in Figure 3.8b. It is shown that the lighting condition is relatively homogeneous (baseline was constant while an inspection of grey level on vertical line along the ZOI). However, speckle image at 600 °C presented < 5% of saturate pixels after 2 hours of heating.

3.3.2 Effects of parameters in the 2D-DIC system on the image contrast at HT

This study aims to determine main influence factors on the image contrast at 600 °C, a representative temperature between 400 °C to 700 °C.

Table 3.2 presents the image contrast, characterized by the MIG and Shanon entropy criteria obtained from the 16 runs of experiments of the DOE. It is seen that among 16 runs of experiments, those that involves using the IR filter and the maximum exposure time (Exp. N° 10, 12, 14 and 16) present the best contrast of images at 600 °C. The values of MIG of these experiments are from 17.7 to 21.5. The Shannon entropy are around 7.0.

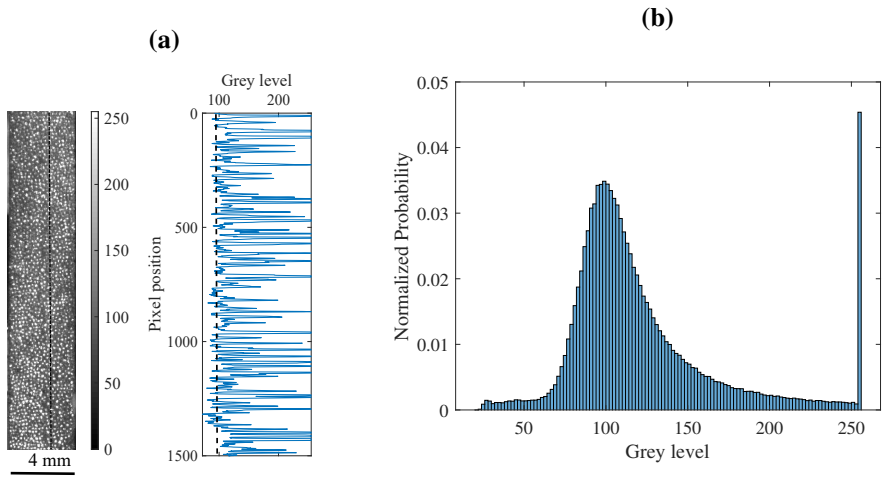

Figure 3.8: (a) Image captured by 2D-DIC system and the grey-level on a vertical line along the ZOI of specimen: the base line measured corresponded to lighting was relatively constant, (b) Histogram of speckle image (made by (M5) technique), captured by the 2D-DIC system at 600 °C

Table 3.2: 16 runs of experiments of the DOE and results (the MIG and the Shannon entropy) for the evaluation of parameters in the 2D-DIC system on the image contrast at 600 °C

N° Exp.	Filter	Intensity	Color light	Exposure time	MIG	Shannon entropy
1	No	Min	No	Min	2.9	4.3
2	No	Min	No	Max	14.1	6.8
3	No	Min	Yes	Min	2.1	3.8
4	No	Min	Yes	Max	16.0	6.7
5	No	Max	No	Min	3.3	5.0
6	No	Max	No	Max	13.0	7.0
7	No	Max	Yes	Min	1.8	3.8
8	No	Max	Yes	Max	13.5	6.9
9	Yes	Min	No	Min	10.4	6.3
10	Yes	Min	No	Max	17.7	7.1
11	Yes	Min	Yes	Min	3.8	4.6
12	Yes	Min	Yes	Max	20.3	7.1
13	Yes	Max	No	Min	13.2	6.6
14	Yes	Max	No	Max	19.3	7.0
15	Yes	Max	Yes	Min	12.8	6.4
16	Yes	Max	Yes	Max	21.5	6.9

The analysis of variance shows the IR filter, exposure time, light intensity, the interaction between IR filter and exposure time and the interaction between the IR filter and light intensity have significant influences on the contrast of images at 600 °C. Table 3.3 resumes results from the analysis of variance on factors influencing the image quality based on two image contrast criteria. The values of percentage of variance on factors are also presented in this table. Details

Table 3.3: Results of the analysis of variance on the influence of parameters of the 2D-DIC system on the image contrast at 600 °C

Parameters	Criteria	
	MIG	Entropy
Filter	Yes (25.77%)	Yes (17.34%)
Intensity	No (1.17%)	No (2.56%)
Color glass	No (0.04)	No (4.45)
Exposure time	Yes (69.25%)	Yes (63.70%)
Interaction: Filter × Intensity	Yes (3.11%)	No (0.22%)
Interaction: Filter × glass	No (0%)	No (0%)
Interaction: Filter × exposure time	No (0.65%)	Yes (17.35%)

on the analysis of variance from the linear regression model were presented in Appendix B.2. It is seen that among 16 runs of experiments, the Exp. N°12 corresponds to the 2D-DIC set-up parameters: use of IR filter, minimum light intensity, green glass and a maximum exposure time (t = 129 s) gives the best contrast of image. The MIG and Shanon entropy are respectively 20.3 and 7.1.

The Pareto diagrams shows the contribution of each parameter makes on the quality of image, assessed by MIG criteria (Figure 3.9a) and by the Shannon entropy criteria. It is seen that in both two diagrams, the exposure time have a major influence on image contrast (more than 60%), followed by the used of IR filter (20%). In Figure 3.9a, two parameters are the main factor influence on the MIG of image while in Figure 3.9b, the others parameters: interaction of filter and the exposure time and the light color contributed minor influences on the dynamic range of grey-levels (represented by Entropy) of image (less than 10%).

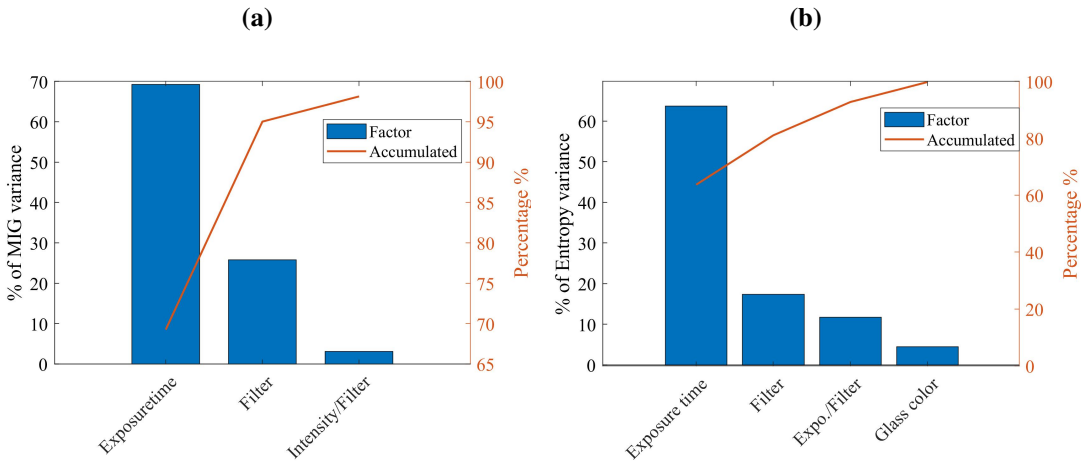

Figure 3.9: Pareto diagrams on the contribution of influence factors on the image quality: (a) assessed by the MIG (b) assessed by the Shanon entropy

Figure 3.10 graphically presents the response value (MIG and Entropy (in average)) corresponding to different levels: (-1) and (+1) of the influence factors. The figures show that graphically the image contrast is changed a lot when the exposure time and the IR filter change their levels (the exposure time passed from the lowest to the highest values, the IR filter is used or not used). Inversely, the change in color light (use or do not use color glass) and intensity (use the lowest light intensity and highest light intensity of the light source) do not make a major change in the image contrast. Furthermore, results show the use of filter IR and longer exposure time increase the image contrast of TA6V specimen speckles by M5 technique.

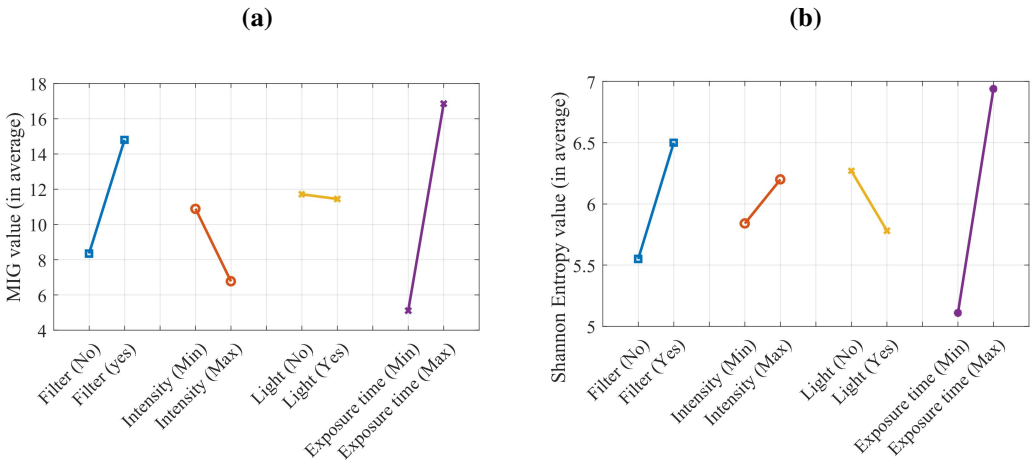

Figure 3.10: (a) MIG (in average) values (b) Entropy values measured from different levels of influence factors at 600 °C

The interactions of filter - light intensity and the filter - exposure time are respectively presented in Figure 3.11a and Figure 3.11a. It is seen that the interactions is linear. In both figures, the use of filter increases the MIG and entropy of images. A maximum light intensity and exposure time increases the image quality as well. The combination of filter and maximal light intensity (Figure 3.11a) and use of filter-maximum exposure time gives the best image quality. Therefore, in experimental set up with maximal light intensity, the use of IR filter and an exposure time t = 119.5 ms would be used to capture the best image quality at 600 °C.

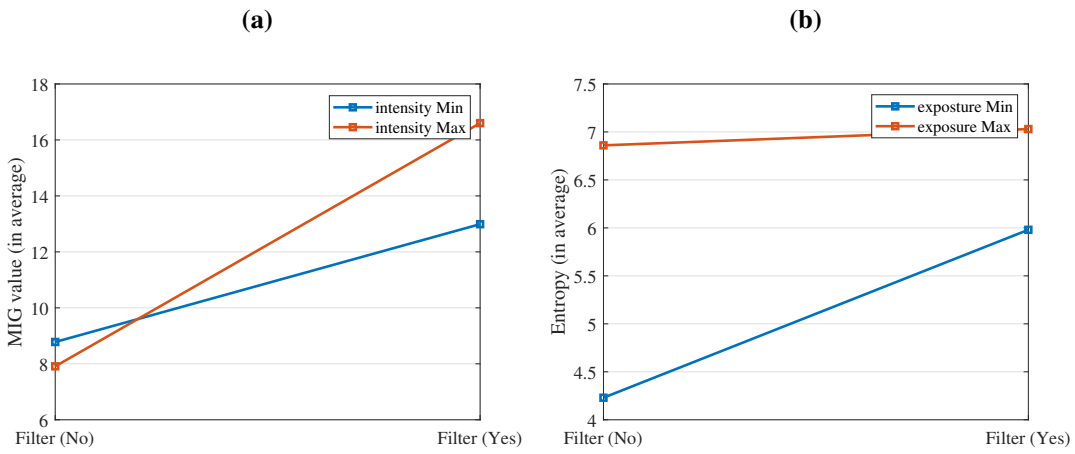

Figure 3.11: Interaction of factors on contrast of images: (a) between IR filter and light intensity (b) between exposure time and IR filter

The image captured and its histogram set-up with these experimental conditions are presented in Figure 3.12.

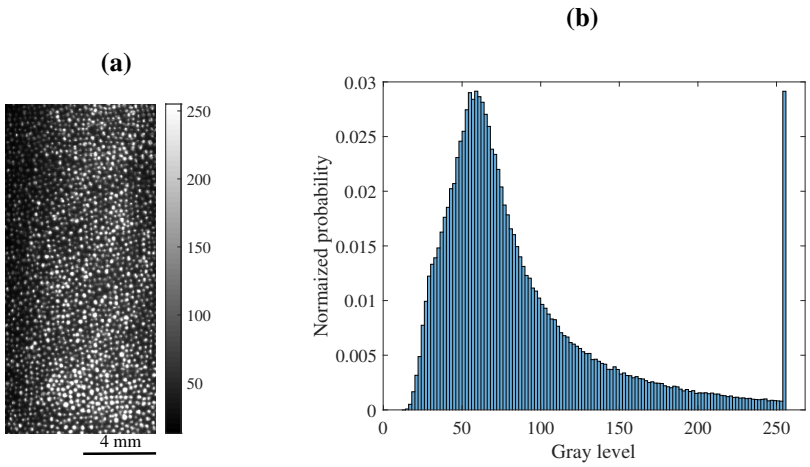

Figure 3.12: (a) Image of the ZOI of the TA6V specimen at 600 °C (b) Histogram of the dynamic range of grey-levels measured on the ZOI of specimen

In conclusion, the four-factor-two-level Taguchi DOE and the analysis of variance on parameters that influence the image contrast showed the IR filter, the exposure time of the camera and its interaction are the two main factors that modify the quality of image (from 17.35% to 25.77% for the IR filter factor and from 63.7% to 69.25% for the exposure time factor). The configuration of 2D-DIC camera system that gives the best contrast of image is:

- using an IR filter (cut off wave length at 700 nm)
- the maximal light intensity with power = 575 W and diffusion angle $\alpha = 5°$
- the exposure time t = 119.5 ms.

3.3.3 Evolution of contrast of image versus time at 600 °C

In order to better understand the origin of pixel saturations that appeared on images at high temperatures, images of TA6V specimen with speckles made by M5 technique were capture every minute. Figure 3.13 presents the images of the ZOI of the TA6V specimen during one hour of heating at 600 °C. It is seen that the speckle pattern on the TA6V specimen was modified by the effect of temperature. The initial image (Figure 3.13a) presented only few saturated pixels (< 0.01%). After 40 minutes of heating (Figure 3.13c), the pixel saturation increases rapidly (Figure 3.14). Saturated pixels are concentrated on speckle dots (Figure 3.13d), suggesting the influence of oxidation of the TA6V material on the image contrast. We remind that the topography and local microstructure on the speckle made by M5 method change after laser (Chapter 2, Figure 2.10 and 2.11). Furthermore, in the M5 speckle technique, the substrate (TA6V specimen) is covered by an oxide layer from the anodization technique. The local change of topography and the microstructure on speckle dots would favor the oxidation that induced the pixel saturation.

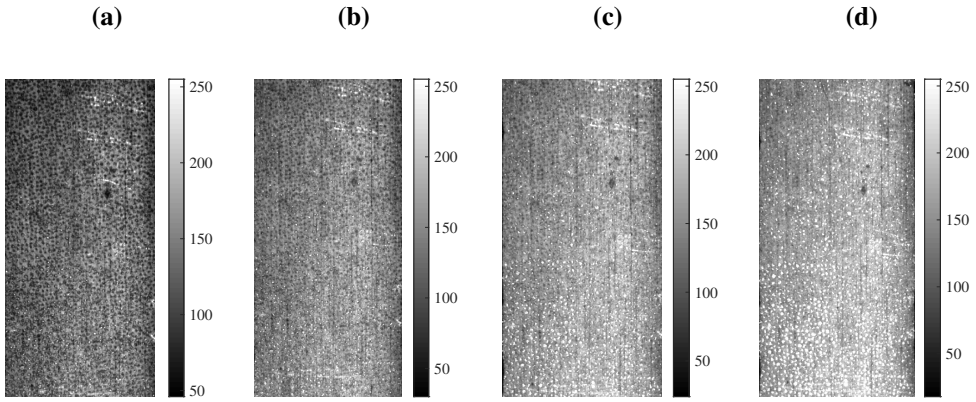

Figure 3.13: Evolution of the speckle image made M5 technique during one hour of heating at 600 °C: (a) initial image (time $t = 0$ s), (b) after $t \approx 30$ min, (c) after $t \approx 40$ min, (d) after $t \approx 50$ min

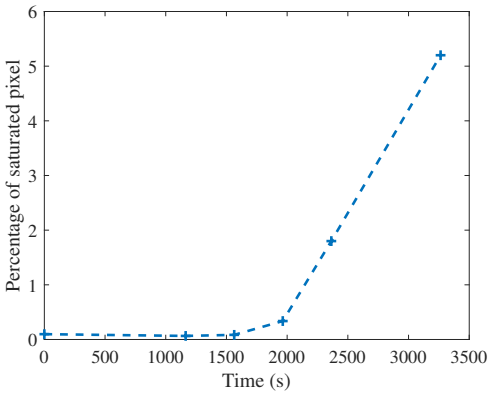

Figure 3.14: Evolution of the percentage of saturated pixels on the ZOI of TA6V specimen with speckles made by the M5 technique versus time at 600 °C

The surface microstructures of a speckle dot before and after heating are compared (Figure 3.15). It is seen that the initial speckle dot made by laser and anodization does not create any pixel saturation. However, after being heated to high temperature (600 °C for one hour), the speckle dot is oxidized. The oxide layer reflects coming lights and becomes more brilliant. The pixel saturation is present (saturated pixels were indicated on Figure 3.15 by a red arrow). A local EDX micro-analysis (accelerated tension = 19 KeV) on the surface of a speckle dot shows that 33% of oxygen is present, suggesting that the pixel saturation is probably from the oxide layer developed on speckles made by M5 technique.

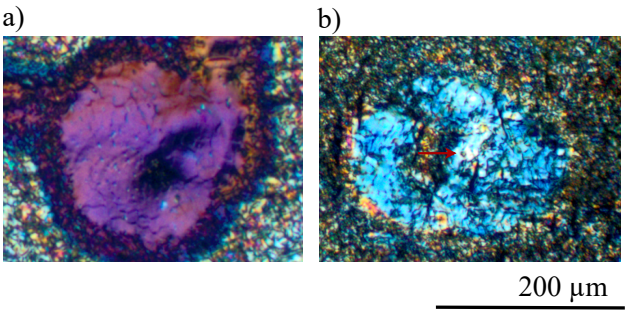

Figure 3.15: Optical microscope of a speckle dot made by M5 technique: a) initial state, b) after one hour of heating at 600 °C

In conclusion, it is observed that after being heated at high temperatures and for a long time (one hour), the pixel saturation on speckle dots made by M5 technique is observed. The optical observation and chemical micro-analysis shows that speckle dots are oxidized. The oxidation could be the origin of the pixel saturation.

3.4 Discussions

3.4.1 Effects of parameters in the 2D-DIC system on the image contrast at HT

The current study aims to implement the 2D-DIC system that adapts to mechanical tests at high temperatures in order to capture images with the best contrast. First, the 2D-DIC system was set-up along the optical axis of a camera by following the order: IR filter-camera-glass color-light source. Afterward, the four-factor-two level DOE was performed in order to evaluate principal factors that influence the image quality at 600 °C. The image contrast was assessed based on two criteria: MIG representing the global contrast image and the Shanon entropy that represents the dynamic range of grey-levels of images.

Results obtained from the analysis of variance show that main parameters that influence the image contrast are: the use of an IR filter, the exposure time of camera and the interaction filter - exposure time. IR filter gives a better image contrast even when the temperature is lower than 700 °C. In general, at these temperatures, the radiation intensity of a TA6V specimen is still low. The result obtained from the DOE is in agreement with previous studies (Vautrot *et al.*, 2014, Berke *et al.*, 2014 and B. Pan *et al.*, 2010b). Other studies show also the role of IR filter is significant at higher temperatures, more than 1000 °C (Claudinon *et al.*, 2002, Grant *et al.*, 2009 and Valeri *et al.*, 2017).

The influence of exposure time on the image contrast is clearly demonstrated in this study. The importance of the exposure time of camera is mentioned by Thai et al. (Thai *et al.*, 2019). The authors discussed that the exposure time is the first parameter that influences the DIC error when setting the DIC system. They showed that an abrupt increase of error in extremely dark or bright images. An appropriate exposure time can minimize the errors. In our experiment, results show that increasing the exposure time raises the contrast of image while keeping a low percentage of saturated pixels because the number of light photons captured by the CCD sensor is increased. The exposure time for a "good" image quality (images are not too dark nor too bright to ensure the correlation) is from 3 ms to 14 ms in case of no IR filter and from 25 ms to 120 ms in case of using an IR filter. The range of exposure time in our experiment is in the order of magnitude compared with other studies (Berke *et al.*, 2014). The exposure time should be chosen depending on experimental conditions to get enough coming light to get the best dynamic range of grey-levels.

Beside the influence of exposure time, results obtained prove that the use of green color light and the light intensity (limited by its power and diffusion angle) have a minor influence on the results for tests under 700 °C. This is explained by the low radiation intensity emitted by objects under 700 °C. In general, blue illumination or cold illumination and the use of an IR filter are recommended at very high temperatures to separate the reflected lights and the radiation of hot objects for a better ratio Signal/Noise (S/N) (Berke *et al.*, 2014).

Our study contributes to confirm the influence of two factors: the IR filter and the exposure time on image contrast at high temperatures from 400 °C to 700 °C by an approach of DOE. The results are generally in agreement with previous studies but most experimental tests in the studies found in the literature are at higher temperatures (about 1000 °C). Nevertheless, our study is limited in considering only four impact factors on the image quality at high temperatures while other factors could involve, for example the camera aperture, the influence of environment temperature to the camera's temperature, the electronic noise of image acquisition.

3.4.2 Problem of the pixel saturation at high temperatures

Finally, in our study, we found that the pixel saturation is not from the radiation of the hot object itself. It is probably due to an oxide layer developed during the heating to high temperatures for a long time. The use of an IR filter or color light therefore cannot eliminate saturated pixels. It is an interesting information because this new observation has not mentioned in any previous studies. To correct the problem, the subset size used for correlation process must be large to reduce DIC errors. It would be interesting to find a solution but not to "tolerate" the pixel saturation problem. As far as we know, the pixel saturation would probably come from the aluminum oxide layer that reflects a lot of white light. According to Ansart et al., the aluminum oxide layer, results from a oxidation reaction has a diffusive reflection property (Ansart *et al.*, 1995). The result would be an interesting information for further studies on the origin of pixels saturation problem observed in our study.

Although the DIC is well known as a flexible method and the 2D-DIC set-up procedure seems to be simple, it is not evident at high temperatures in a limited space. An experimenter has to take into account the effect of temperature (radiation and the modification of speckles chemistry or specimen surface due to high temperature). Actually, to our knowledge, few discussions on the use of 2D-DIC system in unfavorable conditions at high temperatures from 400 °C to 750 °C to obtain the best contrast have been addressed. The 2D-DIC system should be set-up to adapt to real conditions.

3.5 Conclusions and perspectives

Chapter 3 aims to implement a 2D-DIC system adapted for mechanical tensile tests at high temperatures in order to obtain the best image quality for the fewest DIC errors. Available devices of the DIC system in our laboratory consist of a camera and CCD sensor, an IR filter, a light source and color glasses to change the color of the light source. After considering experimental conditions in our laboratory (closing furnace that limits the observation field-of-view of the camera), the spectrum of the light source, the transmission spectrum of color glasses and IR filter, the quantum efficiency of the CCD sensor, a 2D-DIC system is set up along the optical axis of the camera and arranged in the order as follows: IR filter-camera-green glass-the light source.

A four-factor-two-level DOE is used to evaluate the influence of a) the IR filter, b) the use of color light, c) light intensity, d) exposure time on image contrast at 600 °C. Results from analysis of variance show that only two factors: the IR filter and the exposure time, have significant influences on the image contrast, characterized by the MIG and Shanon entropy criteria. With the 2D-DIC set-up conditions: an IR filter to attenuate IR light rays from hot object and an exposure time under 120 ms, images captured present the best contrast (MIG = 21.45 and Shanon entropy = 6.9).

In addition, at high temperatures, saturated pixels are observed because the surface of the specimen is oxidized. It is likely that the reflexion comes from the oxide layer formed on speckle dots made by the M5 speckle fabrication technique. Actually, no solution has been suggested. To correct this problem, the subset size for correlation process must be large enough: at least 39 pixels $\times$ 39 pixels.

Perspectives for further studies should focus on:

- extending the DOE at higher temperatures, for example at 750 °C or taking other factors (camera aperture) that could influence the image contrast,
- studying the self-heating of the camera or the effect of environment temperature on image contrast or noise,
- confirming the origin of pixel saturation problems by finely analyzing the chemical component on speckle dots made by M5 technique at higher temperature in order to find a solution for the pixel saturation problem. If the pixel saturation comes from the reflexion of aluminum oxide layer, a filter with appropriate cut-off reflection wavelength of aluminum oxide layer could reduce the problem of pixel saturations.

CHAPTER

4

Influence of mirage effects on strains measured using the 2D-DIC method at high temperatures

In this chapter, the influence of mirage effects on kinematic fields in experimental mechanics measured by the 2D-DIC method is studied. First of all, the introduction of mirage effects and their relationship with the 2D-DIC strain measurement errors used for experimental mechanics is presented. Mirage effects are a current problematic which should be eliminated in the 2D-DIC strain measurements at high temperatures. Afterward, we present details on the methodology for characterizing the strain measurement errors due to mirage effects at temperatures from 400 °C to 750 °C by the Background Oriented Schlieren (BOS) technique. The results and discussions on spatial and temporal characteristics of 2D-DIC strain measurement errors at different temperatures are presented. Finally, a conclusion on the characteristic of strain measurement errors and perspectives for future work are addressed.

4.1 State-of-the-art

4.1.1 Mirage effect, heat waves and characteristics

4.1.1.1 Introduction to mirage effect

Mirage effect is an optical illusion phenomenon in which images observed by human eyes or cameras are deformed or displaced through a heterogeneous environment, such as, through a hot airflow (Delmas *et al.*, 2013). Mirage effects are classified as the "inferior" or "superior" mirage. In daily life, the most common example of an "inferior" mirage effect is water pools that appear on a road in summer (Figure 4.1a) (Rascaille, 2012). Regarding the "superior" mirage, the typical example is the ship appearing on the horizontal line, above the sea in the early morning (Figure 4.1b) (Patowary, 2019).

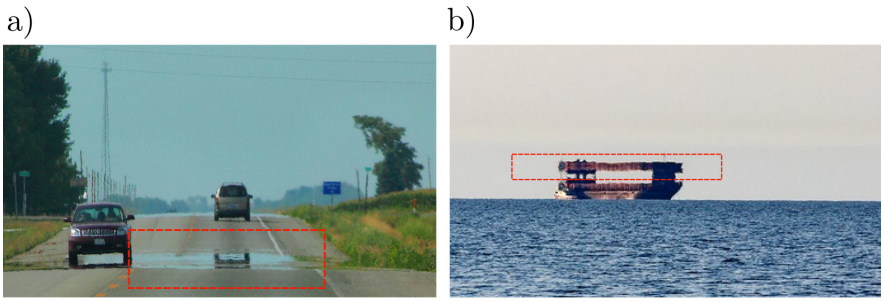

Figure 4.1: (a) An example of an "inferior" mirage: a water pool (in red) is observed on a road in summer (Rascaille, 2012); (b) An example of a "superior" mirage: a ship is seen inversely and positioned above the sea level in a early morning (Patowary, 2019)

Mirage effects can be explained by the fact that light rays are bent while they are passing through an environment having a gradient of refractive index. The gradient of the air refractive index can be caused by a gradient of air temperature (Maurel, 2002). Indeed, the gradient of air temperature influences the air density (ρ), which is related to the air refractive index (n). The relationship between the air refractive index n and air temperature T is described by Equation 4.1 (Delmas *et al.*, 2013).

$$n(T) = 1 + (n_o - 1)\frac{T_o}{T} \tag{4.1}$$

where:

- n is the refractive index of air at temperature T [K];
- n_o is the referent refractive index of air at temperature T_o [K], $T_o = 298$ [K] .

According to Fermat's principle (Maurel, 2002), the gradient of refractive index from environment 1 (n_1) to environment 2 (n_2) causes a deviation of light trajectory, which is written by the Snell's law (Equation 4.2).

$$n_1 \times \sin\theta_1 = n_2 \times \sin\theta_2 \tag{4.2}$$

where:

- n_1 and n_2 are respectively the refractive index of air at temperatures T_1 and T_2

- θ_1 and θ_2 are the incident angle and the reflection angle of a light ray in the environments having refractive indexes n_1 and n_2

From Equations 4.1, it is remarked that the refractive index decreases if air temperature increases. As a consequence, the deflection angle increases (Equations 4.2). It means that a higher air temperature cause more light deviation.

To illustrate the "inferior" and "superior" mirages, Figure 4.2 shows light rays passing through an environment presenting a gradient refractive index. The phenomenon of a water pool observed in a hot summer day can be explained by the fact that the air layer near the road has a higher temperature. Therefore, a thermal gradient is developed above the road. As a consequence, the refractive index, from n1 to n4 (Figure 4.2a) decreases from the height to the ground. The light trajectory is convex. The refraction angles are decreased to a small angle α then reflected. The water-pool observed is indeed a cloud reflected on the road. The ship appeared above the sea is explained with the same mechanism but the light trajectory is concave because the temperature near the sea is lower (Figure 4.2b).

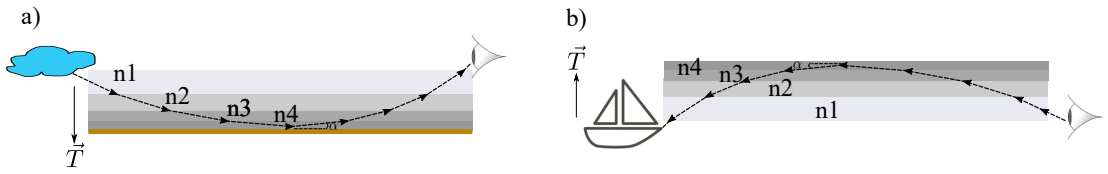

Figure 4.2: a) Illustration of light deviations in the "inferior" mirage: the light ray is convex due to a thermal gradient of heated air near the road; b) Illustration of a "superior" mirage: the light ray is concave due to a thermal gradient of cooled air on the sea

4.1.1.2 Introduction to heat waves

Heat wave is a term used to describe a natural convective air flow formed when there is a thermal gradient in an area (Jones *et al.*, 2018). If this air current passes through an object and a camera, it causes shimmering and/or deformed objects viewed by human eyes and/or a camera. The mechanism and characteristics of the heat waves is beyond our study. Nevertheless, in the first time, the heat wave are probably due to thermal convection instability which is developed by unstable temperature in a fluid, for example the air. The study of Zhao et al. on visual simulation of heat shimmering and the mirage showed that a shimmering object or background is caused by temperature variations from the heat source and the ambient air environment (Zhao *et al.*, 2006). In fluid mechanics, the local instabilities are found in the turbulent regime of convection flow (Incropera *et al.*, 2007 and Yuile *et al.*, 2018). The turbulent regime is characterized by the dimensionless Rayleigh number Ra which is superior to 10^9 ($Ra = \frac{g\beta(T_o - T_\infty)h^3}{\alpha\nu}$, where: g: is the acceleration due to gravity, β is the thermal expansion coefficient of th flow, T_o is the object's temperature, T_∞ is the environment temperature, h is the characteristic length of the object, α is the thermal diffusivity of the flow and ν is the kinematic viscosity of the flow (Delmas, 2012)). Therefore, heat waves may have the same characteristics as a turbulent natural convective flow.

4.1.1.3 Analytical solution for shape distortions caused by heat waves

In the short distance where a recorder (a camera or human eyes) is close to the object (less than 10 meters), heat waves cause distorted and/or shimmering objects. This physical phenomenon

was observed in a study of Delmas et al. (Delmas *et al.*, 2013). In Figure 4.3, the author shows the deformed circles viewed through a layer of heated air.

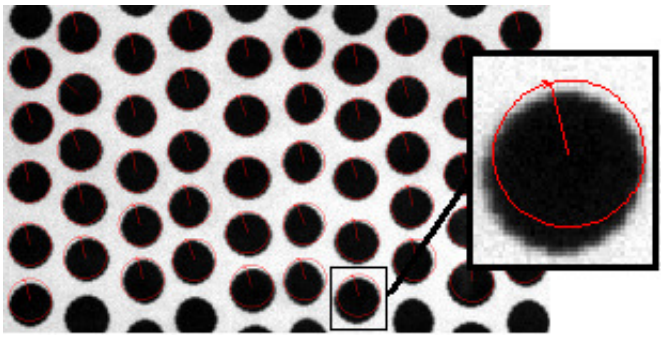

Figure 4.3: An example of shape distortions caused by heat waves: Discs distortion captured by a camera through a layer of heated air. The black disks are deformed compared with their initial shapes marked in red circles (Delmas, 2012)

The displacement or deformation of an object viewed by a camera can be quantified by an analytical model (Jones *et al.*, 2018). Figure 4.4 illustrates a light ray trajectory through hot air. We suppose that AB is an immobilized object that is captured by the camera. The light ray from point B goes straight, regardless of a hot air layer because the incident angle θ is 0°. This point is registered as point B' in the camera sensor. If there is no hot air between the object and the camera, the light ray from point A is registered as point A" on the camera sensor. The light ray trajectory is represented as the blue line in Figure 4.4. If the light ray passing through a hot air layer has a refractive index n <1 (n ≈ 1 is the refractive index of air at room temperature), it is bent (in red), then the point A on object is registered as the point A' on the camera sensor. Light deviation results in a "false" displacement or shape distortion between two images: one image is captured through hot air and the second is captured at ambient temperature.

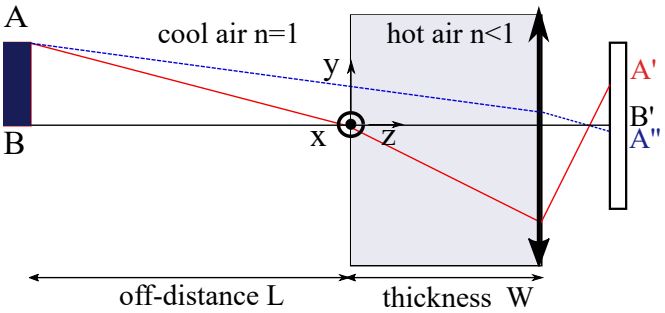

Figure 4.4: Schematic of a light ray through a hot air environment. The trajectories of the light ray through an hot air (in red) and through ambient air (in blue) (with and without passing hot air) show a displacement or a distortion of an object captured by camera through a heat wave (Jones *et al.*, 2018)

The in-plane displacement in two dimensions due to the mirage effect or heat waves is analytically calculated in studies of Jones et al. and Delmas et al. (Jones *et al.*, 2018 and Delmas, 2012). The displacements Δx, Δy in the Oxy plane (2D displacement or distortion) is calculated

by the Equations 4.3 and 4.4 (Jones *et al.*, 2018).

$$\Delta x = x_1 - x_o = (L+W)\frac{1}{n_o}\int_O^W \frac{dn}{dx}dz \tag{4.3}$$

$$\Delta y = y_1 - y_o = (L+W)\frac{1}{n_o}\int_O^W \frac{dn}{dy}dz \tag{4.4}$$

where:

- x_1, y_1 are the physical coordinates of the point P on the camera sensor, captured through a heat wave.
- x_o, y_o are the physical coordinate of the point P on the camera sensor, captured in ambient condition (there is no heat wave)
- L is the distance between an object and a heat wave
- W is the heat wave thickness.

By integrating the relationship between the refractive index and the temperature by the linear approximation (Equation 4.5), Equations 4.3 and 4.4 become Equations 4.6 and 4.7 (Jones *et al.*, 2018).

$$n = mT + n_o \tag{4.5}$$

where:

- n is the refractive index of air at temperature T
- $n_o = 1.00028$ is the refractive index of air at room temperature (25 °C)
- $m = -7.217 \times 10^{-7}\,°\mathrm{C}^{-1}$ is the coefficient of the linear Equation 4.5.

$$\Delta x = x_1 - x_o = (L+W)\frac{m}{n_o}\int_O^W \frac{dT}{dx}dz \tag{4.6}$$

$$\Delta y = y_1 - y_o = (L+W)\frac{m}{n_o}\int_O^W \frac{dT}{dy}dz \tag{4.7}$$

These two Equations 4.6 and 4.7 show that the displacement or shape distortion depends on:

- the thermal gradient dT/dx and dT/dy in two directions Ox and Oy. The shape distortion is more important in an environment presenting a high temperature gradient
- the distance object-hot air (L) and the heat wave layer (W)

The shape distortion due to a thermal gradient was confirmed in a study of Delmas et al. in three dimensions (Delmas *et al.*, 2013). Through experiments and numerical models (ray-tracing code and the model of laminar convection flow generated above a hot disk), the authors showed that the shape distortion is from the temperature gradient, which is from the natural convection between the hot disk and the surrounding environment.

4.1.2 Heat waves on measurements using the 2D-DIC method

4.1.2.1 Influence of heat waves on measurements using the 2D-DIC method

In physics, the shape distortion caused by heat waves is employed as the fundamental techniques for measuring physical parameters such as the air density, the thermal gradient field or calculating particle concentrations (Delmas, 2012). In experimental fluid mechanics, the BOS technique, which is widely used to measure and visualize the air velocity or air density, uses the mirage effect as the working principle (Mayinger *et al.*, 2001 and Raffel, 2015).

With the aim of using the 2D-DIC to measure displacement/strain of materials at high temperature, heat waves is not an advantage. The shape distortion due to heat waves can be mistaken as the mechanical displacement/strain of a specimen although it is not under load. In other words, a displacement or strain measured by the 2D-DIC method at high temperatures can be a "false" measurement. It is called a strain measurement error (Jones *et al.*, 2018).

The effect of heat waves on mechanical tests at high temperatures using the 2D-DIC method was found in different studies. Since the first use of the 2D-DIC method, Turner et al. and Lyons et al. showed the noisy displacement and strain fields while performing 2D-tensile tests on Inconel materials from 315 °C to 650 °C (Turner *et al.*, 1990 and Lyons *et al.*, 1996). The authors observed that some strain data points measured using the DIC method on stress-strain curves of materials at 650 °C were not in-line directly with the linear regression lines. The authors made attention to readers that heated air of the environment must be taken into precaution for High-Temperature Digital Image Correlation (HT-DIC). Studies of Pan et al. using an aerodynamic heating simulation system for high-temperature strain measurements (600 °C) confirmed the influence of heat waves on the mechanical strain of materials (B. Pan *et al.*, 2010b and B. Pan *et al.*, 2014). Novak et al. recorded a standard deviation (STD) of 20 µm in displacement and 1.1×10^{-4} in strain measurements at 800 °C (Novak *et al.*, 2011). Touboul et al. showed noisy stress-strain curves measured by DIC for mechanical tests of P91 steel at 625 °C in the elastic domain (Touboul *et al.*, 2013). Leplay et al., Berny et al. and Doitrand et al. also mentioned the influence of heat haze on small strain measurement in their study on creep behavior of ceramic at elevated temperatures (more than 1000 °C) (Leplay *et al.*, 2015, Berny *et al.*, 2018 and Doitrand *et al.*, 2020).

Table 4.1 summarizes recent the research on kinematic measurement errors using the 2D-DIC method and observations of heat waves on mechanical displacement/strain of materials. It is remarked that most research evaluates the effect of heat waves on displacement or strain measurements by using the standard deviation (STD σ) or the variation σ^2. In addition, the authors noticed that this effect becomes significant when the mechanical strain measurement is "small" (< 0.05 (Lemaitre *et al.*, 2020)), typically when measuring mechanical strains for identifying elastic parameter or measuring thermo-mechanical strains for identifying the thermal coefficient of materials. In this context, heat waves are considered as a "parasite" signal that can bias mechanical strains. Furthermore, strain or displacement measurement errors vary a lot, from one experiment to another. The effect of heat waves on mechanical strain measurements is still a challenge of the DIC method. To our knowledge, there is no complete study on the influence of heat waves on the displacement or strain measurement errors in a temperature range from 400 °C to 800 °C, the hot stamping temperatures.

Table 4.1: Studies on effect of heat waves on kinematic measurements at high temperature

Reference	Temp. (°C)	Aim of research	Measurements of DIC error in static conditions
Turner *et al.*, 1990	600	Develop the 2D-DIC method for tensile tests at HT	Displacement error: STD = 0.074 pixel
Lyons *et al.*, 1996	650 - 700	Develop the 2D-DIC method for tensile tests at HT	Strain variation 4×10^{-4} - 5×10^{-4}
B. Pan *et al.*, 2010b and B. Pan *et al.*, 2014	650	Develop new heating system and novel algorithm allowing strain measurement at HT	Measurement error in strain: STD = 3×10^{-3} - 5×10^{-3}
Orteu *et al.*, 2008	300-1000	Develop a method using 3D-shape measurement for 3D temperature map	Measurement error in strain: STD = 1.2×10^{-3}
Novak *et al.*, 2011	600	Measure strains for tensile tests using the 2D-DIC	Measurement error in strain: STD = 3×10^{-3} - 4×10^{-3}
Delmas *et al.*, 2013	700	Demonstrate the relationship of heat waves and shape distortion	Displacement error: 0.2 mm
Y. Wang *et al.*, 2013	200-450	Measure thermal expansion of a microelectronic material	Measurement error in strain:STD = 2×10^{-3}- 2.5×10^{-3}
Leplay *et al.*, 2015	1300	Measure small strain for creep behavior of ceramic	Error in displacement: STD = 0.13 pixel, in strain STD = 0.6×10^{-4}- 1.1×10^{-4}
Berny *et al.*, 2018	1000	Measure strain deflection on ceramic material	Displacement error: 4 pixels - 5 pixels
Yuile *et al.*, 2018	150	Model convection flow in furnace chamber tensile tests and its links with DIC measurement	Measurement error in strain: STD = 1×10^{-4} - 2.0×10^{-4}

4.1.2.2 Characterization methods for the natural convection flow

As presented in Section 4.1.1, the 2D-DIC measurement errors at high temperatures may be due the thermal instability developed in the turbulent convection flow. Therefore, methods to characterize the convection flow in fluid mechanics can be used to characterize the displacement/strain errors using the 2D-DIC method.

In experimental fluid mechanics, the instantaneous velocity field $\vec{V}(x,y)$ is defined as (Mayinger *et al.*, 2001):

$$\vec{V}(x,y) = \Delta\vec{s}/\Delta t \tag{4.8}$$

where: $\Delta\vec{s}$ is the vector of the measuring displacement and Δt is the time interval of the convection flow.

The relationship between the velocity field and the displacement field $U = [u(x,y)\ v(x,y)]^T$ can be deduced from the velocity field and written in Equation 4.9.

$$\begin{aligned} u(x,y) &= |\vec{V}(x,y)|_x \Delta t \\ v(x,y) &= |\vec{V}(x,y)|_y \Delta t \end{aligned} \tag{4.9}$$

where:

- $|\vec{V}(x,y)|_x$ and $|\vec{V}(x,y)|_y$ are the velocity values of the fluid in Ox and Oy direction
- Δt is the time interval between two consecutive images

The velocity of flow can be measured directly by one-shot measurement using anemometers or indirectly by local pressure, temperature or ultrasound measurement (Caré, 2013). The one-shot measurement methods have reasonable cost with high accuracy and they are still used in experimental fluid mechanics.

Nowadays, two-dimensional (2D) measurements are more employed because they give more information about velocity fields of the convective flow. The 2D-velocity fields can be measured by one of the three techniques: Laser Doppler Velocimetry (LDV), Particles Imaging Velocimetry (PIV) and Back-Oriented Schlieren (BOS) technique. In next paragraphs, we briefly present the working principle as well as the advantages and drawbacks of each technique.

Laser Doppler Velocimetry technique

The velocity of fluid particles (air or liquid) can be measured based on the Doppler effect (Delmas, 2012, Mayinger *et al.*, 2001). The velocity $\vec{V}(x,y)$ of the particles recorded in the flow made a shifting of a frequency f_D compared to its referent frequency f_0 (Mayinger *et al.*, 2001). This technique uses a laser beam split into two beams: the first one is used as the reference beam with frequency f_0 and the second one passes through the fluid having the velocity $\vec{V}(x,y)$. If there is no convection flow, two beams cross and interfere with each other to create fringes having a regular distance I, with frequency f_0. In case the second laser beam passes through the convective flow, the regular frequency is shifted in f_D, which is proportional to the fluid velocity (Equation 4.10) (Mayinger *et al.*, 2001).

$$f_D = \frac{2nsin(\theta/2)}{\lambda} V(x,y) \tag{4.10}$$

where:

- n: refractive index of the fluid
- θ angle between two laser beam
- $V(x,y)$ is the velocity (in amplitude value) of the flow in the directions perpendicular to the incident beam (in-plane velocity).

Particle Imaging Velocimetry techniques

The PIV technique is based on the time tracking of particles which are present in the fluid called tracer particles (Delmas, 2012). Images of tracer particles in the fluid at time t_1 and time t_2 are recorded. Their velocities are calculated by the autocorrelation function (Mayinger *et al.*, 2001). By supposing that the velocity of tracer particles is equal to the velocity of the fluid,

the instantaneous velocity $\vec{V}(x,y)$ of the fluid at time t is calculated by Equation 4.11 (Delmas, 2012).

$$|\vec{V}(x,y)| = \frac{|\Delta\vec{s}|}{\Delta t} \tag{4.11}$$

where: $|\Delta\vec{s}|$ is the amplitude value of displacements of tracer particles during an interval time $\Delta t = t_2 - t_1$ from two consecutive images.

The procedure of measuring fluid's velocity by the PIV technique is described as follows:

- First, tracer particles having the similar density with the fluid are introduced in the fluid
- A laser source (for example Nd:YAG laser with $\lambda = 532$ [nm]-double pulses) illuminates tracer particles with an time interval Δt to capture images at time t_1 and t_2. The laser beam is expanded in a form of a light sheet by a cylinder lens in order to measure the defined velocity field in the fluid.
- Images of tracer particles at time t_1 and t_2 are then recorded by a camera synchronized with the laser beam
- Tracer particles in images are tracked by the auto-correlation function in the Fourier domain to calculate their relative displacements then the fluid velocity.

Background-Oriented Schlieren technique

The BOS is one of optical density visualization techniques. Its principle is based on gradient refraction index (mirage effects) to measure the velocity of the natural convection flow (Raffel, 2015). This technique employs a background containing random dots (speckles) to calculate the displacement or deformation of speckle dots on the background then to deduce the fluid velocity by correlation algorithms. The BOS technique uses the local 2D-DIC algorithm for displacement or strain measurements in fluid based on thermal gradient in an area (Jones *et al.*, 2018).

The BOS technique is considered as an easy-to-use method to visualize and quantify the fluid velocity. Furthermore, it can be extended to 3D by adjusting the focus background plan. It is also a powerful method because it provides a robust and a good spatial resolution. Its precision is in the order of 2-3% of full scale depending on experimental set-up, the DIC algorithm and speckle sizes. The precision of the BOS technique is less than the PIV technique (precision of PIV is about 1%) (Mayinger *et al.*, 2001). The BOS technique presents a great potential as a flow visualization technique. It has widely been developed in recent years to improve its accuracy, spatial resolution and extend to 3D visualization of flow.

Synthesis
Table 4.2 lists the limits of detection, the precision, advantages and drawbacks of three techniques: LDV, PIV and BOS (Caré, 2013 and Raffel, 2015).

Table 4.2: Summary of the principle, accuracy, advantages and drawbacks of three techniques: LDV, PIV and BOS

Technique	LDV	PIV	BOS
Principle	Based on the Doppler effect	Time tracking of tracer particles and auto-correlation function	Gradient of refractive index and the 2D-DIC algorithm
Accuracy	0.5 %	1%	2-3%
Real-time measurements	Yes	Yes	Yes
3D visualization	Yes	Yes	Yes
Advantages	Accurate, a referent method in metrology	Applied in laboratory and industry	"Low cost" and easy to set-up
Drawbacks	Only a small volume of fluid is measured	Results depend on: size and density of tracer particles, signal-to-noise ratio	Results depend on experiment set up conditions and the 2D-DIC algorithm

4.1.3 Objective

Since the range of strain measurement errors of the 2D-DIC at high temperatures found in the literature (Table 4.1) is wide and the strain measurement errors may link with the characteristic of the convection flow, the objective of this chapter is to characterize the strain measurement errors of the 2D-DIC method in a temperature range of 400 °C to 800 °C in a specific environment, i.e., in a closing furnace. Strain measurement errors are measured at "isothermal" and "static" conditions by the BOS technique. They are supposed to be caused only by the gradient of air density between the object and the camera in the furnace. They are measured at different temperatures then used as a data library of the 2D-DIC errors at HT. The data library will be used in Chapter 5: Methods of correction to reduce the influence of heat waves on mechanical strains by the 2D-DIC method at high temperatures.

4.2 Methodology

4.2.1 Experimental set-up for characterization of the 2D-DIC measurement errors

4.2.1.1 Materials

The TA6V planar specimen was used in this study. The geometry of the specimen is presented in Appendix A.3. The ZOI for strain measurements, which was 15 ± 0.3 mm $\times$ 8 ± 0.3 mm, was used as the BOS background to characterize the 2D-DIC strain measurement errors (e_{xx} and e_{yy}). For strain measurement errors from 400 °C to 600 °C, speckles were created by the combining anodization and laser engraving (M5) technique (Figure 2.6). For strain measurement

errors at 700 °C and 750 °C, the speckle pattern was prepared by the painting technique using an air spraying high-temperature paint (Vitcas ® high-temperature white paint and Rust ® Oleum high-temperature black paint (Figure 2.16a) for the best contrast.

4.2.1.2 Testing configuration

Closing furnace for heating specimens

The temperatures for characterizing the strain measurement errors of the 2D-DIC method are in the hot stamping temperature range, which is from 400 °C to 750 °C. The strain measurement errors were measured at 400 °C, 500 °C, 600 °C, 700 °C and 750 °C under "isothermal" and "static" conditions.

The closing electrical-resistance furnace AET was used for heating specimen (Figure 4.5). It is cylindric with dimensions: 50 cm of high and 10 cm of large (internal diameter). The furnace has three heating zones and isolated by a ceramic material and glass wools. The temperature of the furnace is regularized by heat resistance positioned in three zones: upper (10 cm of high), middle (30 cm of high) and lower parts (10 cm of high) (Figure 4.5a). A small glass window (150 mm × 15 mm) on the furnace allows capturing images during experiments (Figure 4.5b).

TA6V samples were firstly heated to target temperatures with a heat rate of 10 °C/min and then maintained in 30 minutes for temperature stabilization. After 30 minutes, a thermal gradient of 2 °C, measured by three thermocouples (type K) implemented along the ZOI of the specimen was recorded. With the accuracy of thermal measurements, the temperature on the ZOI of the TA6V specimen was considered homogeneous and the "isothermal" condition was respected.

Testing machine used to maintain specimens in "static" condition at high temperatures

The testing machine MTS 125 and TestStar ® controller connected to a computer were employed in this study. The testing machine was used to hold the TA6V specimen and to ensure the "static" condition by maintaining a constant pre-load during the experiment. The specimen was gripped on the testing machine by a pin fixation system (Figure 4.5c). A pre-load of 0.1 kN was used to align the specimen, the glass window and the camera. Next, the specimen was heated to the target temperature. During the heating, the thermal dilatation was compensated thanks to the free sliding movement of the lower cross-head. A constant load of was 0.1 kN maintained during experiments for characterizing the strain measurement errors of 2D-DIC at HT.

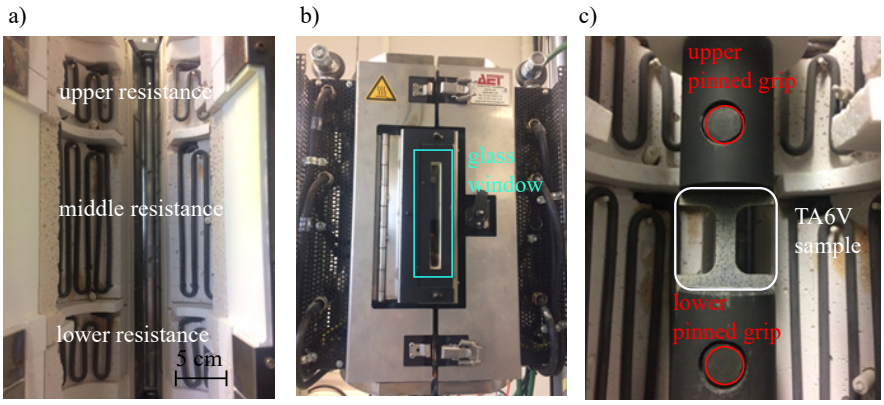

Figure 4.5: a) Three zones of heating: upper, middle and lower zones of the closing furnace; b) Overview of the AET furnace with a glass window of 150 mm of high and 15 mm of large; c) A TA6V specimen was mounted on the testing machine: the specimen was held by the upper-grip and maintained at a constant load of 0.1 kN by the lower-grip

To detect "parasites" signals such as vibrations of the testing machine or abnormal event that can occur during the BOS experiment, the load, the cross-head displacements and the displacement of the ZOI measured using the 2D-DIC method were registered in "isothermal" condition (once the specimen reached its target temperature) with a frequency of 1 Hz for more than 30 minutes.

4.2.1.3 2D-DIC experimental set-up

The 2D-DIC system was set-up in front of the furnace's glass window to capture images of the TA6V specimen. Details about the camera lens, camera sensor, aperture, lighting, distance between the camera and the specimen, magnification, software used for image capturing and strain calculation) were similar to those presented in chapter 2: Speckle preparation techniques at high temperatures (Table 2.3). It is noted that the distance between the object and the camera was 1.2 m, the magnification was 13.9 µm/pixels, the exposure time was from 4 ms to 19 ms for the best dynamic range of grey-levels. The software used for 2D-DIC strain measurements was VIC-2D®.

In chapter 3, the IR filter increases the contrast of images at high temperatures. Nevertheless, from 400 °C to 750 °C, according to the Plank's law, the radiation intensity of the specimen is still low (it is supposed that the emissivity of speckled specimen is equal to 1). Due to the narrow observation window of the closing furnace, the IR filter was not used in this study. In stead of using the IR filter and setting an exposure time of 120 ms, the contrast of image is adjusted by the exposure time such that the dynamic range of grey level is close to the configuration of using the IR filter.

4.2.1.4 Procedure for characterizing 2D-DIC strain measurement errors at HT by the BOS technique

The procedure of characterizing the strain measurement errors by the BOS technique is described as follows:

1. First, a TA6V specimen with speckles was set on the testing machine then loaded at 0.1 kN for the alignment of the specimen, the glass window and the camera.

2. The specimen was then heated with a heat rate of 10 °C/min to target temperature (about 1 hour) then maintained for 30 min for temperature stabilization. The specimen's thermal expansion was compensated by the free displacement of the lower cross-head of the tensile machine by maintaining a constant load of 0.1 kN. The load, displacement of cross-head were registered. Images on the ZOI of the specimen were captured with a frequency of 1 Hz. These three signals were synchronized thanks to an external synchronizer.

3. After 30 min of temperature stabilization, about 300 images of specimens were captured by the 2D-DIC camera system with an acquisition frequency of 5 Hz for 3 min in order to characterize strain measurement errors at HT due to heat waves at five temperatures: 400 °C, 500 °C, 600 °C, 700 °C and 750 °C. For each temperature, four tests were carried out for the repeatability. The 2D-map of strain uncertainties at different temperatures were then calculated by the commercial software VIC-2D® in which the subset size SS, step size ST and strain window SW were optimized by a Taguchi design of experiment (three factors-two levels BOS).

4.2.2 Design of experiments for optimization of 2D-DIC parameters

This study involves determining a set of 2D-DIC parameters (subset size (SS), step size (ST), strain window (SW)) to minimize the measurement errors (uncertainty) using the 2D-DIC method at room temperature. The uncertainty of 2D-DIC measurements at room temperature was characterized by the standard variation (STD) of strain. It can be optimized by choosing appropriate values of SS, ST and SW according to the theory the Virtual Strain Gage (VSG) (Reu, 2015d). In this theory, the strain is calculated from the displacement field and then smoothed by surrounding points (Figure 4.6) (Reu, 2015d).

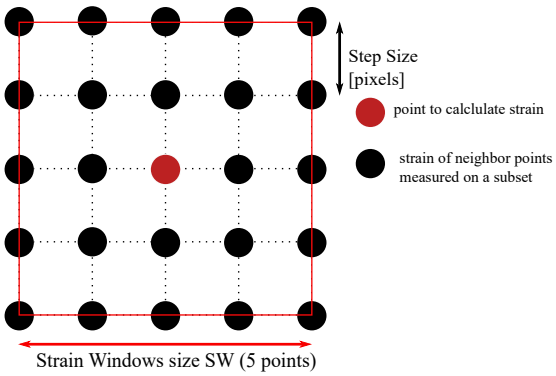

Figure 4.6: Illustration of the strain calculation from SS, ST and SW parameters

To choose a set of optimal 2D-DIC parameters (SS, ST and SW), first, the strain field was calculated between two speckled images at room temperature: the first one was the "referent" image (longitudinal strain $\varepsilon_{yy} = 0$ (Figure 4.7a) and the second one was the "deformed" image which corresponds to a longitudinal strain $\varepsilon_{yy} = 8 \times 10^{-3} - 10 \times 10^{-3}$ (Figure 4.7b). The profile of longitudinal strain ε_{yy} along the ZOI (black line in Figure 4.7c) of the specimen was extracted then used to calculate the standard deviation of longitudinal strain: STD ε_{yy}.

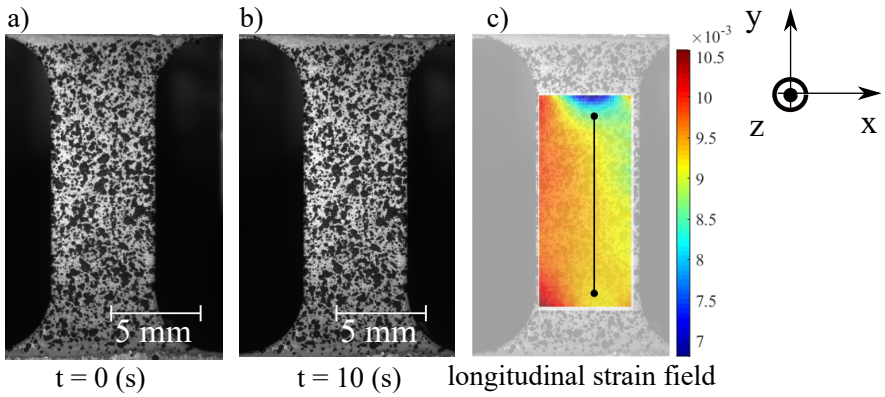

Figure 4.7: The ZOI of the TA6V specimen a) Initial image, b) deformed images, c) Longitudinal strain field ε_{yy} with "virtual strain gage"

Eight runs of experiments with different subset (SS), step size (ST) and strain window (SW) values were performed to determine the effect of three factors on the 2D-DIC uncertainty at 25 °C, evaluated by STD ε_{yy}. Eight runs of experiments were chosen by following a complete three-factor two-level DOE (Goupy *et al.*, 2006). Values of SS, ST and SW were chosen from

29 to 85 pixels, from 7 to 21 pixels and from 9 to 21 points, respectively. They corresponded to the minimum (-1) and maximum (+1) levels of three factors (Table 4.3). The SS was chosen based on the practical guideline of speckle pattern for DIC method: it must contain at least 3 speckle dots (Sutton *et al.*, 2009). Since the speckle radius made by painting was not uniform, the smallest value of the SS was 29 pixels and the highest one was 85 pixels. The ST was one third of SS and the SW was set according to values found in the study of Reu (Reu, 2015d). The response of the DOE was the STD ε_{yy} calculated from strains measured by a virtual strain gage (the black line) within the ZOI of the TA6V specimen (Figure 4.7c). The length of the inspected line ("virtual strain gage") was equivalent to a 15 mm basis of an electrical extensometer. Results were then analyzed by the analysis of variance to determine the influence of each factor on the uncertainty of strain measurements (STD ε_{yy}). Table 4.3 presents the eight runs of experiments with different levels of SS, ST and SW in the DOE.

Table 4.3: Eight runs of experiments in a design of experiments

N° exp.	Encoded values text			Experiment values		
	SS	ST	SW	SS	ST	SW
1	-1	-1	-1	29	7	9
2	-1	-1	+1	29	7	21
3	-1	+1	-1	29	21	9
4	-1	+1	+1	29	21	21
5	+1	-1	-1	85	7	9
6	+1	-1	+1	85	7	21
7	+1	+1	-1	85	21	9
8	+1	+1	+1	85	21	21

The final step is the optimization of 2D-DIC parameters (SS, ST and the SW values) to minimize the 2D-DIC strain uncertainty (minimize the STD ε_{yy}) at room temperature. From results on the analysis of variance, two influencing factors : SS and SW were chosen for the optimization. The SS and SW values belongs to ranges of [29 : 7 : 85] and [9 : 3 : 21] corresponding to the values between encoded levels [-1: 0.2 : +1] of two factors. The response surface (STD ε_{yy}) was plotted as a function of SS and SW to find a local minimum value and the SS, SW corresponding.

4.2.3 Characterization of strain measurement errors at HT

This study involves in characterizing the spatial and temporal strain measurement errors of the 2D-DIC method caused by heat waves in at different temperatures. In Section 4.2.1, the TA6V specimen was supposed to be "immobilized". Therefore, its mechanical strain should be null. Due to the influence of heat waves, strain measured using the 2D-DIC should be "false" strain, called strain measurement errors at HT. The method for characterizing strain measurement errors at HT was inspired by the study of Jones et al. (Jones *et al.*, 2018). The author used immobilized object and a heat source to characterize the convection flow between the camera and the hot object. The strain measurement error, if it is classified in random error, then it is characterized by strain uncertainty from the metrological point of view.

4.2.3.1 Spatial strain measurement errors

The effect of heat waves on spatial strain measurement errors was characterized by the heterogeneity of "false" strain fields measured on the ZOI of the TA6V specimen (background of the

BOS technique) at instantaneous moment (Equation 4.12). The heterogeneous "false" strain at temperature T was quantified by the difference of maximum "false" strain and minimum "false" strain over the ZOI in "isothermal" and "static" conditions (Equations 4.13). This difference was calculated by averaging the maximum and minimum strain errors of more than 300 images for representative value. It is noted also that "false" strain values at borders of the ZOI) were not taken into account because of the border effect (equivalent to 32 pixels).

$$\Delta e_{ij} = \mid \overline{e}_{ij}^{max} - \overline{e}_{ij}^{min} \mid, \quad i,j = x,y \tag{4.12}$$

where: $\overline{e_{ij}}^{min}$,$\overline{e_{ij}}^{max}$ are respectively the minimum "false" strain and the maximum "false" strain on the ZOI of the TA6V specimen, calculated by Equations 4.13 and 4.14 .

$$\overline{e}_{ij}^{min} = \frac{\sum_{k=1}^{N}[min(e_{ij}(m,n,k))]}{N} \quad i,j = x,y \tag{4.13}$$

$$\overline{e}_{ij}^{max} = \frac{\sum_{k=1}^{N}[max(e_{ij}(m,n,k))]}{N} \quad i,j = x,y \tag{4.14}$$

where:

- $e_{ij}(m,n,k)$ is the "false" strain at point $P(m,n)$ at image k
- N is the total images captured during the test (N $\geq$ 300 images).

4.2.3.2 Temporal strain measurement errors

To demonstrate the temporal measurement errors of the 2D-DIC method due to heat waves, strain measurement errors versus time of a random point, i.e., point P1 (Figure 4.8) on the ZOI were plotted. Afterward, strain measurement errors versus time at this point were computed by the Discrete Fourier Transformation (DFT) to find the regular heat waves period and calculate the magnitude of strain measurement errors (Jones *et al.*, 2018).

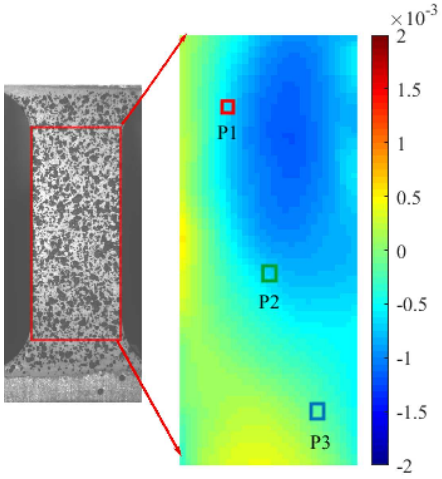

Figure 4.8: Three random points P1, P2 and P3 on the ZOI of the TA6V specimen used for measuring strain measurements errors

4.2.3.3 Spatio-temporal strain measurement errors

To show the spatial and temporal (spatio-temporal) characteristic of 2D-DIC strain measurement errors caused by air convection flow, first, three random points P1, P2 and P3 (Figure 4.8) as representative points on the ZOI were chosen to measure the strain uncertainty versus time.

In the previous section 4.1.1.3, we have presented that the shape distortion or shimmering object was from unstable thermal gradient in an area. The unstable thermal flow can be found in a turbulent flow whose characteristic (velocity) can be described by the normal distribution (Incropera *et al.*, 2007). Therefore, the strain measurement errors in space and in time can be characterized by a normal distribution.

Figure 4.9 presents the areas on which strain measurement errors (in longitudinal direction) were measured at 600 °C at time t_1, t_2, t_3, t_4... The ZOI was divided in sub-domains represented by the grid in Figure 4.9 (areas). The area had dimension of 327 pixels × 327 pixels. The size of area was equivalent to the spatial resolution of the DIC measurement with optimized 2D-DIC parameters: SS = [51-57] pixels, ST = [15-19] pixels, SW = 15 points. Strain measurement errors were far from each other to be significantly different from the metrology point of view. The strain uncertainty in each area was measured then plotted in normal distribution, for example in the Area 1 (Figure 4.10a) and in the Area 2 (Figure 4.10b). The strain measurement uncertainty for one temperature on the ZOI over the time was obtained by adding the normal distribution of all areas (Figure 4.11). Finally, for each temperature, the mean value (μ) and standard deviation (σ) were systematically calculated by the normal distribution fitting. The method was inspired from a study of Jones et al. in which the mean and standard deviation values of strains on the ZOI were calculated during a long-time capturing period (Jones *et al.*, 2018).

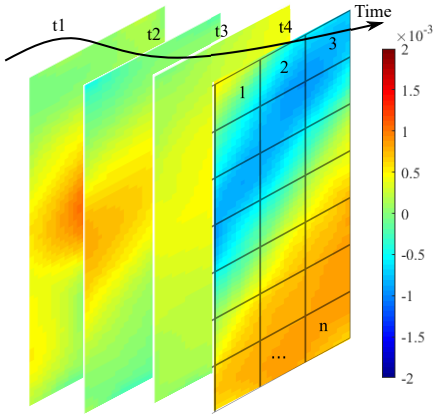

Figure 4.9: Areas on the ZOI and normal distribution of strain uncertainty over the time at 600 °C

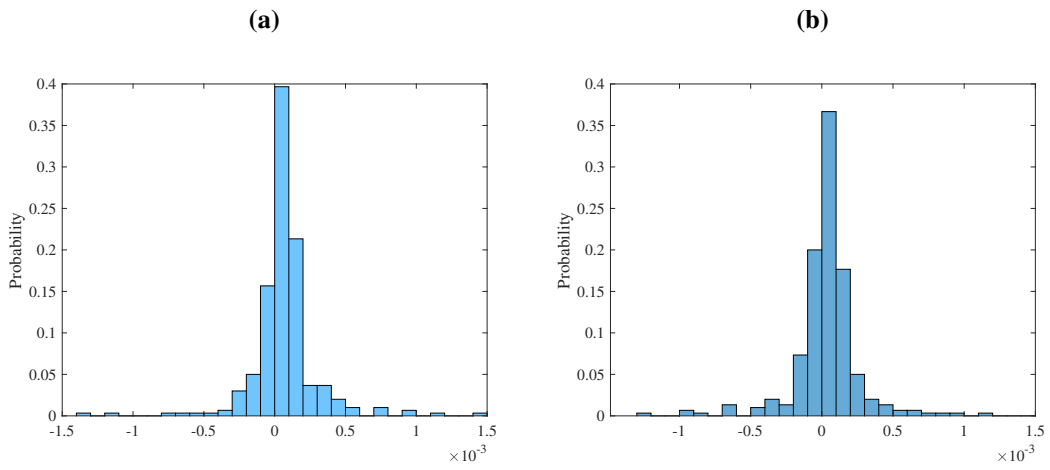

Figure 4.10: (a) Normal distribution of strain uncertainty on Area 1 in Figure 4.9 versus time at 600 °C, (b) Normal distribution of strain uncertainty on Area 2 Figure 4.9 versus time at 600 °C

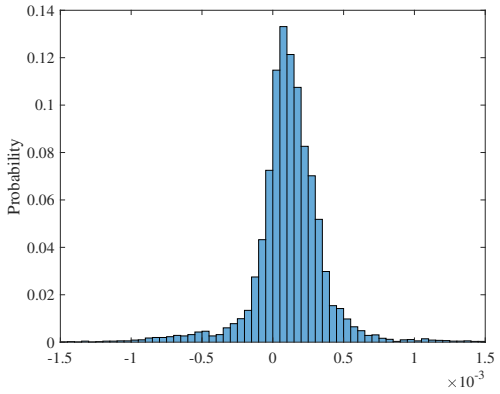

Figure 4.11: Normal distribution of strain uncertainty measured by adding the normal distribution of all areas over the ZOI in Figure 4.9 versus time at 600 °C

4.3 Results

4.3.1 Optimization of local 2D-DIC parameters for strain measurements

4.3.1.1 Influence of 2D-DIC parameters on strain measurement errors

This current study aims to find a set of 2D-DIC parameters (SS, ST, SW) to minimize the 2D-DIC uncertainty (STD ε_{yy}). The influence of each factor is evaluated from the three-factor two-level design of experiments (Table 4.4). It is noticed that the 2D-DIC strain uncertainty using the high values of SS and ST (Exp. 6 and 8) is better than the other runs of experiments.

Table 4.4: Eight runs of experiments and results on the strain uncertainty in the DOE

N° exp.	Encoded values text			Experimental values			Results
	SS	ST	SW	SS	ST	SW	STD ε_{yy}
1	-1	-1	-1	29	7	9	1.3×10^{-3}
2	-1	-1	+1	29	7	21	3.116×10^{-4}
3	-1	+1	-1	29	21	9	3.498×10^{-4}
4	-1	+1	+1	29	21	21	1.405×10^{-4}
5	+1	-1	-1	85	7	9	2.178×10^{-4}
6	+1	-1	+1	85	7	21	1.208×10^{-4}
7	+1	+1	-1	85	21	9	2.182×10^{-4}
8	+1	+1	+1	85	21	21	1.026×10^{-4}

The longitudinal strains ε_{yy} which were measured by the Virtual Strain Gage using the 2D-DIC method are presented in Figure 4.12. The strain profiles of the inspected line with variable parameters: SS, ST and SW are presented in two groups. The first group corresponds to the longitudinal strain ε_{yy} profile of four runs of experiment using a SS of 29 pixels (Figure 4.12a). The second group corresponds to the four others runs using a SS of 85 pixels (Figure 4.12b).

In the first group (Figure 4.12a), three of four strain curves (the violet, the blue, and the orange curves) present discontinuities in strain profiles. The discontinuous strain measurement means a disruption in correlation that should be avoided. It occurs when a large ST and a small SW are used. Only the strain curve corresponds to a small ST and a large SW (the yellow curve) does not present any disruption of strain measurements because the searching region is sufficiently covered. However, it presents local variations that induces an important value of STD ε_{yy}.

In the second group (Figure 4.12b), no strain discontinuities are detected and strains measured vary slightly, from 8.7×10^{-3} to 9.5×10^{-3}. Strain curves with the same value of SW (SW = 21 or SW = 9) are similar whatever the ST values are. The strain uncertainty is therefore independent of the ST. It is explained by the fact that a large subset size increases the accuracy of the searching region. Strain curves with larger SW are smoother than the ones with small SW. In conclusion, strain curves with parameters: SS = 85 pixels, ST = 21 pixels, SW = 21 points or SS = 85 pixels, ST = 9 pixels, SW = 21 points give the smallest strain uncertainty.

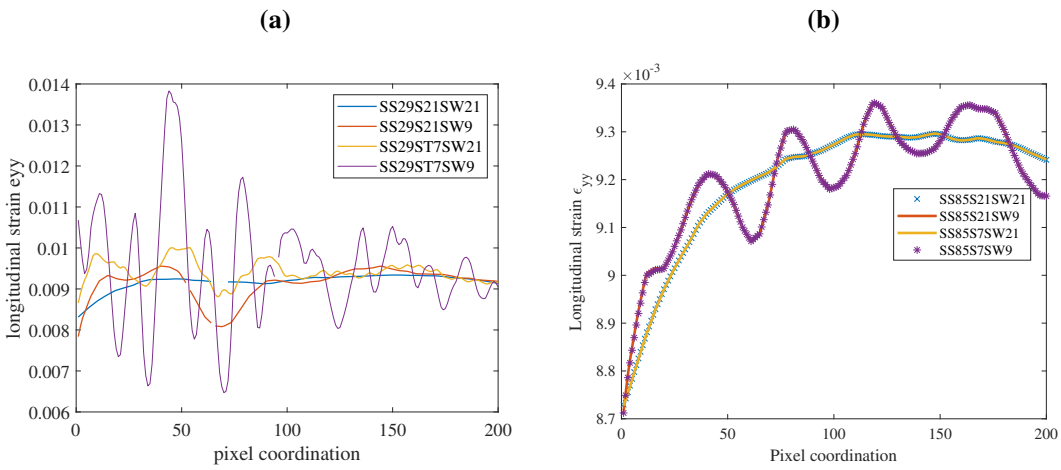

Figure 4.12: (a) Longitudinal strain ε_{yy} profiles corresponding to four runs of experiment using a SS of 29 pixels, (b) Longitudinal strain ε_{yy} profiles corresponding to four runs of experiment using a SS of 85 pixels

The analysis of variance on the results obtained from the design of experiments shows that three factors (SS, ST and SW) and their interactions have significant influences on the strain uncertainty STD ε_{yy}. The contribution of the 2D-DIC parameters and interactions is described in the Pareto diagram (Figure 4.13). As can be seen, the SS and ST have similar impact on the uncertainty of strain measurement (26% for SS and 25% for ST). The strain window SW has only 15% of effect on the uncertainty of strain measurements. The interactions between SS $\times$ SW and SS $\times$ ST contribute nearly 10% to the uncertainty of strain measurements. Therefore, SS and ST have the most significant impacts (about 25%) on the strain uncertainty while the other interactions or factor have less effect on results.

The coefficients of each factor and interactions (the interaction is limited at second degree) determined from the analysis of variance can be expressed by Equations 4.15.

$$\begin{aligned} STD\varepsilon_{yy} = 10^{-4} \times (3.42 - 1.82 \times SS - 1.78 \times ST + 1.41 \times SW \\ +1.22SS \times ST + 0.97ST \times SW - 0.97SW \times ST) \end{aligned} \tag{4.15}$$

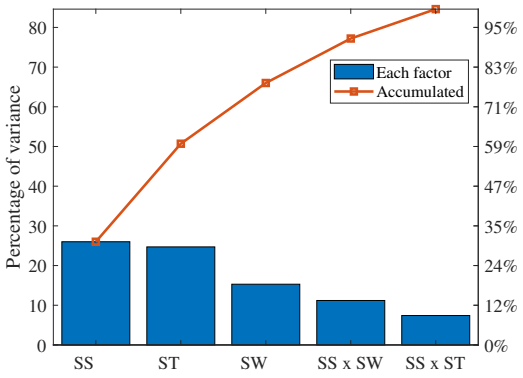

Figure 4.13: Pareto diagram on the contribution of the 2D-DIC factors (SS, ST and SW) and interactions on strain uncertainty at room temperature

Figure 4.14a and Figure 4.14b present respectively two interactions: the first one is between the SS and SW and the second one is between the SS and ST. Two figures show the same tendency: for a small subset (noted as Subset 1 in Figure 4.14), a large strain window (noted as Strain Window 2 in Figure 4.14) or a large step size (noted as step 2 in Figure 4.14) reduces the standard variation of strain measurements (STD ε_{yy}). However, when the subset size is large enough, the effect of strain window size is less important. A large subset size always reduces the uncertainty of strain measurements.

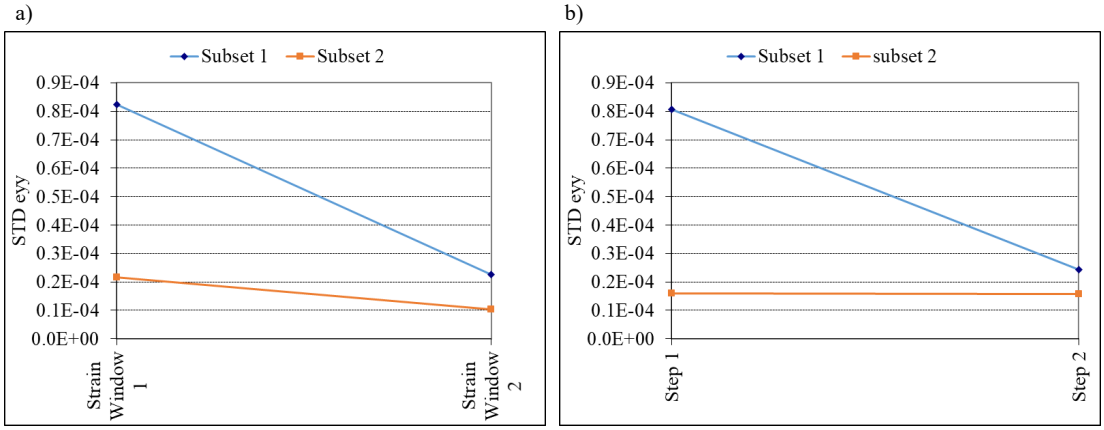

Figure 4.14: (a) Interaction of subset size and strain: STD ε_{yy} (mean value) versus two levels of subset SS and strain window SW; (b) Interaction of subset size and steps: STD ε_{yy} (mean value) versus two levels of SS and ST

4.3.1.2 Optimization of the 2D-DIC parameters

Figure 4.15 presents the optimization surface in three dimension (Figure 4.15a) and iso-contour values of strain uncertainty (Figure 4.15b) as a function of subset size SS and strain window size SW. The strain uncertainty is calculated from Equation 4.15 with SS range of [29 : 7 : 85] and SW range of [9 : 3 : 21]. Figure 4.15 shows that strain uncertainties decrease with an increase of subset size and strain window size. The STD ε_{yy} decreases rapidly by order of two when SS and SW size increase from 29 to 43 pixels and from 9 to 12 pixels, respectively. The STD ε_{yy} decreases slowly if the subset size and strain window size increase from 57 to 85 pixels and 15

to 21 pixels. However, STD ε_{yy} does not present minimal local. For an experimenter, a large subset and large strain window are recommended, but the choice of subset and strain window size is limited by the spatial resolution, defined by Equation 4.16 (Reu, 2015d).

$$SR\,[pixels] = [(SW-1)ST] + SS \tag{4.16}$$

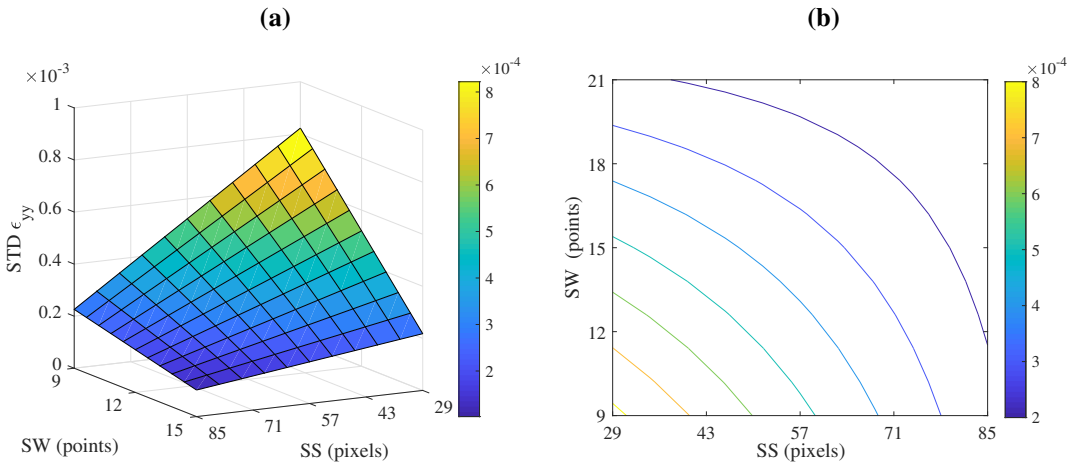

Figure 4.15: (a) 3D-surface response (STD ε_{yy}) as a function of SS and SW parameters, (b) Iso-contour of STD ε_{yy} as a function of SS and SW parameters

In our study, we are interested in elastic parameters of the TA6V material. The strain field is supposed to be homogeneous. Therefore, very high spatial resolution is not necessary in our study. The 2D-DIC parameters chosen are: SS = [51 - 57] pixels, ST = [15 - 19] pixels and SW = [15 - 19] points. The spatial resolution is thereby from 200 pixels to 300 pixels.

4.3.2 Characterization of strain measurement errors at HT

4.3.2.1 Evaluation of static and isothermal conditions for characterizing the 2D-DIC strain measurement errors at HT

The "isothermal" condition of specimens in the closing furnace used for experiments are verified by measuring the temperature of the TA6V specimen by thermocouples (type K). After 2 hours of heating to target temperature, a thermal gradient of 2 °C along the longitudinal length of specimen (15 mm) was recorded. The temperature of the specimen is therefore considered homogeneous during the experiments.

The "static" condition is evaluated by plotting: i) the constant load of 0.1 kN versus time, ii) the displacement of the lower cross-head of testing machine and iii) the averaged strain on the ZOI of specimen measured using the 2D-DIC method versus time (during 30 min) in the isothermal condition. These signals are systematically evaluated for every target temperature. In particular, three signals are measured with attention at 600 °C, 700 °C and 750 °C because from 600 °C, the stiffness of the TA6V specimen decreases rapidly due to the reduction of the Young's modulus of the TA6V material with temperatures (Vanderhasten, 2007). The material risks of being deformed under a small load.

Appendix C.1 presents in detail results on the evaluation of the "static" condition for characterizing the strain measurement errors by the BOS technique. The results are summarized as follows: in the "isothermal" thermal condition, the mechanical load remains constant. Nevertheless, "small" displacements of the cross-head of the testing machine, which is equivalent to the displacement (in average) of the TA6V specimen at 700 °C and 750 °C are recorded. These displacements increase with temperatures. They are about 0.15 mm at 700 °C and 0.25 mm at 750 °C.

Furthermore, the averaged strains on the ZOI measured using the 2D-DIC show that strains increase linearly with time. The strain rates are determined. They are $4 \times 10^{-6}\ s^{-1}$ at 700 °C and $8 \times 10^{-6}\ s^{-1}$ at 750 °C. The displacements of the TA6V specimen at 700 °C and 750 °C in "static" and "isothermal" condition are not fully investigated but it can be explained by the decrease of material stiffness at high temperatures and the load applied on the specimen (0.1 kN). It is reminded that the TA6V specimen was prepared from thin sheets and at high temperatures, so the TA6V material might have creep behavior under a constant load. To our knowledge, no study on creep behavior of material under a load of 0.1 kN was found in the bibliography.

From these observations above, conditions for characterizing the strain measurement errors by the BOS technique are supposed to be isothermal and static ("isothermal" and "static"). Strain measurement errors are random errors due to heat waves. Furthermore, with a short capturing period (no more than 3 min), the mechanical strain is considered neglected compared with strain measurement errors due to heat waves. The "reference" image is chosen at high temperatures in "isothermal " and "static" conditions at the beginning of each experiment tests.

4.3.2.2 Spatial strain measurement errors

The influence of heat waves due to convection flow is characterized by the heterogeneity of strain field in the closing furnace in "static" condition (Figure 4.16 and Figure 4.17) at different temperatures.

It is seen that strain measurement errors in two directions (transversal Ox and longitudinal Oy) increase with temperatures. The "false" strain map at room temperature is nearly homogeneous in two directions. The strain measurement error is less than 2×10^{-4} in absolute value. From 400 °C to 700 °C, "false" strain fields in two directions are not uniform with a presence of the positive "false" strain (expansion) region (in red) and the negative "false" strain (compression) region (in green or blue) (Figure 4.16 and Figure 4.17). The positive and negative "false" strain regions correspond to shape distortions due to different air densities of the convection flow.

On each "false" strain field measured using the 2D-DIC method, the maximum and minimum values of strain are identified. The spatial train measurement error at different temperature is measured by the difference (in average) (Equation 4.12) between the maximum strain (Equation 4.13) and the minimum of "false" strain (Equation 4.14) (Figure 4.16 and Figure 4.17).

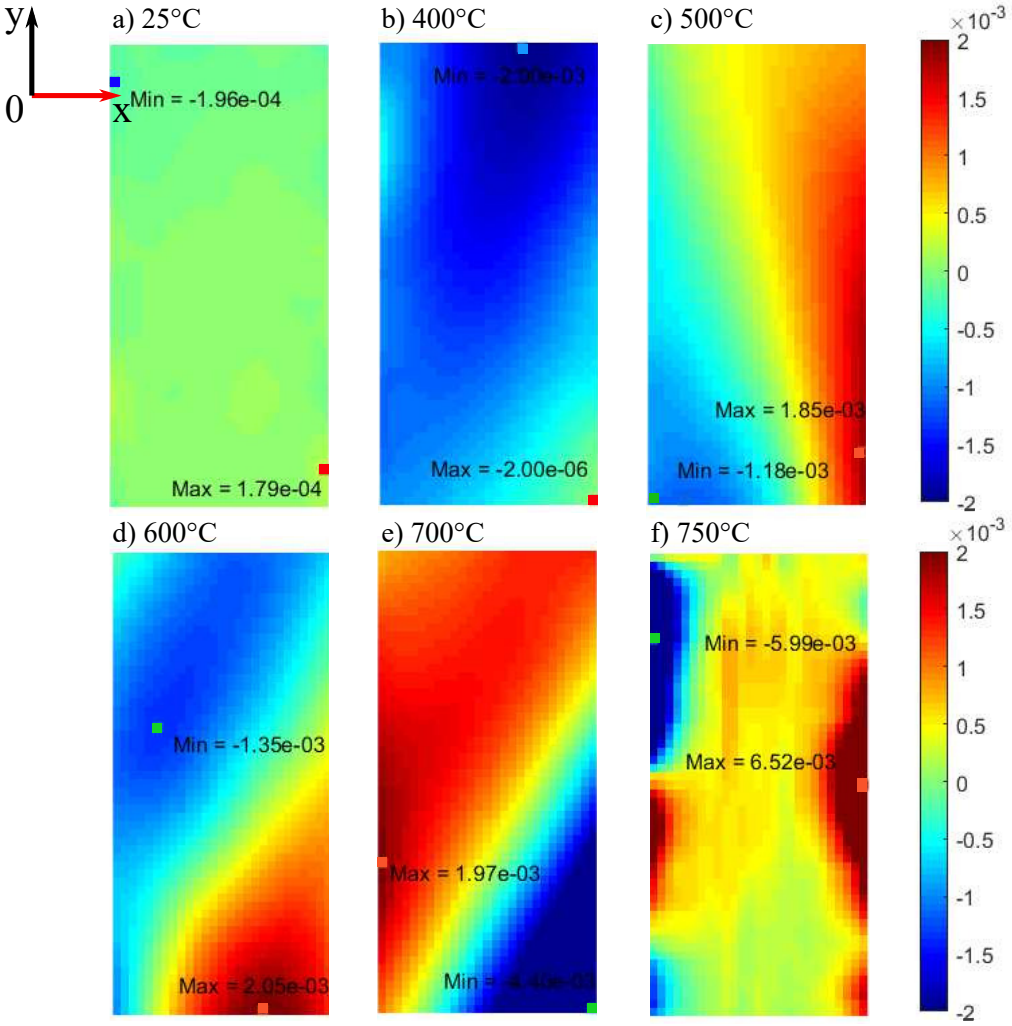

Figure 4.16: Transversal strain measurement errors (e_{xx}) at an instantaneous time t at different temperatures: a) room temperature, b) 400 °C, c) 500 °C, d) 600 °C, e) 700 °C and f) 750 °C. For each temperature the minimum and maximum values of "false" strain are indicated

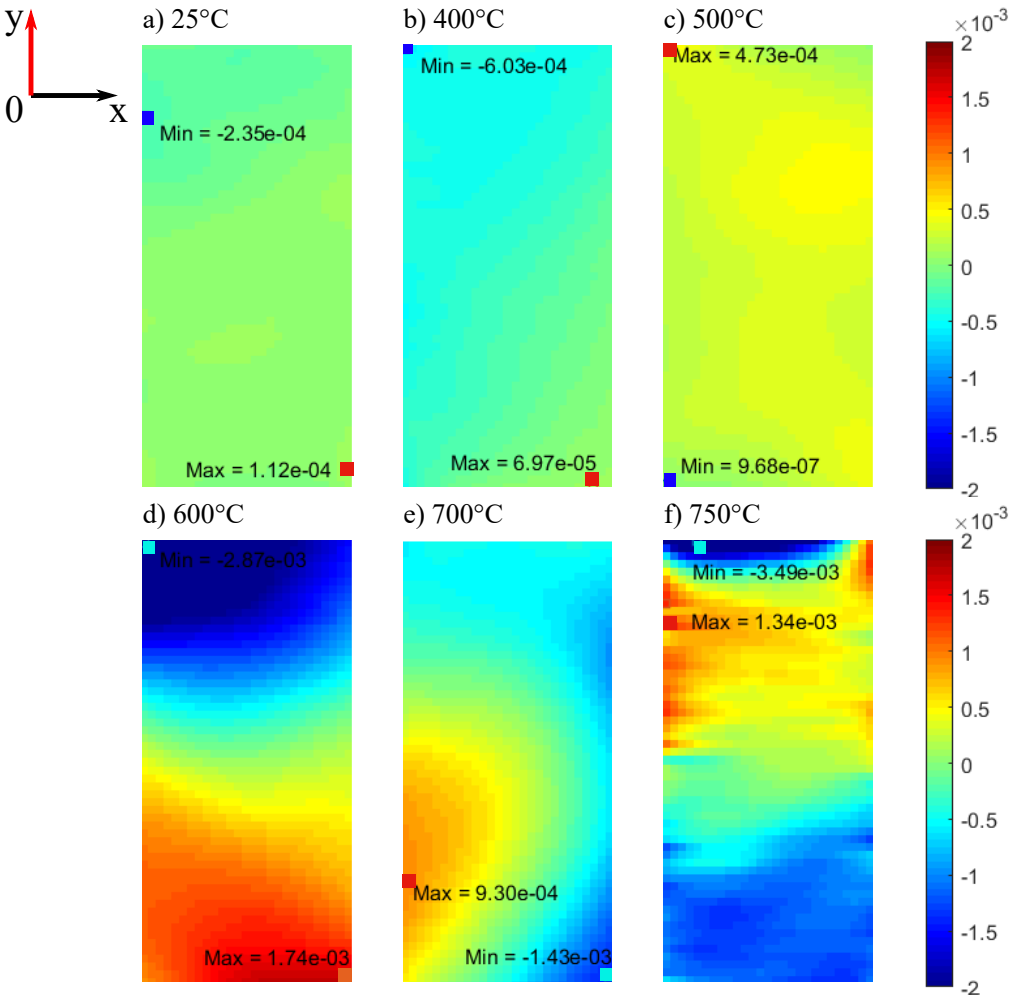

Figure 4.17: Longitudinal strain measurement errors (e_{yy}) at an instantaneous time t at: a) room temperature, b) 400 °C, c) 500 °C, d) 600 °C, e) 700 °C and f) 750 °C. For each temperature, the minimum and maximum values of "false" strain are indicated

Figure 4.18 presents the strain heterogeneity (Equation 4.12) due to heat waves in two directions: Ox (in blue) and Oy (in orange). It shows that globally, the strain heterogeneity increases with temperatures. At room temperature, the spatial strain measurement errors, characterized by the the strain heterogeneity is from 1×10^{-4} to 2×10^{-4}. At 400 °C and above, this value is four times higher, showing the influence of heat disturbances on strain measurements using the 2D-DIC method at HT. Furthermore, from 25 °C to 600 °C, the spatial strain measurement error in the transversal direction e_{xx} is likely more than the longitudinal one. It increases rapidly from 400 °C to 600 °C. Notably, the order of magnitude of spatial strain measurement errors at 500 °C and 600 °C is 2×10^{-3} and 3×10^{-3}, which is within the mechanical elastic strain of materials. The spatial strain measurement error in the longitudinal direction e_{yy}, however, increase slowly with temperature from 400 °C to 600 °C then suddenly rise rapidly at 700 °C and 750 °C. It is surprising that strain errors in the longitudinal direction are more important than those in the transversal direction. It might be linked to the turbulent character of the convection flow in the closing furnace.

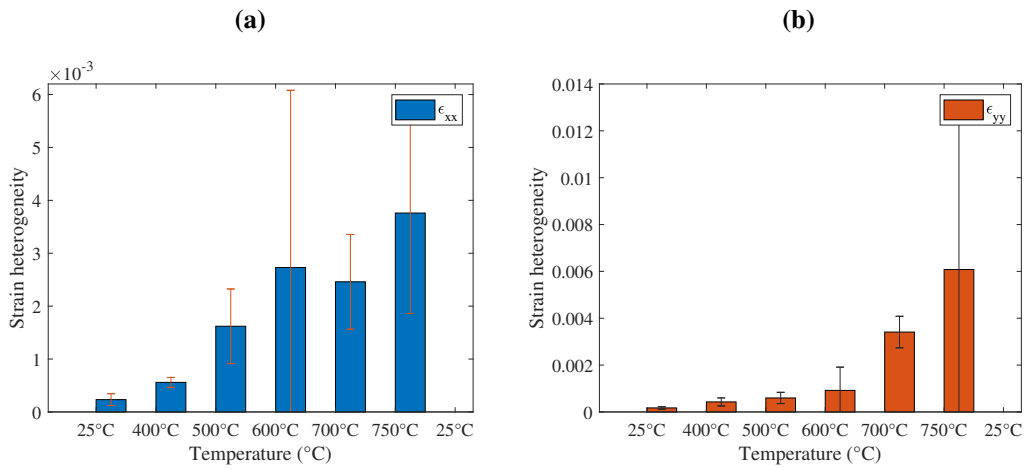

Figure 4.18: Strain heterogeneity measured at different temperatures: a) in transversal direction, b) in longitudinal direction

Table 4.5 summarizes the strain heterogeneity (the average and the STD values) measured at different temperatures. It is clearly that at 25 °C, the spatial strain measurement errors are within 2×10^{-4}. However, these values rises with temperatures. From 400 °C and above, these values are more than 2×10^{-3}, which are in the same order of magnitude of mechanical "strain" measured by the 2D-DIC. Especially, at 750 °C, the longitudinal strain measurement error is 6×10^{-3}, which is three times higher than the mechanical strain in which the elastic property of materials, i.e., the Young's modulus is determined.

Table 4.5: 2D-DIC spatial strain heterogeneity at different temperature

Temperature	Δe_{xx}	Δe_{yy}
25 °C	2.33×10^{-4}	1.72×10^{-4}
400 °C	6.59×10^{-4}	4.2×10^{-4}
500 °C	2.7×10^{-3}	6.0×10^{-4}
600 °C	2.73×10^{-3}	9.11×10^{-4}
700 °C	2.46×10^{-3}	3.41×10^{-3}
750 °C	3.75×10^{-3}	6.08×10^{-3}

4.3.2.3 Temporal strain measurement errors

Temporal strain measurement errors in time domain

The temporal strain measurement error is characterized by time variation of "false" strains at a representative point P1 (Figure 4.8) on the ZOI of the TA6V specimen. Figure 4.19 presents time variations of strain error of point P1, a random point on the ZOI of the TA6V specimen at room temperature. The variation is small, from -5×10^{-5} - 5×10^{-5} in both two directions. The mean values of strain uncertainty are close to 0 with small fluctuations correspond to noise at room temperature.

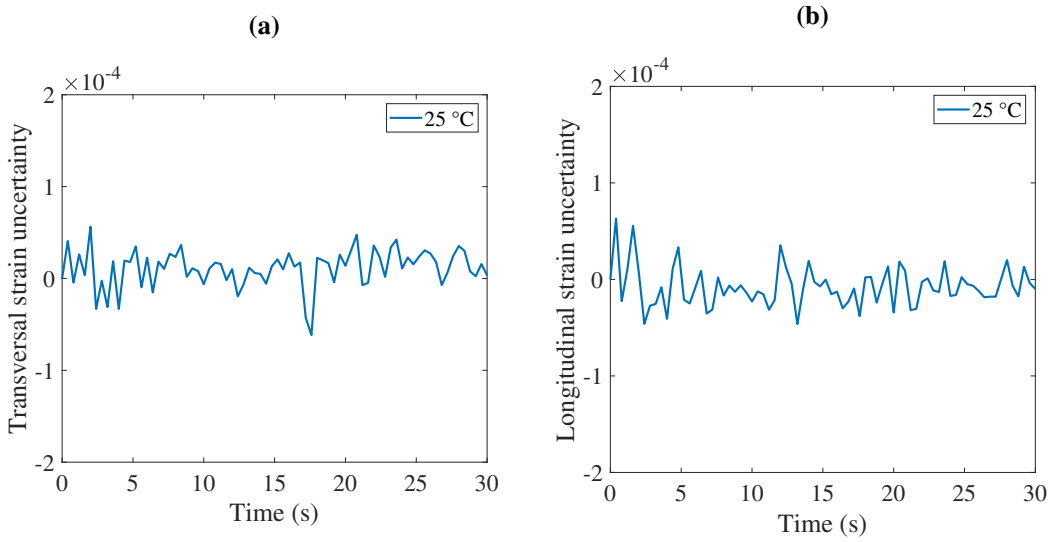

Figure 4.19: (a) Transversal strain measurement error e_{xx}, (b) longitudinal strain measurement error e_{yy} at 25 °C

Figures 4.20 and 4.21 present strain measurement errors of point P1 (Figure 4.18) versus time at various temperatures. It is seen that these errors are random with the presence of low and high strain measurement errors (peaks and valleys). The temporal strain measurement errors increase with temperatures because high strain values (in absolute value) appear more frequently. These peaks and valleys correspond to "false" strain measured when heat waves pass in front of the camera. Heat waves cause important shape distortions. From 400 °C to 600 °C, transversal strain measurement errors are higher than the longitudinal one. It is interesting that at 750 °C, the longitudinal strain measurement error is higher than the transversal ones. These results has the same tendency with the spatial strain measurement errors obtained in Figure 4.18.

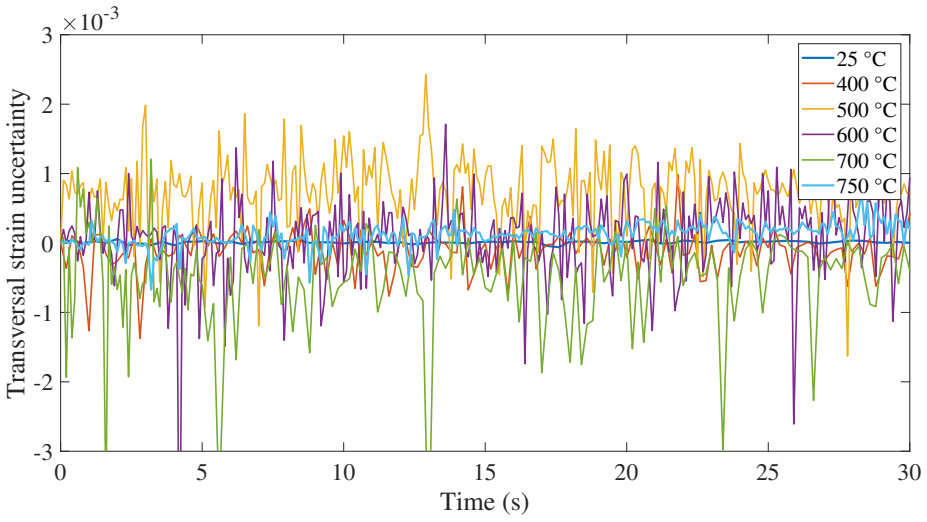

Figure 4.20: Transversal strain measurement errors e_{xx} from 400 °C to 750 °C

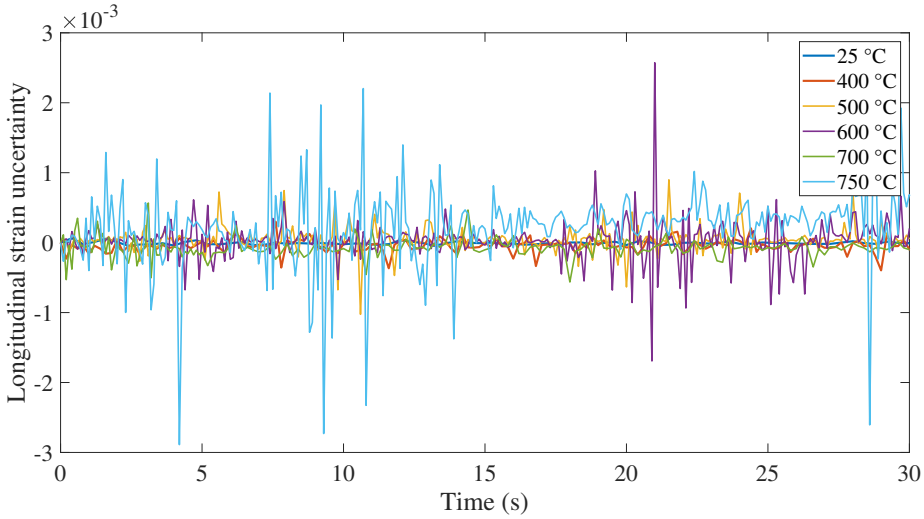

Figure 4.21: Longitudinal strain measurement errors e_{yy} from 400 °C to 750 °C

Temporal strain measurement errors in frequency domain

The Fourier Transformation of temporal strain errors measured at point P1 (Figure 4.8) at different temperatures is presented in Figure 4.22 (at 25 °C) and Figure 4.23 (from 400 °C to 750 °C).

In Figure 4.22, the amplitudes of the temporal strain uncertainty of point P1 in transversal (Figure 4.22a) and longitudinal direction (Figure 4.22b) are plotted versus frequency. The spectra are composed by the mean value of strain measurement errors at frequency f = 0 Hz and other higher values at higher frequencies. The mean values of strain measurement error is found at frequency f = 0 Hz. This mean value is nearly 1×10^{-5} at room temperature. Others values of the strain uncertainty at higher frequencies are low, from 2×10^{-6} to 5×10^{-6}, which correspond to floor noise at room temperature.

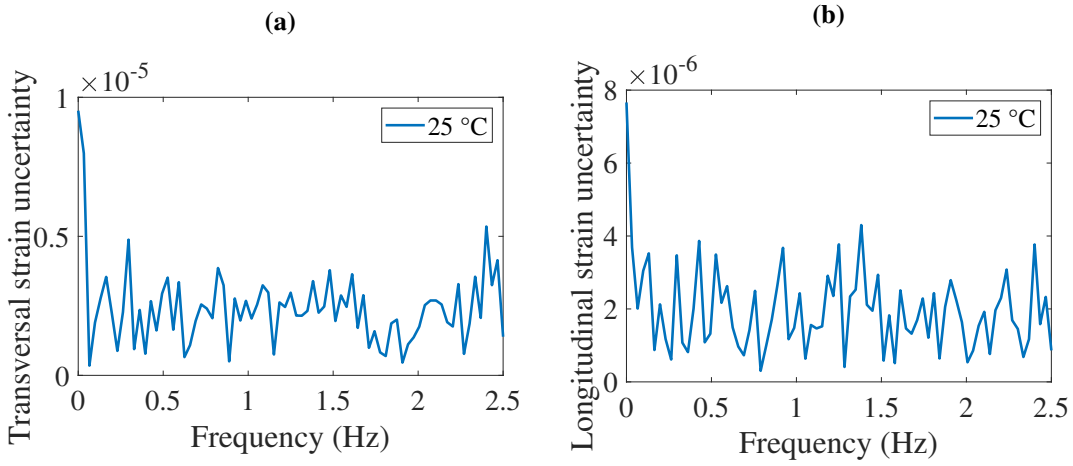

Figure 4.22: (a) Transversal strain measurement errors e_{xx}; (b) Longitudinal strain measurement error e_{yy} at 25 °C in frequency domain

At high temperatures, the mean of strain measurement errors determined at f = 0 Hz are from 1×10^{-4} to 8×10^{-4}, which are higher than those at room temperature (Figure 4.23). The mean values increase with temperatures. This tendency confirms the influence of convection flow to 2D-DIC strain measurements at HT by using the 2D-DIC. At higher frequencies, although some regular peaks (maximal "false" strain measurement errors) and valleys ("minimum" strain measurement errors) are visually observed in the strain uncertainty versus time curves (Figure 4.20 and 4.21), no peaks at a higher frequency that correspond to a frequency of the convection flow are found (Figure 4.23). Therefore, the frequency of heat waves causing strain measurement errors is difficult to detect in the frequency domain.

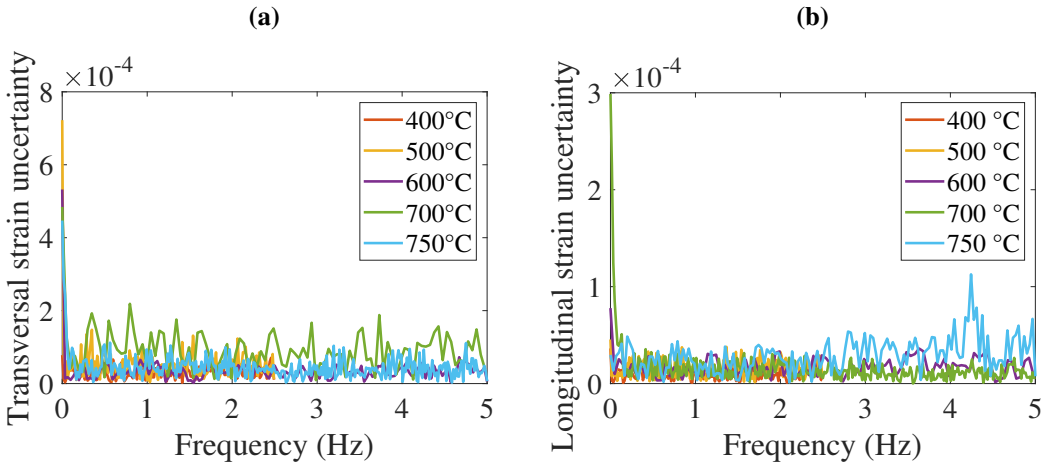

Figure 4.23: (a) Transversal strain measurement errors e_{xx}; (b) Longitudinal strain measurement errors e_{yy} from 400 °C to 750 °C in frequency domain

In conclusion, the analysis of strain measurement errors versus time at a representative point on the ZOI of the TA6V specimen shows the strain uncertainty generally increases with temperatures. In particular, from 600 °C to 750 °C, strain measurement errors increase rapidly, probably due to the emergence of the turbulent flow in the furnace. Furthermore, more regular variations of strain measurement errors appear when the temperature in the furnace increases. However, no frequency corresponding to regular fluctuations is found in the frequency domain by DFT.

4.3.2.4 Spatio-temporal strain measurement errors at HT

Graphical presentation of the spatio-temporal characteristic of strain measurement errors at HT

The spatio-temporal characteristic of the convection flow at different temperatures is presented by the time variation of strain uncertainty measured at three random points P1, P2, and P3 (Figure 4.8) on the ZOI of the specimen.

At 25 °C (Figure 4.24), a small difference of less than 2×10^{-5} of "false" strain measured at three points at an instantaneous time t is observed, meaning the spatial variation of strain measurement errors at room temperature is low. Variation of strain measurement errors versus time is from -1×10^{-4} to 1×10^{-4}. This order of magnitude corresponds to strain uncertainty (Figure 4.24) at room temperature due to noise.

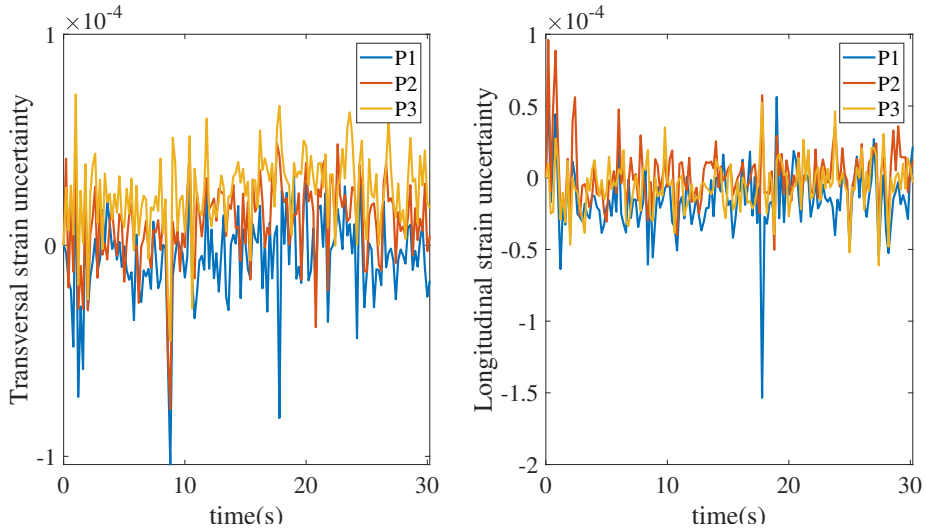

Figure 4.24: Time variations of strain uncertainty in the transversal direction and the longitudinal direction at 25 °C

At higher temperatures, for example at 700 °C (Figure 4.25), there is an important difference (about 2×10^{-4}) in measurement errors at three different points P1, P2, and P3 (Figure 4.8) on the ZOI of the specimen. The strain measurement errors at point P1, P2 and P3 vary in time and in space. Therefore, the strain measurement errors using the 2D-DIC at high temperatures might have both spatial and temporal characteristic (spatio-temporal characteristic).

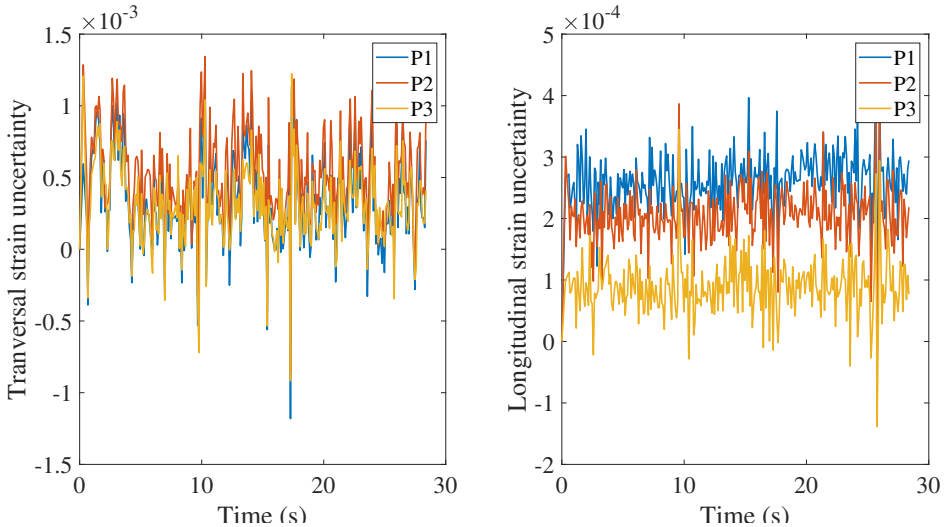

Figure 4.25: Time variations of strain uncertainty in the transversal direction and the longitudinal direction at 700 °C

Normalized histogram of strain measurement errors at HT

The distribution of strain measurement errors at 25 °C (Figure 4.26) shows at room temperature, the errors principally range from -1×10^{-4} to 1×10^{-4}. Their distributions are in the form of a normality curve (Gaussian law). The mean values μ are close to zero. The STD σ are less than

1×10^{-4}. The longitudinal strain measurement error is lower the transversal one (2.78×10^{-5} versus 4.32×10^{-5}, respectively).

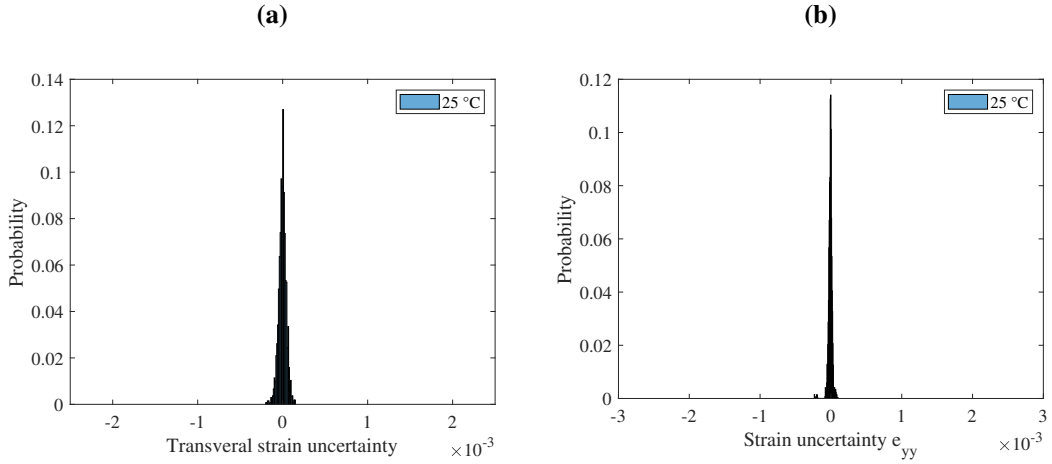

Figure 4.26: Distribution of strain uncertainty measured at 25 °C: a) in transversal direction, b) in longitudinal direction

The distribution of strain measurement errors at temperatures ranged from 400 °C to 750 °C are presented in the Appendix C.2. The distribution of the strain uncertainty at 750 °C (Figure 4.27) is ranged from 0 to 2×10^{-3}, nearly 10 times higher than in the one measured at room temperature. Strain uncertainties at higher temperatures (from 400 °C to 750 °C) are much higher than those at 25 °C.

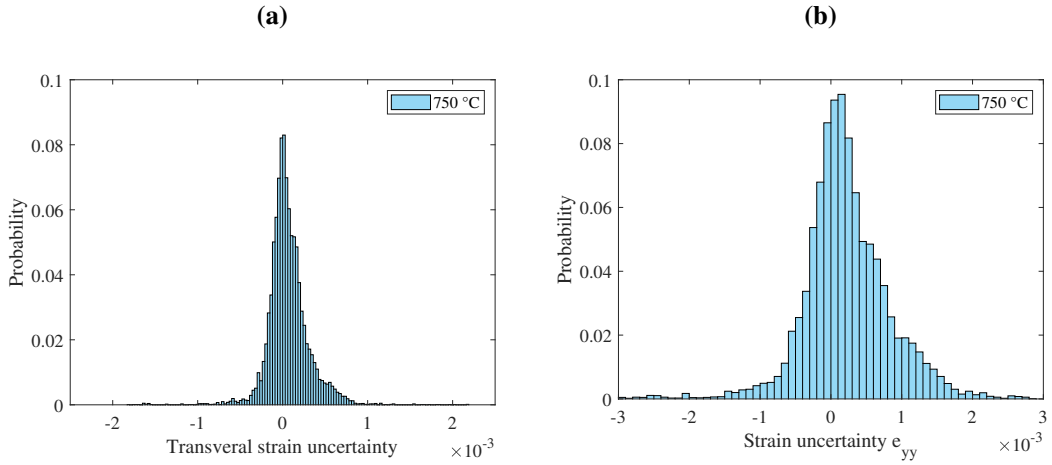

Figure 4.27: Distribution of strain uncertainty measured at 750 °C: a) in transversal direction, b) in longitudinal direction

The STD σ of strain measurement errors $\sigma_{e_{xx}}$ and $\sigma_{e_{yy}}$ (Section 4.2.3.3) are systematically calculated from the distribution of strain measurement errors for each temperature. For each temperature, strain measurement errors are repeated four times for the reproducibility. Results of $\sigma_{e_{xx}}$ and $\sigma_{e_{yy}}$ are presented in Figure 4.28a for transversal strain measurement errors and in Figure 4.28b for longitudinal strain measurement errors.

First, it is observed that at 25 °C, the difference between the $\sigma_{e_{xx}}$ and $\sigma_{e_{yy}}$ from four tests is only about 5×10^{-5}. This difference is about 2×10^{-4} at 400 °C and about 2.5×10^{-4} at 500 °C. The STD of strain measurement errors from four tests are quite similar for temperatures from 25 °C to 500 °C. However, the difference of the $\sigma_{e_{xx}}$ and $\sigma_{e_{yy}}$ from four tests at 600 °C and at 750 °C is more than 2.0×10^{-3}. This difference at 700 °C is an exception (only 4.0×10^{-4}). Therefore, results on the characterization of the strain measurement errors from four tests at 600 °C and at 750 °C are not repeatable.

Furthermore, the STD of strain measurements errors increases with temperatures. It is about 2×10^{-5} at 25 °C and about 3.0×10^{-3} at 750 °C (test 4 in longitudinal direction, Figure 4.28b). The STD of strain measurements errors of two directions are not similar. From 23 °C to 600 °C, the variation (STD) of strain measurements errors in the transversal direction is higher than that in longitudinal direction (Figure 4.28). However, at 750 °C, this variation in the longitudinal direction is higher than the transversal one.

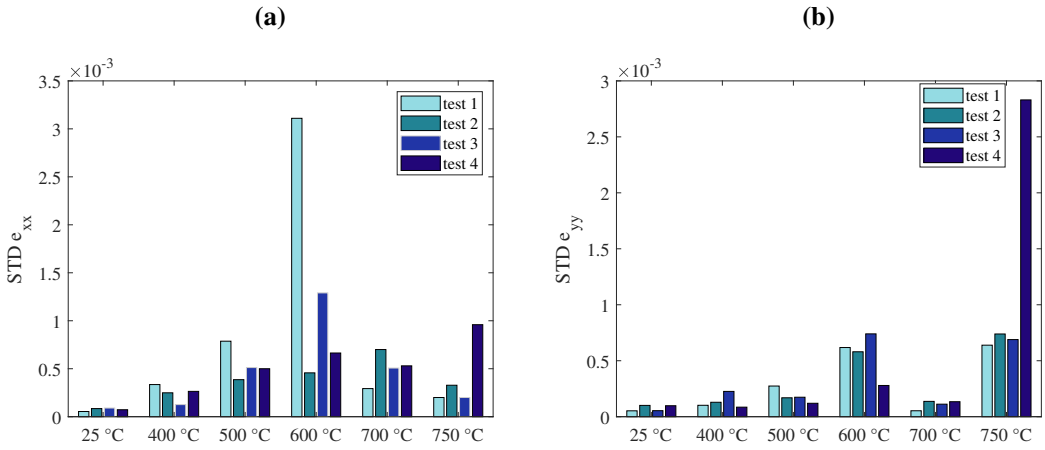

Figure 4.28: (a) STD of the transversal strain measurement errors, (b) STD of the longitudinal strain measurement errors in four experiments from 25 °C to 750 °C

The spatio-temporal characteristic of the strain uncertainty is calculated by normal distribution histogram. The mean values and the standard deviation σ of spatio-temporal measurement errors are summarized in Table 4.6. It is seen that the mean value of strain measurement errors from 400 °C to 750 °C in two directions Ox and Oy are nearly 5×10^{-4}. The mean value at 600 °C are exceptional (1.5×10^{-3} in transversal direction and 4.5×10^{-3} in longitudinal direction). The STD of strain measurement errors for each temperature is higher than its mean value, especially at 750 °C in the longitudinal direction ($\sigma_{e_{xx}}$ is 1.2×10^{-3}).

Table 4.6: 2D-DIC spatio-temporal strain uncertainties at different temperature

Temperature	$\overline{e_{xx}} \pm \sigma_{e_{xx}}$	$\overline{e_{yy}} \pm \sigma_{e_{yy}}$
25 °C	$-3.9 \times 10^{-5} \pm 9.02 \times 10^{-5}$	$-1.65 \times 10^{-4} \pm 5.39 \times 10^{-5}$
400 °C	$1.62 \times 10^{-4} \pm 2.44 \times 10^{-4}$	$-1.34 \times 10^{-4} \pm 1.36 \times 10^{-4}$
500 °C	$4.97 \times 10^{-4} \pm 5.46 \times 10^{-4}$	$8.15 \times 10^{-5} \pm 1.85 \times 10^{-4}$
600 °C	$1.48 \times 10^{-3} \pm 1.24 \times 10^{-3}$	$4.15 \times 10^{-3} \pm 4.83 \times 10^{-4}$
700 °C	$1.11 \times 10^{-4} \pm 5.08 \times 10^{-4}$	$6.86 \times 10^{-5} \pm 1.08 \times 10^{-4}$
750 °C	$7.74 \times 10^{-5} \pm 4.22 \times 10^{-4}$	$-3.83 \times 10^{-4} \pm 1.22 \times 10^{-3}$

In conclusion, results on 2D-DIC strain measurement errors at HT, characterized by the BOS technique in the "isothermal" and "static" conditions show the link between the temperature and 2D-DIC measurement errors. The spatio-temporal characteristic of strain measurement errors shows from room temperature to 400 °C (Figure 4.28), the strain measurement errors are probably due to the temporal variations of strain measurement errors. The strain measurement errors in four tests are quite repeatable. At higher temperature, for example at 600 °C and 750 °C, measurement errors are probably from both spatial and the temporal variations of measurement errors. Furthermore, measurements errors (strain uncertainties) at 600 °C and 750 °C are not repeatable (Figure 4.28). This tendency may link to the convection flow in the furnace at from 600 °C and above becomes more turbulent than lower temperatures (at 400 °C and 500 °C).

4.4 Discussions

4.4.1 Optimization of local 2D-DIC parameters at room temperature (RT)

In section 4.3.1, the effect of DIC parameters: subset size (SS), step size (ST) and strain window (SW) on the strain uncertainty is investigated. According to Haddadi et al., errors from three parameters are linked to the 2D-DIC algorithm (Haddadi *et al.*, 2008). These three parameters can cause random errors or systematic errors in strain measurement. For an uniform and "small" strain, DIC errors are mainly random ones, which is characterized by the strain uncertainty via the standard deviation (STD) parameter (Yaofeng *et al.*, 2007).

Influence of the subset size and the strain window size on strain uncertainty
Regarding the influence of the subset size on the strain uncertainty, results obtained by Figure 4.12 show a large subset size decreases the random error. For a same speckle size, a large subset contains more speckle features that improve the accuracy of the correlation process. Results are in agreement with the studies of Sutton et al. and Haddadi et al. (Sutton *et al.*, 2009 and Haddadi *et al.*, 2008). Yaofeng et al. suggests a lower limit of subset size is set for a uniform deformation (Yaofeng *et al.*, 2007). Our results confirm the important effect of the subset size on the strain uncertainty. The subset size is chosen based on the speckle size. It is recommended to be three times larger than the speckle size (Sutton *et al.*, 2009) and five times larger than the feature size (speckle radius) (Wigger *et al.*, 2018).

Furthermore, Figure 4.14a also shows the interaction between the subset and strain window. According to the Virtual Strain Gage theory (Reu, 2015d), the strain window generally plays a role in smoothing noise and reducing the uncertainty of strains. Our study shows that in a small subset regime, the role of the strain window in reducing noise is more significant than

in a large subset regime. It can be explained by a higher accuracy in the displacement field when a larger subset size is chosen because the strain field (in small mechanical strain, less than 2×10^{-3}) is calculated approximately from the first order derivative of the displacement field. A less displacement uncertainty induces a less strain uncertainty and vice versa.

Influence of the step size on strain uncertainty
According to the 2D-DIC principle, the step size is related to the overlapped area where the correlation is performed. In other words, a smaller step size means a larger overlapped area being re-searched; therefore, it is more time-consuming. According to Wang et al., a smaller step size increases the strain accuracy because of a higher data density (Y. Wang *et al.*, 2012). Nevertheless, it increases the strain uncertainty because noise from displacement is involved. Our results obtained in Figure 4.14b show the interaction between the step size and subset size. If the subset size is small, smaller step size induces more noise (higher STD ε_{xx}). If the subset size is sufficiently large, the step size does not affect the uncertainty of measurements: The standard deviation of strain measured by 2D-DIC is similar regardless of the step size and strain size window. Results are in line with a study of Wigger et al. on the effects of step size on the strain uncertainty under zero load (Wigger *et al.*, 2018).

Optimization of the 2D-DIC parameters
The Virtual Strain Gage (VSG) allows to evaluate the strain uncertainties, which depends on 2D-DIC parameters (SS, ST and SW). In practice, the VSG theory helps an mechanical experimenter to estimate the spatial strain resolution of a measurement. The spatial strain resolution should be also balanced with the strain uncertainty. These two parameters should be carefully studied for each mechanical test configuration. In our study, since we are working in the homogeneous mechanical strain (the elastic regime of materials), the strain uncertainty is expected to be minimum. An optimization of DIC parameters is therefore processed. A set of "optimal" DIC parameters (SS, ST and SW) is also found. There is no local minimum point on the optimized surface response, meaning that large subset and strain window sizes are recommended. In our study, to observe the strain measurement errors due to convection flow, a SS = [51 - 63] pixels, ST = [15 - 19] pixels and a strain SW = [15 - 19] points are chosen. However, the spatial resolution is quite low, at least 200 pixels. The strain uncertainty linked with experiment set-up is between 5×10^{-5} - 1×10^{-4} which is close to the results in a study of Jones et al. and Triconnet et al. (Jones *et al.*, 2018 and Triconnet *et al.*, 2009).

Through a statistical approach (DOE) (Tables 4.3 and 4.3), our study confirms the influence of the subset size, step size and strain window on the uncertainty of strain measurements obtained by the 2D-DIC method. A large subset, step size and strain windows are preferred for the lowest strain uncertainty. Results are in agreement with the study of Wang et al. (Y. Wang *et al.*, 2016). Our study suggest a practical method: the design of experiment, another approach to rapidly evaluate the effect of the 2D-DIC parameters on the strain uncertainty. However, our study is limited in evaluating the strain uncertainty (random error). Other sources, which may cause bias errors, for example from speckles, interpolation function, subset shape function are supposed to be negligible. It would be interesting to consider the influence of 2D-DIC parameters on the accuracy of strain measurements.

4.4.2 Spatio-temporal characteristic of 2D-DIC strain measurement errors at HT

Spatial strain measurement errors at HT

In section 4.3.2, results on the strain measurement errors by the BOS technique showed a non-uniform strain fields on the ZOI of TA6V specimen at high temperatures (Figure 4.16 and 4.17). Furthermore, a significant difference in strain uncertainty at high temperatures compared with the one measured at room temperature are observed (Figure 4.18). Our results confirm the influences of heat waves that were observed in many previous studies, for example, the study of Jones et al. at 150 °C and other authors, for instance, Novak et al., Lyons et al., Berny et al., and Doitrand et al., (Novak *et al.*, 2011, Lyons *et al.*, 1996, Berny *et al.*, 2018, Doitrand *et al.*, 2020, Jones *et al.*, 2018).

The results show that the spatial strain measurement errors (mean values from four tests of experiment which are presented in Figure 4.18) generally increases with temperatures which are probably linked with an increase of local gradient of air density. This link is demonstrated by Delmas et al. by both experimental and numerical methods (Delmas *et al.*, 2013 and Yuile *et al.*, 2018). The interesting point is, from 400 °C to 600 °C, the strain measurement errors in transversal direction are higher than those in longitudinal direction. From 700 °C to 750 °C, strain uncertainties in longitudinal direction are higher than those in transversal direction. Strain uncertainties increase rapidly from 600 °C to 750 °C. With limited access and equipment in our experiments, it is impossible to explain these observations. To our knowledge, there are no publications studying heat exchange mechanism in a closing furnace and its influence on the strain measurement errors by the 2D-DIC method. However, a simple heat exchange model between the specimen's temperature and air temperature of the closing furnace can encourage us for further study. The numerical model should take into the heat exchange by convection and radiation heat exchange mechanism. Results from the convecto-radiative model could explain the strain measurement error versus temperature tendency that is observed thanks to the BOS technique.

Temporal strain measurement errors at HT

Besides the spatial characteristic, the strain measurement errors also present the temporal characteristic. It is shown that the temporal strain uncertainty generally increase with temperatures, except strain measurement errors at 700 °C (Figure 4.20 and 4.21). The temporal strain measured on a point on the ZOI of TA6V specimen presents peaks (the highest measurement errors) and valleys (the lowest measurement errors) corresponding to the heat waves passing through the camera and the specimen. These peaks are more and more frequent at higher temperatures, especially at 600 °C and 750 °C. Although time variations of these peaks and valleys seem regular, no evidence of heat waves frequencies are found in the frequency domain. They might be masked by peaks from the noise base of room temperature. The results are quite similar to a study of Jones et al. on the influence of heat waves on DIC measurements at 150 °C (Jones *et al.*, 2018). The authors observed regular variations by plotting the strain of a subset center versus time and concluded that heat waves frequencies are within 50 Hz. In a study on measuring creep strain of ceramic materials at 1200 °C, Berny et al. also observed peaks with high strain (Berny *et al.*, 2018).

Spatio-temporal strain measurement errors at HT

Because of spatial and temporal characteristics, spatio-temporal strain measurement errors can be classified as a random error and/or bias error (Reu, 2016). The characteristic of measurement errors (random or bias) from heat waves is still in discussion. The analysis on the spatio-temporal

strain measurement errors shows that below 500 °C, the strain uncertainty measured in four experiment is reproducible. The order of magnitude is small (less than 7×10^{-4}) (Figure 4.28a). However, from 600 °C and above, strain measurement error becomes non-repeatable (Figure 4.28b). In addition, above 600 °C, strain measurement errors are probably due to the spatial variations and temporal variations. This can be explained by the fact that at higher temperature, the convection flow becomes more turbulent. Air density in the turbulent flow becomes more heterogeneous in space and in time.

The order magnitude of spatio-temporal strain measurement errors depends on temperatures: the values (the sum of the mean and the σ) are from 6.4×10^{-4} at 400 °C to 3.5×10^{-3} at 700 °C (Table 4.6). As far as we know, strain measurement errors is in the same order of magnitude compared with previous studies. For example, Lyons et al. found a standard deviation of strain STD e_{xx} of 4×10^{-4} or STD e_{yy} of 5×10^{-4} at temperatures of 600 °C and 700 °C (Lyons *et al.*, 1996). Pan et al. found the STD e_{xx} increases from 10^{-4} to 5×10^{-3} from 100 °C to 600 °C but the STD e_{yy} rises more slowly, from 10^{-4} to 10^{-3} (B. Pan *et al.*, 2014). Leplay et al. observed a strain uncertainty of 4×10^{-3} due to heat waves at 1200 °C (Leplay *et al.*, 2015). Finally, a STD of strain measurement errors equal to 1.2×10^{-3} is noticed in a study of Orteu et al. at 700 °C (Orteu *et al.*, 2008). The strain measurement errors found in literature are quite variable, which depends on experiment conditions. The results obtained from this study contributes to the data library of strain measurement errors at high temperatures due to heat waves.

In conclusion, our study presents the influence of heat waves in the closing furnace on the 2D-DIC measurement errors at high temperatures, which is only observed and still a challenging research theme in the 2D-DIC method. The study also suggests the heat waves have spatio-temporal characteristic for temperatures ranging from 400 °C to 800 °C, which has not been investigated before. The spatio-temporal characteristic of strain measurement errors is in agreement with a study of Jones et al. at a lower temperature (at 150 °C) and with a study of Berny et al. at higher temperature (about 1000 °C) (Jones *et al.*, 2018 and Berny *et al.*, 2018). However, values of strain measurement errors seem related to both the air movement in the closing furnace and also the specimen geometry. Convection flow might be different when the sample or furnace is changed. Further studies should focus on an experimental method to visualize of the convection flow in the furnace.

4.5 Conclusion and perspectives

In this chapter, mirage effects and their influence on kinematic measurements in experimental mechanics are presented. Mirage effects or heat waves due to thermal gradient induce "false" strain or "false" displacement measured by the 2D-DIC. The "false strain" due to heat waves is supposed to cause only random errors. It is therefore measured by the strain uncertainty and characterized by the BOS technique in the testing furnace in which the background is the ZOI of the TA6V specimen. During the experiments, the specimen is maintained at "isothermal" and "static" conditions.

Before characterizing strain uncertainties caused by heat waves, optimized 2D-DIC parameters with a subset size = [51 - 57] pixels, a step size = [15 -19] pixels and a strain window = [15 - 19] points are chosen to minimize the strain uncertainty at room temperature. The 2D-DIC strain uncertainties at high temperatures are compared with the ones at room temperature.

Results show the spatial strain measurement errors, measured by the strain heterogeneity (Equation 4.12) rise with temperatures. The order of magnitude is approximately calculated (in average values) presented in Table 4.5. It is from $2.3 \times 10^{-4} \pm 1.7 \times 10^{-4}$ at 25 °C to $3.7 \times 10^{-3} \pm 6.1 \times 10^{-3}$.

The temporal strain uncertainty is shown by the presence of some regular peaks and valleys corresponding to heat waves passing in front of the camera. Peaks or valleys are more frequent at higher temperatures. However, frequencies of heat waves are not detected in the frequency domain.

The spatio-temporal strain measurement errors are calculated by a normal distribution histogram in which "false" strain are measured on the ZOI and during test experiments. The mean values and the standard deviation of spatio-temporal uncertainties presented in Table 4.6, show that the measurement errors rise with temperatures. These values are from $-4 \times 10^{-5} \pm 9.0 \times 10^{-5}$ in the transversal direction and $-1.6 \times 10^{-4} \pm 5.4 \times 10^{-5}$ in the longitudinal direction at 25 °C, to $7.7 \times 10^{-5} \pm 4.4 \times 10^{-4}$ in the transversal direction and $-3.83 \times 10^{-4} \pm 1.2 \times 10^{-3}$ at 750 °C. The experiments on the characterization of strain measurement errors at high temperatures, notably from 600 °C to 750 °C are hardly repeatable (Figure 4.28). This tendency may link to the characteristic of the convection flow in the closing furnace. Nevertheless, in this study, this hypothesis is not demonstrated.

For the perspectives, to improve some limitations in this study, further studies should focus on:

- confirming the origin of an increase of strain measurement errors versus time in long-temp experiments. We supposed in our experiments that the "static" condition is ensured. As we mentioned, an increase of strain errors versus time can be from material's behavior or effect of heat waves itself. It should be interesting to develop another strain measurement method, independently of the 2D-DIC method, such as the extensometer at high temperature to confirm the "static" condition during the characterizing the strain measurement error tests
- developing an optical method, i.e., the shadowgraphy method (Delmas *et al.*, 2013) that allows a visualization of the convection flow in the furnace. This method should be developed in parallel with the 2D-DIC method. Two independent measurement methods can confirm the link of spatio-temporal characteristic of strain measurement error and the convection flow. Furthermore, they might also explain the non-repeatable and high strain errors for temperatures higher than 600 °C.

CHAPTER

5

Correction methods for reducing strain measurement errors due to heat waves at HT

In chapter 4, the influence of heat waves due to convection flows on 2D-DIC strain measurements is characterized. Heat waves cause probably random strain measurement errors, named 2D-DIC uncertainties. The 2D-DIC uncertainties at HT are spatial and temporal, characterized by the strain heterogeneity (the spatial characteristic) and strain variations versus time that appear during the image capturing (the temporal characteristic).

In chapter 5, correction methods for reducing the effects of heat waves on strain measurements using the 2D-DIC method during mechanical tensile tests are suggested. The chapter starts with the state-of-the-art on correction methods for reducing strain measurement errors due to heat waves. The methodology presents first the correction methods to improve the accuracy of mechanical strains measured by the 2D-DIC at HT. Next, the efficiency of correction methods is demonstrated by two application examples on "small" strain ($\varepsilon < 0.02$, Lemaitre *et al.*, 2020). Two application examples are identifications of the Young's modulus (E) and the Thermal Expansion Coefficient (TEC) of the TA6V material from 25 °C to 700 °C. The results and discussions sections refer to the efficiency of correction methods applied for 2D-DIC method to measure the "small" strain of mechanical tests at high temperatures. Finally, the chapter addresses conclusion and perspectives for future studies.

5.1 State-of-the-art

5.1.1 Identification of elastic parameters of materials using strains measured by the 2D-DIC method at room temperature

Since the early years of 1980s, DIC was developed and it becomes one of the most-used contactless measurement system in experimental mechanics, thanks to its accuracy and simple implementation. According to Sutton et al., the 2D-DIC algorithm is nowadays well-developed (Sutton *et al.*, 2017). The spatial resolution can reach up to sub-pixels by using appropriate interpolation sub-pixel functions, i.e., Bcubic or Spline. For example, Smith et al. showed that the strain uncertainty given by the local-2D-DIC method in experimental condition is less than 1×10^{-4} (Smith *et al.*, 1998). Wang et al. demonstrated by theory and by experiment that the strain accuracy by the local-2D-DIC depends on the displacement errors and the amount of deformation (Y. Wang *et al.*, 2016). The estimated strain accuracy is from -1×10^{-4} to 1×10^{-4} if imposed deformation is less than 0.05. For global-2D-DIC, Hild et al. showed that the displacement uncertainty σ is less than 0.01 pixels, and the strain uncertainty is about 1.5×10^{-3} (Hild *et al.*, 2006).

Thanks to the robustness and high accuracy of 2D-DIC algorithm and the well-controlled experimental conditions, many studies use the 2D-DIC method to measure small strains (from 0.01% to 1%) at room temperature. Small strains are then used to identify the elastic parameters of materials, for example the Young's modulus and the Poisson's coefficient.

In the local-2D-DIC approach, elastic parameters are obtained a posteriori, usually by the Least-Square Linear Regression method. For example, Hoult et al. and Sutton et al. used local-2D-DIC to successfully measure the Poisson's ratio of materials at room temperature (Hoult *et al.*, 2013 and Sutton *et al.*, 2009). The Poisson's ratio, which is defined as the ratio between the transversal strain and the longitudinal strain for isotropic and the material's elastic behavior is close to the reference value. Tung et al. used local-2D-DIC to calculate the Young's modulus of Aluminum alloy and steel material in fatigue experiments using far-field microscopy (Tung *et al.*, 2010). Strains measured by the 2D-DIC method are in agreement with those measured by an extensometer, showing the possibility of this method to measure "small" strains at room temperature. Huang et al. compared the Young's modulus of the concrete material measured by the traditional strain gage and the virtual strain gage offered by the local- 2D-DIC (Huang *et al.*, 2010). The Young's modulus values measured by two methods are similar within less than 5% of relative difference. Zhang et al. used the 2D-DIC method to measure the elastic properties of arterial tissues in the field of biomechanics, because the 2D-DIC method does not influence the stiffness of the material (D. Zhang *et al.*, 2002). The authors suggested that the 2D-DIC method could be an alternative solution when the use of a mechanical strain gage is impossible.

In the global-2D-DIC approach, the elastic parameters of materials are solved a priori by inverse methods (Hild *et al.*, 2006). For instance, Pierron et al. used the beam element in the finite element method and the Virtual Field Method (VFM) to determine the elastic properties of a soft foam (Pierron *et al.*, 2012). Leclerc et al. used the Integrated Finite Element method (I-FEM) to calculate the Poisson's ratio of a composite material (Leclerc *et al.*, 2009). Passieux et al. used the Finite Element Method Updating method (FEMU) to determine the elastic parameters (Young's modulus and Poisson's ratio) in an in-plane orthogonal test (Passieux *et al.*, 2015). Hild et al. employed the global-2D-DIC methods: Q4-DIC and Q8-DIC elements to determine the Young's modulus of the steel specimen by the Brazilian tests (Hild *et al.*, 2012).

5.1.2 Problematics of 2D-DIC strain measurements at HT

In the previous section 5.1.1, it is seen that both the local-2D-DIC and global-2D-DIC methods provide accurate and robust kinematic measurements. The local-2D-DIC can be widely used for the identification of material's parameters in the elastic domain at room temperature. However, at high temperatures, strain measurements are disturbed by thermal effects, notably the heat waves, which are discussed in chapter 4. Figure 5.1 presents a uniaxial stress-strain curve of the TA6V material at 500 °C with the mechanical strain measured using the local-2D-DIC method. The strain is calculated from a virtual strain gage equivalent to a mechanical strain gage with a basis of 5 mm. It is seen that the stress-strain curve is noisy because many strain points are not in-line with the expected stress-strain curve (the straight line of a linear stress-strain curve).

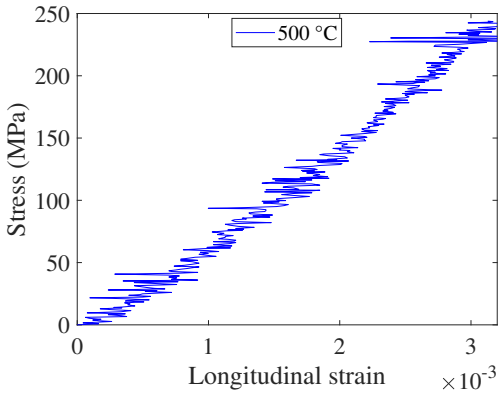

Figure 5.1: Stress-strain curve of a uniaxial tensile test using strains measured by the local-2D-DIC method at 500 °C

The difficulty of using the 2D-DIC method in experimental mechanics at HT can be explained partially by the influence of heat waves on kinematic measurements. Indeed, it has already been noticed by many previous studies. Lyons et al. and Grant et al. mentioned this problem while identifying the Young's modulus of materials at temperatures ranging from 650 °C to 1000 °C (Lyons *et al.*, 1996 and Grant *et al.*, 2009). Dong et al., De Strycker et al., Novak et al. and Pan et al. noticed the influence of heat disturbance on thermo-mechanical strains to calculate the thermal expansion coefficient (TEC) of materials (Dong *et al.*, 2020, De Strycker *et al.*, 2010, Novak *et al.*, 2011 and B. Pan *et al.*, 2014). Sakanashi et al., Doitrand et al. and Leplay et al. had the same notice while studying the creep behavior of ceramic material at 1000 °C (Sakanashi *et al.*, 2017, Doitrand *et al.*, 2020 and Leplay *et al.*, 2015). The authors remarked that strain measurement points are dispersed. The high dispersion in strain measured by the 2D-DIC method reduces the reliability of measurements (the coefficient of Linear Regression (R^2) is reduced). The authors discussed that it is necessary to correct the strain or displacement fields by 2D-DIC in order to obtain the "true" mechanical strain of thermo-mechanical tests.

5.1.3 Methods for reducing strain measurement errors due to heat waves

Facing the problem of highly dispersed strains measured using 2D-DIC at HT, the solutions suggested in the literature can be classified into two groups: a) "technical" solutions in which additional devices are employed, b) "numerical" solutions with improved-2D-DIC algorithms.

5.1.3.1 "Technical" solutions

Regarding "technical" solutions, one of the common methods to mitigate the effect of heat waves on strain measurements is using forced air flow, for example the airflow knife (Novak *et al.*, 2011) or a ventilator (Lyons *et al.*, 1996, Turner *et al.*, 1990, B. Pan *et al.*, 2014, Hammer *et al.*, 2014 and Berny *et al.*, 2018). The study of Jones et al. confirmed the fan reduces the displacement uncertainty, but errors can not be totally eliminated (Jones *et al.*, 2018). Furthermore, fans can modify the heat exchange between the object and the environment. They are not appropriate to industrial applications because a forced convection can modify the cooling rate; therefore, it changes the shape or microstructure properties of an industrial piece after hot stamping. The second solution is performing mechanical tests in the vacuum chamber (Z. Pan *et al.*, 2020, W. Wang *et al.*, 2017 and Reu *et al.*, 2019). Reu et al. showed that the uncertainty of DIC error is reduced more than ten times compared with that in the room condition (Reu *et al.*, 2019). However, mechanical tests in the vacuum requires costly equipment. The specimen used for mechanical tests in the vacuum chamber is small (several centimeters). The scale is not compatible with industrial or semi-industrial applications, in which, stamped parts generally measure several meters. The third solution is increasing the exposure time (Leplay *et al.*, 2015 and Doitrand *et al.*, 2020) but a long-exposure time can saturate pixels, leading to the correlation disruption. The final solution is using the techniques for visualizing the convection flow, i.e., the BOS or PIV techniques. With these techniques, the field of strain errors caused by heat waves is subtracted from the strain fields measured by 2D-DIC at HT. Bao et al. used the BOS technique, a color camera and the speckle projection technique to separate the mechanical strain and the strain error fields (Bao *et al.*, 2019). Ma et al. employed the PIV technique to separate the mechanical strain and the strain errors caused by heat waves (C. Ma *et al.*, 2019). The authors demonstrated that the strain measurement errors from air disturbance are totally removed from the kinematic field. Nevertheless, the BOS or PIV techniques require additional expensive equipment.

5.1.3.2 "Numerical" solutions

The numerical solutions aims to improve the 2D-DIC algorithm by average methods. For example, Su et al. used the grey-scale average method for reducing a high strain uncertainty due to thermal disturbances from radiation and heat waves (Su *et al.*, 2015). In this method, the grey-level of each pixel is averaged from a number of images, i.e., 2, 5 or 10 images. The ZNCC coefficient of correction decreases, meaning that the quality of correlation increases. The effect of grey-scale average methods on minimizing the thermal disturbance is more significant at temperatures above 700 °C. De Strycker et al. and Dong et al. used the space average method to determine the thermal coefficient of steel by the 2D-DIC method from room temperature to 600 °C (De Strycker *et al.*, 2010 and Dong *et al.*, 2020). The authors showed the TEC of steel measured after being averaged has only 4% of difference compared with the value measured by a strain extensometer. Chen et al. combined the average algorithm and air controller to minimize temperature's effect on mechanical strains for the TEC coefficient of Austenitic chromium-nickel stainless steel (L. Chen *et al.*, 2016).

Beside spatial average method, Chi et al. and Wang et al. developed temporal-space subset framework in which many images are averaged in time (Chi *et al.*, 2018 and X. Wang *et al.*, 2017). Berny et al. used the regularized spatio-temporal algorithm in the global-2D-DIC and updated the reference image to reduce the effect of heat waves on "small" strain (Berny *et al.*, 2018). Results from previous research showed the efficiency of improved-2D-DIC by decreasing 50% of bias errors (X. Wang *et al.*, 2017). The improved algorithms of the 2D-DIC method

present a great potential for mitigating air disturbance but requires a lots of images. Jones et al. proposed different solutions: spatial average by using multi-cameras, time averaging and using different types of filters (high-pass or low-pass filters) in static conditions as correction methods of air disturbance (Jones *et al.*, 2018). These solutions presents promising results but have not yet applied in real mechanical tests. Finally, Delmas et al. suggested the Abel transformation to retrieve the "false" displacement field caused by the convection flow (Delmas *et al.*, 2013). The "false" displacement field was then used to calculate the "true" mechanical strain. However, the convection flow must be well controlled. It is noted that numerical solutions do not require any additional devices; hence, they present a great potential as correction methods of heat waves. Nevertheless, it seems that numerical methods require a huge image storage in order to retrieve "true" strains at high temperatures.

5.1.4 Objective

The strain measured using the 2D-DIC method at HT contains the mechanical strain and the strain measurement errors due to heat waves. It is named the "total" strain. With the aim to improve the 2D-DIC method to measure "true" strains (mechanical strain) in mechanical tests at HT, in this chapter, we suggest a correction method that allows retrieving the mechanical strain from the "total" strain measured by the local-2D-DIC at high temperatures. The correction method does not require addition images, it is based on the characteristic of strain measurement errors in space and in time determined in Chapter 4 in order to eliminate the effect of air disturbance on 2D-DIC strain measurements. Application examples on the efficiency of corrections method are to calculate the Young's modulus (E) of the TA6V material at different temperatures and its thermal expansion coefficient (TEC) from 25 °C to 600 °C in the longitudinal direction from the strain measured using the local-2D-DIC method.

5.2 Correction methods for reducing strain errors at HT

In this section, the "total" strains measured by the 2D-DIC method at high temperatures in mechanical tests are presented. Afterward, the methodology for correction methods that reduce the temporal and spatial strain measurement errors due to heat waves from "total" strains is described. Finally, results obtained from correction methods are presented.

5.2.1 "Total" strains measured using the 2D-DIC method at HT

To illustrate the effect of heat waves on the strain measured using the 2D-DIC method, Figure 5.2 plots the "total" strain measured at different temperatures (25 °C, 400 °C, 500 °C and 600 °C) versus time. These "total" strains are obtained from the loading-unloading mechanical tensile tests at HT using the local-2D-DIC method. The protocol of this tensile test will be detailed in Section 5.3.1. Only unloading strains (strains measured from the unloading path of the tensile tests) are presented in Figure 5.2. It is observed that at 25 °C, the strain versus time plot (in blue) is nearly a straight line. It is expected that because the material is in the elastic domain and at room temperature, there is no heat waves. However, at higher temperatures, the strain versus time plots are noisy because strain measurement points are not in-line with the expected strain versus time curves. The strain versus time plots at higher temperatures presents strains that are regularly very high (peaks) and very low (valleys) and correspond to heat waves passing in front of the camera during mechanical tests.

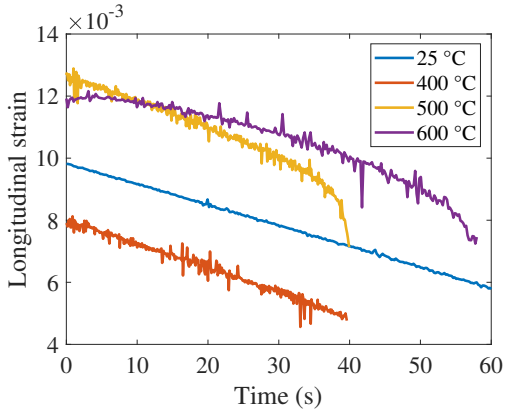

Figure 5.2: Strain-time curves (in the unloading paths) with strain measured from the local 2D-DIC of TA6V material at different temperatures

Figure 5.3 presents the stress-strain curves using "total" strains measured by the 2D-DIC method at different temperatures. It is seen that the stress-strain curve at 25 °C (Figure 5.3a) is a linear straight line. This is due to the fact that the "total" strain used in Figure 5.2 to plot the stress versus strain curve presents no noise. On contrary, because of noise from heat waves that are present in Figure 5.2, the stress-strain curves at HT (Figure 5.3b) present a lot of noise. Noise in "total" strain reduces the reliability of measurements. The elastic parameters, such as the Young's modulus from the stress-strain curves at HT using "total" strain by the linear regression method is influenced. Therefore, it is necessary to correct the "total" strain obtained from the local-2D-DIC method at high temperatures. In the next section, corrections methods will be applied on the "total" strain fields measured directly from the local-2D-DIC method.

Furthermore, it is observed that there is an offset of strain in each stress-strain curve: the stress-strain curves do not start at strain equal to 0. It is due to the alignment of the specimen in the grips of the servo-hydraulic testing machine that happened at the beginning of each tensile tests. This offset in strain will be presented more in detail in Section 5.3.2.1.

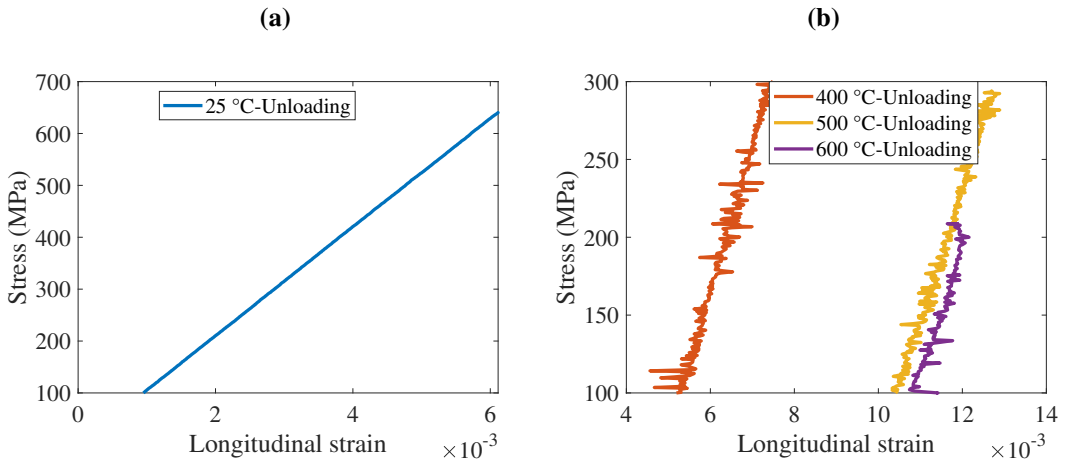

Figure 5.3: Stress-strain curves using "total" strain measured by the 2D-DIC method in tensile tests at different temperatures

5.2.2 Methodology on correction methods to reduce 2D-DIC strain measurement errors at HT

Corrections methods use the temporal filters and the spatial filters to reduce the influence of heat waves on the "total" strain measured by the 2D-DIC method. In chapter 4, it is supposed that the 2D-DIC errors due to heat waves are random error, characterized by temporal variations of strain versus time (temporal characteristic) and by the strain heterogeneity field (spatial characteristic). Therefore, temporal filters could minimize fluctuations in strains versus time plots by filtering errors caused by heat waves. The spatial filters could reduce the heterogeneity of "total" strain fields by smoothing over the strain field.

5.2.2.1 Temporal filters

From the observation on the strain variations versus time and the hypothesis on random errors caused by heat waves, it would be interesting to apply temporal low-pass filters for "total" strain versus time curves at HT. Low-pass filters can eliminate highly dispersed strain measurement points caused by heat waves while keeping the "continuous" signals that are mechanical strains. In the frequency domain, the mechanical signal should appear at the frequency of 0 Hz while strain measurement errors should appear at higher frequencies.

To evaluate the efficiency of low-pass filters in reducing errors due to heat wave, two types of low-pass filters: the linear filters and the non-linear low-pass filter were applied for the "total" strain versus time curves at HT (Figure 5.2). In the linear filters, there were three types of filters: the moving mean, the low-pass filter and the Gaussian filter. The non-linear low-pass filter was the median filter.

To find the filter that presents the best efficiency on reducing strain measurement errors, first, filters having the same filter size were compared. The filter size chosen for the moving mean, the Gaussian filter and the median filter was 3 [points]. The cut-off frequency of the low-pass filter was 0.3 Hz, which corresponded to the low frequency of heat waves observed in the chapter 4. The efficiency of each filter was evaluated by the norm of the residual (norm) obtained from the linear fitting of the strain versus time curves (Figure 5.2) after correction. The norm was calculated by Equation 5.1.

$$norm = \frac{\sum_{i=1}^{N}(\varepsilon_{exp} - \hat{\varepsilon}_{fit})^2}{N-1} \tag{5.1}$$

where:

- ε_{exp} is the "total" strain measured by the 2D-DIC method at HT
- $\hat{\varepsilon}_{fit}$ is the fitted strain by linear regression
- N is the total strain measurement points

Afterward, the filter having the best efficiency in reducing measurement errors was optimized for its parameters, i.e., the cut-off frequency in the low-pass filter. The aim of the optimization study is to minimize the 2D-DIC temporal errors at HT due to heat waves.

Finally, strain measurements after correction were then transformed in the frequency domain by the DFT transformation to verify if the mechanical strain (appears at the frequency of 0 Hz) was conserved.

5.2.2.2 Spatial filters

From the observation on the spatial characteristic of 2D-DIC strain measurement errors and the hypothesis on random error, spatial low-pass filters were applied for "total" strain fields to reduce the influence of heat waves. Spatial low-pass filters can smooth strain fields, therefore mechanical strain fields in the elastic domain measured using the 2D-DIC method can be more homogeneous. The mechanical strain map can be separated from the "total" strain map based on two following hypotheses.

- The "total" strain measured using the 2D-DIC method at time t and at temperature T would be the sum of the mechanical strain and the spatial strain error due to heat waves (Equation 5.2)

$$\varepsilon_{yy}^{total}(t) = \varepsilon_{yy}^{mechanical}(t) + e_{yy}^{error}(t,T) \tag{5.2}$$

- Under mechanical load lower than the yield strength of the material, the mechanical strain would be homogeneous on the ZOI of the TA6V sample.

The procedure to separate the mechanical strain field and the spatial strain error field due to heat waves are described as follows:

- First, instantaneous "total" strain fields at time t having a strain heterogeneity of $\geq 2.5 \times 10^{-4}$ were identified. The strain heterogeneity of 2.5×10^{-4} is the mean value of the strain uncertainty of the 2D-DIC method at 25 °C, which is related to the experimental set-up condition.

- Afterward, different types of spatial filters: the median filter, the Gaussian filter and the low-pass filter were chosen to evaluate their efficiency on eliminating heterogeneous strain caused by heat waves. The performance of filters was evaluated by the reduction of strain heterogeneity before and after correction.

- Next, the spatial filter with the best performance was used for the optimization study in which filter parameters i.e., the filter sizes were varied to evaluate the reduction of the strain heterogeneity.

- The mechanical strain field at time t was subtracted from the "total" strain field and the strain error field by Equation 5.2.

5.2.3 Efficiency of correction methods in reducing strain errors at HT

In section 5.2.1, we have presented noisy stress-strain curves using "total" strain measured by the 2D-DIC method from tensile tests at HT. The study aims to minimize the random errors by using filters. The filter methods use temporal low-pass filters to eliminate highly dispersed strain measurement points on the strain versus time curves then employ spatial low-pass filters to smooth the "total" strain fields obtained by the 2D-DIC method in tensile tests at HT. In this section, results on the reduction of strain errors by using low-pass filters are presented.

5.2.3.1 Efficiency of temporal low-pass filters

Comparison of the efficiency of different temporal low-pass filters

Figure 5.4 presents the unloading curves of longitudinal strain-time measured by the 2D-DIC method at 400 °C before (in blue) and after using different temporal filters. The curve at 400 °C was chosen to present the general tendency on the effectiveness of the temporal filters on strain measurements. It is seen that the "total" strain-time curve (in blue) is noisy by the presence of strain points that are out of the linear strain-time plot. Other curves are strain versus time after filtering with different temporal filters: the moving average with size = 3 points (in red), the median filter with size r = 3 points (in violet), the low-pass filter with a cut-off frequency of 0.3 Hz (in orange) and the Gaussian filter with size r = 3 points (in green). It is noticed that globally, four curves reduce highly-dispersed strain measurement points due to heat disturbance. Visually, the low pass-filter with a cut-off frequency of 0.3 Hz gives higher effect (Figure 5.4b) compared with others. After filtering, the shape of the longitudinal strain-time curve is wavy. The wavy shape correspond to signals at frequency lower than 0.3 Hz. The other filters give similar effects on reducing strain errors due to heat waves: high peaks are eliminated but small strain variations remain.

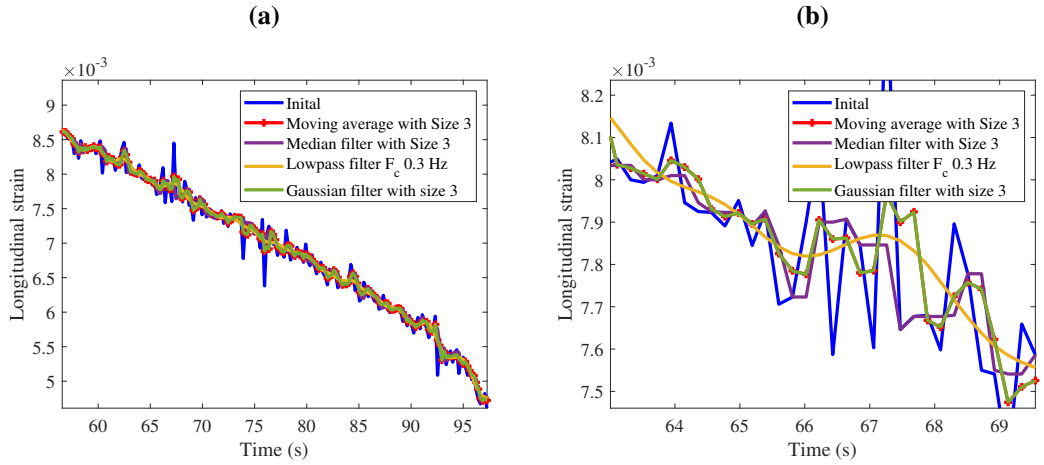

Figure 5.4: Comparison of the efficiency of different filters in reducing random errors caused by heat waves: (a) The longitudinal strain versus time curves at 400 °C before and after filtering, (b) Zoom of the strain-time curves from time t = 63 s to 70 s

To quantitatively evaluate the effect of temporal filters on reducing strain measurement errors, the norm of the residual (*norm* in Equation 5.1) determined from strain-time curves after filtering are compared. They are presented in Table 5.1. The norm of the linear fitting from strain-time plots shows that the median, the Gaussian and the moving average have the same effect on reducing random errors (the norm of residuals is reduced by 45%). The low-pass filter with cut-off frequency of 0.3 Hz reduces more than 60% of highly-dispersed strain points on the curve. From this result, the low-pass frequency filter is chosen for the "optimization" study in which the cut-off frequency is varied to reduce temporal errors due to heat waves.

Table 5.1: Efficiency of filters in reducing temporal errors due to heat waves

	Before	After			
	Initial signal	Moving filter	Gaussian filter	Median filter	Low-pass filter
Characteristic		r = 3 points	r = 3 points	r = 3 points	Fs = 0.3 Hz
Norm	2×10^{-3}	1.1×10^{-3}	1.1×10^{-3}	1.1×10^{-3}	7.8×10^{-4}
Reduction of error (%)		45 %	45 %	45 %	61%

Optimization of the temporal low-pass filter

In previous paragraph, it is seen that the frequency filter presents the best efficiency in reducing temporal strain errors on the "total" strain-time curves. For this reason, the low-pass frequency filter with different cut-off frequencies are employed for the optimization. The optimization aims to minimize the 2D-DIC temporal strain errors due to heat waves.

Figure 5.5a presents "total" strain-time curves after filtering with different cut-off frequencies at 500 °C. Here only the curves at 500 °C is presented but the low-pass frequency filter is systematically applied for all "total" strain-time curves at HT. Figure 5.5b displays the zoom on strain measurements from time of 55 s to 62 s. It is observed that lower cut-off frequencies render smoother signals after filtering. The filters with cut-off frequency lower than 0.2 Hz show more effect on reducing temporal strain errors caused by a heat disturbance. Only strains measurements at low frequency (less than cut-off frequency of the filter) remain. They have the wavy shape in Figure 5.5b.

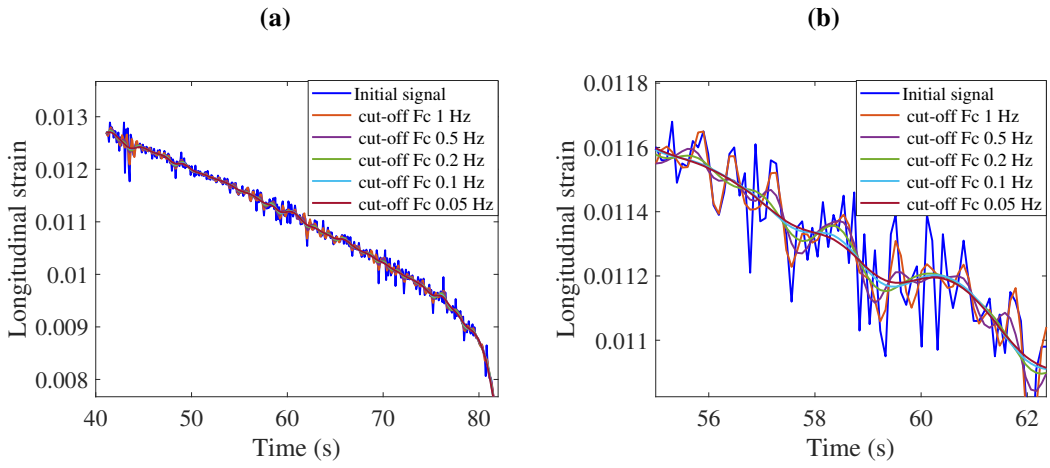

Figure 5.5: Effect of cut-off frequencies of the temporal low-pass frequency filter on reducing random errors caused by heat waves. (a) The unload strain versus time of the tensile tests at 500 °C before and after filtering with different cut-off frequencies, (b) Zoom of the strain-time curves from 55 s to 62 s

Amplitudes of strains after low-pass filtering

Figure 5.6 shows that the amplitude of the mechanical strains after filtering with different cut-off

frequency in the frequency domain. The amplitude of the "mechanical" is obtained by the DFT of the strain-time curves in Figure 5.5 .

It is shown that signals at frequencies higher than 0.2 Hz, which correspond to noise, after filtering are nearly zero. Their magnitude is under 1×10^{-4}. The lower cut-off frequencies eliminate more noise. It means that logically, temporal low-pass frequency filter with cut-off frequency close to 0 Hz is better in reducing strain errors due to heat disturbances.

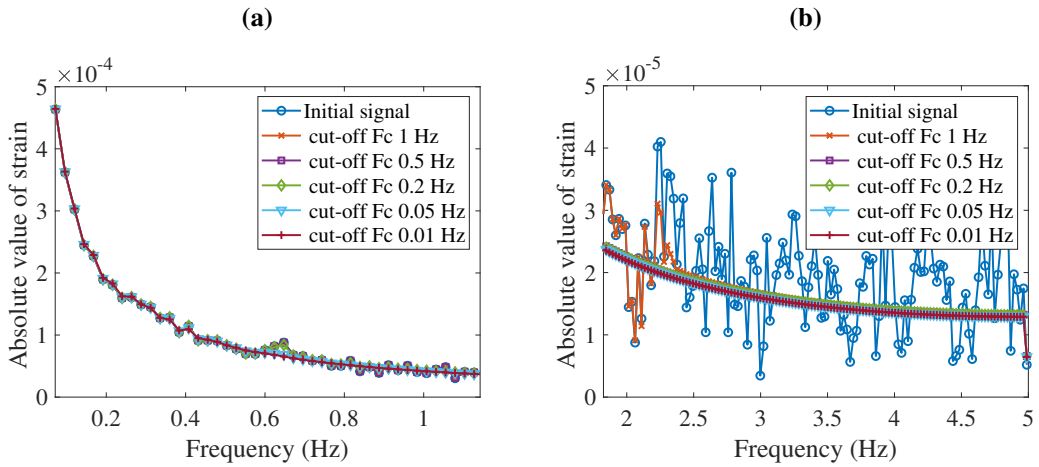

Figure 5.6: Amplitude of strain measurements after filtering in the frequency domain:(a) The whole frequency from 0 Hz to 5 Hz (b) Zoom on frequencies from 2 Hz to 3 Hz

The amplitude of the "continuous" signal at frequency F = 0 Hz, the mechanical strains, is presented in Table 5.2. The mechanical strain obtained after the filter is conserved whatever the cut-off frequencies are.

Table 5.2: Influence of cut-off filter (Fc) on the amplitude of mechanical signal after filter

	Initial signal	Cut-off frequency of temporal filter (Fc)				
		1 Hz	0.5 Hz	0.2 Hz	0.05 Hz	0.01 Hz
Amplitude	0.0109	0.0109	0.0109	0.0109	0.0109	0.0109

In conclusion, the efficiency of temporal low-pass filters are evaluated to eliminate temporal strain errors due to heat waves. Among four filters, the low-pass filter using a cut-off frequency lower than 0.2 Hz presents the best reduction of strain measurement errors, which appear at higher frequency. The mechanical signal at frequency f = 0 Hz is conserved.

5.2.3.2 Efficiency of spatial low-pass filters

Comparison of the efficiency of different spatial filters

Figure 5.7a presents the "total" longitudinal strain map (ε_{yy}) having high strain heterogeneity at time t at 500 °C. It is noted that the strain map at 500 °C is chosen to represent the tendency obtained from results but the "total" strain maps presenting high strain heterogeneity of all temperatures are systematically filtered. Figure 5.7b-5.7d present the ε_{yy} maps after filter by: i) the median filter with size r = 3 points (Figure 5.7b); ii) the Gaussian filter with size r = 3

points and the STD $\sigma = 2$ (Figure 5.7c); iii) spatial low-pass filter with a cut-off frequency of 0.2 Hz (Figure 5.7d). Visually, it is seen that the strain maps after four filters are nearly similar. The strain map obtained after median filter presented missing information at the corner (border effect) (Figure 5.7b) because of unavailable neighbor pixels at four corners.

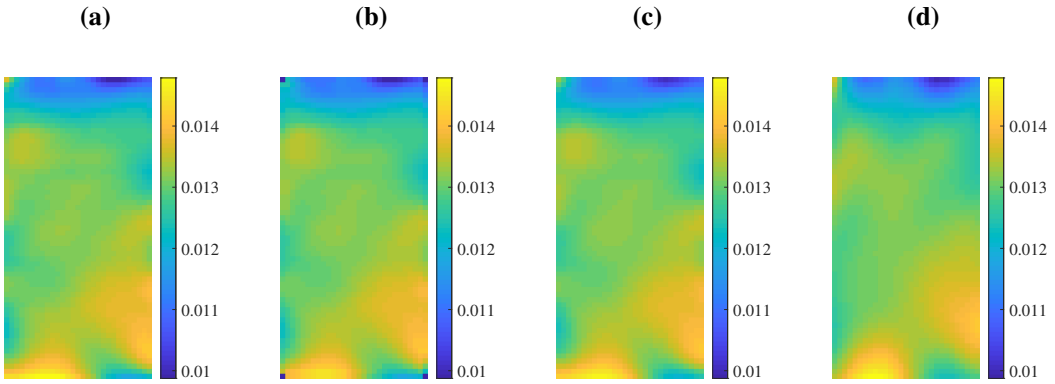

Figure 5.7: Comparison of the filter's efficiency in reducing the spatial strain errors due to heat waves at 500 °C: (a) "Total" strain map having a high strain heterogeneity, (b) After a median filter with size $r = 3$ points, (c) Gaussian filter with size $r = 3$ points and STD $\sigma = 2$, (d) Low-pass filter with cut-off frequency Fc = 0.2 Hz

To qualitatively compare the efficiency of spatial filters, the efficiency of filters can be characterized by the strain the heterogeneity (Δe_{yy}), the maximal, the minimal, the mean and the standard deviation STD of strain maps after filtering (Table 5.3). It is seen that four filters had nearly the same efficiency: the strain heterogeneity (Δe_{yy}) is reduced to about 4.6×10^{-3}; the STD after filtering is 6.5×10^{-4}. The median filter is an exception because of the border effect (strain values at the borders are equal to 0 that render the STD of e_{yy} sightly greater than other filters. The Gaussian filter gives a slightly lower Δe_{yy} compared with other filters. It shows a better efficiency in reducing strain heterogeneity, which characterize the spatial strain error at HT. Among four types of spatial filters used, the Gaussian filter presents a better performance on reducing strain heterogeneity. It is afterward optimized by varying the size r and the standard deviation σ.

Table 5.3: Comparison of the efficiency of spatial filters for reducing strain heterogeneity due to heat waves

Filter	Initial	Median filter	Gaussian filter	Low-pass filter
Δe_{yy}	4.9×10^{-3}	1.44×10^{-2}	4.6×10^{-3}	4.7×10^{-3}
max. of (e_{yy})	1.48×10^{-2}	1.44×10^{-2}	1.47×10^{-2}	1.48×10^{-2}
min. of (e_{yy})	9.9×10^{-3}	0	1.01×10^{-2}	9.9×10^{-3}
mean of (e_{yy})	1.30×10^{-2}	1.30×10^{-2}	1.30×10^{-2}	1.30×10^{-2}
STD of e_{yy}	6.68×10^{-4}	9.17×10^{-4}	6.65×10^{-4}	6.39×10^{-4}

Optimization of the spatial Gaussian filter

The performance of the Gaussian filter depends on two parameters: filter size (r) and STD (σ). Figure 5.8 presents four strain maps after the Gaussian filter with two parameters. The first one

corresponds to the parameters: r = 5, σ = 5, the second one corresponds to the parameters: r = 5, σ = 293, the third one corresponds to the parameters: r = 293, σ = 5 and the fourth one corresponds to the parameters: r = 293 σ = 293.

Visually, a small value of σ and/or r (Figure 5.8a-c) does not significantly reduce the effect of heat waves on "total" strain maps. With a set of Gaussian parameters (r = 293 and σ = 293), the "total" strain map after filter is nearly homogeneous.

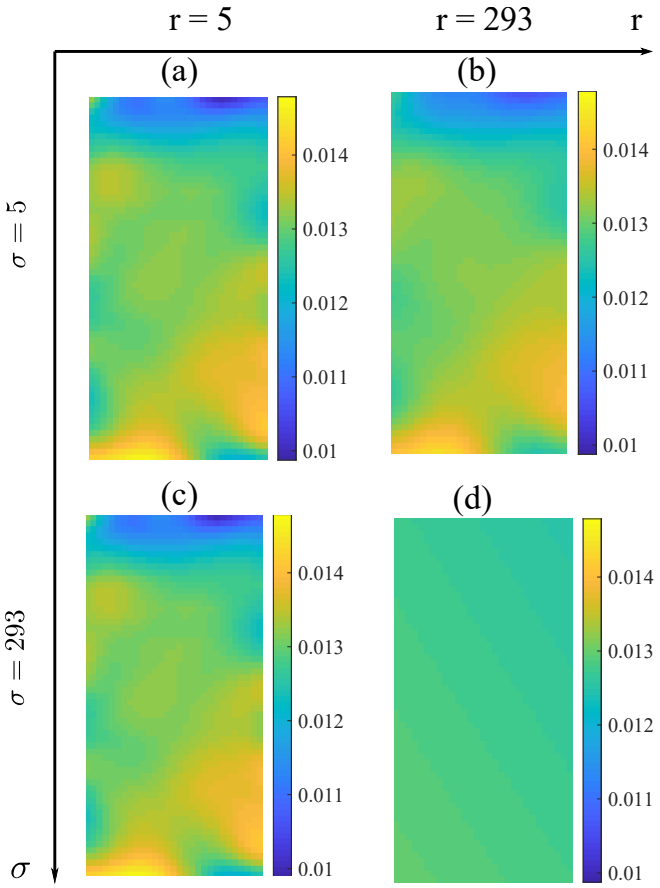

Figure 5.8: Effect of Gaussian filter parameters: r and σ on the strain map after filtering at 500 °C

Table 5.4 presents quantitatively the strain heterogeneity Δe_{yy} after varying the r and σ of the spatial Gaussian filter, correspond to four strain maps in Figure 5.8. It is seen that the filter size r has more influence on reducing the strain heterogeneity. Furthermore, with the highest values of r and σ (r = 293 and σ = 293), the strain heterogeneity is the lowest ($e_{yy} = 4.57 \times 10^{-4}$ instead of $e_{yy} = 4.6 \times 10^{-3}$ with r = 5 and σ = 293 or $e_{yy} = 3.7 \times 10^{-3}$ with r = 293 and σ = 5).

Table 5.4: Influence of r and σ parameters in the Gaussian filter on the strain heterogeneity

	$r = 5$	$r = 293$
$\sigma = 5$	4.6×10^{-3}	3.7×10^{-3}
$\sigma = 293$	4.6×10^{-3}	4.57×10^{-4}

Figure 5.9 graphically presents the strain heterogeneity obtained by varying parameters r and σ from 5 to 300 with an interval of 50. It is seen that with parameters $r > 90$ and $\sigma > 43$, the efficiency of the Gaussian filter on reducing the strain heterogeneity becomes significant. A high σ reduces the strain heterogeneity more rapidly than σ. The higher values of two parameters r and σ allow more homogeneous strain maps. From the practical view point, Figure 5.9 shows that to obtain a strain heterogeneity close to the one at room temperature (2.5×10^{-4}), the r and σ should be a great value: r and $\sigma \geq 200$.

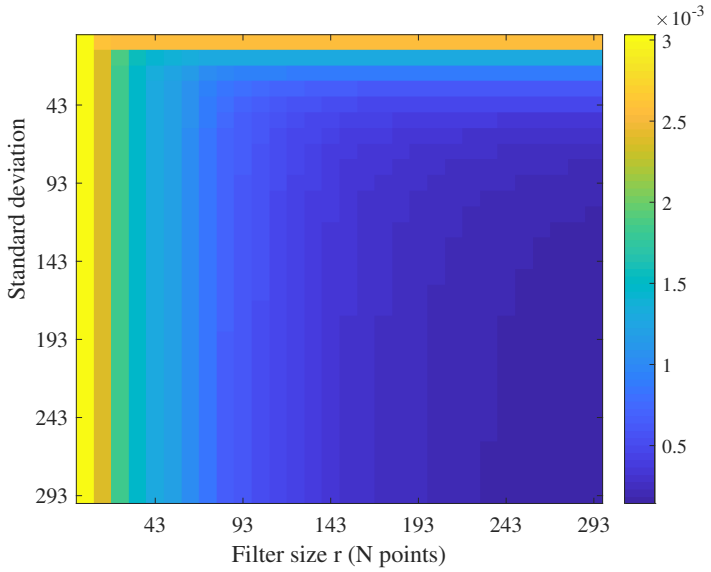

Figure 5.9: Effect of Gaussian filter parameters r and σ on the strain map after filtering at 500 °C

Optimized spatial Gaussian filter for reducing spatial strain errors

From the results on the optimization of the Gaussian filter, an algorithm of finding appropriate r and σ parameters of the spatial Gaussian filter is suggested in order to reduce the spatial strain errors at HT. The algorithm minimizing the spatial strain error, characterized by the heterogeneity of the strain map measured by the 2D-DIC at high temperature is proposed as follows:

Algorithm 1: Algorithm to smooth strain maps having a high heterogeneity at HT

Data: Instantaneous strain fields at time t, spatial Gaussian filter
Result: Strain fields after filtering
Initialization: calculate initial Δe_{yy};
spatial Gaussian filter with $r_o = 5$, $\sigma_o = 5$ (r_o and σ_o should be an odd integer number);
while $\Delta e_{yy} \geq 2.5 \times 10^{-4}$ **do**
    Gaussian filtering;
    Calculate Δe_{yy};
    if $\Delta e_{yy} \leq 2.5 \times 10^{-4}$ **then**
        break;
    else
        $r \leftarrow r + 5$;
        $\sigma \leftarrow \sigma + 5$;
    end
end

The Gaussian parameters r and σ found by using the algorithm to minimize the longitudinal strain heterogeneity at 400 °C are $r = 99$ and $\sigma = 260$. With these parameters, the spatial strain error is reduced to 2.3×10^{-4}.

The same Gaussian parameters ($r = 99$ and $\sigma = 260$) are applied to smooth the instantaneous strain maps with high heterogeneity at 500 °C, 600 °C and 700 °C. Figure 5.10 presents the longitudinal strain before and after using the optimized Gaussian filter $r = 99$ and $\sigma = 260$ at different temperatures. It is shown that the longitudinal strain heterogeneity at 400 °C and 500 °C after filter is significantly reduced, more than 80% and 70% respectively. After filtering, longitudinal strain maps which initially have great heterogeneity are decreased to $2.4 \times 10^{-4} \pm 1.0 \times 10^{-4}$ at 400 °C and $5.3 \times 10^{-4} \pm 2.9 \times 10^{-4}$ at 500 °C. However, with this optimized Gaussian filter $r = 99$ and $\sigma = 260$ applied for strain maps at 600 °C and 700 °C, the strain heterogeneity after filtering are decreased by more than 60% at 600 °C and 700 °C. After filter, the strain heterogeneities at 600 °C and 700 °C are $1.7 \times 10^{-3} \pm 7.0 \times 10^{-4}$ and $1.7 \times 10^{-3} \pm 8.0 \times 10^{-4}$ respectively. It would be interesting to increase the Gaussian parameters for filtering at 600 °C and 700 °C in order to minimize spatial strain errors caused by heat waves.

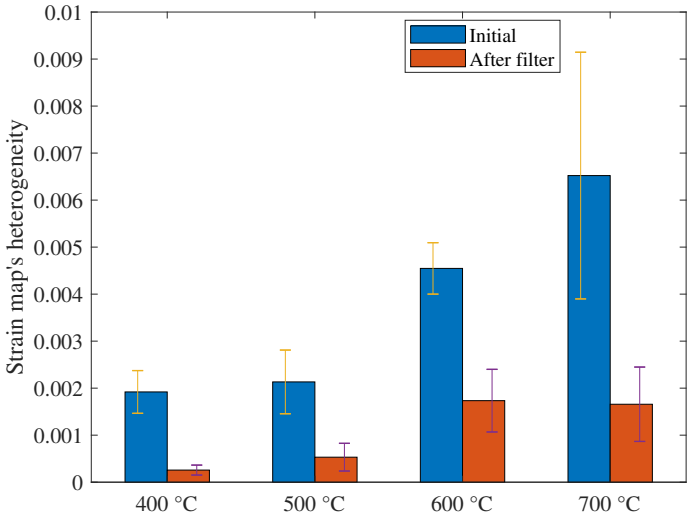

Figure 5.10: Longitudinal strain heterogeneity (in average) before and after the Gaussian filter with the parameters: $r = 99$ and $\sigma = 260$

Having observed that the strain heterogeneity decreases with an increase of the Gaussian parameters r and σ, Algorithm 1 is suggested to reduce strain heterogeneity at 500 °C, 600 °C and 700 °C. The algorithm aims to minimize instantaneous "total" strain maps which are measured by the 2D-DIC method at HT and have high strain heterogeneities greater than 2.5×10^{-4}. The value of 2.5×10^{-4} corresponds to the strain uncertainty at room temperature at which no heat waves occur.

Table 5.5 compares values of filter size (r) and STD (σ) depending on temperatures obtained from Algorithm 1. Since the strain heterogeneity increases with temperatures, values of r and σ increase for smoothing strain maps.

Table 5.5: Optimized parameters r and σ of the spatial Gaussian filter for reducing the strain heterogeneity at different temperatures

Temp.	Gaussian parameters		Strain heterogeneity e_{yy}	
	r	σ	Before filter	After filter
400 °C	99	260	$1.9 \times 10^{-3} \pm 5 \times 10^{-4}$	2.5×10^{-4}
500 °C	141	185	$2.1 \times 10^{-3} \pm 7 \times 10^{-4}$	2.5×10^{-4}
600 °C	739	936	$4.5 \times 10^{-3} \pm 5 \times 10^{-4}$	2.5×10^{-4}
700 °C	750	953	$6.5 \times 10^{-3} \pm 2.6 \times 10^{-3}$	2.5×10^{-4}

Using the optimized spatial Gaussian to separate the thermo-mechanical strain and the spatial strain errors caused by heat waves

After filtering by the optimized Gaussian filter, with the use of Equation 5.2, the thermo-mechanical strain fields at HT are separated from the "total" strain map which is measured using the 2D-DIC method.

Figure 5.11a presents thermo-mechanical strain (Figure 5.11a) subtracted from the "total" strain maps (Figure 5.11b) and the "false" strain due to heat waves (Figure 5.11c) at 500 °C. After filtering, the strain heterogeneity at time t at 500 °C is decreased by more than 65%. The strain heterogeneity is 2.5×10^{-4} while its initial value is 3.8×10^{-3}. The thermo-mechanical strain is nearly homogeneous. The "false" strain map due to the mirage effect has strain values from -2×10^{-3} to 2×10^{-3}, which are slightly higher than the strain heterogeneity at 500 °C determined in "static" and "isothermal" condition (Chapter 4).

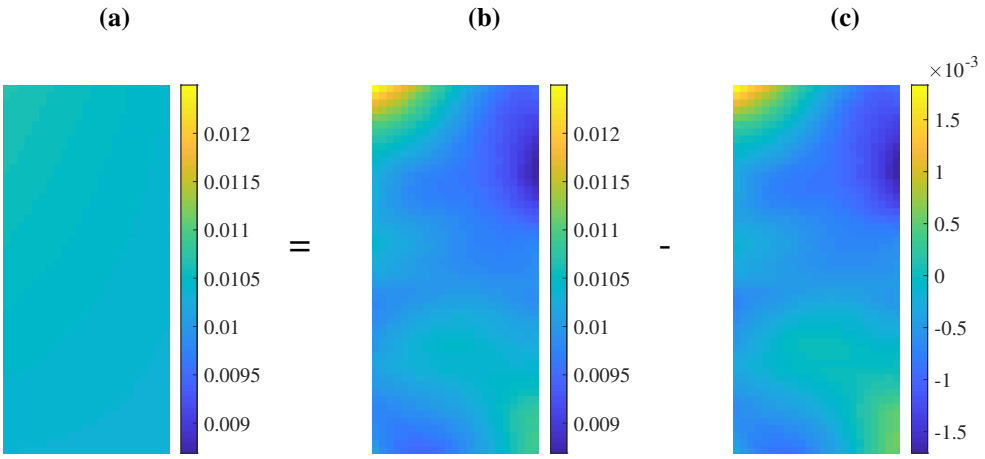

Figure 5.11: (a) Thermo-mechanical strain (in longitudinal direction) map obtained after the optimized Gaussian filter at 500 °C, (b) "Total" strain map measured using the 2D-DIC method, (c) "False" strain map caused by heat waves

Figure 5.12a presents thermo-mechanical strain subtracted from the "total" strain maps (Figure 5.12b) and the "false" strain map (Figure 5.12c) at 700 °C. With the optimized spatial filter, the heterogeneity of thermo-mechanical strain was minimized. The mechanical strain is from 0.0105 to 0.011. The "false" strains due to heat waves has values from -1.7×10^{-3} to 2.7×10^{-3}, close to the strain heterogeneity at 700 °C determined in "static" and "isothermal" condition (Chapter 4).

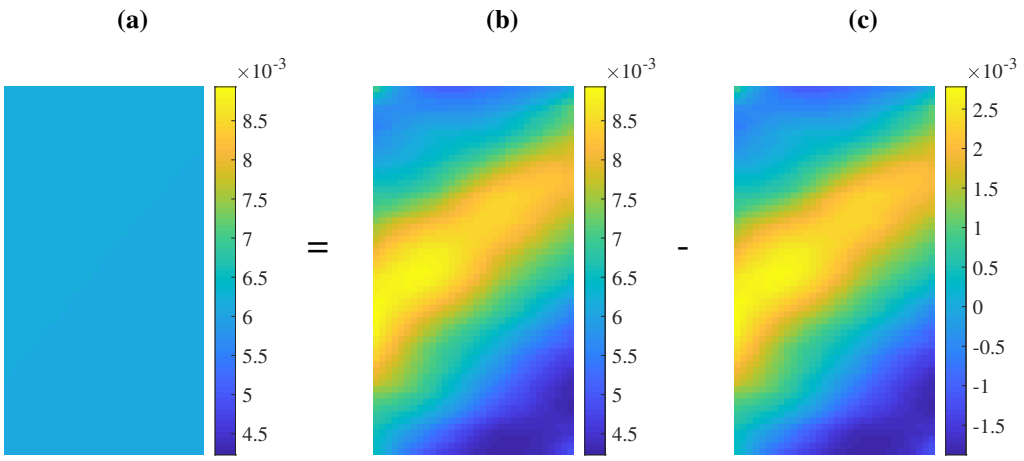

Figure 5.12: (a) Thermo-mechanical strain map in longitudinal direction obtained after the optimized Gaussian filter at 700 °C, (b) "Total" strain map measured using the 2D-DIC method, (c) "False" strain map caused by heat waves

In conclusion, from the optimized Gaussian filters, the thermo-mechanical strains at HT of tensile tests are separated from the "total" strain maps measured by the 2D-DIC method and the spatial strain error field due to heat waves. The mechanical strains maps are homogeneous (the strain heterogeneity is less than 2.5×10^{-4}). The spatial strain error maps in tensile tests have values close to the order of magnitudes of strain heterogeneity measured in "static" and "isothermal" conditions (Chapter 4).

5.2.4 Result synthesis

In this section, correction methods using the temporal and spatial filters are suggested to minimize the random errors caused by heat waves.

The temporal filters are firstly used to eliminate highly dispersed strain measurements in the "total" strain versus time curves by the 2D-DIC method. Among four types of temporal filters, the temporal low-pass frequency filter presents the best reduction of strain variations. A cut-off frequency lower than 0.1 Hz can eliminate most temporal strain errors that correspond to the passage of heat waves through the camera and the specimen.

The spatial filters are then employed to smooth strain maps at time t having a high strain heterogeneity ($\geq 2.5 \times 10^{-4}$). Among four types of spatial filters, the spatial Gaussian filter presents the best efficiency in reducing strain errors due to heat waves. An optimized Gaussian filter can reduce the strain heterogeneity at HT to the spatial strain error at room temperature. The optimized Gaussian filter have two parameters: r and σ that depend on temperatures. The thermo-mechanical strain at HT can be separated from the "total" strain map measured by the 2D-DIC method.

5.3 Application examples of correction methods in thermo-mechanical tests at HT

In this section, the correction methods using filters are applied for thermo-mechanical tests to measure the mechanical and/or thermo-mechanical strains at HT. Two types of mechanical tests are employed in this study: uniaxial tensile tests to calculate the Young's modulus of the TA6V material at different temperatures and an experiment to calculate the thermal expansion coefficient of this material from 100 °C to 600 °C. The section starts with methodology for thermo-mechanical tests. Afterward, results on the elastic properties of the material (the Young's modulus E and the Thermal Expansion Coefficient TEC) before corrections are presented. Finally, the efficiency of filters applied in experimental mechanics is demonstrated by results of the elastic properties of the material after corrections.

5.3.1 Methodology

The section first presents the material and devices employed for thermo-mechanical tests. Next, a new protocol of loading/unloading tensile test that improves the accuracy of the Young's modulus from tensile tests, followed by the procedure of an experiment to calculate the TEC of the TA6V material. Finally, a post-processing using filters applying for mechanical tests to reduce strain errors measured due to mirage effects is addressed.

5.3.1.1 Materials and devices

The TA6V planar specimen was used in tensile tests to determined the elastic parameters of the TA6V material (E and TEC). The microstructure of the TA6V material is presented in Appendix A.1. The geometry of planar specimens is presented in Appendix A.3. The ZOI area of the TA6V specimen is 15 mm by 8 mm (Figure A.4).

The TA6V specimen was heated by the AET closing furnace with a heat rate of 10 °C min^{-1} (Figure 4.5a-b). The heating process lasted from 45 minutes to one hour to reach the target temperature and to get a homogeneous temperature on the specimen ("isothermal" condition). After one hour of heating, a thermal gradient of 2 °C on the ZOI of the specimen (25 mm), measured by three thermal couples (type K with an uncertainty of 0.5 °C) was recorded.

The mechanical machine used for tensile tests is the MTS 125 testing machine with load capacity of 50 kN and the TestStar ® software controller connected to a computer (Figure 4.5c).

The DIC system used for strain measurements was the 2D-DIC camera system. The local DIC approach was employed to calculate Lagrange strain fields. Speckles used for tensile tests from 25 °C to 600 °C were made by the M5 method: combining anodization and laser engraving (Figure 2.14d) while at 700 °C, speckles were made by high-temperature paint (Figure 2.15a) (see Chapter 2). The experimental set-up conditions and local 2D-DIC parameters were optimized from the results in Chapter 3 and Chapter 4. The frequency for image capturing in the tests for Young's modulus identification was 5 Hz. The frequency for image capturing in the tests for the TEC of the TA6V material was 0.2 Hz. Finally, mechanical signals, force and displacement of cross-head of MTS testing machine and strains measured using the 2D-DIC system were synchronized by an external trigger.

5.3.1.2 Identification of the Young's modulus of the TA6V material

Development of the loading/unloading protocol for tensile tests
In order to improve the accuracy of Young's modulus by strain measured using the 2D-DIC method, we developed a load/unloading protocol for tensile tests that may reduce the systematic

errors of strains using the 2D-DIC method related to experimental set-up conditions, i.e., the rigid body motion and the sample rotation at the beginning of tensile tests. The sample rotation and rigid body motion are also related to the limitation of pinned grips in the MTS servo-hydraulic testing machine (Davis, 2004). The loading/unloading tests were also used in a study of Pham to calculate the apparent Young's modulus of very thin sheet specimens at room temperature (Pham, 2014).

The loading/unloading tensile tests loaded the specimen to a level of stress under yield strength of the material for the alignment of the specimen-furnace window-camera then unloaded the specimen to 8 MPa. TA6V samples were loaded and unloaded with a stress rate of 8 MPa s^{-1}. Strains in the unloading paths measured by 2D-DIC method were used to identify the Young's modulus of the TA6V material. By this method, mechanical strain measured by using the 2D-DIC method could be improved because the systematic strain errors related to the rotation of the specimen and the rigid body motion can be suppressed.

The Young's modulus is determined in the elastic domain of material. From the practical point of view, the highest stresses applied on samples must be lower than the yield strength of the TA6V material. It is noted that the yield strength of the TA6V material strongly depends on temperatures. The yield strength of TA6V at different temperatures was based on the literature and it is presented in Table 5.6. Through the literature review, it is shown that the yield strength of TA6V material at high temperatures varied from different sources. For example, Sirvin et al. found TA6V has lower yield strength at 400 °C and 500 °C compared with those found in a study of Odenberger et al. (Sirvin *et al.*, 2019 and Odenberger *et al.*, 2013). The authors found that yield strength has the same order of magnitude with that in a study of Surand (Surand, 2013). The wide range of yield strength should be linked to the material's microstructure and heat treatment.

Table 5.6: The maximal stress levels applied on TA6V specimens in loading/unloading tests at different temperatures and yield strength of the TA6V material in the literature

Temp. °C	Highest stress	Yield strength & Reference
25 °C	673 MPa	880 MPa - 924 MPa (Odenberger, 2005)
400 °C	362 MPa	580 MPa (Surand, 2013) - 691 MPa (Odenberger *et al.*, 2013)
500 °C	318 MPa	550 MPa (Vanderhasten, 2007) - 580 MPa (Surand, 2013)
600 °C	209 MPa	330 MPa (Surand, 2013) - 480 MPa (Vanderhasten, 2007)
700 °C	106 MPa	200 MPa (Vanderhasten, 2007)

In order to evaluate the efficiency of the loading/unloading protocol in suppressing the strain errors due to sample's rotation and rigid motion, an extensometer having a 15 mm basis, a measuring range of +27%/-13% and an accuracy of ± 1% (Model 634-31F-24, MTS®, Landmark USA) was implemented on the ZOI of TA6V samples at 25 °C. Strains measured by the strain gage were compared with those measured using the 2D-DIC method.

At high temperatures, due to the closing furnace and limited space in the closing furnace, it was impossible to implement a high-temperature extensometer. Therefore, thermo-mechanical strains were only measured by the 2D-DIC method.

Calculations of apparent Young's modulus from stress-strain curves at HT
The Green-Lagrange strains (in longitudinal direction Oy: ε_{yy} and in transversal direction Ox: ε_{xx}) were calculated from the optimized 2D-DIC parameters, which were obtained in chapter 4: SS = 57 pixels, ST = 17 pixels, SW = 15 points. The strain measurements from the virtual strain gage was 5 mm with a magnification of 14 µm/pixel. It is also noted that during the tensile tests, the out-of-plane displacement could influence in-plane strains (ε_{xx} and ε_{yy}) (Sutton *et al.*, 2008 and Murienne *et al.*, 2016). Nevertheless, the distance between the camera and the specimen was set at 1.2 m which is sufficiently far to neglect the systematic error due to the out-of-plane displacement (Oz direction) compared to the strain uncertainty at room temperature.

Stress was calculated from the ratio of the force applied on the specimen and the section of the ZOI of the specimen (Equation 5.3)

$$\sigma_{yy}(t) = \frac{F(t)}{S_o} = \frac{F(t)}{e_o \times b_o} \tag{5.3}$$

where:

- e_o is the initial thickness of the specimen
- b_o is the initial width of the specimen

In the elastic domain where the strain is small: $|\varepsilon|$ from 2×10^{-2} to 5×10^{-2}, the variation of specimen's section can be negligible (Lemaitre *et al.*, 2020). The true stress that takes into account the variation of specimen section is similar to the engineering stress.

The apparent Young's modulus of the TA6V material was determined from the linear part of stress-strain curves. To avoid the influence of the mis-alignment of the specimen on mechanical strain, the Young's modulus was calculated from the unloading path of stress-strain curves by the Linear Regression method.

5.3.1.3 Identification of the TEC of the TA6V material

The planar specimen was used to measure the TEC in longitudinal direction (ε_{yy}) of the TA6V material using the testing machine and the 2D-DIC method. The specimen was heated with a heating rate of 10 °C min^{-1} by the AET closing furnace to 600 °C. During heating, the temperature on the ZOI of the specimen was measured by the three thermo couples, type K. Furthermore, during the heating, free thermal expansion of the specimen in longitudinal direction was controlled by maintaining a constant pre-load of 100 N, equivalent to a stress of 8 MPa.

Speckles were created by high-temperature paint (Rust® Oleum and Vitcas ®) because the paint can resist high temperature and a maximum strain of 0.2 (Results in Chapter 2). The 2D-DIC camera system and 2D-DIC parameters was similar to those used in tensile tests. The longitudinal strain were measured by the 2D-DIC method using a virtual extensometer equivalent to 5 mm.

The apparent TEC coefficient in the longitudinal directions Oy was calculated by Equation 5.4:

$$\alpha_{yy} = \frac{\Delta\varepsilon_{yy}}{\Delta T} \tag{5.4}$$

where: ε_{yy} is the strain measured using the 2D-DIC method during the heating from 25 °C to 600 °C temperature (ΔT)

To precisely determined the TEC of the TA6V material and demonstrate the efficiency of filter corrections, the TEC was calculated from the strain-temperature curves by Linear Regression method. Finally, the longitudinal TEC coefficient of the TA6V specimen using the 2D-DIC method was compared with the one measured using a thermal dilatometer (Netzsch dilatometer 402 C, Germany), heating rate of 20 °C min^{-1} with the same TA6V material. The specimen used for the thermal dilatometer was cut from a TA6V sheet in the rolling direction. Its dimension was 15 mm × 8 mm× 1.6 mm.

5.3.1.4 Application of correction methods for mechanical tests

"Total" strains measured using the 2D-DIC method during mechanical tests were corrected with temporal filter and spatial filters by following a procedure of post-processing described as follows:

- First, the "total" strains versus time during mechanical tests were filtered by temporal low-pass filter using a cut-off frequency of 0.05 Hz
- Next, instantaneous strain fields at time t having a strain heterogeneity greater than 2.5×10^{-4} were filtered by the optimized Gaussian spatial filter with size r and STD σ depending on temperatures. The value of 2.5×10^{-4} is the strain heterogeneity related to the spatial strain error at room temperature.
- To evaluate the efficiency of filter methods, the Young's modulus, the TEC and the Linear Regression coefficients R^2 were calculated from the stress-strain and strain-temperature curve after the filter corrections. They were compared with those before the filter corrections.

5.3.2 Results

In this section, the elastic parameters of the TA6V material before correction are first presented (the Young's modulus and the TEC coefficient). We also demonstrate accuracy improvements in measuring the Young's modulus by using the loading/unloading uniaxial tensile tests. Afterward, we present the efficiency of correction methods using filters in reducing strain errors due to heat waves while performing thermo-mechanical tests at HT.

5.3.2.1 Identification of the Young's modulus at HT before correction

Stress-strain curves and Young's modulus of the TA6V material at room temperature
In order to evaluate the influence of sample rotation and the rigid-body motion of the TA6V specimen on mechanical strains measured by the 2D-DIC method, strains measured by the 2D-DIC method and those by the extensometer methods are compared. The lengths of the virtual strain gauge (from the 2D-DIC method) and the physical extensometer are respectively 5 mm and 15 mm.

Figure 5.13a presents the evolution of stress (in amber), the strain measured by using the virtual strain gage (blue) and the extensometer (orange) versus time at 25 °C. It is seen in Figure 5.13a that the strains measured using the virtual strain gage, the extensometer and stress (controlled by TestStar controller) versus time are correctly synchronized by an external trigger.

At the beginning of the loading, there is a difference between strains measured by the virtual strain gauge and those by the extensometer. The difference is caused by the sample alignment in the pinned grip and sample rotation. Indeed, as the physical extensometer is clipped on the sample, the rotation of the sample does not influence the strain measurements by using this method. The stress-strain curve of TA6V at 25 °C with strains measured by the extensometer is linear and nearly reversible. The loading stress-strain curve is similar to the unloading one. The Young's modulus calculated is 108 GPa with $R^2 = 0.999$ (Figure 5.4b).

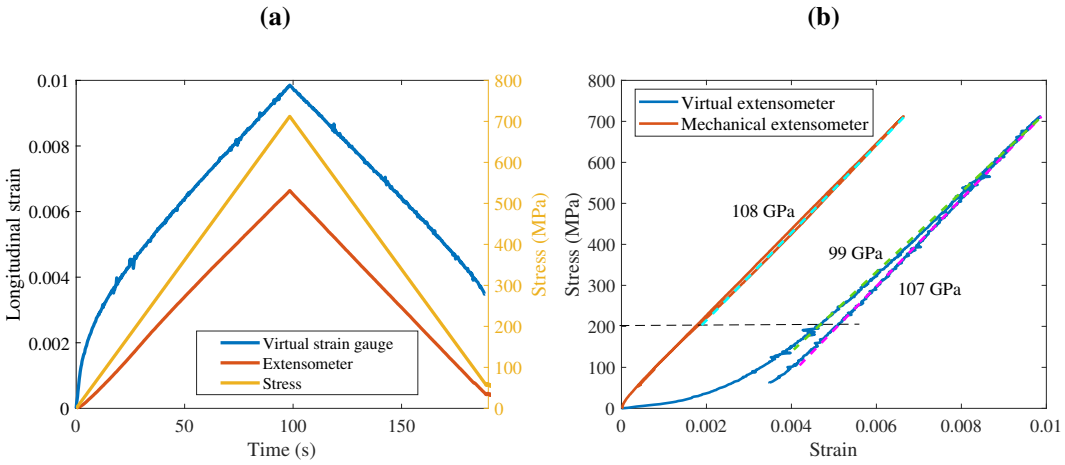

Figure 5.13: a) Stress (in amber) versus time, strains versus time measured by the virtual strain gage (in blue) and the physical extensometer (in orange) versus time during the loading/unloading tensile test; b) Stress-strain curves with strains measured using the virtual strain gage (blue) and the the one with strain measured using the physical extensometer (in orange) at 25 °C

On the contrary, the beginning of the strain-time curve measured using the 2D-DIC method (Figure 5.13a) is not linear. By calculating the rotation field (Equation 5.5), it is seen in Figure 5.14 that from 2 s to 6 s (at the beginning of a loading/unloading tensile test), the sample is rotated to 2.6°, which influences the mechanical strain measured by 2D-DIC.

$$\omega_{xy} = \frac{1}{2}\left(\frac{\partial u}{\partial y} - \frac{\partial v}{\partial x}\right) \tag{5.5}$$

where:

- ω_{xy} in-plane rotation of Oxy plane
- u, v are the displacements in horizontal direction Ox and in longitudinal direction Oy, respectively
- x, y are the coordinates of the pixels in horizontal direction Ox and in longitudinal direction Oy, respectively.

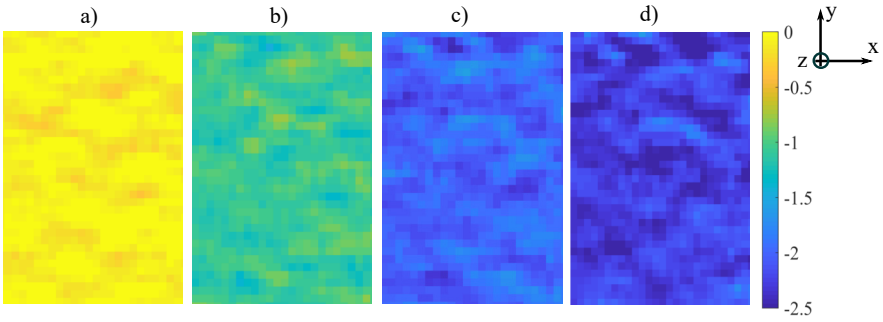

Figure 5.14: Rotation map on the ZOI of specimen during the loading/unloading tensile tests: a) at 0.2 s; (b) at different time t = 2 s, (c) at 4 s, (d) at 6 s

On the unloading path, the strain-time curve measured by 2D-DIC (the blue curve in Figure 5.13a) is linear and parallel to the unloading strain-time curve measured by the extensometer (the orange curve in Figure 5.13a). The apparent Young's modulus calculated from the loading stress-strain curve is 99 GPa while from the unloading stress-strain curve, it is 107 GPa. The apparent Young's modulus calculated from the unloading stress-strain curve using the 2D-DIC method is close to the one calculated from the stress-strain curve using the extensometer (108 GPa $\pm$ 0.01 GPa).

In conclusion, it is seen that the apparent Young's modulus determined from strains measured using the 2D-DIC method is influenced by the sample alignment and rigid body motion that occur at the beginning of tensile tests. The apparent Young's modulus can be biased if it is determined in the loading stress-strain curve. The sample alignment problem of samples in the pinned grip is already mentioned by Davis and Lord while they performed tensile tests by a servo-hydraulic tensile machine (Davis, 2004 and Lord *et al.*, 2010). The authors called the problem the "foot" effect and suggested an offset to eliminate this problem. Results in our study are in agreement with their observations. Therefore, it is better to determine the apparent Young's modulus in the unloading stress-strain curve of the tensile tests.

Stress-strain curves and the Young's modulus of TA6V material at HT

In the previous section, we suggest that the apparent Young's modulus should be determined from the unloading stress-strain of tensile tests at room temperature. The loading/unloading tensile and the identification method for Young's modulus are applied at high temperatures. The experimental conditions (temperature and the highest stress) corresponding to each tensile test is presented in Table 5.6.

Figure 5.15 presents the stress-strain curves of tensile tests at 400 °C and 500 °C. The stress versus strain at 400 °C (Figure 5.15a) and at 500 °C (Figure 5.15b) display similar shape as the one at 25 °C: a non-linear behavior on the loading curve due to sample alignment then a linear response in the unloading curve. Furthermore, at the end of the unloading curve at 500 °C, strains decrease rapidly, which is probably because of the sample's rotation due to the gap between the pinned grip and the specimen's head. Straight lines in Figures 5.15a and 5.15b indicate the stress and strain range for determining the Young's modulus by Linear Regression method. The apparent Young's moduli determined at 400 °C and 500 °C are respectively 91 GPa and 83 GPa.

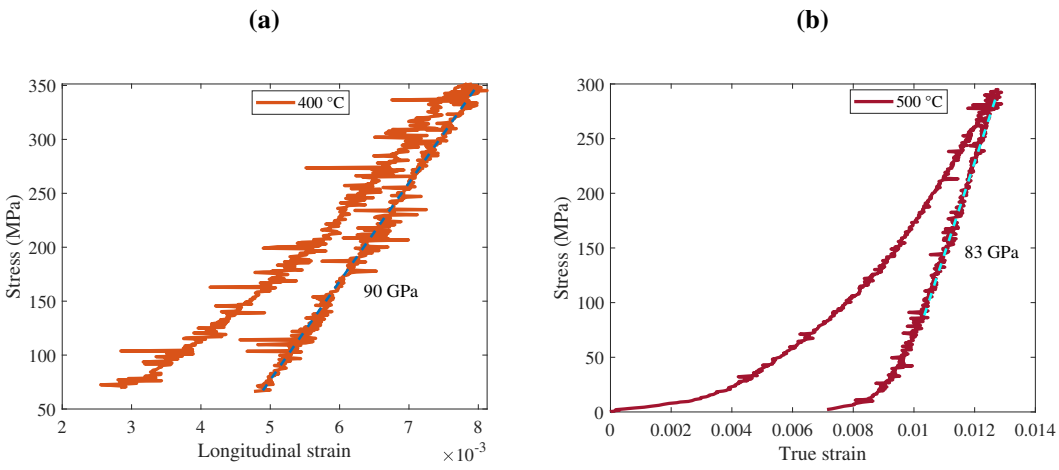

Figure 5.15: Stress-strain curves of the loading/unloading tensile tests at: a) 400 °C; b) 500 °C

Figure 5.16 presents the stress-strain curves of tensile tests at 600 °C and 700 °C. The initial portion of the loading stress-strain curve at 600 °C presents various non-linear behavior, which is probably due to the alignment of specimens and the mooring system of the servo-hydraulic testing machine. The beginning part of the loading stress-strain curve at 700 °C presents perturbations that could be due to the sample distortion caused by the contact problem between the sample and the pinned grip at the beginning of tensile tests (Appendix D).

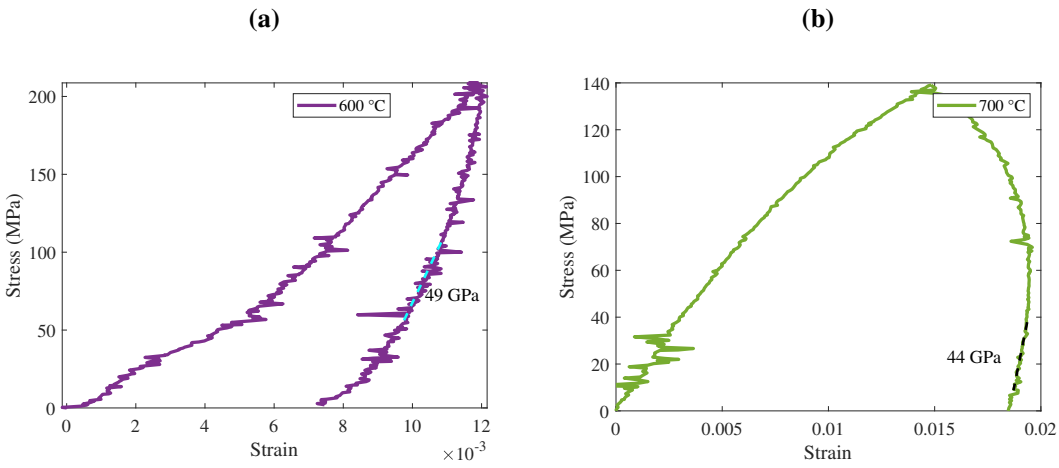

Figure 5.16: Stress-strain curves of the loading/unloading tensile tests at: a) 600 °C; b) 700 °C

The unloading stress-strain curves at these temperatures are non-linear, unlike the shape of unloading stress-train curves of other lower temperatures. The unloading stress-strain curves at 600 °C and 700 °C are not linear, even the applied load was under the yield stress found in the literature (Table 5.6). This is more remarkable when we observe the stress-strain curves at 700 °C since the material on the ZOI of the specimen continued to be stretched during the unloading. The reason could be due to creep occurred during the tensile test because of the low

stress rate applied in the unloading (Figure 5.16b). As a consequence, the linear stress-strain regions of the unloading curves at 600 °C and 700 °C are not obvious. It is difficult to distinguish the linear region for Young's modulus identification. The Young's moduli at 600 °C and 700 °C are determined within low stress applied on the specimen, in the relatively linear stress range that is perceived by "eyes", from 50 MPa to 100 MPa for 600 °C (Figure 5.16a) and from 20 MPa to 40 MPa for 700 °C (Figure 5.16b). They are respectively 49 GPa and 44 GPa. It is noted that these values are approximated. They are only informative.

The apparent Young's modulus of the TA6V material measured using the 2D-DIC method at different temperature are presented in Table 5.7. The coefficients of linear regression R^2 and the stress range for calculating the Young's modulus by the Linear Regression method are also presented. The R^2 coefficient at 25 °C is excellent because there are no heat waves at room temperature. The Young's modulus found at 25 °C is similar to the one found by Sirvin et al. (Sirvin *et al.*, 2019). From 400 °C to 700 °C, the R^2 coefficients decrease because strain measurements are dispersed due to heat waves at HT. The Young's moduli at 400 °C and 500 °C in this study are in the order of magnitude compared with values found in the literature. However, apparent Young's moduli at 600 °C and 700 °C are lower than those in the study of Vanderhasten (Vanderhasten, 2007). This can be explained by the creep behavior that influences the strain measurements. The microstructure of the TA6V material in our study might be different from the literature.

In summary, it is seen that a non-linear behavior appears on the initial portion of the stress-strain curve during the loading path of tensile tests. The non-linear strain is probably due to the sample rotation and rigid body motion caused by the limitations of pinned grip and mooring system in the servo-hydraulic tensile machine, which is demonstrated by rotation fields of the specimen measured using the 2D-DIC method at 25 °C. From 25 °C to 500 °C, apparent Young's moduli determined in the unloading stress-strain curves are 10%-15% lower than values found in the literature. From 600 °C to 700 °C, low stress rate creates plastic deformations because the material may present a creep behavior under low stress. The phenomenon is noticed in Surand's study about creep behavior of TA6V at 600 °C, even the applied load was lower than the yield strength of TA6V (Surand, 2013). Therefore, the elastic region of material from 600 °C is extremely difficult to identify. The Young's moduli of TA6V at 600 °C and 700 °C are approximated (Table 5.7).

Table 5.7: Young's modulus of TA6V at different temperatures determined from the unloading stress-strain curves and reference values

Temp. [°C]	Stress range	Young's modulus	R^2	References
25 °C	150 MPa - 600 MPa	107 ± 4 GPa	0.999	110 ± 10 GPa (Sirvin *et al.*, 2019), 109 ± 3 GPa (Vanderhasten, 2007)
400 °C	150 MPa - 350 MPa	90 ± 2 GPa	0.980	103 ± 13 GPa (Sirvin *et al.*, 2019), 87 ± 3 GPa (Vanderhasten, 2007)
500 °C	100 MPa - 300 MPa	80 ± 1 GPa	0.979	97 ± 17 GPa (Sirvin *et al.*, 2019), 81 ± 1 GPa (Vanderhasten, 2007)
600 °C	50 MPa - 100 MPa	49 GPa*	0.783	76 ± 27 GPa (Vanderhasten, 2007)
700 °C	0 MPa - 40 MPa	44 GPa*	0.984	71 ± 33 GPa (Vanderhasten, 2007)

* The Young's modulus values is determined from one tensile test

Finally, the stress-strain curves of TA6V at high temperatures are noisy due to the heat disturbance. The R^2 coefficients decrease with temperatures. It is necessary to apply correction methods for strain fields measured using the 2D-DIC method at HT. That is why, in next Section 5.3.3, we present results the stress-strain curves at HT after correction methods for reducing the effect of heat waves.

5.3.2.2 Identification of the TEC of the TA6V material before correction

Figure 5.17a presents the evolution of the specimen temperature (in blue) and the longitudinal strain (in orange) versus time. A non-linear increase of temperatures and longitudinal strains at the beginning of heating (from 0 to 500 s) occurs. This is probably due to the characteristics of the closing furnace. Perturbations on temperatures and longitudinal strains at the beginning the heating is beyond our study. Figure 5.17b presents the evolution of longitudinal strains measured using 2D-DIC versus temperatures. From 150 °C (Figure 5.17b), the longitudinal strain increases linearly with time. The determined longitudinal TEC coefficient is from 1.1×10^{-5} to 1.4×10^{-5} for temperature range from 150 °C to 600 °C. These values are in the order of magnitude with the value measured using the dilatometer: $\alpha_{yy} = 1.1 \times 10^{-5}$ and with the one found in the literature (Julien, 2017). The wide values of TEC could be due to the microstructure of the samples, which were prepared from TA6V sheet by the waterjet cutting process but also from the accuracy of the 2D-DIC method. Furthermore, the R^2 coefficient for temperature range from 150 °C to 600 °C by the Linear Regression method was from 0.974 to 0.984, which is lower than the one obtained by the dilatometer (R^2 = 0.996). This is due to the high dispersion of strain measurements due to the heat waves effect (Figure 5.17b). The R^2 coefficient and the strain-temperature using the 2D-DIC method are then improved by filter correction methods to reduce strain errors from heat waves.

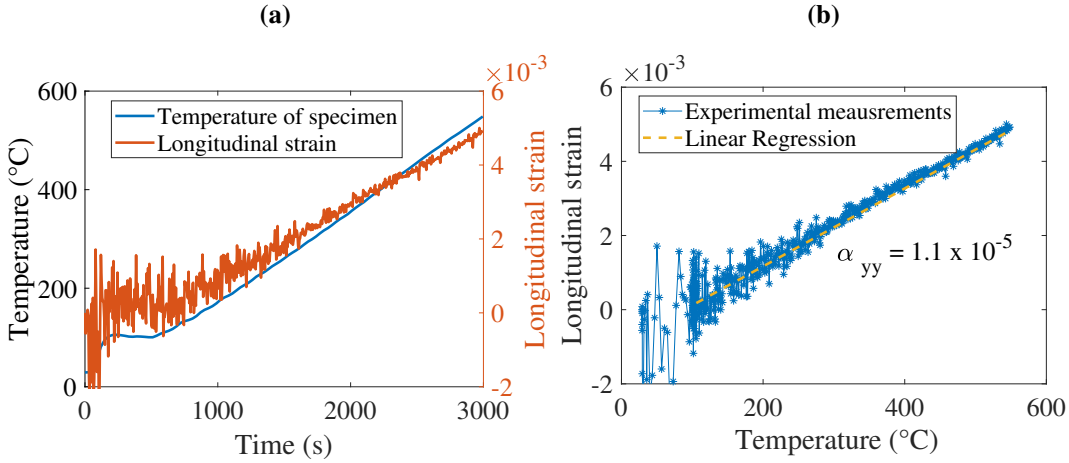

Figure 5.17: (a) Evolution of the TA6V's specimen temperature (in average) and the longitudinal strain measured using 2D-DIC versus time (b) Longitudinal strain versus temperatures

5.3.3 Efficiency of correction methods in measuring strains of mechanical tests at HT

5.3.3.1 Young's modulus of the TA6V material at HT after corrections

The post-processing using filter correction methods is applied for two applications: determination of the Young's modulus E and the coefficient TEC of the TA6V material at HT. The temporal strain errors are corrected using the temporal low-pass filter with cut-off frequency of 0.05 Hz. The mechanical strain fields is separated from the "total" strains using the optimized Gaussian filter. The optimized Gaussian filter uses the filter with size r and STD σ that depends on temperatures.

Figure 5.18 compares the loading/unloading stress-strain curves of tensile tests at 400 °C before (in blue) and after correction (in red). The temporal low-pass filter with a cut-off frequency of 0.05 Hz and the spatial Gaussian filter with size r of 99 and STD σ of 260 were applied on the strains measured by 2D-DIC method at 400 °C. Before the correction, the stress-strain curve is noisy because of heterogeneous strain fields, for example the strain maps at point 1 and 3 on Figure 5.18. After the correction, the stress-strain curve is clearly smoother. Strain maps at point 1 and 3 become homogeneous (point 2 and 4 in the blue curve). The apparent Young's moduli of TA6V at 400 °C determined by the unloading stress-strain curves before and after correction are similar: They are 89 GPa before and 90 GPa after filter. The coefficient R^2 is much improved. Indeed, it increases from 0.983 before filtering to 0.999 after filtering. It is evident that low-pass filters in time and space (temporal low-pass frequency and Gaussian filter) reduce random errors from thermal perturbations.

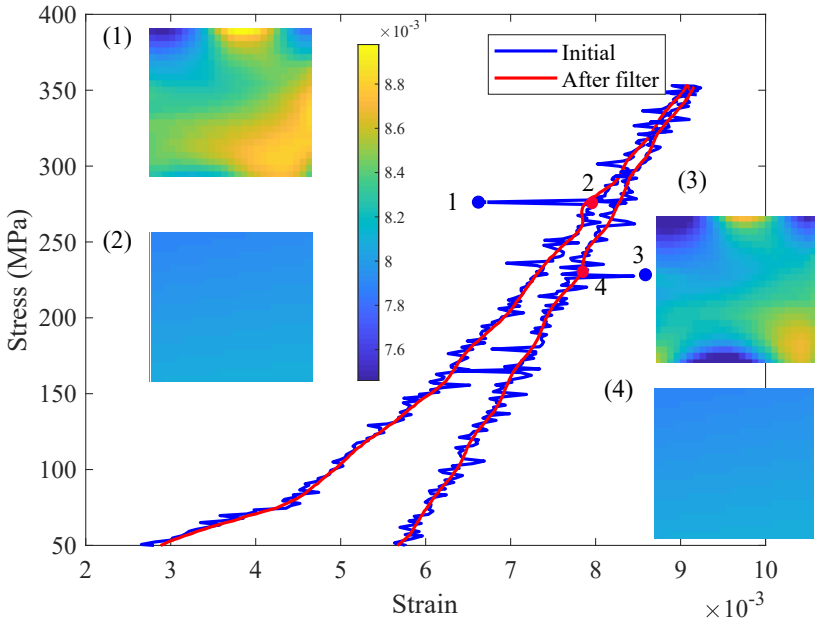

Figure 5.18: Stress-strain curves initial and after correction with low pass filter and Gaussian filter at 400 °C

Figure 5.19 compares unloading stress-strain curves before and after filtering at different temperatures 500 °C - 700 °C. The same tendency is observed on the stress-strain curves after filtering. They are smoother than initial curves without correction.

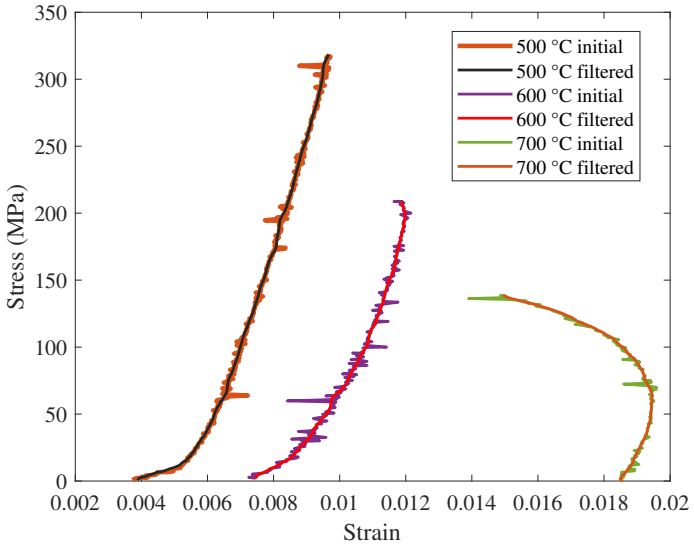

Figure 5.19: Stress-strain curves before and after correction with low-pass filter and Gaussian filter

The Young's modulus of the TA6V material and the R^2 coefficients at different temperatures are re-calculated and compared with those before correction (Table 5.8). It is seen that after correction, the apparent Young's moduli at 400 °C and 500 °C do not changed much. The R^2 coefficients after correction are excellent. The apparent Young's moduli calculated and the R^2 coefficients from the stress-strain curves at 600 °C and 700 °C are significantly improved. Results show a better mechanical strain measurements after correction methods.

Table 5.8: Young's modulus of the TA6V material at different temperatures and corresponding coefficients R^2

Temp.	Before filtering		After filtering	
°C	Young's modulus	R^2	Young's modulus	R^2
400 °C	90 ± 2 GPa	0.980	91 ± 1 GPa	0.999
500 °C	80 ± 1 GPa	0.979	81 ± 1 GPa	0.993-0.997
600 °C	49* GPa	0.783	54 GPa	0.989
700 °C	42* GPa	0.914	46 GPa	0.984

* Tensile tests at these temperatures were performed once

5.3.3.2 Thermal Expansion Coefficient of the TA6V material after corrections

The same post-processing with correction methods was applied on strain-temperature curves in order to determine the TEC of TA6V in the longitudinal direction with strains measured by the 2D-DIC. Figure 5.20 presents longitudinal strains versus temperatures curves of the TA6V specimen during heating. The blue curve is the "total" strains measured by the 2D-DIC method versus temperatures while the red one is the filtered strains versus temperatures. After being corrected by the low-pass frequency filter (cut-off frequency of 0.05 Hz), the strains versus temperatures curve are smoother. However, the wavy shape of the curve remains. On Figure 5.20, instantaneous strain maps at time t before the Gaussian filter (image (1)) and after filter

(image (2)) are also presented. It is seen that the strain map after filtering is clearly more homogeneous. Strain heterogeneity is reduced to 3.9×10^{-4} by using a Gaussian filter size of r = 99 and σ = 260. The TEC coefficient in the longitudinal direction Oy measured before and after filter is not changed: $\alpha_{yy} = 1.4 \times 10^{-5} \pm 5 \times 10^{-6}$ °C^{-1}. However, the R^2 coefficient after filter is significantly improved, from R^2 = 0.984 to R^2 = 0.996.

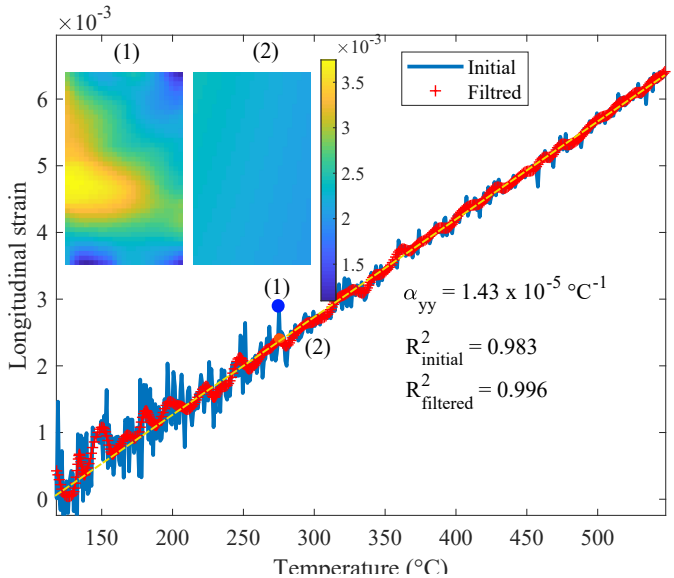

Figure 5.20: Strain measured on the ZOI of specimen versus temperature before (in blue) and after correction methods (in red)

5.3.4 Results synthesis

Two applications of the correction method using temporal and spatial low-pass filters are applied to measure "elastic" strain using the 2D-DIC method. Strains after corrections are used to determine:

- the Young's modulus of the TA6V material from 25 °C to 700 °C in isothermal condition,
- the thermal expansion coefficient (TEC) of the TA6V material from 150 °C to 600 °C

Before correction, an improvement in mechanical tests by using the loading/unloading protocol is suggested. It is proven that the new protocol can suppress the systematic error of strains measured by the 2D-DIC method due to the misalignment and sample rotation of the specimen at the beginning of tensile tests. The apparent Young's modulus of the TA6V material, determined by strains measured in the unloading tensile tests is more accurate and close to the reference values.

The efficiency of the filter correction method is demonstrated by two applications: measuring the Young's modulus from 400 °C to 700 °C and the TEC in longitudinal direction of the TA6V material from 100 °C to 600 °C. It is shown that after the temporal low-pass frequency filter, the strain curves present less dispersed strain measurement points therefore the R^2 coefficients are improved. The values of Young's modulus are slightly improved and while the longitudinal TEC coefficient remains unchanged. Furthermore, thanks to the spatial Gaussian filter, the instantaneous strain fields having high strain heterogeneity are significantly smoother.

5.4 Discussions

5.4.1 Efficiency of correction methods for reducing strain measurement errors caused by heat waves

5.4.1.1 Hypothesis employed in correction methods using filters

Previous studies in the literature (section 5.1.2) have documented the influence of heat waves on kinematic measurements at high temperatures. They suggest many methods to reduce these errors. Due to the limitations of equipment and the experimental set-up environment, techniques or methods suggested can not be applied in our case study. Therefore, another post-processing method on kinematic field that renders more reliable measurements (measurement points are less dispersed and more accurate) is suggested. The post-processing uses the temporal low-pass frequency filter which reduces the temporal strain errors. The Gaussian filter, with appropriate parameters can reduce spatial strain errors from heat waves and separate the mechanical strain fields from the "false" strain, caused by the convection flow surrounding the specimen. It is noted that the filtering methods are based on three "strong" hypotheses:

- the continuity condition of solid mechanics. The mechanical strain would be linear and "continuous" with time within the elastic domains. Therefore, mechanical signals would appear at the frequency of 0 Hz,
- the material's strain field would be homogeneous on the ZOI of the specimen in the elastic domain,
- heat waves cause only random errors.

5.4.1.2 Discussion on the efficiency of correction methods using filters

First, results from temporal correction shows a higher efficiency of using low-pass filter compared with the other filter types, i.e., the median, the Gaussian and the moving average. After the filtering with a 0.3 Hz-cut-off frequency, the random error is reduced by 61% while the other types of filter show the same performance: 45% of reduction. This is the reason why the temporal low-pass frequency filter is chosen to study the influence of cut-off frequency on the mechanical signal. In a range of cut-off frequency from 0.01 to 2.5 Hz, the closer the cut off-frequency is to 0 Hz, the more random errors are eliminated, providing less dispersion in the strain measurements of tensile tests. The wavy strain curves after filtering is obtained because signals in frequency lower than the cut-off frequency are remained. Furthermore, the mechanical signal at fundamental frequency (0 Hz) is conserved, showing the efficiency of the temporal low-pass frequency filter.

Secondly, the effect of four spatial filters on reducing the spatial strain errors appeared in instantaneous strain fields is evaluated. Among four filters, the spatial Gaussian filter presented the best efficiency on reducing the strain heterogeneity caused by heat waves. The optimized Gaussian filter with optimized parameters of the filter size r and the STD σ permits to reduce the strain heterogeneity at HT to 2.5×10^{-4}. Therefore, instantaneous strain fields after filter are significantly more homogeneous than their uncorrected strain fields.

Results obtained in this study are in agreement with a study of Jones et al. (Jones *et al.*, 2018). The authors showed that the Butterwoth filter with cut-off frequency of 0.1 Hz reduced both the spatial and temporal STD of displacement and strain and also conserved the initial magnitude.

Besides the low-pass filter, the average methods are usually used in order to mitigate the heat disturbance. Lyons et al. increased the subset size (Lyons *et al.*, 1996) while Chen et al., Dong et al. and De Strycker et al. used image averaging method, a direct smoothing method to reduce the strain heterogeneity (L. Chen *et al.*, 2016, Dong *et al.*, 2020 and De Strycker *et al.*, 2010). Furthermore, the Spatial-Temporal Subset (STS-DIC) framework developed by Chi et al. demonstrated its efficiency in significantly reducing the STD of displacement while measuring the TEC of a metallic material (Chi *et al.*, 2018). Wang et al. compared the performance of the STS-DIC method with the temporal average, a post-processing procedure for smoothing strain curves (X. Wang *et al.*, 2017). However, the performance of the new method is better compared with the spatial DIC (in both the global-2D-DIC and the local 2D-DIC) only if images present a high level of noise.

5.4.1.3 Application examples of correction methods to measure elastic properties of the TA6V material

After correction methods using filters, the strain measurements are used to calculate the apparent Young's modulus of the TA6V material at different temperatures: 25 °C to 700 °C and the TEC of the TA6V material from 150 °C to 600 °C.

Results showed that after correction, the coefficients by the Linear Regression method R^2 from the stress-strain and strain-temperature curves are significantly improved. The R^2 coefficients after correction are generally higher than 0.98 while without correction, the R^2 are lower than 0.98. It means that strain measurements using the 2D-DIC and correction methods are more reliable. The R^2 coefficients after correction method are slightly lower than those in the study of Chi et al. (Chi *et al.*, 2018). The strain heterogeneity observed during tensile tests because of heat waves is also minimized.

The Young's modulus and the TEC of TA6V material from 100 °C to 600 °C are lower but still in the order of magnitude of those found in the literature (Vanderhasten, 2007, Odenberger *et al.*, 2013, Sirvin *et al.*, 2019 and Surand, 2013). De Strycker et al. found that the Young's modulus measured by 2D-DIC system is lower than that measured by an extensometer (De Strycker *et al.*, 2010). The lower values found could be related to the systematic strain errors that are related to experimental conditions of the DIC system or linked with the microstructure of the TA6V material.

Results obtained in our study show a high potential of using the 2D-DIC method with filter correction methods to measure the elastic parameters of materials at HT. The method is flexible, easy-to-implement and does not require expensive devices. It could be a reliable method to estimate the order of magnitude of elastic parameters of materials at HT.

5.4.2 Contribution and limitations of correction methods

5.4.2.1 Contribution

The correction methods use the temporal and spatial filters to reduce the highly dispersed strain measurement points in space and in time by the 2D-DIC method. The amplitude of mechanical strain measurements during tensile tests are conserved while white noise and strain errors due to mirage effects at frequency higher than 0.05 Hz are significantly reduced. Furthermore, instantaneous strain maps during tensile tests at high temperatures, which are sometimes significantly influenced by heat disturbances during tensile tests are smoother. The

mechanical strain maps and the strain errors can be separated, giving more information about the mechanical signal (the interesting signal) and also the convection flow in the furnace during tests. The Young's modulus and the thermal expansion coefficient are calculated with more accuracy by the Linear Regression Method: the coefficients R^2 are more than 0.98.

Contrary to correction methods that are suggested in the section 5.1.3, the post-processing method using filters in our study requires neither additional devices nor many images. It is noted also that the correction methods using filter are inspired by a study of Jones et al. in which filters were applied for a static object (Jones *et al.*, 2018). The contribution of this study is improving the 2D-DIC method to measure "small" thermo-mechanical strain at HT. The mirage effect and heat waves problem is still a challenging subject of the 2D-DIC method.

5.4.2.2 Limitations

The limitation of correction methods comes from three hypotheses (Section 5.4.1.1). First, in these correction methods using filters, it is assumed that the mechanical continuity is strictly respected. The mechanical strains would be continuous and appear at the lowest frequency.

Furthermore, mechanical strain are supposed to be homogeneous in the elastic domain. The subset size, and the step size are large to minimize the white noise and the influence of heat waves. Therefore, the spatial resolution is low, 57 pixels, which is equivalent to $\approx$ 800 µm. It means that local plastic deformation of materials that can appear under or near yield strength of material would not be detected.

Finally, the "false" strain due to mirage effects are supposed to be random. The frequency of heat waves are higher than mechanical strain, which should be the "continuous" signal. The magnitude of strain errors depends on experimental conditions, i.e., furnace meaning that filter parameters (size, cut-off frequency) are no longer true if conditions change.

5.4.2.3 Procedure to apply the correction methods using filters on mechanical tests at HT

In order to identify the elastic parameter of materials using the improved-2D-DIC method (the 2D-DIC and correction methods), the general procedure to minimize the effect of heat waves on strain measurements at high temperatures are suggested as follows:

1. First, the strain uncertainty at room temperature related to experimental set up conditions (lighting, exposure time, 2D-DIC algorithm) would be measured.
2. The "false" strain errors caused by convection flow should be quantified in term of their magnitude and frequency by techniques for characterizing the convection flows, i.e., the BOS technique.
3. Temporal strain error would be corrected by using temporal low- pass frequency filter with an appropriate cut-off frequency. The cut-off frequency should be lower than the heat wave's frequency, which depends on the characteristic of the heat flow.
4. Instantaneous spatial strain maps that are heavily influenced by heat waves (characterized by high strain heterogeneity) would be identified then corrected by the optimized Gaussian filter. The optimized Gaussian filter has r and σ parameters depending on temperatures. It minimizes the spatial strain error due to heat waves to the strain uncertainty at 25 °C.

5.5 Conclusion and perspectives

Chapter 5 presents correction methods using temporal and spatial filters that minimize the effect of heat waves on strains measured by the 2D-DIC method at high temperatures.

The correction methods used the temporal low-pass frequency filter that reduces mostly temporal strain errors due to heat waves. This filter, with a cut-off frequency lower than 0.05 Hz can reduce more than 75% of errors from noise and heat waves. Moreover, the amplitude of the "continuous" signal, the thermo-mechanical strains is conserved. The spatial Gaussian filter is applied only on instantaneous strain maps which present important spatial strain errors, which are characterized by the strain heterogeneity due to heat waves. The Gaussian filter can separate the thermo-mechanical strain field and the strain error field. The optimized Gaussian filter with parameters: size r and the standard deviation σ which depends on temperatures.

Strain fields after correction are then employed to identify the TA6V material's properties at high temperatures: the Young's modulus and the thermal expansion coefficient of the material from 25 °C to 600 °C. Before the correction, the loading/unloading uniaxial tensile tests protocol with a stress rate of 8 MPa s^{-1} is developed to reduce the effect of sample rotation and the alignment of gripping system of the servo-hydraulic testing machine on the apparent Young's modulus of the TA6V material. After correction methods, the apparent Young's modulus of the TA6V material at 400 °C and 500 °C, determined by the Linear Regression method has the same order of magnitude with values found in the literature. The apparent Young's modulus of TA6V material at 600 °C and 700 °C is lower than values found in the references, probably due to the creep behavior of the TA6V specimen at very high temperatures. After correction methods, the coefficients R^2 are improved. Instantaneous strain fields having high strain heterogeneity due to heat waves become more homogeneous as well.

The longitudinal TEC coefficient of the TA6V material is determined by strain measured by improved-2D-DIC method (the 2D-DIC and correction methods). It is from 1.1×10^{-5} to 1.4×10^{-5} °C^{-1}, which is higher than the value determined by the dilatometer method. After the correction methods, the R^2 coefficient is also significantly improved and instantaneous strain fields having high strain heterogeneity due to heat waves become smoother.

In this study, there are three hypotheses, which give rise to two main limitations: the correction methods can reduce only random 2D-DIC errors caused by heat waves and the correction method works in the elastic domain. Further studies would focus on:

- using the correction methods to identify other elastic properties of the material at high temperatures, for example the Poisson ratio of the TA6V material at HT,
- improving the spatial resolution of 2D-DIC method at high temperature by reducing the size of subset,
- extending the corrections methods to the early plastic behavior of materials at HT to identify the plastic deformation strain map that could occur during tensile tests,
- applying the 2D-DIC and correction methods to measure strains in semi-industrial case study: cooling a hot-stamp piece (in 2D) to room temperature, for example: cooling the Omega-shape piece.

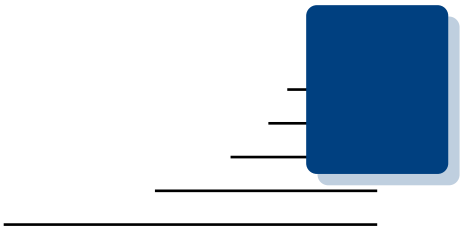

Conclusion

Conclusion

In the industrial context, the general objective of the Ph.D. thesis is to develop a full-field measurements method that enables reliable strain measurements of a piece during the cooling phase of the hot stamping process (400 °C - 750 °C). After the literature review on kinematic measurement methods used in experimental mechanics, i.e., the strain gage, the fringe projection, the grid method and so on and having considered available devices in our laboratory, the local-2D-DIC method is chosen to measure "small" strain (the mechanical strain ε is from 0.02 to 0.05) of the TA6V material at HT.

The 2D-DIC method is the most widely used non-contact method for experimental mechanics at room temperature. The method is able to measure mechanical strains with high accuracy. Nevertheless, it is necessary to improve the 2D-DIC method at high temperatures because the it presents some limitations because of temperature effects. Therefore, the Ph.D. thesis aims to:

- find speckle patterns that resist high temperatures and high strains
- improve the image contrast captured by visible camera
- correct the effect of heat waves that make mechanical strain less reliable (high dispersion and less accuracy)

To improve the 2D-DIC method at HT, some effort has been directed to solve each problem.

The speckle problematic for high temperature mechanical tests is first resolved and it is presented in chapter 2. The chapter aims to find a speckle pattern respecting "good" speckle criteria, highly resistant to temperatures (from 400 °C to 750 °C) and strain (strain is at least 1.0). For this purpose, six speckle fabrication techniques are suggested. These six different speckles are repeatable because they are produced from a computer-generated speckle pattern that meets criteria for a "good" speckle pattern for the DIC method. They are classified into two groups: the "additive" speckles on which the matter is added on TA6V samples and the "subtractive"

speckles on which the matter is subtracted from TA6V samples. The "additive" techniques include the painting (M1), direct anodization (M2), inverse anodization (M3) techniques. The "subtractive" techniques include the laser engraving (M4), combining anodization and laser engraving (M5) and combining paint and laser engraving (M6) technique. Among these six techniques, the speckle pattern made by combining anodization and laser technique M5 stands out for the best quality (morphology and contrast criteria) and a strain resistance up to a value of 2.0 (200%). This speckle fabrication method is recommended for temperatures from 25 °C to 600 °C. From 600 °C and higher temperatures, the speckle pattern made by M6 technique (combining paint and laser) is more appropriate to mechanical tests for strain measurements of less than 0.22.

Chapter 3 is dedicated to the setting of the 2D-DIC system and to evaluate the influence of parameters in the 2D-DIC system on image contrast at HT. After considering the constraint of experimental conditions: a limited field-of-view for capturing images because of the closing furnace for heating TA6V samples, the 2D-DIC configuration is implemented in front of the mechanical testing machine. A design of experiment (DOE) at 600 °C, (a representative temperature of the hot stamping temperatures), in which the influence on the image contrast of four 2D-DIC parameters is evaluated. Four parameters are the light intensity, the use of an IR filter, the light color and the exposition time of the camera. By the analysis of variance, at 600 °C, it is suggested that two factors having significant impacts on the contrast of images are: the use of IR filter and the exposition time of the camera. The interaction between two factors has an influence on the contrast of images as well. The 2D-DIC system configuration for the best image contrast is using an IR filter with a cut-off wavelength of 700 nm, an exposition time of 120 ms and a diffused white light with a high power (575 W). The MIG and the Shanon entropy of speckle images obtained from this set-up configuration are respectively 19.27 - 21.45 (MIG) and 6.6 - 6.9 (Shanon entropy).

Chapter 4 involves in characterizing strain measurement errors due to the mirage effect or heat waves. In our experimental conditions, it is supposed that the 2D-DIC strain measurement errors come from the convection flow developed in the closing furnace. The strain measurement errors are characterized by the BOS technique from 400 °C to 750 °C in isothermal conditions. In the BOS technique, the ZOI of TA6V samples is the background and TA6V samples are supposed to be immobilized by the testing machine during the experiment. Results show that the strain measurement error due to heat waves depends on working temperatures. The characteristics of strain measurement error are spatial and temporal. The spatial strain measurement error is characterized by heterogeneous "false" strain fields on the ZOI even TA6V samples are immobilized (in "static" condition). The order of magnitude (in average value) of strain measurement errors increase with temperatures. It is also different in two directions Ox and Oy. The temporal strain measurement error is characterized by regular variations of "false" strain measured on a fixed point of the ZOI. The frequency of the temporal strain error is low, about 0.2 Hz-1 Hz and depends on heat waves passing through the sample and the camera. The strain measurement errors versus temperatures are used as data for Chapter 5: correction methods for reducing strain measurement errors at HT.

Chapter 5 suggests improvements in 2D-DIC method (implementation and algorithm) for experimental tests at high temperatures by using results obtained from previous chapters: Chapter 2, 3 and 4. Indeed, speckles made by M5 technique was employed for temperatures from 25 °C to 600 °C. The optimized 2D-DIC system with the IR filter and exposition time was set up for experimental tests. The spatial and temporal characteristics of strain measurement errors are used for a post-processing that minimizes the effect of heat waves on mechanical

strains measured by the 2D-DIC method. The post-processing uses low-pass filters to reduce the dispersion of strain measurements versus time and the heterogeneity of instantaneous strain fields during experiment tests.

The temporal strain error in strain measurements is corrected first. A temporal low-pass filter with cut-off frequency of less than 0.3 Hz can eliminate more than 60% of highly-dispersed strain measurement points on the curves of mechanical strains versus times. Low cut-off frequencies reduce the dispersion of strain measurements by the 2D-DIC method. Furthermore, the temporal low-pass filter does not modify the magnitude of mechanical strains measured by the 2D-DIC method.

After the temporal strain errors are corrected by a temporal low-pass filter, the spatial strain error in strain measurements due to heat waves is processed. With the same methodology, instantaneous strain fields with high heterogeneity (more than 2.5×10^{-4}) during mechanical tests are identified then smoothed by the Gaussian filter. The Gaussian filter with the size $r = 99$ and STD $\sigma = 260$ can eliminate more than 60% of strain heterogeneity for temperatures from 400 °C to 600 °C. Higher filter size and STD values improve the homogeneity of the mechanical strain fields. The mechanical strain map and the spatial strain error maps due to the heat waves are then separated.

Finally, the post-processing method is used for two application examples: The first one is to determine the Young's modulus of the TA6V material at different temperatures, from 400 °C to 750 °C. The second one is to determine the TEC of TA6V material from 150 °C to 600 °C. Results obtained are very encouraging. Mechanical strains measured by 2D-DIC method after correction are more reliable. The coefficients of linear regression R^2 of stress-strain curves of TA6V material at HT are increased. Their values are more than 0.99 after corrections instead of 0.97 before correction, confirming that strain measurements are more reliable. The Young's modulus of the TA6V material after corrections are slightly lower than referent values. Regarding the strain versus temperature curve of the TA6V material, the R^2 coefficient after correction is 0.998 instead of its initial value R^2: 0.980. The TEC of TA6V material determined from 150 °C to 600 °C is higher than the value measured by the dilatometer: it is $1.4 \times 10^{-5} \pm 5 \times 10^{-6}$ °C^{-1} versus 9.0×10^{-6}-1.1×10^{-5} obtained from the dilatometer.

In conclusion, this Ph.D. thesis contributes to developing the 2D-DIC method for measuring mechanical strains in thermo-mechanical tests at high temperatures (from 400 °C to 750 °C). Improvements in the speckle patterns, the set-up of 2D-DIC system and the methods for correcting errors due to heat waves on strain measurements are suggested. Results from two applications present a great potential of the improved-2D-DIC method for measuring thermo-mechanical strain of a piece during the cooling phase of the hot-stamping process.

Perspectives

The contribution of this Ph.D thesis is to demonstrate that despite temperature effects, it is possible to obtain reliable (low dispersion and sufficiently accurate) "small" mechanical strain ($\varepsilon \approx 0.02 - 0.05$) by improving the 2D-DIC method at HT. Nevertheless, during the Ph.D. thesis, with limited time, we cannot treat all subjects related to the DIC method for kinematic measurements at high temperatures. The following subjects should be extended to complete the global objective of the Ph.D. in the industrial context.

In chapter 2, the strain resolution using "additive" methods: M1, M2, M3 is limited by the resolution of the polymer mask. An improvement of the design of experiment (DOE), for example a DOE of four factors: the radius of speckle dot, laser power, scanning speed and scanning strategy can be performed. This DOE can take into account the influence of the target size on the speckle radius that could increase the strain resolution. Furthermore, the matter transfer step is limited by the paint's viscosity. A technique to decrease the paint's viscosity, for example diluting the paint with solvent, would favor the paint transfer on TA6V specimen.

In chapter 3, the configuration of 2D-DIC system is adapted only to experimental conditions of our laboratory. With this actual configuration, it is seen that images captured by camera show a small variation of lighting on the ZOI of TA6V sample. More effort on the development of 2D-DIC system, for example, a reflection mirror system in order to get a homogeneous light condition should be addressed (Denis *et al.*, 2019). Furthermore, the oxidation of the TA6V material leading to the pixel saturation problem is not totally understood. It should be interesting to find its origin, i.e., a fine analysis on the chemical composition of the oxide layer on a speckle dots should be performed. If the oxide layer is the aluminine, the effective technique to eliminate the pixel saturation problem is to use a filter having cut-off wavelengths appropriate to the aluminine spectrum.

In chapter 4, it is supposed that the strain measurement errors come from a thermal gradient in the closing furnace. The thermal gradient can be observed by air density by optical methods, for example, the shadowgraphy technique. Therefore, it should be interesting to combine the shadowgraphy and the BOS technique to confirm the origin of strain measurement errors. For example, Delmas et al. used the shadowgraphy and the BOS techniques to visualize and measure the displacement of convection flow generated from a hot disk at 700 °C (Delmas, 2012).

In chapter 5, although the correction methods show its efficiency through two applications, it should be interesting to apply the 2D-DIC method with correction methods in a semi-industrial or industrial case study, for example cooling an Omega shape specimen after the hot stamping process (Sirvin *et al.*, 2019). Afterward, the full-field strain measurements can be used to compare results obtained from experimental tests and those given by numerical simulations.

Finally, based on very encouraging results obtained from the Ph.D. thesis, our motivation is continuing to develop the 3D-DIC method in the configuration of a hot stamping process (high temperatures and limited space) to measure continuously mechanical strains for cooling a 3D-piece after the hot stamping process.

Appendix

Appendix A

A.1 TA6V microstructure

Figure A.1 illustrates the TA6V microstructure at room temperature. The materials is composed by two phm ases: the α phase in darker color which is rich in Aluminum element and the β phase in brighter color which is rich in Vanadium element.

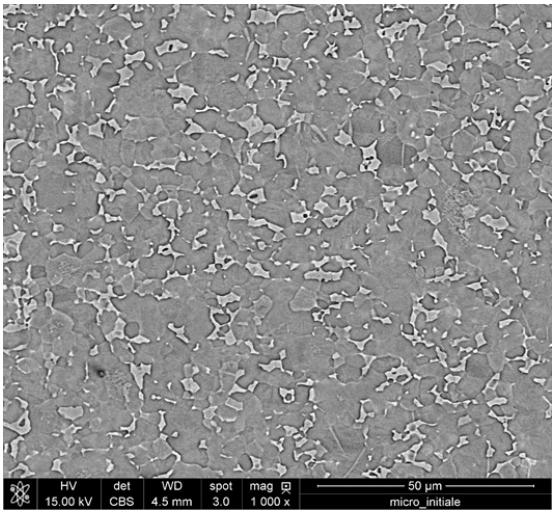

Figure A.1: Microstructure of TA6V material at room temperature

A.2 Selective Laser Melting (SLM) machine and the different laser trajectory strategies for melting the metallic powder

Figure A.2 presents the Laser Selective Melting SLM machine using a laser source to create speckle patterns on polymer (for speckle technique M1, M2, M3) and on TA6V samples. The left-hand side photo is the overview of the SLM®125HL (SLM®solution, Lübeck, Germany). The right-hand side photo display the laser chamber where specimens were sticked on a plateau then engraved by a laser source.

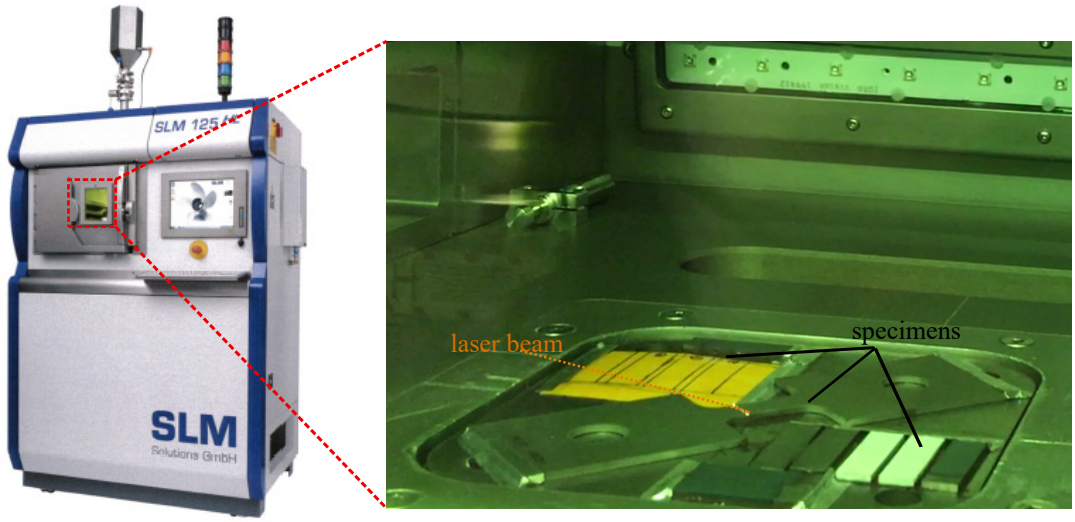

Figure A.2: Presentation of the SLM125HL machine used to created the speckle pattern on the polymer thin film and on TA6V samples

Figure A.3 illustrates three types of laser scanning strategy of the SLM 125HL machine. The first strategy is the contouring (Figure A.3a) where laser scanning is circular (round lines). The second strategy is the hatching (Figure A.3b) where laser scanning is straight (simple lines). The third strategy is the mix of contouring and hatching (Figure A.3c) where laser scanning is straight inside the circle and then circular for one contouring line.

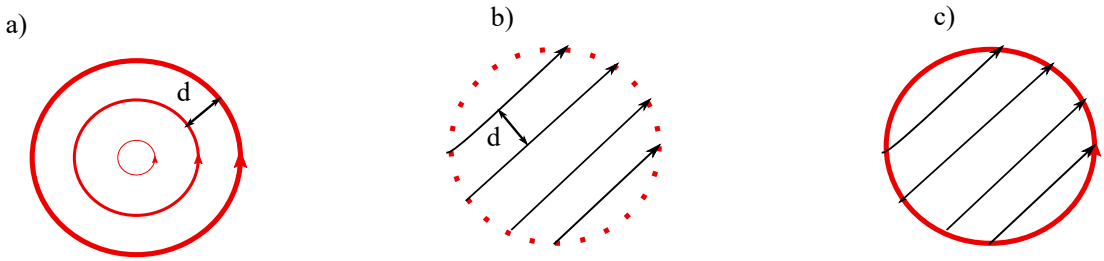

Figure A.3: Three types of laser scanning strategy in the SLM machine: (a) Contouring, (b) Hatching, (c) Mix of Contouring and Hatching

A.3 TA6V specimen geometry used for tensile tests

Figure A.4 presents a two-dimensional TA6V specimen drawing (in the plan Oxy) used for tensile tests. The specimen's dimension is 125 mm × 38 mm × 1.6 mm in length × width × thickness. The ZOI of specimen is 15 mm × 8 mm.

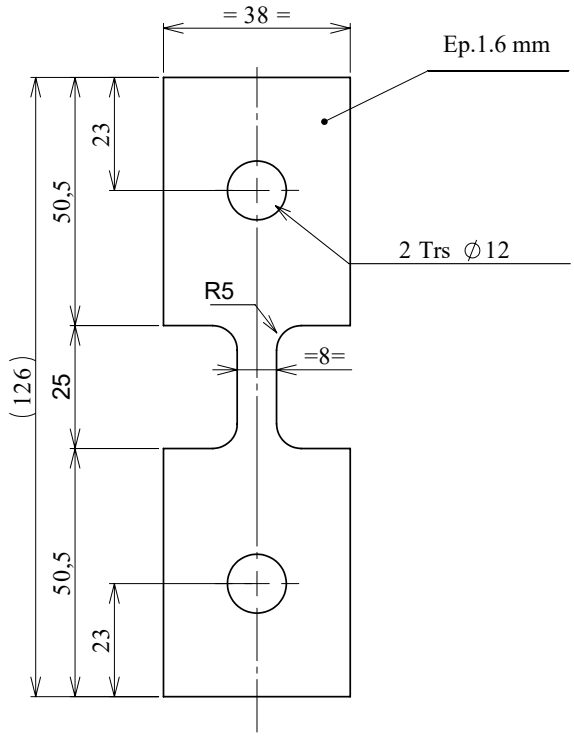

Figure A.4: Two-dimensional TA6V specimen drawing used for tensile tests

APPENDIX

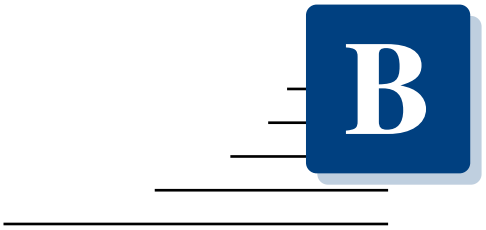

Appendix B

B.1 Transmission spectrum of short-pass 650 nm filter

Figure B.1 presents the transmission spectrum of the short-pass 650 nm filter. The transmission versus wavelength of the filter showed that the transmission was more than 80%.

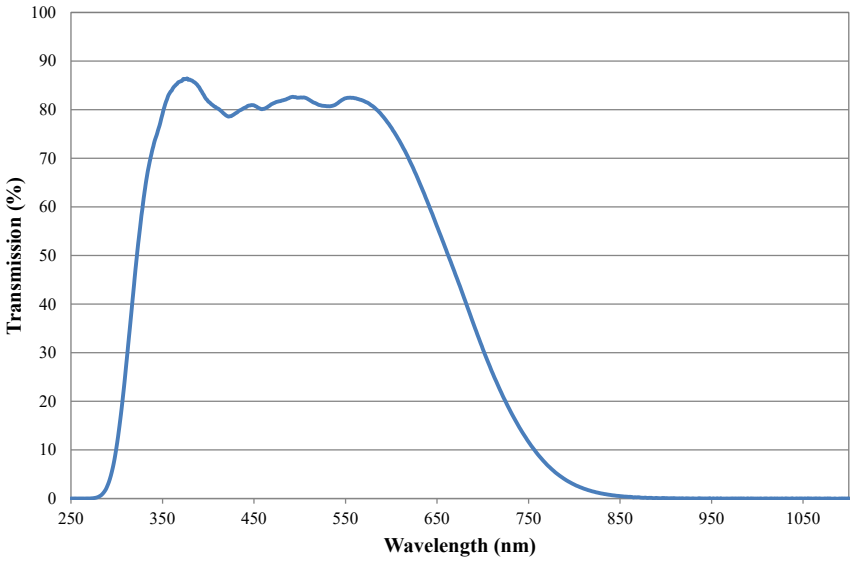

Figure B.1: Transmission spectrum of the short-pass 750 nm filter

B.2 Analysis of variance of the influence factors on image quality at high temperature

Figure B.2 and B.3 display results of the analysis of variance on the parameters of the 2D-DIC system (four factors: IR filter, light intensity, the use of green light and the exposition time) on image contrast, evaluated by two criteria: MIG and Shannon entropy value. For each parameter, the sum square of variance, the degree freedom, The Fisher test F and the probability P was calculated. The parameter having $P < 0.05$ (5% of confidence) means that this factor have significantly influence on result.

Analysis of Variance

Source	Sum Sq.	d.f.	Mean Sq.	F	Prob>F
Filter	102.931	1	102.931	11.22	0.0203
Intensity	1.009	1	1.009	0.11	0.7536
Color	4.926	1	4.926	0.54	0.4966
Gray level	570.708	1	570.708	62.22	0.0005
Filter*Intensity	3.012	1	3.012	0.33	0.5914
Filter*Color	1.324	1	1.324	0.14	0.7196
Filter*Gray level	0.084	1	0.084	0.01	0.9276
Intensity*Color	13.115	1	13.115	1.43	0.2854
Intensity*Gray level	0.174	1	0.174	0.02	0.8957
Color*Gray level	5.586	1	5.586	0.61	0.4705
Error	45.864	5	9.173		
Total	748.734	15			

Figure B.2: (a) Analysis of variance of factors influence on image contrast characterized by MIG criterion at 600 °C

Analysis of Variance

Source	Sum Sq.	d.f.	Mean Sq.	F	Prob>F
Filter	3.6653	1	3.6653	20.59	0.0062
Intensity	0.5417	1	0.5417	3.04	0.1416
Color	0.9399	1	0.9399	5.28	0.07
Gray level	13.4579	1	13.4579	75.59	0.0003
Filter*Intensity	0.0458	1	0.0458	0.26	0.6336
Filter*Color	0.0031	1	0.0031	0.02	0.9005
Filter*Gray level	2.4759	1	2.4759	13.91	0.0136
Intensity*Color	0.0259	1	0.0259	0.15	0.7185
Intensity*Gray level	0.3969	1	0.3969	2.23	0.1956
Color*Gray level	0.6981	1	0.6981	3.92	0.1046
Error	0.8902	5	0.178		
Total	23.1407	15			

Figure B.3: (a) Analysis of variance of factors influence on image contrast characterized by Shannon entropy criterion at 600 °C

B.3 EDX-micro analysis on the surface of a speckle dot after three hours of heating at 600 °C

Figure B.4 presents the spectrum measured by EDX micro-analysis (E= 19 KeV) technique on the surface of a speckle dot after being heated at 600 °C. The elements detected on the surface were Oxygen, Vanadium, Titanium and Aluminum. Table B.1 presents the % of element (in weight and in atomic) of elements detected on the surface of a speckle dot after being heated at 600 °C for three hours. A high percent of oxygen element suggested that the speckle dot was strongly oxidized during the heat.

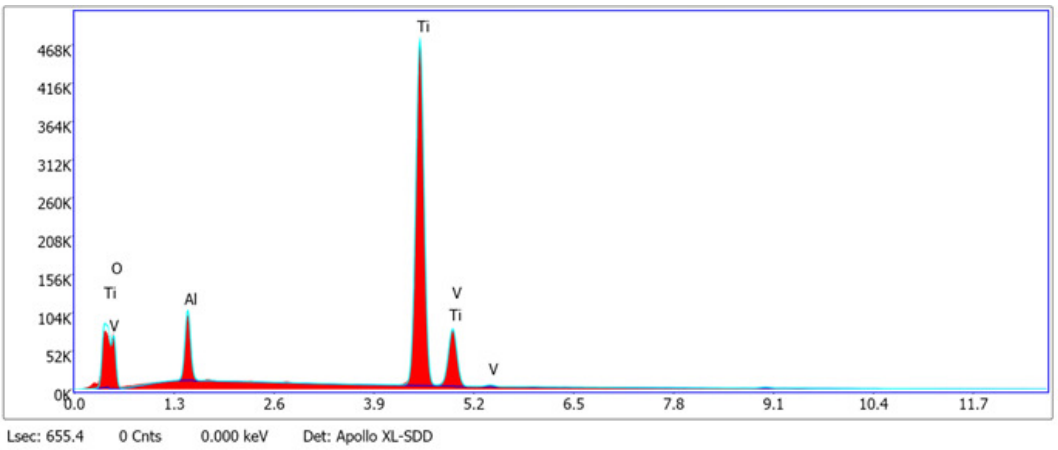

Figure B.4: EDX micro-analysis spectrum on the surface of a speckle dot made by M5 technique after three hours of heating at 600 °C

Table B.1: Mass percentage and atomic percentage of each element detected on the surface of a speckle dot made by M5 technique after three hours of heating at 600 °C

Element	Weight %	Atomic %
O (K)	31.63	56.47
Al (K)	6.17	6.53
Ti (K)	59.5	35.48
V (K)	2.7	1.51

APPENDIX

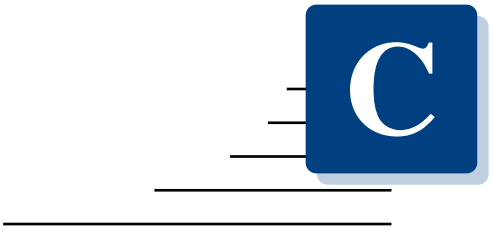

Appendix C

C.1 Evaluation of "static" condition for experiments of characterizing the strain uncertainty at HT

C.1.1 Introduction

In section 4.3.2, a pre-load of 0.1 kN applied on the TA6V specimens was maintained during the experiments for strain measurement errors at high temperatures. At very high temperatures, specimen could be deformed under a small load (0.1 kN). To ensure the "static" condition of the TA6V specimen for each experiment, the load signal, the displacement of the lower cross-head of the testing machine and the displacement on the ZOI measured by the 2D-DIC method were verified.

C.1.2 Methodology

To ensure the the "static" condition of the TA6V specimen for each experiment, the load signal, the displacement of the lower cross-head of the testing machine and the displacement on the ZOI measured by the 2D-DIC method, with the magnification of 13.9 µm/pixel, were registered for 20 min - 30 min (long-time experiment) in "static" and "isothermal" condition. The displacement of the lower cross-head of the testing machine corresponds to the global displacement of the specimen (displacement of all areas on the specimen). The sampling frequency of three signals

are 1 Hz. Table C.1 presents the experiments and the temperatures corresponding, in which the three signals were registered during the experiments. It is noted that for each experiment was performed once.

Table C.1: Experiments and corresponding temperatures in which the load, the displacement of the lower cross-head of the testing machine and the displacement on the ZOI measured by the 2D-DIC method were registered in "isothermal" and "static" conditions

Test N°	T °C	Time registration
1	600 °C	25 minutes
2	700 °C	25 minutes
3	750 °C	20 minutes

C.1.3 Results

C.1.3.1 Mechanical load applied on specimens in "static" conditions

Figure C.1 plots the mechanical load applied on the TA6V specimen versus time during more than 20 min at 600 °C, 700 °C and 750 °C. These three temperatures are particularly paid attention because the stiffness of specimen is low due to the reduction of the Young's modulus of the TA6V material (Vanderhasten, 2007). It can be easily deformed under load.

During the acquisition time, the mean value of loading is 96.3 N which is close to the programmed load (100 N). The load registered at three temperature varies from slightly from 90 N to 105 N. At 700 °C and 750 °C, there are only some load values which are about 80 N or 120 N. These fluctuations are probably due to load regularization controlled by the TestStar® controller during experiment or noise measurement. The load applied on the specimen is relatively stable during the experiments.

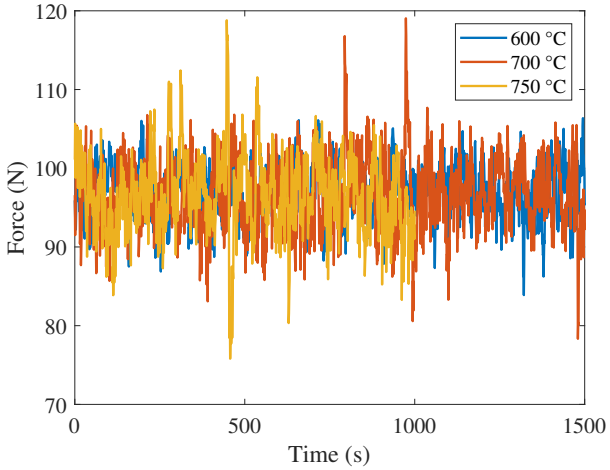

Figure C.1: Mechanical load measured during more than 15 min of experiments in "isothermal" and "static" conditions

C.1.3.2 Displacements measured on the specimen in "static" condition

The displacements of the lower cross-head were measured (Figure C.2a) then compared with those measured on the ZOI using the 2D-DIC method (Figure C.2b) at three temperatures: 600 °C, 700 °C and 750 °C.

It is shown in that the displacements of the cross-head and the ZOI of the specimen at 600 °C is nearly null. It means that the specimen is "immobilized" under a constant load of 0.1 kN. However, at 700 °C and 750 °C, displacements of specimens measured by the displacement of the lower cross-head of the testing machine and by the 2D-DIC method increase with time. The specimen are probably deformed or moved during long-time experiments. The displacements of specimen increases with temperatures. There is also a difference of displacements measured by the cross-head of the testing machine and the one measured by the 2D-DIC method. The displacement of the cross-head of the testing machine represents the global displacement of specimen while the displacement measured by the 2D-DIC represents local displacement on the ZOI of the specimen. The global displacement is more than three times higher than the local one.

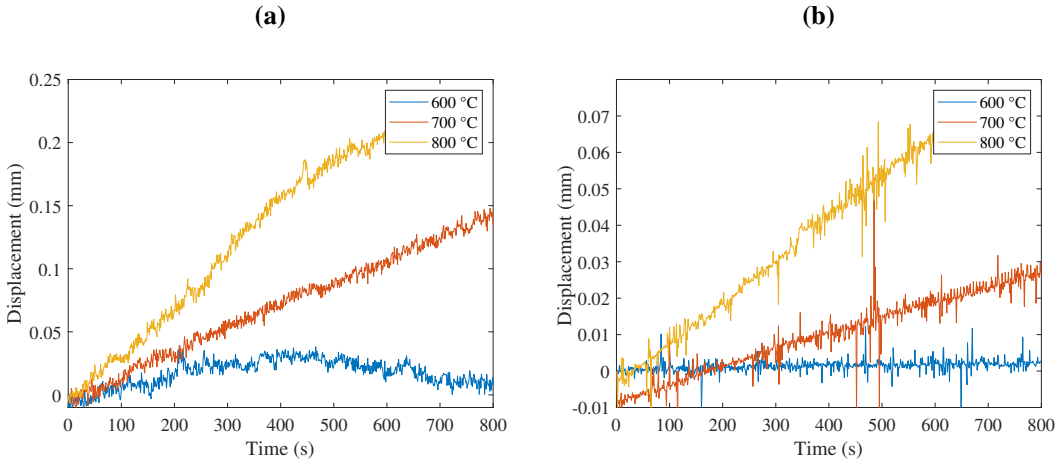

Figure C.2: (a) Displacement of cross-head, (b) Displacement of the ZOI of the TA6V specimen during more than 15 min in "isothermal" and "static" condition

To explain the difference between the global displacement measured by the cross-head and the local one measured by the 2D-DIC method, the form of specimen at initial state and after long-time experiment is compared. Figure C.3 presents the deformation of the lower head of a TA6V specimen after one hours of experiment under a constant load of 0.1 kN at 750 °C. On Figure C.3, the red circle presents the original head of the specimen before experiments. It is observed that the head is deformed after the long-time experiment. The deformation is probably due to the contact between the pinned grip and the head of specimen at high temperatures. A finite element model that simulates the contact pinned grip-TA6V specimen will be presented in Appendix D to explain the observation in Figure C.3.

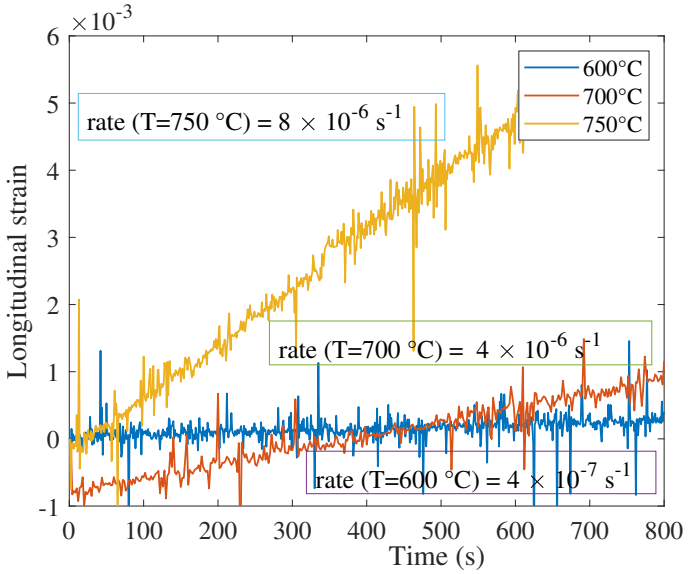

Figure C.4: Longitudinal strain versus time on the ZOI measured by the 2D-DIC method at three temperatures (600 °C, 700 °C, then 750 °C)

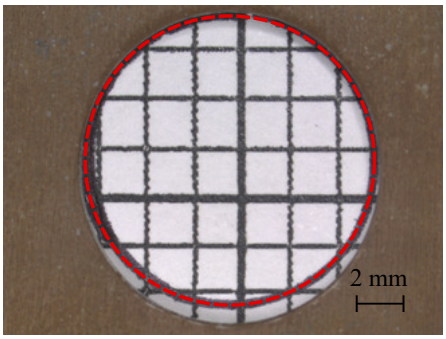

Figure C.3: Shape of a pinned head of a TA6V specimen in static condition after one-hour experiment. The dash red line indicates the initial form of the head

C.1.3.3 Strain rates measured using the 2D-DIC method in "static" condition

It is noted that small displacements on the ZOI of specimen occurred at 700 °C and 750 °C. These displacements increase nearly linearly with time. Therefore, strains on the ZOI measured using the 2D-DIC increase linearly with time. Strain rates of three temperatures are then estimated by the linear regression method (Figure C.4).

The strain rate at 600 °C is minor (4×10^{-7} s^{-1}) while those at 700 °C and 750 °C are higher (4×10^{-6} s^{-1} and 8×10^{-6} s^{-1}). Nevertheless, strain rates at three temperatures remain low. Since the experiment for characterizing the strain measurement errors due to heat waves last only several minutes, it is supposed that mechanical strains at 700 °C and 750 °C would not influence the strain measurement errors due to heat waves.

C.1.4 Conclusion

In this study, the "static" condition for the experiment of characterizing the strain measurement errors due to heat waves is evaluated. The condition is examined by the load, the displacement of the specimen measured by the displacement of the cross-head of the testing machine and the displacement on the ZOI of the specimen measured using the 2D-DIC method during more than 20 min. It is shown that at 600 °C, there is no mechanical strain. The specimen is "immobilized" under a constant load and "isothermal" condition for long time. Nevertheless, at 700 °C and 750 °C, the specimen is deformed or moved under a constant load and "isothermal" condition for long time. It is observed that the head of the specimen is deformed after one hour of experiment. Strain rates on the ZOI of the specimen are determined. They are respectively 4×10^{-6} s^{-1} at 700 °C and 8×10^{-6} s^{-1} at 750 °C. The low strain rates can be negligible compared with the strain uncertainty due to heat waves.

C.2 Histograms of strain measurement errors due to heat waves at HT

Histograms of the strain measurement errors in the "static" and "isothermal" conditions at 25 °C, 400 °C, 500 °C, 600 °C, 700 °C and 750 °C were systematically presented in following figures.

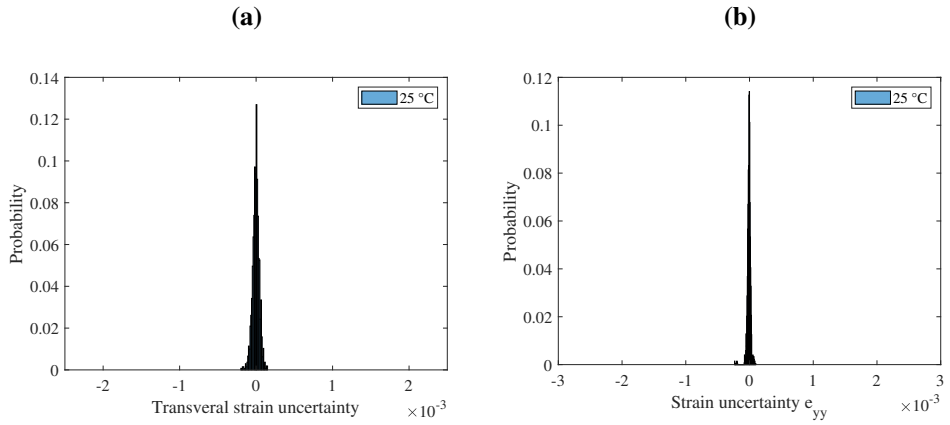

Figure C.5: Histograms of (a) transversal strain uncertainty e_{xx}; (b) longitudinal strain uncertainty e_{yy} measured at 25 °C

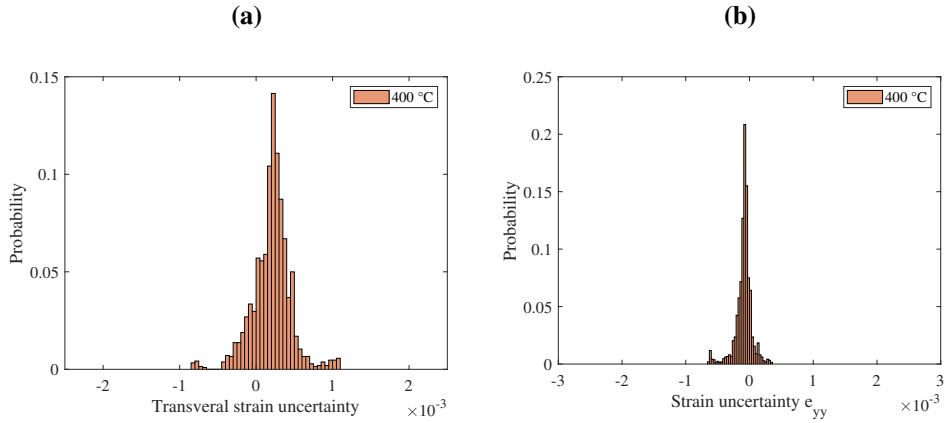

Figure C.6: Histograms of (a) transversal strain uncertainty e_{xx}; (b) longitudinal strain uncertainty e_{yy} measured at 400 °C

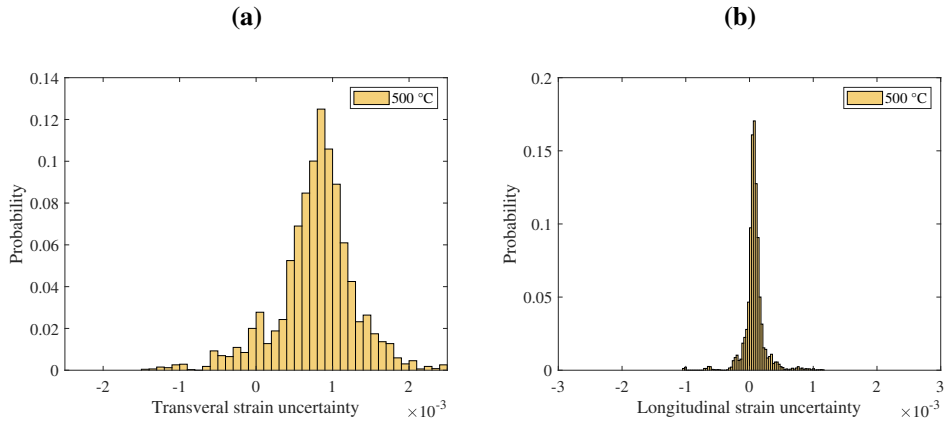

Figure C.7: Histograms of (a) transversal strain uncertainty e_{xx}, (b) longitudinal strain uncertainty e_{yy} measured at 500 °C

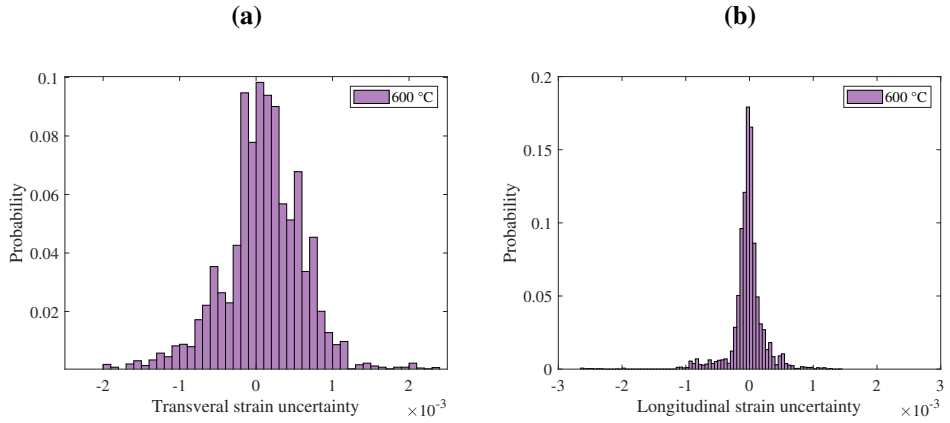

Figure C.8: Histograms of (a) transversal strain uncertainty e_{xx}; (b) longitudinal strain uncertainty e_{yy} measured at 600 °C

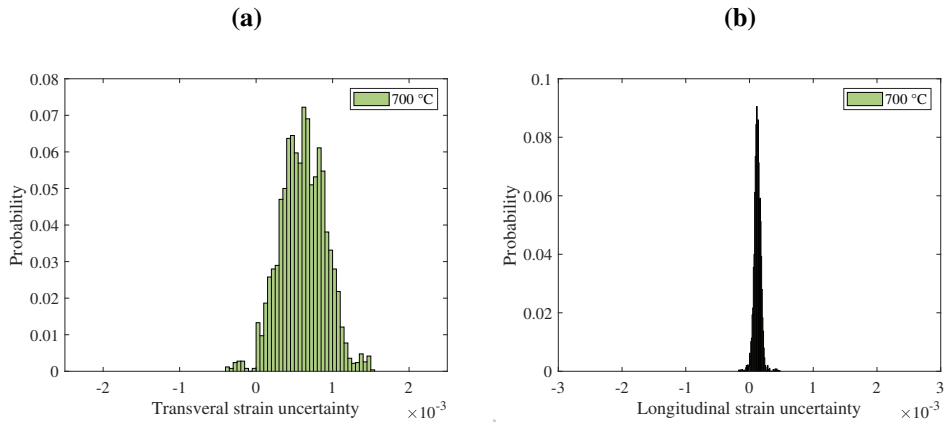

Figure C.9: Histograms of (a) transversal strain uncertainty e_{xx}; (b) longitudinal strain uncertainty e_{yy} measured at 700 °C

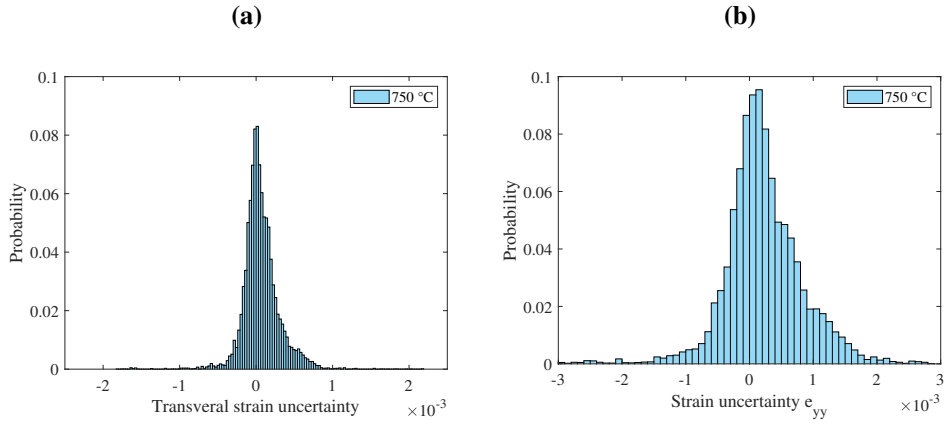

Figure C.10: Histograms of (a) transversal strain uncertainty e_{xx}; (b) longitudinal strain uncertainty e_{yy} measured at 750 °C

APPENDIX

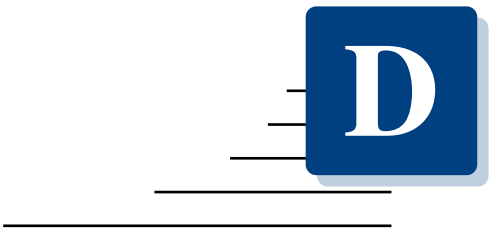

Appendix D

D.1 Introduction

D.1.1 Problematic

In chapter 5, the 2D-DIC and correction methods using filters are applied to measure thermo-mechanical strain of tensile tests on the TA6V material at high temperatures. The tensile tests are performed by the MTS servo-hydraulic testing machine with pinned grips (Figure 4.5c). The geometry of the TA6V specimen used for tensile tests are presented in Appendix A.3.

Tensile tests at high temperatures are performed in quasi-static condition with a stress rate of $8\,\mathrm{MPa\,s^{-1}}$, controlled by the displacement of the lower cross-head of the testing machine. The highest stress applied on the TA6V specimen is less than the yield strength of the TA6V material, which depends on temperatures (Table 5.6). Nevertheless, after tensile tests at high temperatures, i.e., at 700 °C, we observed that the lower-head of TA6V samples is plastically deformed with 0.5 mm (Figure D.1a). Furthermore, the ZOI of the specimen is lightly distorted after tensile tests (Figure D.1b).

a) b)

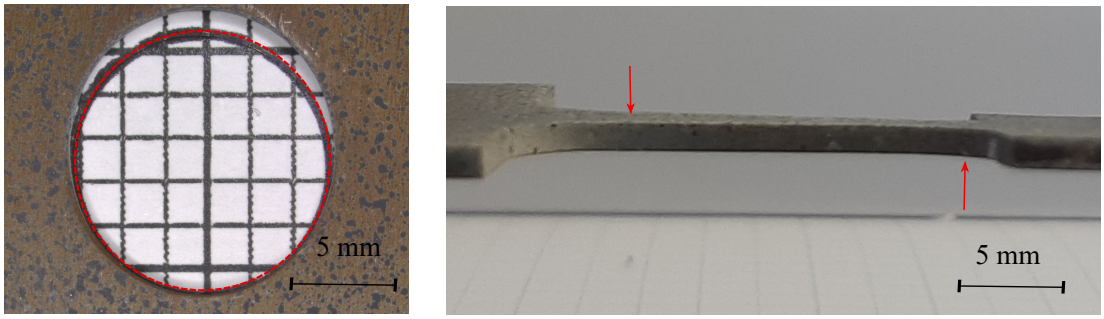

Figure D.1: a) Plastic deformation of the lower-head, b) Distortion on the ZOI of the TA6V specimen after a tensile test at 700 °C

D.1.2 Objective

This study aims to visualize the stress field on the TA6V specimen during tensile test at high temperatures, for example at 700 °C in order to understand the origin of previous observations after high-temperature tensile tests (the plastic deformation of the lower-head of the TA6V specimen and the distortion on the ZOI of the specimen. To this end, an E.F. model of a tensile test at 700 °C is performed. The E.F. model integrates the Hertz contact between the pinned grip and the head of the TA6V specimen). The stress and contact pressure between the pin and the head of the TA6V specimen obtained from the E.F. model is compared with those calculated from the analytical solution.

D.2 Analytical solution of Hertz contact

The solution of the Hertz contact between two cylinders (pin and the circular head of the TA6V specimen) with their axes in parallel to each other is suggested by Atanackovic and Chandrasekara et al. (Atanackovic, 2000 and Chandrasekaran *et al.*, 1987). According to the authors, the semi-contact length (contact radius) (b) is calculated by Equation D.1 (case of one cylinder is placed inside inside another cylinder with larger radius).

$$b = 1.13\left(\frac{F}{l}(\eta_1+\eta_2)\frac{R_1R_2}{R_1-R_2}\right)^{1/2} \tag{D.1}$$

where:

- $\eta_i = \frac{1-\nu_i^2}{E_i}$, $i = 1,2$, E_i is Young's modulus , ν_i is Poisson's ratio of the materials of two cylinders
- R_i, $i = 1,2$ is the radius of the cylinder
- F is the concentrated load applied at the center of one cylinder (the pin)
- l is the length of cylinders

The pressure contact is maximal at the contact radius center and vanishes at the end of contact region. It is calculated by Equation D.2.

$$p_{max} = \frac{F}{\pi bl} \tag{D.2}$$

With numerical values that are taken in Table D.1, the contact radius calculated for a concentrated force applied of 1.36 kN is 0.23 mm. The maximal contact pressure at the center of contact radius is 118 MPa.

Table D.1: Data set used for calculating the analytical solution of Hertz contact between the pin and the head of the TA6V specimen at 700 °C

Parameters	Cylinder 1 (Pin)	Cylinder 2 (Head of specimen)
Material	Inconel 718	TA6V
Young's modulus (E_i [GPa]) at 700 °C	220	60
Poisson's ratio (ν_i)	0.3	0.31
Radius (R_i [mm])	5.89	6.00
Load applied (F [N])	1.36×10^3	
Cylinder length (l [mm])	1.6	

D.3 EF model of Hertz contact between the pin and the head of the TA6V specimen

D.3.1 EF model

The E.F. model aims to calculate the stress distribution on the TA6V specimen during the tensile test in quasi-static condition (load rate is 1×10^{-3} s^{-1}) at 700 °C. The model takes into account the contact between the pinned grip (the pin) and the lower-head of the TA6V specimen. The E.F. model is calculated using Abaqus/CAE, V6.14 software (Dassault System ™, Velizy, France), solver Standard Implicit.

D.3.1.1 Parts in E.F. model

The E.F. model contains two parts: the pin, which is considered as a 3D-rigid body and the TA6V specimen, which is considered as 3D-deformable solid. The pin is in form of a cylinder, has a radius of 5.98 mm and a thickness of 1.6 mm. The geometry and dimension of the TA6V specimen is presented in Appendix A.3. Figure D.2 presents parts of the TA6V specimen and the pin.

D.3.1.2 Material properties

The Young's modulus of the TA6V material at 700 °C is 60 GPa. The Poisson's ratio of this material is 0.31. The E.F. model is limited at elastic behavior of the material.

D.3.1.3 Assembly

Once two parts are built, they are assembled based on the common center point (the pin's center and head's center of the specimen). Figure D.2 presents the dimension of the each parts and the assembly of the E.F. model.

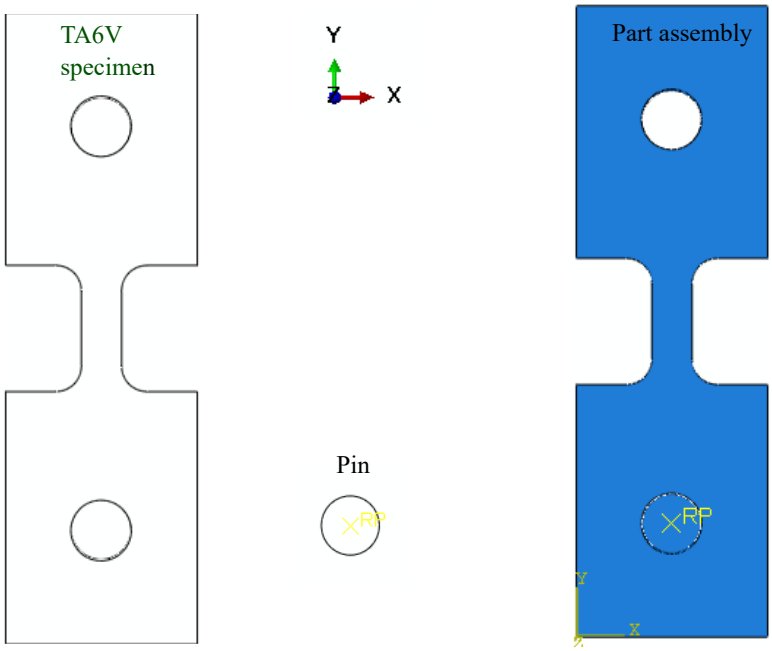

Figure D.2: Parts (TA6V specimen and pin) and assembly of the E.F. model

D.3.1.4 Interaction

In this model, the contact between the surfaces of the pin and the lower head of the TA6V specimen is defined. The contact is frictionless. The surface of the pin is defined as the master surface (in red) and the surface of the lower head is defined as the slave (in pink) surface. The Surface-to-surface contact created between the pin and the TA6V specimen is presented in Figure D.3.

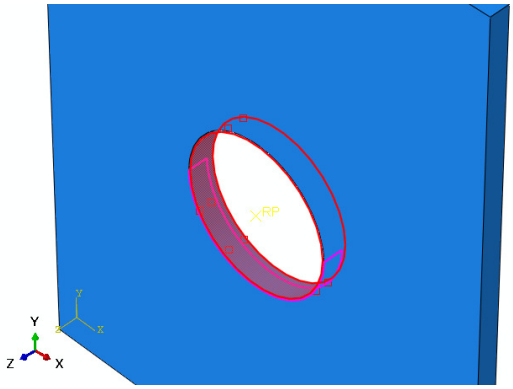

Figure D.3: Surface-to-surface contact created between the pin and the TA6V specimen

D.3.1.5 Boundary conditions and loading

The boundary conditions applied on the upper-head is the encastrement: the displacement and rotation of nodes on the surface are null (Ux=Uy=Uz=Rx=Ry=Rz=0) (Figure D.4a).

A displacement of 1.6 mm, which is equivalent to a load of 1.36 kN is applied the reference point (RF) on the pin. The reference point is created to simulate a displacement of the cross-head of the testing machine in the static condition. The displacement applied on the RF point is presented in Figure D.4b.

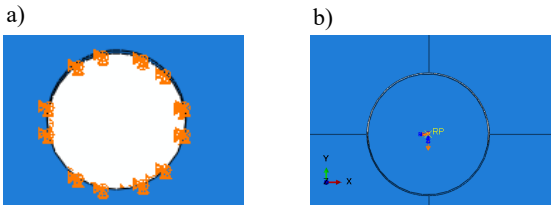

Figure D.4: Boundary conditions (encastrement) and displacement of the reference point applied on the specimen

D.3.1.6 Meshing

The contact zone is finely meshed with an element size of 0.5 mm in order to calculate accurately the contact radius and the contact pressure. Meanwhile, the ZOI of the specimen is also finely meshed with size of 0.5 mm. The element type used for the TA6V specimen is C3D8. The element type used for the pin is R3D4. The meshing on the contact zone and on the ZOI specimen is presented in Figure D.5.

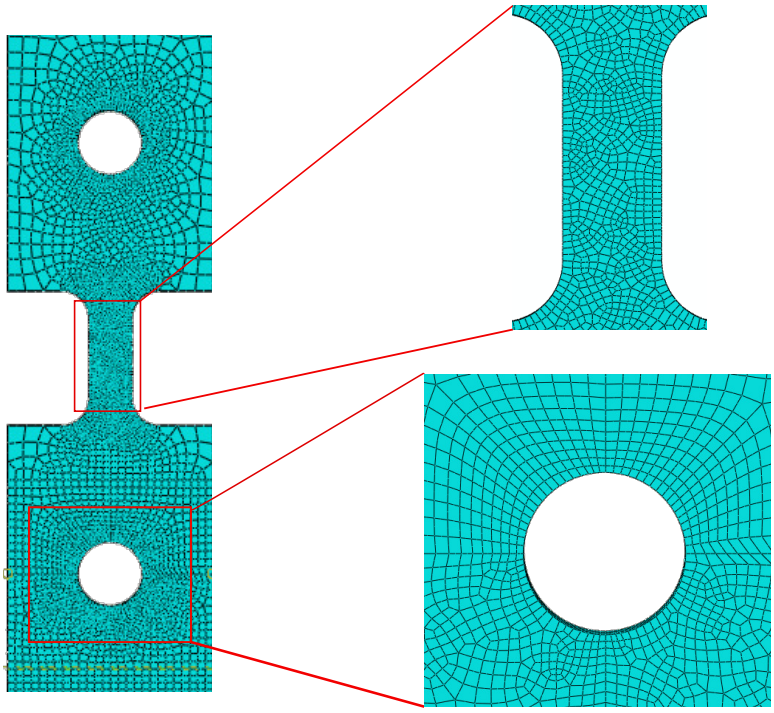

Figure D.5: Meshing of the E.F. model. The contact zone and the ZOI zone are finely meshed with element size of 0.5 mm

D.3.2 Results

Figure D.6 presents respectively the longitudinal displacement and strain fields of the TA6V specimen undergoing a displacement of 1.6 mm. It is shown that the displacement of the pin induces a displacement of 0.053 mm at the contact of the pin and the lower-head. A high deformation near the border of the lower-head is observed. This deformation is greater than the one found on the ZOI of the specimen.

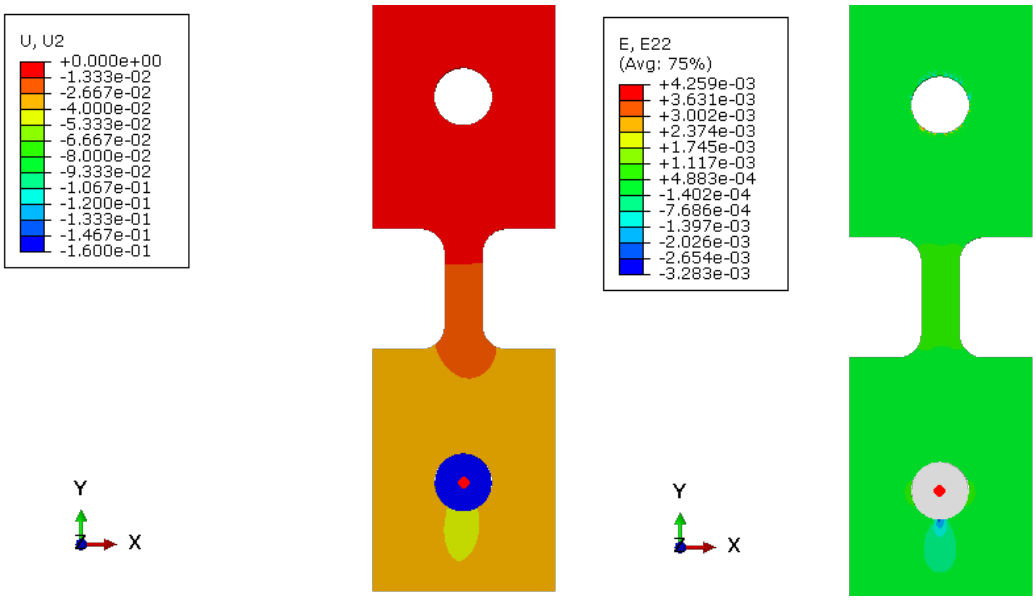

Figure D.6: Longitudinal displacement and train of the TA6V specimen undergoing a displacement of 1.6 mm

Figure D.7 displays the longitudinal stress of the TA6V specimen. The contact radius is 0.276 mm. It is seen the contact between the pin and specimen induces an important compressive stress in longitudinal direction on specimen. At the center of the contact radius, the order of magnitude is from −132 MPa to −179 MPa. This compressive stress, if it is higher than yield strength of TA6V material at 700 °C, it can induce a plastic deformation of the lower-head of the TA6V specimen.

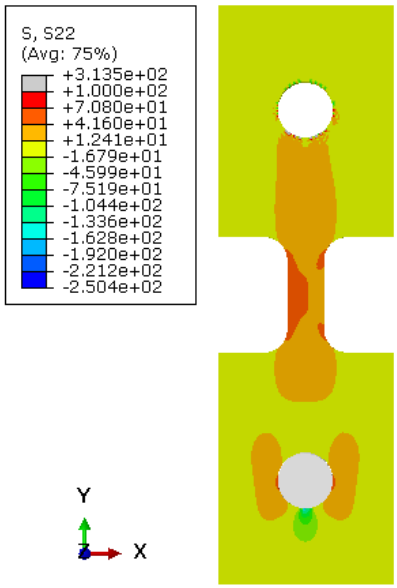

Figure D.7: Longitudinal stress on the TA6V specimen undergoing a displacement of 1.6 mm

Furthermore, it is observed that on the ZOI of the TA6V specimen, the stress filed is not totally homogeneous. The stress on the left side of the ZOI is slightly higher than the right side. This difference of stress can induce distortion or the out-of-plane deformation that was observed after tensile tests.

Figure D.8 presents the contact radius on which the pressure contact CPRESS is calculated. Figure D.9 presents the profile of pressure contact on the contact radius (about 3 mm). The maximal pressure contact is not at the center of contact radius but it is on the left-hand side element. The maximal pressure contact is 700 MPa. The average of contact pressure on the contact radius is 243 MPa $\pm$ 288 MPa.

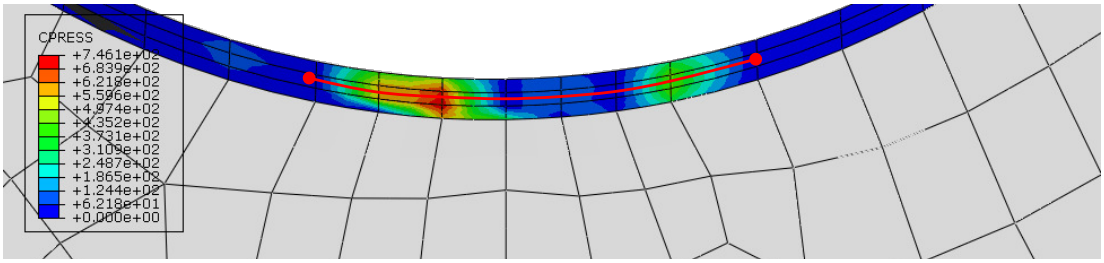

Figure D.8: Contact radius on which the CPRESS is inspected

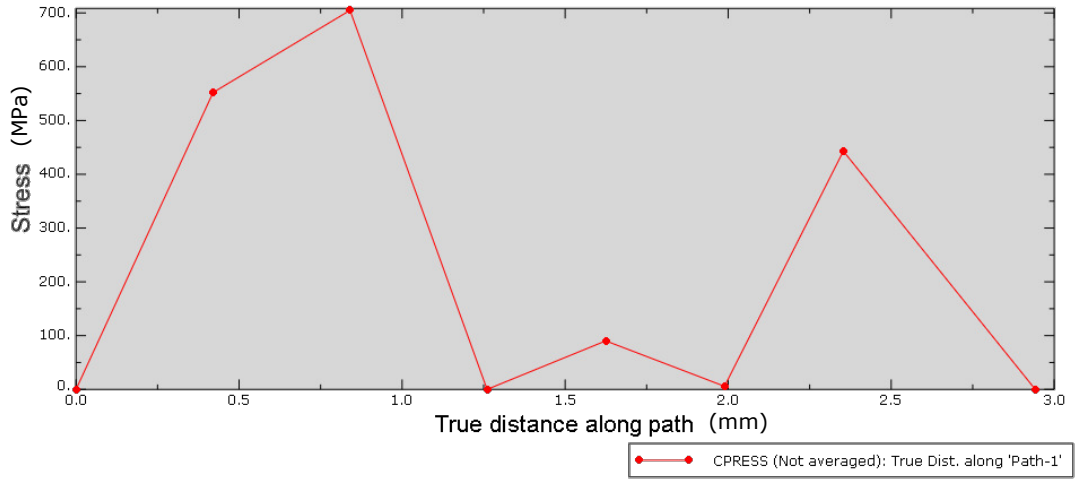

Figure D.9: CPRESS profile on the contact radius (about 3 mm)

D.4 Discussions

D.4.1 Comparison between the analytical solution and EF model

The maximal stress at the contact region obtained by the analytical solution stress is σ_{yy} = -118 MPa while the maximal stress obtained by the E.F. model is -159 MPa in average. The difference between the result obtained by the analytical solution and the numerical model one is 34%. This difference is quite important. The E.F. may not be enough relevant for calculating accurately stress on specimen but it is helpful to understand the origin of the plastic deformation on the lower-head of the specimen.

D.4.2 Limitations of the EF model

The E.F. model and analytical solution of the Hertz contact takes into account only the elastic behavior of the material. The E.F. model within elastic behavior is not enough relevant to explain exactly the plastic deformation of the specimen's head and the specimen distortion. An improvement on the contact zone, for example the friction properties and the plastic-elastic behavior of material could contribute to apprehend undesirable deformation observed during tensile tests.

D.5 Conclusion

After mechanical tensile tests at high temperatures, i.e., at 700 °C, a plastic deformation at the contact zone between the pin and the lower-head of TA6V specimen is observed. Furthermore, an distortion of on the ZOI of the TA6V specimen is noticed. In order to understand the origin of these "undesirable" deformation, an E.F. model that takes into account the elastic behavior of TA6V material and contact between the pin and the TA6V specimen is suggested. Results on stress distribution obtained from the E.F. model shows that the maximal value of stress at the contact pin-TA6V specimen is -159 MPa (in average), which is different by 34 % compared with the analytical solution. This important stress at the contact region can explain the plastic deformation of the specimen's head. Nevertheless, the model is limited at the elastic behavior of the material. Investigation in the elasto-plastic behavior of material or the friction in the contact zone should be performed in order to approach observations that are seen on the TA6V specimen after tensile tests at high temperatures.

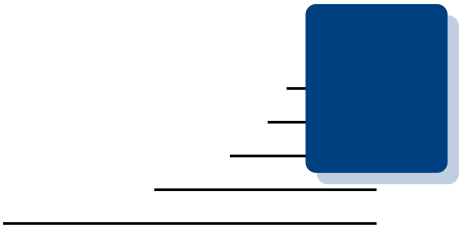

Acronyms

2D-DIC Two-Dimensional Digital Image Correlation .... vii, viii, x, xiv–xvii, xix, xx, 3–5, 7, 14, 15, 18, 34, 37, 39–41, 45, 46, 48–52, 54, 63, 65, 77, 78, 82, 85, 89–97, 101–103, 106, 111, 112, 114–127, 129, 130, 132, 134, 137–141, 144–151, 153, 157–166, 168–180, 185, 189–193, 197, 224

3D-DIC Three-Dimensional Digital Image Correlation 3, 14

ASTM American Society for Testing and Materials 23

BOS Background Oriented Schlieren .... viii, xx, 5, 7, 15, 106, 110, 113–117, 119, 126, 127, 137, 139, 141, 146, 175, 178, 180

BSE Back-Scattered Electron mode working in the Electronic Scanning Microscope 63

C Laser scanning strategy by mode Contouring 59

CAD Computer Aid Design 62

CCD Charge Couple Device ..... xiv, 84, 93, 94, 101, 103

CMOS Complementary Metal-Oxide-Semiconductor 84

d Distance between two nearest speckle dots 63

DFT Discrete Fourier Transformation 120, 133, 150, 153

DIC Digital Image Correlation .... xiii, 3–5, 10, 13–15, 27, 33, 38, 39, 41, 42, 44, 45, 48, 50, 54, 58, 75–78, 84, 86–88, 101, 111, 114, 145, 161, 173, 174, 177, 180, 224

DOE Design of Experiment .... xix, xx, 15, 60, 61, 66, 79, 82, 89, 91–95, 99, 101–103, 118, 122, 138, 178, 180

E Young's modulus of materials 144, 148, 160, 161, 170

EDX Engergy Dispersive X-ray microanalysis 93

E.F. Finite Element Analysis method . . . . . x, xviii, 197, 199, 200, 203, 204

EGM Equilibrium Gap Method 49

FBG Fiber Bragg Grating sensors 18, 26, 27

FEMU Update Finite Element Method . . . . . vi, 49, 50, 145

FEMU-F Update Finite Element Method with equilibrium method 50

FEMU-U Update Finite Element Method with displacement method 50

FEMU-U-F Update Finite Element Method with mixed of displacement method and equilibrium method 50

FIB Focused Ion Beam 37

FT Fourier Transform algorithm 36

H Laser scanning strategy by mode Hatching 59

H+C Laser scanning strategy by mode mix of Hatching and Contouring 59, 62, 66, 67, 79

HT High Temperature . . . . . viii, ix, xiv, xvi, xvii, 4, 14, 15, 24, 54, 55, 57, 62, 63, 79, 86, 89–91, 115–117, 119, 129, 132–134, 137, 139, 144, 146, 148–151, 153, 155, 157–160, 163, 164, 166, 168, 170, 173–180

HT-DIC High-Temperature Digital Image Correlation 111

IR Infrared 117

ISO International Standard Organization 23

LDV Laser Doppler Velocimetry technique . . . . . xx, 113, 115

M1 Speckle preparation technique by using paint (airbrushing or spraying) . . . . . vii, xix, 5, 59–62, 64, 67–69, 71–76, 78–80, 177, 180, 181

M2 Speckle preparation technique by direct anodization . . . . vii, xix, 5, 59–62, 67–69, 71–76, 78–80, 177, 180, 181

M3 Speckle preparation technique by inverse anodization . . . . vii, 5, 59–62, 67–69, 71–73, 75, 76, 78, 79, 177, 180, 181

M4 Speckle preparation technique by laser engraving . . . . . vii, xiv, xix, 5, 59, 62, 64, 71–76, 78, 79, 177

M5 Speckle preparation technique by combining anodization and laser . . . . . vii, xiv, xv, xvii, xx, 5, 59, 62–65, 69, 71–76, 78–80, 89, 93, 95, 98–101, 103, 115, 161, 177, 178, 186, 187

M6 Speckle preparation technique by combining anodization and paint . . . . vii, xiv, xix, 5, 59, 62, 64, 68, 71–76, 78–80, 177

MEMS Micro-electromechanical systems 31

MIG Mean Intensity Gradient ..... xiv, xvii, xix, 6, 39, 63, 64, 71–74, 77–80, 90, 93, 95–98, 101, 103, 178, 185

NCC Normalized cross correlation criterion 42

P Laser power [W] 59–62, 66, 67, 71, 79

PIV Particles Image Velocimetry technique ..... xx, 113–115, 146

r Speckle radius 63

R^2 Coefficient of Least Squared, determined by the Linear Regression method 146, 168, 174, 176

S Laser scanning strategy 59–62, 66, 67, 79

SEM Scanning Electron Microscope 63, 69, 93

SLM Selective Laser Melting manufacturing process 69, 75, 79, 181, 182

SS Subset Size, in [pixel] ..... xv, 117–119, 121–126, 137, 138, 163

SSD Sum of Square Difference criterion 42

ST Step Size, in [pixel] ..... xv, 117–119, 121–126, 137, 138, 163

STD Standard deviation ..... xvi, 19, 67, 111, 117, 118, 125, 130, 134–137, 154, 155, 158, 164, 170, 173, 179

STS-DIC Spatial-Temporal Subset Digital Image Correlation 173

SW Strain Window, in [points] ..... xv, 117–119, 121–126, 137, 138, 163

TA6V Ti-6Al-4V titanium alloy 57

TEC Thermal Expansion Coefficient ..... ix, 15, 39, 144, 146–148, 160, 161, 163, 164, 169–174, 176, 179, 224

V Laser scanning speed, in [m/s] 59–62, 66, 67, 71, 79

VDIC Volumic Digital Image Correlation 14

VFM Virtual Field Method ..... vi, 37, 49, 51, 145

VSG Virtual Strain Gage, in [pixel] 117, 138

WFT Window Fourier Transform algorithm 36

ZNCC Zeros Normalized Cross-Correlation 88, 147

ZNSSD Zero normalized sum of square difference 42, 48, 49, 65

ZOI Zone of Interest .... xiii, xv–xviii, xx, 2, 7, 13, 22, 23, 27, 45, 61, 64, 65, 85, 89, 90, 94, 95, 99, 115–122, 126, 127, 130, 133, 134, 139, 141, 151, 161–163, 165, 167, 173, 178, 180, 182, 189, 190, 192, 193, 197, 200–202, 204

ZSSD Zero-mean sum of square difference 42

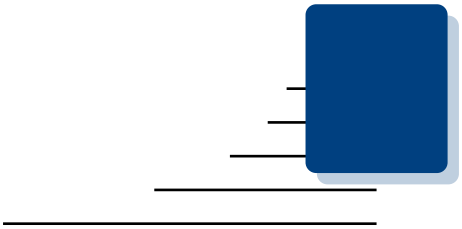

Bibliography

(Anderson, 1991) R. R. Anderson. "Polarized light examination and photography of the skin". *Archives of Dermatology* 127.7 (1991), pp. 1000–1005 (cit. on p. 84).

(Ansart *et al.*, 1995) F. Ansart, H. Ganda, R. Saporte, and J. P. Traverse. "Study of the oxidation of aluminium nitride coatings at high temperature". *Thin Solid Films* 260.1 (1995), pp. 38–46 (cit. on p. 102).

(Anwander *et al.*, 2000) M. Anwander, B. G. Zagar, B. Weiss, and H. Weiss. "Noncontacting strain measurements at high temperatures by the digital laser speckle technique". *Experimental Mechanics* 40.1 (2000), pp. 98–105 (cit. on p. 39).

(Atanackovic, 2000) T. M. Atanackovic. *Theory of Elasticity for Scientists and Engineers*. 1st ed. 2000.. 2000 (cit. on p. 198).

(Avril *et al.*, 2008) S. Avril, M. Bonnet, A. S. Bretelle, M. Grédiac, F. Hild, P. Ienny, F. Latourte, D. Lemosse, S. Pagano, E. Pagnacco, and F. Pierron. "Overview of identification methods of mechanical parameters based on full-field measurements". *Experimental Mechanics* 48.4 (2008), pp. 381–402 (cit. on pp. 37, 49–51).

(Badulescu *et al.*, 2011) C. Badulescu, M. Grédiac, H. Haddadi, J. D. Mathias, X. Balandraud, and H. S. Tran. "Applying the grid method and infrared thermography to investigate plastic deformation in aluminium multicrystal". *Mechanics of Materials* 43.1 (2011), pp. 36–53 (cit. on p. 37).

(Badulescu *et al.*, 2009) C. Badulescu, M. Grédiac, J. D. Mathias, and D. Roux. "A procedure for accurate one-dimensional strain measurement using the grid method". *Experimental Mechanics* 49.6 (2009), pp. 841–854 (cit. on p. 37).

(Bai *et al.*, 2018) R. Bai, H. Jiang, Z. Lei, D. Liu, Y. Chen, C. Yan, W. Tao, and Q. Chu. "Virtual field method for identifying elastic-plastic constitutive parameters of aluminum alloy laser welding considering kinematic hardening". *Optics and Lasers in Engineering* 110.January (2018), pp. 122–131 (cit. on p. 51).

(Bao *et al.*, 2019) S. Bao, Y. Wang, L. Liu, Y. Lu, and P. Yan. "An error elimination method for high-temperature digital image correlation using color speckle and camera". *Optics and Lasers in Engineering* 116.January (2019), pp. 47–54 (cit. on p. 147).

(Bathe, 2006) K.-J. Bathe. *Finite element procedures*. Prentice-Hall, 2006 (cit. on p. 42).

(Beermann *et al.*, 2018) R. Beermann, L. Quentin, E. Reithmeier, and M. Kästner. "Fringe projection system for high-temperature workpieces–design, calibration, and measurement". *Applied Optics* 57.15 (2018), p. 4075 (cit. on p. 34).

(Berke *et al.*, 2014) R. B. Berke and J. Lambros. "Ultraviolet digital image correlation (UV-DIC) for high temperature applications". *Review of Scientific Instruments* 85.4 (2014), p. 045121 (cit. on pp. 88, 94, 101, 102).

(Berny *et al.*, 2018) M. Berny, T. Archer, A. Mavel, P. Beauchêne, S. Roux, and F. Hild. "On the analysis of heat haze effects with spacetime DIC". *Optics and Lasers in Engineering* 111 (2018), pp. 135–153 (cit. on pp. 111, 112, 139, 140, 147).

(Besnard *et al.*, 2006) G. Besnard, F. Hild, and S. Roux. ""Finite-element" displacement fields analysis from digital images: application to Portevin–Le Châtelier bands". *Experimental Mechanics* 46.6 (2006), pp. 789–803 (cit. on pp. 43–45).

(Bigas *et al.*, 2006) M. Bigas, E. Cabruja, J. Forest, and J. Salvi. "Review of CMOS image sensors". *Microelectronics Journal* 37.5 (2006), pp. 433–451 (cit. on p. 85).

(BIPM *et al.*, 2008) IEC BIPM, ILAC IFCC, IUPAP IUPAC, and OIML ISO. *International vocabulary of metrology—Basic and general concepts and associated terms (VIM), 3rd edn. JCGM 200: 2008*. 2008 (cit. on p. 19).

(Bonnaire, 2015) R. Bonnaire. "Caractérisation mécanique des orthèses: Application aux ceintures de soutien lombaire dans le cadre de la lombalgie". PhD thesis. École des Mines de Saint-Étienne, 2015 (cit. on pp. 32–34, 37).

(Bornert *et al.*, 2009) M. Bornert, F. Brémand, P. Doumalin, J. C. Dupré, M. Fazzini, M. Grédiac, F. Hild, S. Mistou, J. Molimard, J-J. Orteu, L. Robert, Y. Surrel, P. Vacher, and B. Wattrisse. "Assessment of digital image correlation measurement errors: Methodology and results". *Experimental Mechanics* 49.3 (2009), pp. 353–370 (cit. on pp. 49, 77).

(Bornert *et al.*, 2018) M. Bornert, P. Doumalin, J. C. Dupré, C. Poilâne, L. Robert, E. Toussaint, and B. Wattrisse. "Assessment of Digital Image Correlation Measurement Accuracy in the Ultimate Error Regime: Improved Models of Systematic and Random Errors". *Experimental Mechanics* 58.1 (2018), pp. 33–48 (cit. on p. 86).

(Boyer, 1996) R. R. Boyer. "An overview on the use of titanium in the aerospace industry". *Materials Science and Engineering: A* 213.1-2 (1996), pp. 103–114 (cit. on p. 11).

(Brémand *et al.*, 2011) F. Brémand, M. Cottron, P. Doumalin, J.-C. Dupré, and V. Valle. "Mesures en mécanique par méthodes optiques". *Techniques de l'ingénieur* R1850 (2011) (cit. on pp. 28, 31, 33).

(Caré, 2013) I. Caré. "Mesures locales de la vitesse d'un fluide". *Techniques de l'ingénieur* 3.R2110 (2013) (cit. on pp. 113, 115).

(Chandrasekaran *et al.*, 1987) N. Chandrasekaran, W. E. Haisler, and R. E. Goforth. "Finite element analysis of Hertz contact problem with friction". *Finite elements in analysis and design* 3.1 (1987), pp. 39–56 (cit. on p. 198).

(Chartrel, 2016) B. Chartrel. "Analyse et optimisation des procédés de formage de pièces en alliage de Titane". PhD thesis. Paris Sciences et Lettres, 2016, p. 136 (cit. on pp. 3, 14, 55, 57).

(L. Chen *et al.*, 2016) L. Chen, Y. Wang, X. Dan, Y. Xiao, and L. Yang. "Experimental research of digital image correlation system in high temperature test". *Seventh International Symposium on Precision Mechanical Measurements*. Vol. 9903. International Society for Optics and Photonics. 2016, p. 990306 (cit. on pp. 147, 174).

(Z. Chen *et al.*, 2015) Z. Chen, C. Quan, F. Zhu, and X. He. "A method to transfer speckle patterns for digital image correlation". *Measurement Science and Technology* 26.9 (2015), p. 95201 (cit. on pp. 62, 76).

(Chi *et al.*, 2018) Y. Chi and B. Pan. "Spatial-Temporal Digital Image Correlation: A Unified Framework". *arXiv preprint arXiv:1812.04826* (2018) (cit. on pp. 147, 174).

(Chiappini *et al.*, 2017) G. Chiappini, L. M. Mattucci, M. El Mehtedi, and M. Sasso. "Identification of plastic behaviour and formability limits of aluminium alloys at high temperature". *Conference Proceedings of the Society for Experimental Mechanics Series* 3 (2017), pp. 233–241 (cit. on p. 37).

(Chu *et al.*, 1985) T. C. Chu, W. F. Ranson, and M. A. Sutton. "Applications of digital-image-correlation techniques to experimental mechanics". *Experimental Mechanics* 25.3 (1985), pp. 232–244 (cit. on p. 45).

(Claudinon *et al.*, 2002) S. Claudinon, P. Lamesle, J.-J. Orteu, and R. Fortunier. "Continuous in situ measurement of quenching distortions using computer vision". *Journal of Materials Processing Technology* 122.1 (2002), pp. 69–81 (cit. on p. 101).

(Crammond *et al.*, 2013) G. Crammond, S. W. Boyd, and J. M. Dulieu-Barton. "Speckle pattern quality assessment for digital image correlation". *Optics and Lasers in Engineering* 51.12 (2013), pp. 1368–1378 (cit. on p. 77).

(CyrilBath, 2020) CyrilBath. *Superplastic forming process*. 2020 (cit. on p. 12).

(Davis, 2004) J. R. Davis. *Tensile testing*. ASM international, 2004 (cit. on pp. 162, 166).

(De Strycker *et al.*, 2010) M. De Strycker, L. Schueremans, W. Van Paepegem, and D. Debruyne. "Measuring the thermal expansion coefficient of tubular steel specimens with digital image correlation techniques". *Optics and Lasers in Engineering* 48.10 (2010), pp. 978–986 (cit. on pp. 146, 147, 174).

(Delmas, 2012) A. Delmas. "Contribution à l'étude de l'effet mirage : application aux mesures dimentionelle et thermique par caméras visibles, proches infrarouge et infrarouge". PhD thesis. Université de Toulouse et Université Libre de Bruxelles, 2012 (cit. on pp. 14, 48, 108, 109, 111, 113, 114, 180).

(Delmas *et al.*, 2013) A. Delmas, Y. Le Maoult, J.-M. Buchlin, T. Sentenac, and J.-J. Orteu. "Shape distortions induced by convective effect on hot object in visible, near infrared and infrared bands". *Experiments in fluids* 54.4 (2013), p. 1452 (cit. on pp. 4, 10, 107, 109, 110, 112, 139, 141, 148).

(Delpueyo *et al.*, 2012) D. Delpueyo, M. Grédiac, X. Balandraud, and C. Badulescu. "Investigation of martensitic microstructures in a monocrystalline Cu-Al-Be shape memory alloy with the grid method and infrared thermography". *Mechanics of Materials* 45 (2012), pp. 34–51 (cit. on p. 37).

(Demazel *et al.*, 2018) N. Demazel, H. Laurent, J. Coër, M. Carin, P. Le Masson, J. Favero, R. Canivenc, and H. Salmon-Legagneur. "Investigation of the progressive hot die stamping of a complex boron steel part using numerical simulations and Gleeble tests". *The International Journal of Advanced Manufacturing Technology* 99.1-4 (2018), pp. 803–817 (cit. on pp. 55, 57).

(Demirel, 2009) M. Demirel. "Contribution à l'optimisation des mesures de température et de déformations par capteur à fibre optique à réseau de Bragg: application au procédé de fabrication des composites par infusion de résine". PhD thesis. École des Mines de Saint-Étienne, EMSE, 2009 (cit. on p. 26).

(Denis *et al.*, 2019) Y. Denis, E. Guzman-Maldonado, F. Morestin, and N. Hamila. "Ultraviolet Digital Image Correlation for Molten Thermoplastic Composites under Finite Strain". *Experimental Mechanics* 59.4 (2019), pp. 439–451 (cit. on pp. 84, 86, 180).

(Dey, 2018) S. Dey. *Hands-On Image Processing with Python: Expert techniques for advanced image analysis and effective interpretation of image data*. Packt Publishing Ltd, 2018 (cit. on p. 83).

(Diamanti *et al.*, 2008) M. V. Diamanti, B. Del Curto, and M. P. Pedeferri. "Interference colors of thin oxide layers on titanium". *Color Research and Application* 33.3 (2008), pp. 221–228 (cit. on p. 58).

(Doitrand *et al.*, 2020) A. Doitrand, R. Estevez, M. Thibault, and P. Leplay. "Fracture and Cohesive Parameter Identification of Refractories by Digital Image Correlation Up to 1200° C". *Experimental Mechanics* (2020), pp. 1–14 (cit. on pp. 111, 139, 146, 147).

(Dong *et al.*, 2017) Y. Dong and B. Pan. "A review of speckle pattern fabrication and assessment for digital image correlation". *Experimental Mechanics* 57.8 (2017), pp. 1161–1181 (cit. on pp. 3, 5, 13, 14, 45, 56, 59, 63, 75–78).

(Dong *et al.*, 2019) Y. Dong, J. Zhao, and B. Pan. "Ultraviolet 3D digital image correlation applied for deformation measurement in thermal testing with infrared quartz lamps". *Chinese Journal of Aeronautics* June (2019), pp. 1–8 (cit. on p. 88).

(Dong *et al.*, 2020) Y. Dong, J. Zhao, and B. Pan. "Ultraviolet 3D digital image correlation applied for deformation measurement in thermal testing with infrared quartz lamps". *Chinese Journal of Aeronautics* 33.3 (2020), pp. 1085–1092 (cit. on pp. 146, 147, 174).

(Felipe-Sesé *et al.*, 2014) L. Felipe-Sesé, P. Siegmann, F. A. Díaz, and E. A. Patterson. "Simultaneous in-and-out-of-plane displacement measurements using fringe projection and digital image correlation". *Optics and Lasers in Engineering* 52.1 (2014), pp. 66–74 (cit. on p. 34).

(Ferdinand, 1999) P. Ferdinand. "Capteurs à fibres optiques à réseaux de Bragg". *Techniques de l'ingénieur* 6735 (1999), pp. 1–24 (cit. on pp. 26, 27).

(Genovese *et al.*, 2006) K. Genovese, L. Lamberti, and C. Pappalettere. "Mechanical characterization of hyperelastic materials with fringe projection and optimization techniques". *Optics and Lasers in Engineering* 44.5 (2006), pp. 423–442 (cit. on p. 34).

(Ghosh *et al.*, 1979) A. K. Ghosh and C. H. Hamilton. "Mechanical behavior and hardening characteristics of a superplastic Ti-6AI-4V alloy". *Metallurgical transactions A* 10.6 (1979), pp. 699–706 (cit. on pp. 2, 12).

(Goupy *et al.*, 2006) J. Goupy and L. Creighton. *Introduction aux plans d'expériences*. Vol. 3. Dunod Paris, 2006 (cit. on pp. 60, 91, 118).

(Grant *et al.*, 2009) B. M. B Grant, H. J. Stone, P. J Withers, and M. Preuss. "High-temperature strain field measurement using digital image correlation". *The Journal of Strain Analysis for Engineering Design* 44.4 (2009), pp. 263–271 (cit. on pp. 88, 101, 146).

(Grediac *et al.*, 2006) M. Grediac, F. Pierront, S. Avril, and E. Toussaint. "The Virtual Fields Method for Extracting Constitutive Parameters From Full-Field Measurements: a Review". *Strain* 42 (2006), pp. 233–253 (cit. on p. 51).

(Grediac *et al.*, 2014) M. Grediac and F. Sur. "50 th Anniversary Article : Effect of Sensor Noise on the Resolution and Spatial Resolution of Displacement and Strain Maps Estimated with the Grid Method". *Strain* 50 (2014), pp. 1–27 (cit. on p. 85).

(Grédiac *et al.*, 2016) M. Grédiac, F. Sur, and B. Blaysat. "The Grid Method for In-plane Displacement and Strain Measurement: A Review and Analysis". *Strain* 52.3 (2016), pp. 205–243 (cit. on pp. 34–37, 46, 51).

(Haddadi *et al.*, 2008) H. Haddadi and S. Belhabib. "Use of rigid-body motion for the investigation and estimation of the measurement errors related to digital image correlation technique". *Optics and Lasers in Engineering* 46.2 (2008), pp. 185–196 (cit. on pp. 47, 48, 137).

(Hammer *et al.*, 2014) J. T. Hammer, J. D. Seidt, and A. Gilat. "Strain measurement at temperatures up to 800 °C utilizing digital image correlation". *Advancement of Optical Methods in Experimental Mechanics, Volume 3*. Springer, 2014, pp. 167–170 (cit. on pp. 14, 55–57, 85, 147).

(Hao *et al.*, 2002) Q. Hao, Y. Song, and Y. Wang. "Effect of CCD integration time on quality of moving image". *Electronic Imaging and Multimedia Technology III* 4925 (2002), pp. 441–446 (cit. on p. 86).

(Harvent, 2010) J. Harvent. "Mesure de formes par corrélation multi-images: application à l'inspection de pièces aéronautiques à l'aide d'un système multi-caméras". PhD thesis. Université de Toulouse, Université Toulouse III-Paul Sabatier, 2010 (cit. on p. 11).

(He *et al.*, 2016) T. He, L. Liu, A. Makeev, and B. Shonkwiler. "Characterization of stress-strain behavior of composites using digital image correlation and finite element analysis". *Composite Structures* 140 (2016), pp. 84–93 (cit. on p. 50).

(Hild *et al.*, 2006) F. Hild and S. Roux. "Digital image correlation: From displacement measurement to identification of elastic properties - A review". *Strain* 42.2 (2006), pp. 69–80. eprint: 0511122 (physics) (cit. on p. 145).

(Hild *et al.*, 2012) F. Hild and S. Roux. "Comparison of Local and Global Approaches to Digital Image Correlation". *Experimental Mechanics* 52.9 (2012), pp. 1503–1519 (cit. on p. 145).

(Hoult *et al.*, 2013) N. A. Hoult, W. Andy Take, C. Lee, and M. Dutton. "Experimental accuracy of two dimensional strain measurements using Digital Image Correlation". *Engineering Structures* 46 (2013), pp. 718–726 (cit. on pp. 47, 48, 145).

(Hu *et al.*, 2018) Y. J. Hu, Y. J. Wang, J. B. Chen, and J. M. Zhu. "A new method of creating high-temperature speckle patterns and its application in the determination of the high-temperature mechanical properties of metals". *Experimental Techniques* 42.5 (2018), pp. 523–532 (cit. on pp. 56, 57, 77).

(Huang *et al.*, 2010) Y. H. Huang, L. Liu, F. C. Sham, Y. S Chan, and S. P. Ng. "Optical strain gauge vs. traditional strain gauges for concrete elasticity modulus determination". *Optik* 121.18 (2010), pp. 1635–1641 (cit. on p. 145).

(Inagaki *et al.*, 2014) I. Inagaki, T. Takechi, Y. Shirai, and N. Ariyasu. "Application and features of titanium for the aerospace industry". *Nippon steel & Sumitomo metal technical report* 106.106 (2014), pp. 22–27 (cit. on pp. 2, 11).

(Incropera *et al.*, 2007) F. P. Incropera, D. P. Dewitt, A. S. Lavine, and T. L. Bergman. *Fundamentals of heat and mass transfer*. John Wiley & Son, 2007 (cit. on pp. 87, 108, 121).

(Jones *et al.*, 2018) E. M. C Jones and P. L. Reu. "Distortion of digital image correlation (DIC) displacements and strains from heat waves". *Experimental Mechanics* 58.7 (2018), pp. 1133–1156 (cit. on pp. 4, 14, 48, 85, 86, 108–111, 114, 119–121, 138–140, 147, 148, 173, 175).

(Julien, 2017) R. Julien. "Comportement thermomécanique et évolution microstructurale d'un alliage Ti-6Al-4V forgé $\alpha + \beta$, durant la trempe : expérimentations, analyses et modélisation" (2017), p. 200 (cit. on p. 169).

(Kim *et al.*, 2020) C. Kim, J. H. Kim, and M. G. Lee. "A virtual fields method for identifying anisotropic elastic constants of fiber reinforced composites using a single tension test: Theory and validation". *Composites Part B: Engineering* 200.May (2020), p. 108338 (cit. on p. 51).

(Kumar *et al.*, 2010) S. Kumar, T. S. N Sankara Narayanan, S. Ganesh Sundara Raman, and S. K. Seshadri. "Thermal oxidation of Ti6Al4V alloy: Microstructural and electrochemical characterization". *Materials Chemistry and Physics* 119.1-2 (2010), pp. 337–346 (cit. on p. 79).

(Lauak, 2020) Lauak. *Example of titanium superplastic forming (SPF) part*. 2020 (cit. on p. 11).

(Lava *et al.*, 2013) P. Lava, W. V. Paepegem, S. Coppieters, I. D. Baere, Y. Wang, and D. Debruyne. "Impact of lens distortions on strain measurements obtained with 2D digital image correlation". *Optics and Lasers in Engineering* 51.5 (2013), pp. 576–584 (cit. on p. 84).

(Le *et al.*, 2017) B. D. Le, S. D. Tran, V. T.N. Dao, and J. Torero. "Deformation capturing of concrete structures at elevated temperatures". *Procedia Engineering* 210 (2017), pp. 613–621 (cit. on p. 88).

(Le Goër *et al.*, 1992) J.-L. Le Goër and J. Avril. "Capteurs à jauges extensométriques". *Techniques de l'ingénieur. Mesures et contrôle* R1860 (1992), R1860–1 (cit. on p. 23).

(Leclerc *et al.*, 2009) H. Leclerc, J-N. Périé, S. Roux, and F. Hild. "Integrated digital image correlation for the identification of mechanical properties". *International Conference on Computer Vision/Computer Graphics Collaboration Techniques and Applications*. 2009, pp. 161–171 (cit. on pp. 50, 145).

(Lecompte *et al.*, 2006) D. Lecompte, A. Smits, S. Bossuyt, H. Sol, J. Vantomme, D. Van Hemelrijck, and A. M. Habraken. "Quality assessment of speckle patterns for digital image correlation". *Optics and Lasers in Engineering* 44.11 (2006), pp. 1132–1145 (cit. on pp. 49, 77).

(Lecompte *et al.*, 2007) D. Lecompte, A. Smits, H. Sol, J. Vantomme, and D. Van Hemelrijck. "Mixed numerical-experimental technique for orthotropic parameter identification using biaxial tensile tests on cruciform specimens". *International Journal of Solids and Structures* 44.5 (2007), pp. 1643–1656 (cit. on p. 50).

(Lemaitre *et al.*, 2020) J. Lemaitre, J.-L. Chaboche, A. Benallal, and R. Desmorat. *Mécanique des matériaux solides-3e éd.* Dunod, 2020 (cit. on pp. 8, 36, 45, 111, 144, 163).

(LePage *et al.*, 2016) W. S. LePage, S. H. Daly, and J. A. Shaw. "Cross Polarization for Improved Digital Image Correlation". *Experimental Mechanics* 56.6 (2016), pp. 969–985 (cit. on pp. 78, 84, 85).

(Leplay *et al.*, 2015) P. Leplay, O. Lafforgue, and F. Hild. "Analysis of Asymmetrical Creep of a Ceramic at 1350 °C by Digital Image Correlation". *Journal of the American Ceramic Society* 98.7 (2015), pp. 2240–2247 (cit. on pp. 111, 112, 140, 146, 147).

(Leplay *et al.*, 2012) P. Leplay, J. Réthoré, S. Meille, and M.-C. Baietto. "Identification of asymmetric constitutive laws at high temperature based on Digital Image Correlation". *Journal of the European Ceramic Society* 32.15 (2012), pp. 3949–3958 (cit. on p. 88).

(Lord *et al.*, 2010) J. D. Lord and R. M. Morrell. "Elastic modulus measurement—obtaining reliable data from the tensile test". *Metrologia* 47.2 (Mar. 2010), S41–S49 (cit. on p. 166).

(Lyons *et al.*, 1996) J. S Lyons, J. Liu, and M. A. Sutton. "High-temperature deformation measurements using digital-image correlation". *Experimental mechanics* 36.1 (1996), pp. 64–70 (cit. on pp. 55, 57, 111, 112, 139, 140, 146, 147, 174).

(C. Ma *et al.*, 2019) C. Ma, Z. Zeng, H. Zhang, and X. Rui. "A Correction Method for Heat Wave Distortion in Digital Image Correlation Measurements Based on Background-Oriented Schlieren". *Applied Sciences* 9.18 (2019), p. 3851 (cit. on p. 147).

(S. Ma *et al.*, 2019) S. Ma, S. Zhou, and Q. Ma. "Image distortion of working digital camera induced by environmental temperature and camera self-heating". *Optics and Lasers in Engineering* 115 (2019), pp. 67–73 (cit. on p. 85).

(Martin *et al.*, 2013) G. Martin, D. Caldemaison, M. Bornert, C. Pinna, Y. Bréchet, M. Véron, J. D. Mithieux, and T. Pardoen. "Characterization of the High Temperature Strain Partitioning in Duplex Steels". *Experimental Mechanics* 53.2 (2013), pp. 205–215 (cit. on p. 37).

(Mauduit *et al.*, 2017) D. Mauduit, M. L. Fournier, K. Grondin, T. Pottier, and Y. Le-Maoult. "Industrial applications of the superplastic forming by using Infra-Red heater". *Procedia Engineering* 207 (2017), pp. 1898–1903 (cit. on p. 12).

(Maurel, 2002) A. Maurel. *Optique géométrique cours. Tome 1*. Edition Berlin, 2002, p. 224 (cit. on p. 107).

(Mayinger *et al.*, 2001) F. Mayinger and O. Feldmann. *Optical Measurements, Techniques and Applications*. Springer Science & Business Media, 2001, p. 416 (cit. on pp. 111–114).

(Mazzoleni *et al.*, 2015) P. Mazzoleni, E. Zappa, F. Matta, and M. A. Sutton. "Thermo-mechanical toner transfer for high-quality digital image correlation speckle patterns". *Optics and Lasers in Engineering* 75 (2015), pp. 72–80 (cit. on pp. 59, 62, 76).

(Molimard *et al.*, 2005) J. Molimard, R. Le Riche, A. Vautrin, and J. R. Lee. "Identification of the four orthotropic plate stiffnesses using a single open-hole tensile test". *Experimental Mechanics* 45.5 (2005), pp. 404–411 (cit. on p. 50).

(Motra *et al.*, 2014) H. B. Motra, J. Hildebrand, and A. Dimmig-Osburg. "Assessment of strain measurement techniques to characterise mechanical properties of structural steel". *Engineering Science and Technology, an International Journal* 17.4 (2014), pp. 260–269 (cit. on p. 22).

(Mueller, 1938) H. Mueller. "The theory of photoelasticity". *Journal of the American Ceramic Society* 21.1 (1938), pp. 27–33 (cit. on p. 28).

(Murienne *et al.*, 2016) B. J. Murienne and T. D. Nguyen. "A comparison of 2D and 3D digital image correlation for a membrane under inflation". *Optics and Lasers in Engineering* 77 (2016), pp. 92–99 (cit. on p. 163).

(Nguyen *et al.*, 2012) T. N. Nguyen, J. M. Huntley, R. L. Burguete, and C. R. Coggrave. "Multiple-view shape and deformation measurement by combining fringe projection and digital image correlation". *Strain* 48.3 (2012), pp. 256–266 (cit. on p. 34).

(Novak *et al.*, 2011) M. D. Novak and F. W. Zok. "High-temperature materials testing with full-field strain measurement: Experimental design and practice". *Review of Scientific Instruments* 82.11 (2011), p. 115101 (cit. on pp. 111, 112, 139, 146, 147).

(Odenberger, 2005) E. Odenberger. "Material characterisation for analyses of titanium sheet metal forming". PhD thesis. Luleå tekniska universitet, 2005 (cit. on pp. 2, 162).

(Odenberger *et al.*, 2013) E. Odenberger, J. Hertzman, and P. Thilderkvist. "Thermo-mechanical sheet metal forming of aero engine components in Ti-6Al-4V – PART 1 : Material characterisation" (2013), pp. 391–402 (cit. on pp. 12, 13, 162, 174).

(Odounga *et al.*, 2018) B. Odounga, R. Moutou Pitti, E. Toussaint, and M. Grédiac. "Mode I fracture of tropical woods using grid method". *Theoretical and Applied Fracture Mechanics* 95 (2018), pp. 1–17 (cit. on pp. 35, 36).

(Orteu *et al.*, 2006) J.-J. Orteu, D. Garcia, L. Robert, and F. Bugarin. "A speckle-texture image generator". *Proceedings of SPIE, the International Society for Optical Engineering* 6341 (2006), 63410H–1 (cit. on p. 58).

(Orteu *et al.*, 2008) J.-J. Orteu, Y. Rotrou, T. Sentenac, and L. Robert. "An innovative method for 3-D shape, strain and temperature full-field measurement using a single type of camera: principle and preliminary results". *Experimental mechanics* 48.2 (2008), pp. 163–179 (cit. on pp. 112, 140).

(B. Pan *et al.*, 2014) B. Pan, T. Jiang, and D. Wu. "Strain measurement of objects subjected to aerodynamic heating using digital image correlation: experimental design and preliminary results". *Review of Scientific Instruments* 85.11 (2014), p. 115102 (cit. on pp. 111, 112, 140, 146, 147).

(B. Pan *et al.*, 2010a) B. Pan, Z. Lu, and H. Xie. "Mean intensity gradient: An effective global parameter for quality assessment of the speckle patterns used in digital image correlation". *Optics and Lasers in Engineering* 48.4 (2010), pp. 469–477 (cit. on pp. 3, 39, 63).

(B. Pan *et al.*, 2010b) B. Pan, D. Wu, and Y. Xia. "High-temperature deformation field measurement by combining transient aerodynamic heating simulation system and reliability-guided digital image correlation". *Optics and Lasers in Engineering* 48.9 (2010), pp. 841–848 (cit. on pp. 14, 55, 57, 77, 85, 88, 94, 101, 111, 112).

(B. Pan *et al.*, 2013) B. Pan, L. Yu, D. Wu, and L. Tang. "Systematic errors in two-dimensional digital image correlation due to lens distortion". *Optics and Lasers in Engineering* 51.2 (2013), pp. 140–147 (cit. on pp. 40, 47, 84).

(Z. Pan *et al.*, 2020) Z. Pan, S. Huang, Y. Su, M. Qiao, and Q. Zhang. "Strain field measurements over 3000 °C using 3D-Digital image correlation". *Optics and Lasers in Engineering* 127 (2020), p. 105942 (cit. on p. 147).

(Pannier *et al.*, 2006) Y. Pannier, S. Avril, R. Rotinat, and F. Pierron. "Identification of elasto-plastic constitutive parameters from statically undetermined tests using the virtual fields method". *Experimental Mechanics* 46.6 (2006), pp. 735–755 (cit. on p. 37).

(Passieux *et al.*, 2015) J. C. Passieux, F. Bugarin, C. David, J. N. Périé, and L. Robert. "Multiscale Displacement Field Measurement Using Digital Image Correlation: Application to the Identification of Elastic Properties". *Experimental Mechanics* 55.1 (2015), pp. 121–137 (cit. on pp. 50, 145).

(Patowary, 2019) K. Patowary. *Fata Morgana Mirage*. 2019 (cit. on p. 107).

(Patterson, 2002) E. A. Patterson. "Digital photoelasticity: Principles, practice and potential". *Strain* 38.1 (2002), pp. 27–39 (cit. on p. 28).

(Pavageau *et al.*, 2004) S. Pavageau, R. Dallier, N. Servagent, and T. Bosch. "A new algorithm for large surfaces profiling by fringe projection". *Sensors and Actuators, A: Physical* 115.2-3 SPEC. ISS. (2004), pp. 178–184 (cit. on p. 34).

(Peng *et al.*, 2012) B. Peng, Q. Zhang, W. Zhou, X. Hao, and L. Ding. "Modified correlation criterion for digital image correlation considering the effect of lighting variations in deformation measurements". *Optical Engineering* 51.1 (2012), p. 017004 (cit. on p. 85).

(Pham, 2014) C. H. Pham. "Vrillage de tôles métalliques ultra-minces après emboutissage". PhD thesis. Université Bretagne Sud, 2014 (cit. on p. 162).

(Pierron *et al.*, 2012) F. Pierron and M. Grédiac. *The virtual fields method: extracting constitutive mechanical parameters from full-field deformation measurements*. Springer Science & Business Media, 2012 (cit. on p. 145).

(Poncelet *et al.*, 2015) M. Poncelet and H. Leclerc. "A Digital Image Correlation Algorithm with Light Reflection Compensation". *Experimental Mechanics* 55.7 (2015), pp. 1317–1327 (cit. on pp. 78, 85).

(Pottier, 2011) T. Pottier. "Identification paramétrique par recalage de modèles éléments finis couplée à des mesures de champs cinématiques et thermiques". PhD thesis. Université de Savoie, 2011 (cit. on pp. 46, 50, 51).

(Raffel, 2015) M. Raffel. "Background-oriented schlieren (BOS) techniques". *Experiments in Fluids* 56.3 (2015), p. 60 (cit. on pp. 7, 111, 114, 115).

(Rascaille, 2012) E. Rascaille. *Random Road Shots 3b: Country Highway Mirage*. 2012 (cit. on p. 107).

(Rastogi, 2003) P. K. Rastogi. *Photomechanics*. Springer Science & Business Media, 2003 (cit. on pp. 28, 31, 33, 84).

(Reu, 2013) P. Reu. "Stereo-rig Design: Lighting-Part 5". *Experimental Techniques* 37.3 (2013), pp. 1–2 (cit. on p. 85).

(Reu, 2014) P. Reu. "All about speckles: aliasing". *Experimental Techniques* 38.5 (2014), pp. 1–3 (cit. on pp. 41, 49, 55, 75, 77).

(Reu, 2015a) P. Reu. "All about speckles: Contrast". *Experimental Techniques* 39.1 (2015), pp. 1–2 (cit. on pp. 47, 48, 55, 75).

(Reu, 2015b) P. Reu. "All about speckles: Speckle density". *Experimental Techniques* 39.3 (2015), pp. 1–2 (cit. on pp. 47, 55).

(Reu, 2015c) P. Reu. "All about Speckles: Speckle size measurement". *Experimental Techniques* 39.3 (2015), pp. 1–2 (cit. on pp. 48, 55, 75).

(Reu, 2015d) P. Reu. "Virtual Strain Gage Size Study". *Experimental Techniques* 39.5 (2015), pp. 1–3 (cit. on pp. 45, 49, 118, 119, 126, 137).

(Reu, 2016) P. Reu. "A realistic error budget for two dimension digital image correlation". *Advancement of Optical Methods in Experimental Mechanics, Volume 3*. Springer, 2016, pp. 189–193 (cit. on pp. 47, 48, 86, 139).

(Reu *et al.*, 2019) P. Reu and E. M. C Jones. "Eliminating air refraction issues in DIC by conducting experiments in vacuum". *Advancement of Optical Methods & Digital Image Correlation in Experimental Mechanics*. Vol. 3. Springer, 2019, pp. 85–87 (cit. on p. 147).

(Robert, 2013) L. Robert. *Mechanical characterisation of materials from optical measurements*. Habilitation à diriger des recherches. 2013 (cit. on pp. 25, 26).

(Rollin *et al.*, 2016) M. Rollin, L. Velay V.and Penazzi, T. Pottier, T. Sentenac, L. Iranzo-Perez, A. Dupuy, and G. Khelifati. "Thermo-Mechanical Modeling of Distortions Promoted during Cooling of Ti-6Al-4V Part Produced by Superplastic Forming". *Materials Science Forum* 838-839 (2016), pp. 196–201 (cit. on pp. 2, 12).

(Sakanashi *et al.*, 2017) Y. Sakanashi, S. Gungor, A. N. Forsey, and P. J. Bouchard. "Measurement of Creep Deformation across Welds in 316H Stainless Steel Using Digital Image Correlation". *Experimental Mechanics* 57.2 (2017), pp. 231–244 (cit. on p. 146).

(Saletti *et al.*, 2016) D. Saletti and P. Forquin. "A comparison of DIC and grid measurements for processing spalling tests with the VFM and an 80-kpixel ultra-high speed camera". *European Physical Journal: Special Topics* 225.2 (2016), pp. 311–323 (cit. on p. 37).

(Schreier *et al.*, 2000) H. W. Schreier, J. R. Braasch, and M. A. Sutton. "Systematic error in digital image correlation by intensity interpolation". *Optical Engineering* 39.November (2000), pp. 2915–2921 (cit. on pp. 45, 49).

(Sciammarella *et al.*, 2012) C. A. Sciammarella and F. M. Sciammarella. *Experimental mechanics of solids*. John Wiley & Sons, 2012 (cit. on pp. 2, 3, 13, 20–22, 28, 29, 33).

(Sharpe, 2008) W. N. Sharpe. *Springer handbook of experimental solid mechanics*. Springer Science & Business Media, 2008 (cit. on pp. 3, 20–25, 27–31, 38).

(Simončič *et al.*, 2017) S. Simončič and P. Podržaj. "An Improved Digital Image Correlation Calculation in the Case of Substantial Lighting Variation". *Experimental Mechanics* 57.5 (2017), pp. 743–753 (cit. on p. 85).

(Sirvin *et al.*, 2019) Q. Sirvin, V. Velay, R. Bonnaire, and L. Penazzi. "Mechanical behaviour modelling and finite element simulation of simple part of Ti-6Al-4V sheet under hot/warm stamping conditions". *Journal of Manufacturing Processes* 38 (2019), pp. 472–482 (cit. on pp. 2, 12, 13, 56–58, 85, 162, 168, 174, 180).

(Smigielski, 2001) P. Smigielski. "Holographie optique-Interférométrie holographique". *Techniques de Ingénieur* R42143210 (2001) (cit. on p. 30).

(Smith *et al.*, 1998) B. W Smith, X. Li, and W. Tong. "Error assessment for strain mapping by digital image correlation". *Experimental Techniques* 22.4 (1998), pp. 19–21 (cit. on p. 145).

(Song *et al.*, 2018) J. Song, J. Yang, F. Liu, and K. Lu. "High temperature strain measurement method by combining digital image correlation of laser speckle and improved RANSAC smoothing algorithm". *Optics and Lasers in Engineering* 111 (2018), pp. 8–18 (cit. on p. 39).

(Song *et al.*, 2020) J. Song, J. Yang, F. Liu, and K. Lu. "Quality assessment of laser speckle patterns for digital image correlation by a Multi-Factor Fusion Index". *Optics and Lasers in Engineering* 124 (2020) (cit. on pp. 38, 39).

(Southon *et al.*, 2018) N. Southon, P. Stavroulakis, R. Goodridge, and R. Leach. "In-process measurement and monitoring of a polymer laser sintering powder bed with fringe projection". *Materials and Design* 157 (2018), pp. 227–234 (cit. on p. 34).

(Stutz *et al.*, 2014) L. Stutz, W. Beck, S. Arends, M. Horstmann, V. Ventzke, and N. Kashaev. "Material saving and cost reduction with hot forming of U-shaped titanium part: Materialeinsparung und Kostenreduzierung durch Heißumformung von U-förmigen Titanbauteilen". *Materialwissenschaft und Werkstofftechnik* 45.9 (2014), pp. 841–846 (cit. on pp. 2, 12, 13).

(Su *et al.*, 2015) Y. Q. Su, X. F. Yao, S. Wang, and Y. J. Ma. "Improvement on measurement accuracy of high-temperature DIC by grayscale-average technique". *Optics and Lasers in Engineering* 75 (2015), pp. 10–16 (cit. on pp. 88, 147).

(Surand, 2013) M. Surand. "Étude du comportement viscoplastique en traction et en fluage de l'alliage TA6V de 20 à 600 degrés Celsius". PhD thesis. Institut National Polytechnique de Toulouse, 2013 (cit. on pp. 162, 168, 174).

(Surrel, 1996) Y. Surrel. "Design of algorithms for phase measurements by the use of phase stepping". *Applied Optics* 35.1 (1996), p. 51 (cit. on p. 34).

(Sutton *et al.*, 2017) M. A. Sutton, F. Matta, D. Rizos, R. Ghorbani, S. Rajan, D. H. Mollenhauer, H. W. Schreier, and A. O. Lasprilla. "Recent progress in digital image correlation: background and developments since the 2013 WM Murray Lecture". *Experimental Mechanics* 57.1 (2017), pp. 1–30 (cit. on pp. 3, 14, 46, 145).

(Sutton *et al.*, 2009) M. A. Sutton, J.-J. Orteu, and H. Schreier. *Image Correlation for Shape, Motion and Deformation Measurements : Basic Concepts, Theory and Applications*. 2009 (cit. on pp. 3, 39–42, 45, 47–49, 51, 119, 137, 145).

(Sutton *et al.*, 2008) M. A. Sutton, J. H. Yan, V. Tiwari, H. W. Schreier, and J.-J. Orteu. "The effect of out-of-plane motion on 2D and 3D digital image correlation measurements". *Optics and Lasers in Engineering* 46.10 (2008), pp. 746–757 (cit. on pp. 47, 163).

(Tang *et al.*, 2019) Y. Tang, M. Yue, X. Fang, and X. Feng. "Synchronous full-field measurement of temperature and deformation based on separated radiation and reflected light". *Optics and Lasers in Engineering* 116.January (2019), pp. 94–102 (cit. on p. 88).

(Thai *et al.*, 2019) T. Q. Thai, R. S. Hansen, A. J. Smith, J. Lambros, and R. B. Berke. "Importance of Exposure Time on DIC Measurement Uncertainty at Extreme Temperatures". *Experimental Techniques* (2019) (cit. on pp. 3, 85, 88, 102).

(Tong, 2005) W. Tong. "An evaluation of digital image correlation criteria for strain mapping applications". *Strain* 41.4 (2005), pp. 167–175 (cit. on pp. 48, 49).

(Touboul *et al.*, 2013) M. Touboul, J. Crepin, G. Rousselier, F. Latourte, and S. Leclercq. "Identification of Local Viscoplastic Properties in P91 Welds from Full Field Measurements at Room Temperature and 625 °C". *Experimental Mechanics* 53.3 (2013), pp. 455–468 (cit. on p. 111).

(Triconnet *et al.*, 2009) K. Triconnet, K. Derrien, F. Hild, and D. Baptiste. "Parameter choice for optimized digital image correlation". *Optics and lasers in Engineering* 47.6 (2009), pp. 728–737 (cit. on p. 138).

(Tung *et al.*, 2010) S. H. Tung, M. H. Shih, and J. C. Kuo. "Application of digital image correlation for anisotropic plastic deformation during tension testing". *Optics and Lasers in Engineering* 48.5 (2010), pp. 636–641 (cit. on p. 145).

(Turner *et al.*, 1990) J. L. Turner and S. S. Russell. "Application of digital image analysis to strain measurement at elevated temperature". *Strain* 26.2 (1990), pp. 55–59 (cit. on pp. 55, 57, 111, 112, 147).

(Valeri *et al.*, 2017) G. Valeri, B. Koohbor, A. Kidane, and M. A. Sutton. "Determining the tensile response of materials at high temperature using DIC and the Virtual Fields Method". *Optics and Lasers in Engineering* 91.November 2016 (2017), pp. 53–61 (cit. on pp. 3, 14, 51, 88, 101).

(Vanderhasten, 2007) M. Vanderhasten. "Ti-6Al-4V: Deformation map and modelisation of tensile behaviour". PhD thesis. Katholieke Universiteit Leuven, 2007, p. 150 (cit. on pp. 2, 11, 58, 126, 162, 168, 174, 190).

(Vautrot *et al.*, 2014) M. Vautrot, P. Balland, O. S. Hopperstad, L. Tabourot, J. Raujol-Veillé, and F. Toussaint. "Experimental Technique to Characterize the Plastic Behaviour of Metallic Materials in a Wide Range of Temperatures and Strain Rates: Application to a High-Carbon Steel". *Experimental Mechanics* 54.7 (2014), pp. 1163–1175 (cit. on pp. 56, 57, 88, 101).

(B. Wang *et al.*, 2016) B. Wang and B. Pan. "Subset-based local vs. finite element-based global digital image correlation: A comparison study". *Theoretical and Applied Mechanics Letters* 6.5 (2016), pp. 200–208 (cit. on p. 44).

(P. Wang *et al.*, 2010) P. Wang, S. Drapier, J. Molimard, A. Vautrin, and J. C. Minni. "Characterization of Liquid Resin Infusion (LRI) filling by fringe pattern projection and in situ thermocouples". *Composites Part A: Applied Science and Manufacturing* 41.1 (2010), pp. 36–44 (cit. on p. 34).

(S. Wang *et al.*, 2015) S. Wang, X. F. Yao, Y. Q. Su, and Y. J. Ma. "High temperature image correction in DIC measurement due to thermal radiation". *Measurement Science and Technology* 26.9 (2015), p. 095006 (cit. on p. 88).

(W. Wang *et al.*, 2017) W. Wang, C. Xu, H. Jin, S. Meng, Y. Zhang, and W. Xie. "Measurement of high temperature full-field strain up to 2000 °C using digital image correlation". *Measurement science and technology* 28.3 (2017), p. 035007 (cit. on pp. 88, 147).

(X. Wang *et al.*, 2017) X. Wang, H. Liu X.and Zhu, and S. Ma. "Spatial-temporal subset based digital image correlation considering the temporal continuity of deformation". *Optics and Lasers in Engineering* 90 (2017), pp. 247–253 (cit. on pp. 147, 174).

(Y. Wang *et al.*, 2012) Y. Wang, P. Lava, S. Coppieters, M. De Strycker, P. Van Houtte, and D. Debruyne. "Investigation of the uncertainty of DIC under heterogeneous strain states with numerical tests". *Strain* 48.6 (2012), pp. 453–462 (cit. on p. 138).

(Y. Wang *et al.*, 2016) Y. Wang, P. Lava, P. Reu, and D. Debruyne. "Theoretical analysis on the measurement errors of local 2D DIC: part II assessment of strain errors of the local smoothing method–approaching an answer to the overlap question". *Strain* 52.2 (2016), pp. 129–147 (cit. on pp. 138, 145).

(Y. Wang *et al.*, 2013) Y. Wang and W. Tong. "A high resolution DIC technique for measuring small thermal expansion of film specimens". *Optics and Lasers in Engineering* 51.1 (2013), pp. 30–33 (cit. on p. 112).

(Wigger *et al.*, 2018) T. Wigger, C. Lupton, and J. Tong. "A parametric study of DIC measurement uncertainties on cracked metals". *Strain* 54.6 (2018), e12291 (cit. on pp. 137, 138).

(Wittevrongel *et al.*, 2015) L. Wittevrongel, P. Lava, S. V. Lomov, and D. Debruyne. "A Self Adaptive Global Digital Image Correlation Algorithm". *Experimental Mechanics* 55.2 (2015), pp. 361–378 (cit. on p. 42).

(Xavier *et al.*, 2007) J. Xavier, S. Avril, F. Pierron, and J. Morais. "Novel experimental approach for longitudinal-radial stiffness characterisation of clear wood by a single test". *Holzforschung* 61.5 (2007), pp. 573–581 (cit. on p. 37).

(Xavier *et al.*, 2009) J. Xavier, S. Avril, F. Pierron, and J. Morais. "Variation of transverse and shear stiffness properties of wood in a tree". *Composites Part A: Applied Science and Manufacturing* 40.12 (2009), pp. 1953–1960 (cit. on p. 37).

(Yan *et al.*, 2018) Z. Yan, W. Liu, Z. Tang, X. Liu, N. Zhang, M. Li, and H. Zhang. "Review on thermal analysis in laser-based additive manufacturing". *Optics and Laser Technology* 106 (2018), pp. 427–441 (cit. on p. 76).

(Yaofeng *et al.*, 2007) S. Yaofeng and J. H. L Pang. "Study of optimal subset size in digital image correlation of speckle pattern images". 45 (2007), pp. 967–974 (cit. on p. 137).

(Yoneyama *et al.*, 2006) S. Yoneyama, H. Kikuta, A. Kitagawa, and K. Kitamura. "Lens distortion correction for digital image correlation by measuring rigid body displacement". *Optical Engineering* 45.2 (2006), pp. 1–9 (cit. on p. 84).

(Yuile *et al.*, 2018) A. Yuile, R. Schwerz, M. Roellig, R. Metasch, and S. Wiese. "Heat haze effects in thermal chamber tensile tests on Digital Image Correlation". *2018 19th International Conference on Thermal, Mechanical and Multi-Physics Simulation and Experiments in Microelectronics and Microsystems (EuroSimE)*. IEEE. 2018, pp. 1–7 (cit. on pp. 108, 112, 139).

(Zhan *et al.*, 2008) Y. Zhan, S. Xue, Q. Yang, S. Xiang, H. He, and R. Zhu. "A novel fiber Bragg grating high-temperature sensor". *Optik* 119.11 (2008), pp. 535–539 (cit. on p. 27).

(D. Zhang *et al.*, 2002) D. Zhang, C. D. Eggleton, and D. D. Arola. "Evaluating the mechanical behavior of arterial tissue using digital image correlation". *Experimental Mechanics* 42.4 (2002), pp. 409–416 (cit. on p. 145).

(T. Zhang *et al.*, 2014) T. Zhang, Y. Liu, D. G. Sanders, B. Liu, W. Zhang, and C. Zhou. "Development of fine-grain size titanium 6Al–4V alloy sheet material for low temperature superplastic forming". *Materials Science and Engineering: A* 608 (2014), pp. 265–272 (cit. on p. 12).

(Zhao *et al.*, 2006) Y. Zhao, Y. Han, Z. Fan, F. Qiu, Y.-C. Kuo, A. E. Kaufman, and K. Mueller. "Visual simulation of heat shimmering and mirage". *IEEE transactions on visualization and computer graphics* 13.1 (2006), pp. 179–189 (cit. on p. 108).

(Zheng *et al.*, 2020) Q. Zheng, N. Mashiwa, and T. Furushima. "Evaluation of large plastic deformation for metals by a non-contacting technique using digital image correlation with laser speckles". *Materials & Design* 191 (2020), p. 108626 (cit. on pp. 39, 56, 57).

(Zuo *et al.*, 2018) C. Zuo, S. Feng, L. Huang, T. Tao, W. Yin, and Q. Chen. "Phase shifting algorithms for fringe projection profilometry: A review". *Optics and Lasers in Engineering* 109.200 (2018), pp. 23–59 (cit. on pp. 32, 34).

RÉSUMÉ

Développement d'une méthode de corrélation d'images numériques en deux dimensions (2D-DIC) pour la mesure de champs de déformation à chaud applicable à la mise en forme d'alliage de titane

Afin de prédire la forme finale des pièces pour les structures aéronautiques après mise en forme à chaud et refroidissement, des modèles de simulations numériques par éléments finis sont utilisés. Pour une validation des champs de déformation obtenus par des modèles de calcul au cours du refroidissement des pièces, il est nécessaire de comparer les résulats calculés à ceux mesurés. Ceci nécessite l'utilisation d'une méthode de mesure fidèle et précise de la cinématique au cours du refroidissement, i.e., lors du passage d'une température de 750 °C à 25 °C. Parmi les méthodes de mesure de champs, la méthode de corrélation d'images numériques (DIC) peut répondre à cette demande. Cependant, cette méthode nécessite d'être améliorée à hautes températures car elle est moins fiable à cause de trois problématiques : (i) la tenue du mouchetis, (ii) la perte de contraste et (iii) l'effet mirage. L'objectif principal de cette thèse est donc d'améliorer la mesure de champs cinématiques à hautes températures, entre 400 °C et 700 °C, en utilisant la méthode de corrélation d'images en deux dimensions (2D-DIC), par la levée des trois verrous scientifiques précédemment cités. Premièrement, une méthode de fabrication de mouchetis résistant à hautes températures et à des grandes déformations est développée. Grâce à la génération numérique de mouchetis, ceux-ci sont répétables et leur taille, distance et densité sont contrôlées. La résolution spatiale est donc améliorée. Deuxièmement, la mise en place de système 2D-DIC est optimisée pour les tests mécaniques dans un espace réduit, comme un four fermé. Cette optimisation permet une amélioration notable du contraste de l'image. Troisièmement, des méthodes de correction pour réduire l'erreur de mesure de déformation causée par l'effet mirage sont suggérées. Une application de cette approche est réalisée dans le cadre de la mesure du module de Young et du coefficient de dilatation thermique d'un alliage TA6V jusqu'à 700 °C. Après l'application des éléments correctifs proposés aux mesures, les valeurs de module de Young et de coefficient de dilation sont réalisés et les valeurs obtenues sont proches de celles de références présentes dans la littérature. Le coefficient de corrélation linéaire R^2 de la courbe liant la déformation à la contrainte obtenue lors de l'essai de traction passe, à 600 °C par exemple, de 0,783 à 0,989. Pour conclure, les résultats obtenus dans cette thèse montrent que la méthode 2D-DIC avec les corrections proposées peut être envisagée pour mesurer de manière fiable des champs de déformation lors de tests mécaniques à chaud. Le passage à des mesures sur pièces mise en forme reste à réaliser.

MOTS-CLÉS : Corrélation d'images numériques, Métrologie, mesure de champs cinématique, Hautes températures, Effet mirages, Alliage de titane.

ABSTRACT

Development of Two-Dimension Digital Image Correlation method (2D-DIC) at high temperatures applicable for the titanium alloy forming process

To predict final shape of aerospace parts manufactured by hot forming processes, numerical models by finite elements are usually suggested. To validate these numerical models, it is necessary to develop a reliable full-field measurement method applied for the cooling phase of the part, from 750 °C to 25 °C. Among kinematic measurement methods, the Digital Image Correlation (DIC) can satisfy this requirement. Nevertheless, the DIC method at high temperatures needs to be improved because of three main problems: i) the speckle resistance, ii) the loss of image contrast and iii) the mirage effect. The study aims to improve the Two-Dimension Digital Image Correlation (2D-DIC) method by dealing with these three problems. First, a speckle fabrication method that can resist high temperatures and high strain is developed. The speckle pattern is repeatable and its size, distance and density are controlled thanks to a computer-generated speckle pattern. Therefore, the spatial strain resolution is improved. Secondly, the 2D-DIC system is improved for a mechanical test in a limited space (in a closing furnace). Thirdly, correction methods to reduce the influence of mirage effects on strain measurements using the 2D-DIC method is suggested. Results obtained from three studies are then used to measure "small" strain of experimental tests at high temperatures. The Young's modulus and the Thermal Expansion Coefficient (TEC) of the material are identified from improved- 2D-DIC method for temperatures up to 700 °C. After corrections, the Young's modulus and the TEC of the TA6V material are close to reference values found in literature. The coefficient R^2 from the linear regression method to determine the Young's modulus from tensile test at 600 °C increases from 0.783 to 0.989. In conclusion, results show a great potential of using the improved-2D-DIC method for full-field kinematic measurements of mechanical tests at high temperatures. The perspective of this study is to measure thermo-mechanical strain fields on an industrial piece during the cooling phase using the improved-2D-DIC method.

KEYWORDS: Digital Image Correlation, Metrology, Kinematic measurements, High temperature, Mirage effect, Titanium alloy.